FEDERAL UNIVERSITY OF JUIZ DE FORA

INSTITUTE OF EXACT SCIENCES
COLLEGE OF ENGINEERING

GRADUATE PROGRAM IN COMPUTATIONAL MODELING

Filipe Fernandes de Paula

Conservative Numerical Methods to Solve the Two-Phase Flow in Porous Media Including Foam Displacement

Juiz de Fora

2022

Filipe Fernandes de Paula

Conservative Numerical Methods to Solve the Two-Phase Flow in Porous Media Including Foam Displacement

Thesis submitted to the Graduate Program in Computational Modeling of Federal University of Juiz de Fora as partial fulfillment of the requirements for the degree of Doctor in Computational Modeling.

Advisor: Prof. Dr. Iury Higor Aguiar da Igreja

Coadvisor: Prof. Dr. Grigori Chapiro

Coadvisor: Prof. Dr. Thiago de Oliveira Quinelato

Juiz de Fora

2022

Ficha catalográfica elaborada através do Modelo Latex do CDC da UFJF com os dados fornecidos pelo(a) autor(a)

F. de Paula, Filipe.
Conservative Numerical Methods to Solve the Two-Phase Flow in Porous Media Including Foam Displacement / Filipe Fernandes de Paula. – 2022.
173 f. : il.

Advisor: Iury Higor Aguiar da Igreja
Coadvisor: Grigori Chapiro
Coadvisor: Thiago de Oliveira Quinelato
Doctorate Thesis – Federal University of Juiz de Fora, Institute of Exact Sciences
College of Engineering. Graduate Program in Computational Modeling, 2022.

1. Hybrid mixed methods. 2. Finite volume methods. 3. Foam injection. 4. Mobility reduction. I. Higor Aguiar da Igreja,, Iury, orient. II. Título.

Filipe Fernandes de Paula

Conservative Numerical Methods to Solve the Two-Phase Flow in Porous Media Including Foam Displacement

Tese apresentada ao Programa de Pós-Graduação em Modelagem Computacional da Universidade Federal de Juiz de Fora como requisito parcial à obtenção do título de Doutor em Modelagem Computacional. Área de concentração: Modelagem Computacional.

Aprovada em 15 de dezembro de 2022.

BANCA EXAMINADORA

Prof(a)Dr(a). Iury Higor Aguiar da Igreja - Orientador

Universidade Federal de Juiz de Fora

Prof(a)Dr(a). Grigori Chapiro - Coorientador

Universidade Federal de Juiz de Fora

Prof(a)Dr(a). Thiago de Oliveira Quinelato - Coorientador

Universidade Federal do Paraná

Prof(a)Dr(a). Pacelli Lidio José Zitha

Technische Universiteit Delft

Prof(a)Dr(a). Maicon Ribeiro Correa

Universidade Estadual de Campinas

Dr(a). José Sérgio de Araújo Cavalcante Filho

Petróleo Brasileiro S.A.

Dr(a). Márcio Rentes Borges

Laboratório Nacional de Computação Científica

Prof(a)Dr(a). Bernardo Martins Rocha

Universidade Federal de Juiz de Fora

Juiz de Fora, 15/12/2022.

Documento assinado eletronicamente por **José Sérgio de Araújo Cavalcante Filho**, **Usuário Externo**, em 15/12/2022, às 16:00, conforme horário oficial de Brasília, com fundamento no § 3° do art. 4° do Decreto n° 10.543, de 13 de novembro de 2020.

Documento assinado eletronicamente por **Pacelli Lídio José Zitha**, **Usuário Externo**, em 15/12/2022, às 16:03, conforme horário oficial de Brasília, com fundamento no § 3° do art. 4° do Decreto n° 10.543, de 13 de novembro de 2020.

Documento assinado eletronicamente por **Thiago de Oliveira Quinelato**, **Usuário Externo**, em 15/12/2022, às 16:05, conforme horário oficial de Brasília, com fundamento no § 3° do art. 4° do Decreto n° 10.543, de 13 de novembro de 2020.

Documento assinado eletronicamente por **Iury Higor Aguiar da Igreja**, **Professor(a)**, em 15/12/2022, às 16:29, conforme horário oficial de Brasília, com fundamento no § 3° do art. 4° do Decreto n° 10.543, de 13 de novembro de 2020.

Documento assinado eletronicamente por **Bernardo Martins Rocha**, **Professor(a)**, em 15/12/2022, às 16:35, conforme horário oficial de Brasília, com fundamento no § 3° do art. 4° do Decreto n° 10.543, de 13 de novembro de 2020.

Documento assinado eletronicamente por **Grigori Chapiro**, **Professor(a)**, em 15/12/2022, às 17:33, conforme horário oficial de Brasília, com fundamento no § 3° do art. 4° do Decreto n° 10.543, de 13 de novembro de 2020.

Documento assinado eletronicamente por **Maicon Ribeiro Correa**, **Usuário Externo**, em 16/12/2022, às 13:14, conforme horário oficial de Brasília, com fundamento no § 3° do art. 4° do Decreto n° 10.543, de 13 de novembro de 2020.

Documento assinado eletronicamente por **Marcio Rentes Borges**, **Usuário Externo**, em 16/12/2022, às 14:25, conforme horário oficial de Brasília, com fundamento no § 3º do art. 4º do Decreto nº 10.543, de 13 de novembro de 2020.

A autenticidade deste documento pode ser conferida no Portal do SEI-Ufjf (www2.ufjf.br/SEI) através do ícone Conferência de Documentos, informando o código verificador **1080525** e o código CRC **CE58543B**.

I dedicate this work to my wife and son.

ACKNOWLEDGEMENTS

First of all, I would like to thank God, the creator of the Universe, Whom sustained me in all this difficult times we are living.

To my family, my beloved wife, son and my parents, for their encouragement and unconditional support in these difficult years of formation.

To Professor Iury Igreja, my advisor, Thiago Quinelato and Grigori Chapiro, my co-advisors, for guidance, support and great help, who played a crucial role in this work.

To the professors of the Graduate Program in Computational Modeling for their teachings, to the staff, who during these years, contributed in some way to our personal and professional enrichment and to SHELL Brazil for the financial support in this journey.

This research was carried out in association with the R&D project registered as ANP 20715-9, “Modelagem matemática e computacional de injeção de espuma usada em recuperação avançada de petróleo” (Universidade Federal de Juiz de Fora (UFJF) / Shell Brasil / ANP) – Mathematical and computational modeling of foam injection as an enhanced oil recovery technique applied to Brazil pre-salt reservoirs, sponsored by Shell Brasil under the ANP R&D levy as “Compromisso de Investimentos com Pesquisa e Desenvolvimento”. This project is carried out in partnership with Petrobras.

"*All models are wrong, but some are useful*"

George E. P. Box

RESUMO

Esta tese se dedica a investigar numericamente como a heterogeneidade, a gravidade e a adsorção de surfactantes afetam o deslocamento de espuma em um meio poroso saturado com água e gás. A presença de espuma na mistura água-gás atua no controle de mobilidade da fase gasosa, contribuindo para a redução dos efeitos de *viscous fingering* e da segregação gravitacional. Para modelar estes fenômenos, uma formulação de fluxo fracionário baseada no conceito de pressão global é empregada, resultando em um sistema de equações diferenciais parciais que descrevem dois problemas acoplados de natureza matemática distintas. A metodologia numérica é baseada na divisão do sistema de equações em dois subsistemas que agrupam equações do mesmo tipo e na aplicação de um método de elementos finitos híbridos para resolver o problema hidrodinâmico e um método de volumes finitos de alta ordem para resolver as equações de transporte. Neste sentido, um algoritmo sequencial é proposto utilizando um esquema de aproximação no tempo implícito e adaptativo. Resultados numéricos validam e mostram uma boa eficiência do algoritmo proposto quando confrontado com resultados de laboratório e comparado com técnicas numéricas usualmente empregadas para escoamentos multifásicos. Além disso, simulações computacionais em cenários complexos, que envolvem heterogeneidades, gravidade, compressibilidade do gás e fenômenos de adsorção mostram a notável capacidade da espuma de aumentar a eficiência de varredura quando comparado ao escoamento na ausência de espuma.

Palavras-chave: Método de elementos finitos. Método de volumes finitos. Espuma. Surfactante. Redução de mobilidade. Meios porosos heterogêneos.

ABSTRACT

This thesis is dedicated to numerically analyzing how heterogeneity, gravity, and surfactant adsorption affect foam displacement in a porous medium saturated with gas and water. The presence of foam in the water-gas mixture acts to control the mobility of the gas phase, contributing to reducing the effects of viscous fingering and gravity override. In order to model these phenomena, a fractional flow formulation based on the global pressure concept is employed, resulting in a system of partial differential equations that describe two coupled problems of distinct mathematical nature. The numerical methodology is based on splitting the system of equations into two subsystems that group equations of the same kind and on applying a hybrid finite element method to solve the hydrodynamic problem and a high-order finite volume method to solve the transport equations. Numerical results validate and show the proposed algorithm's efficiency compared with laboratory results and numerical techniques usually used for multiphase flows. Furthermore, computer simulations in complex scenarios involving heterogeneities, gravity, gas compressibility, and adsorption phenomena show the remarkable ability of foam to increase sweep efficiency when compared to flow in the absence of foam.

Keywords: Finite element methods. Finite volume methods. Foam. Surfactant. Mobility reduction. Heterogeneous porous media.

LIST OF FIGURES

List of Tables

LIST OF ABBREVIATIONS AND ACRONYMS

BDF	Backward Differentiation formula.
BHP	Bottom-Hole Pressure.
EOR	Enhanced Oil Recovery.
ERK	Explicit Runge-Kutta.
FEM	Finite Element Method.
FVM	Finite Volume Method.
FOSSIL	Foam Displacement Simulator.
KNP	Kurganov-Noelle-Petrova.
KT	Kurganov-Tadmor.
MRF	Mobility Reduction Factor.
ODE	Ordinary Differential Equation.
PDE	Partial Differential Equation.
PV	Pore Volume.
REA	Reconstruct Evolve Average.
RK	Runge-Kutta.
SAG	Surfactant Alternating Gas

LIST OF SYMBOLS

A	Parameter of the linear kinetic model that controls the sharpness of the transition from weak to strong foam.
$\mathbf{A}$	Vector of variables in the equilibrium adsorption model.
CC	Geometric factor for well modeling.
C_{mrf}	Maximum gas mobility reduction in linear kinetic model.
C_{s}	Surfactant concentration.
$\bar{C}_{\text{s}}$	Boundary condition on the surfactant concentration.
C_{s}^{eq}	Concentration of surfactant adsorbed onto equilibrium sites on the porous medium.
$C_{\text{s}}^{\text{kin}}$	Concentration of surfactant adsorbed onto kinetic sites on the porous medium.
$C_{\text{s}}^{\text{ref}}$	Reference surfactant concentration for strong net foam generation in the Kovscek's model.
d	Parameter of the stochastic bubble population model related to the modification on foam viscosity.
$\mathfrak{d}$	Spatial dimension.
F_1	Function of the STARS model related to the concentration of surfactant.
F_2	Function of the STARS model related to the action of water saturation in foam behavior.
F_3	Function of the STARS model related to the presence of oil.
F_4	Function of the STARS model related to the gas velocity.
F_5	Function of the STARS model related to the capillary number.
f	Fractional flux function.
$f_{\text{w}\rightarrow\text{s}}^{\text{kin}}$	Net rate of mass transfer from the aqueous phase to the solid phase via time-dependent (kinetic) adsorption.
$fmmob$	Maximum gas mobility reduction in STARS model.
$\mathbf{g}$	Gravity acceleration.
$\mathbf{H}$	Convective numerical flux in the finite volume method.
$\mathbb{K}$	Permeability tensor.
K_1	Parameter of the stochastic bubble population model related to the foam viscosity modification.
K_2	Parameter of the stochastic bubble population model related to the foam viscosity modification.
K_1^{eq}	First Langmuir equilibrium adsorption parameter.
K_2^{eq}	Second Langmuir equilibrium adsorption parameter.
K_1^{kin}	First Langmuir kinetic adsorption parameter.
K_2^{kin}	Second Langmuir kinetic adsorption parameter.
K_{c}	Rate of foam creation in the linear kinetic model.
K_{g}	Rate of foam creation in the stochastic bubble population model.
K_{d}	Rate of foam destruction in the stochastic bubble population model.

K_{des}	Rate of desorption.
k_{-1}	Function of Kovscek's model related to foam coalescence.
k_1	Function of Kovscek's model related to foam generation.
k_{-1}^0	Function of Kovscek's model related to foam coalescence.
k_1^0	Function of Kovscek's model related to foam generation.
k_{rg}	Relative permeability of foamed gas.
k_{rg}^0	Relative permeability of gas in absence of foam.
k_{rg}'	Endpoint of gas relative permeability.
k_{rw}	Endpoint of water relative permeability.
k_{rw}'	Water relative permeability endpoint.
n_{D}	Non-dimensional foam texture.
$\bar{n}_{\text{D}}$	Boundary condition on the non-dimensional foam texture.
n_{f}	Foam texture.
n_{D}^{LE}	Foam texture in local equilibrium.
$\mathbf{n}$	Unit outer normal vector.
$n_{\max}$	Maximum foam texture.
p	Global pressure.
$\bar{p}$	Boundary condition on global pressure.
$\mathbf{P}$	Diffusive numerical flux in the finite volume method.
p_{bh}	Well bottom hole pressure.
P_{c}	Capillary pressure.
P_{c}^*	Limiting capillary pressure.
$P_{\text{c, max}}^*$	Maximum value for limiting capillary pressure in Kovscek's model.
q	Source/sink term.
Q	Well mass flow rate.
r_{p}	Pore radius.
r_{c}	Foam coalescence rate.
r_{eq}	Equivalent radius for well modeling.
r_{g}	Foam generation rate.
SF	Critical water saturation in STARS model.
$sfbet$	Sharpness of transition between high quality and low quality foam in STARS model.
$\mathbf{S}$	Vector of variables for the mathematical model.
S	Saturation.
$\bar{S}$	Boundary condition on saturation.
S_{gr}	Residual gas saturation.
S_{w}^*	Limiting water saturation in the linear kinetic model.
S_{wc}	Connate water saturation.
$\mathbf{u}$	Total superficial velocity.
$\bar{u}$	Boundary condition on total superficial velocity.
$\bar{u}_{C_{\text{s}}}$	Boundary condition on total superficial velocity in the surfactant equation.
$\bar{u}_{n_{\text{D}}}$	Boundary condition on total superficial velocity in the foam texture equation.

$\mathbf{v}$	Interstitial velocity.
W_{frac}	Well fraction for well modeling.
$\mathbf{x}$	Position vector.
α	Parameter of the stochastic bubble population model related to the foam viscosity modification.
Γ	Boundary of the porous medium.
Γ^-	Part of the boundary of the porous medium without diffusive flow.
γ	Parameter of the stochastic bubble population model related to the capillary pressure functions.
ζ	Stochastic bubble population model parameter related to the relative permeability function.
κ_{xx}	xx component of the permeability tensor.
κ_{yy}	yy component of the permeability tensor.
κ	Scalar permeability value.
λ	Mobility.
μ	Viscosity.
ρ	Mass density.
ρ_s	Rock density.
τ	Stress acting on the fluid.
τ_{y}	Yield stress.
ϕ	Porosity.
σ_{wg}	Water-gas surface tension.
ω	Parameter of Kovscek's model to the effect of increasing bubble texture on foam-generation sites.
Ω	Porous medium physical domain.

List of Subscripts

g	Gas phase.
inj	Fluid injection.
i	Spatial direction (x, y or z).
l	Cell index in the finite volume method.
$l \pm 1/2$	Boundary of the cell with index l in the finite volume method.
w	Water phase.
β	General fluid phase (water and gas).

List of Superscripts

0	Initial condition.
D	Dirichlet boundary condition type.
n	Approximation in the previous time step.
N	Neumann boundary condition type.
$n+1$	Approximation in the current time step.
f	Foam.

Contents

1 INTRODUCTION

The oil recovery by injection of gas is a technique that has been used since the 1930s [9]. The sweep efficiency of gas, however, can be affected by gravity (through the *gravity override* phenomenon [10, 11, 12, 13, 14, 15, 16], that occurs when the injected gas accumulates in the upper layers of the reservoir) and by the development of preferential paths (*viscous fingering* [14, 17, 18, 19, 20, 21], due to the gas lower density and viscosity and due to heterogeneities of the porous medium). These challenges can be overcome by enhanced oil recovery (EOR) techniques, processes which recover oil by injecting materials not usually present in the reservoir [22].

An effective EOR technique that can be applied to improve reservoir sweep efficiency is the injection of foam to control gas mobility [10, 13, 14, 15, 21, 23, 24, 25]. Foam in porous media can be defined as a gas dispersion in a liquid such that the liquid phase is continuous and some part of the gas phase is discontinuous. The thin liquid films that separate gas bubbles are called lamellae. The foam injection EOR technique consists of injecting foaming agents, such as surfactants or polymers, in aqueous solutions responsible for creating bubbles in the gas phase. In this sense, the surface tension (or interfacial tension) between the liquid and gas phases must be sufficiently low [26]. Surfactants are a species added to the aqueous solution to alter the surface tension, in order to generate foam in porous media [26]. This approach is also used in environmental remediation problems aimed at decontamination and blocking of pollutants in groundwater and aquifers [27, 28, 29], as well in applications in soil remediation [30] and in agriculture industry, where foam can be used as a carrier for liquid fertilizers [31]. In addition, the reduced mobility caused by foam significantly improves the CO_2 storage potential [32].

The usage of foam in oil recovery is mainly motivated by the reduction of the gas phase mobility [34], since the apparent viscosity of foam is much higher than the viscosity of gas [35, 36, 37]. The improved gas mobility control provided by foam displacement results in a better sweep efficiency, reducing viscous fingering and gravity override [13, 10], as depicted in Figure 1. Although the presence of an oil phase can modify the foam behavior, this thesis considers the flow dynamics of water, gas and foam in porous media since the presence of oil in foam displacement is not fully understood and represents a modeling challenge [33, 38, 39, 40]. In addition, the absence of oil is a reasonable assumption near the injection wells/boundary [41, 42], and a detailed investigation of the water-gas-foam flow behavior can guide the injection for improved sweep efficiency in real applications.

The improvement in sweep efficiency can be affected by the surfactant injection technique adopted [23, 24, 25, 43]. Several injection techniques have been studied, such as the co-injection of pre-foamed gas or surfactant with gas and water at fixed foam quality (i.e., the foamed gas fractional flow) or the alternate injection of foam or surfactant with gas, known as Surfactant Alternating Gas (SAG) [24]. In SAG, foam is formed when the injected gas meets the previously

Figure 1 – Schematic of gas injection vs. foamed gas injection. The foam generation reduces gas mobility, and the wavefront profile is modified.

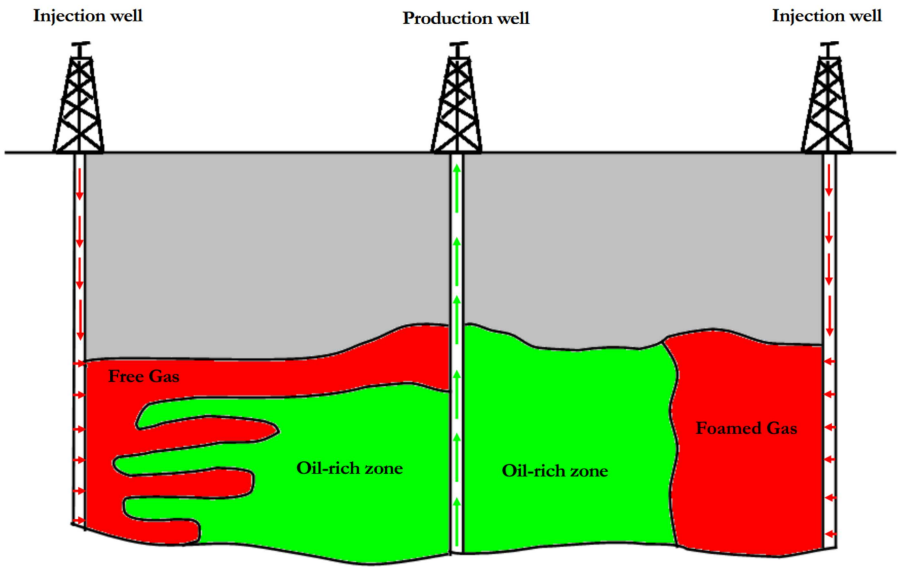

Source: [33].

injected surfactant solution slug and when the surfactant solution meets the previously injected gas slug [43]. The SAG process demonstrated its efficiency in reducing gravity override [24], and viscous fingering in layered porous media [25].

When injecting surfactant solution into porous media (aiming at foam generation), a critical effect inevitably comes up: adsorption. This phenomenon is a process in which the mass of the surfactant species dissolved into the liquid phase (adsorbate) adheres to and accumulates on the surface of a solid (adsorbent) [44]. The attraction of the adsorbate causes the adsorption effect to the surface of the porous medium solid matrix or by reactions between the aqueous solution species and the solid [45]. A consequence of this phenomenon is reducing the amount of surfactant available for foam generation in the liquid phase, directly affecting the effectiveness of foam in the porous media flow. Therefore, it is very important to consider this phenomenon, as it can significantly impact the costs and efficiency of chemical flooding processes, dictating the economic viability of such techniques [46].

1.1 Mathematical Modeling

The multi-phase flow in porous media is modeled by Darcy's law coupled with the mass conservation law for the fluid phases. In order to account for the foam effects, several approaches have been proposed. These approaches can be divided into two main groups: implicit and explicit (also known as mechanistic) foam models [21, 39]. The implicit models the control of gas mobility by a mobility reduction factor that depends on flow variables, such as: water saturation, capillary pressure, surfactant concentration, etc. The implicit models are easily

integrated into the conventional two-phase flow model, and no additional Partial Differential Equation (PDE) is required. In those models, foam is usually assumed to be in local equilibrium, i.e., the bubble creation and coalescence rates are equal, resulting in a dynamic equilibrium of the number of bubbles in the domain. The local equilibrium assumption is based on the fact that the time scale of the mechanisms of foam generation and coalescence are significantly shorter than the time for foam propagation [40]. In the explicit approach, explicit foam parameters (such as foamed-gas velocity and bubble density) are used to model the change in gas viscosity, mobility, and/or relative permeability. As an explicit approach, population balance models are adopted to simulate foam creation, destruction, and transport through porous media. In this approach, it is common to define the foam texture as a quantity representing the number of bubbles (or lamellae) per unit of volume [47, 48, 49].

Models of gas mobility reduction by foam are commonly associated with a decrease in gas relative permeability [50], which the foam behavior is usually defined as Newtonian or based on a modification of the apparent viscosity of gas [8, 34, 51, 52]. The previous assumption leads to non-Newtonian fluid behavior of foam. More realistic foam behavior is usually reported as shear-thinning [52, 34, 53, 51, 39, 54], in which the apparent viscosity decreases with increasing shear rate. An expression to compute shear-thinning effects was derived and validated experimentally by Hirasaki and Lawson [53], which define the apparent viscosity of the gas as dependent on the gas velocity and foam texture.

Mechanisms of foam creation and coalescence play an important role in foam models [34, 55]. Furthermore, the mechanistic models can represent foam both as a Newtonian fluid that obeys Newton's law of viscosity or as a non-Newtonian fluid, of which the viscosity is not constant and is dependent on the shear rate. The explicit models can represent the foam flow physics more realistically than the implicit ones [21, 39]. Among the dynamics of bubble generation and coalescence, we highlight the first-order model proposed by [50, 52], and the approaches associated with the limiting capillary pressure or the gradient of gas pressure introduced in [34, 55]. Moreover, an equation accounting for surfactant concentration that models the transport of the surfactant diluted in the aqueous phase is added. In some cases, it is possible to simplify the population balance equation by assuming a local equilibrium state where foam creation and coalescence rates are equal. In these cases, the computational cost and the complexity of numerically solving the problem can be significantly reduced [2, 5, 50].

The limiting capillary pressure is a critical value reached when the capillary pressure attempting to rupture the bubble is counterbalanced by the disjoining pressure [56]. Thus, above the limiting capillary pressure, foam becomes unstable and immediately coalesces. The surfactant stabilizes the gas/liquid interface preventing the immediate destruction of formed bubbles. Aronson *et al.* propose in [56], through experiments with different surfactants, a limiting capillary pressure dependence on the surfactant concentration. Highly concentrated foaming solutions and robust surfactants lead to high limiting capillary pressures [55, 56]. Therefore, the higher the value of the limiting capillary pressure, the more stable the bubbles, generating a more

significant mobility reduction of the gas phase. A similar behavior is described by the limiting water saturation (equivalent to limiting capillary pressure), at which foam collapses [50, 57].

The mathematical models for multi-phase foam flow are usually solved using explicit-in-time finite difference schemes [39, 58, 59, 60, 61]. However, even in simpler cases, the finite difference approach can fail to represent the effects of surfactant and foam [62]. Therefore, the numerical methodology to be used must be carefully planned. Also, the use of commercial software is prevalent in the literature [57, 63]. The most common approach in commercial software is to represent the effect of foam on fluid displacement using an implicit foam model by including a factor, which is a function of the flow variables, that directly reduces the mobility of the gas phase [21, 39].

1.2 Injectivity

Foam flow simulation can also present problems related to injectivity when the foam injection is performed using wells. Specifically, when adopting the Peaceman well model [64] (the most used in commercial software, such as STARS [4]) in foam simulations, the well injectivity can be significantly underestimated when combined with a coarse grid [65, 62, 42, 66, 67, 68, 69]. The problem of injectivity loss in foam simulations occurs because the Peaceman equation assumes uniform water saturation near the well. That issue can be exacerbated in numerical simulations due to the reservoir spatial discretization, in which inevitably, the dimensions of any grid block containing a well are much larger than the wellbore radius itself [64]. This well modeling approach is usually not adequate when dealing with viscous fluids, such as heavy oil [4], polymer solution [66], or foam [68, 62]. In this context, an alternative to circumvent the injectivity estimate issue using well grid partitioning is presented in this thesis and published in [70].

1.3 Numerical Methods

The numerical approach for solving equations that emerge from the two-phase flow in porous media, including the foam effects, should handle several complexities due to discontinuity, non-linearity, stiffness, and natural instabilities, among others [71]. The numerical methods should also present important properties, such as local conservation of mass, shock capture, non-oscillatory solutions, accurate approximations, and reduced numerical diffusion effects. An effective numerical methodology to solve the foam displacement model and to address its inherent complexities is based on rewriting the problem in terms of global pressure, as in [72, 73]. In this approach, one has two distinct weakly coupled problems [72]: a hydrodynamic problem and a transport problem. The next step is to decouple the system of Partial Differential Equations into two subsystems of equations, each of a different mathematical nature. Thus, each

subsystem can be solved by specific numerical methods, such as the finite element and finite volume methods, according to the mathematical properties of each problem and the balance between accuracy and computational efficiency required in the solution of each subsystem.

Mixed finite element methods are widely used to approximate Darcy's problem. However, these methods restrict the flexibility in constructing finite element approximations due to the need for compatibility between the approximation spaces for pressure, and velocity [74, 75]. In this context, the stable approximation spaces of Raviart-Thomas [76], constructed to meet the conditions of compatibility between velocity and pressure approximation spaces, are usually adopted. The Raviart-Thomas spaces are characterized by the imposition of the continuity of the normal velocity component combined with specific discontinuous interpolations for pressure. In addition, a hybrid mixed finite element approach is chosen to discretize the mathematical problem. Hybrid methods solve a global problem constructed from local problems defined in each element. The link between the global and the local problems is made through Lagrange multipliers, which are defined at the interface of the elements, aiming to weakly impose the continuity conditions between the elements of the mesh. In this way, hybrid formulations allow the elimination of local problems at the level of each element in favor of the Lagrange multiplier; this technique is known as static condensation. Thus, the global system only involves the degrees of freedom associated with the multiplier, significantly reducing the computational cost [77].

On the other hand, several methods have been proposed for the numerical treatment of the transport equations with hyperbolic mathematical nature, especially using the finite volume method [78]. The pioneering scheme in solving this nonlinear hyperbolic partial differential equation is the Lax-Friedrichs (LxF) method [79], which is a first-order central scheme. Despite the simplicity of the LxF method, which does not require solving the Riemann problem, this scheme presents excessive numerical diffusion of $\mathcal{O}\left(\Delta x^2/\Delta t\right)$. Nessyahu and Tadmor developed in [80] a second-order generalization of the LxF method, known as the NT method, presenting numerical diffusion of $\mathcal{O}\left(\Delta x^4/\Delta t\right)$. However, the NT scheme does not support a semi-discrete formulation, and because of the CFL (Courant-Friedrichs-Lewy) condition, which requires reduced time steps, significant refinement in the mesh is required to reduce the effects of numerical diffusion. In order to circumvent numerical diffusion problems, Kurganov and Tadmor (KT) [81] proposed a second-order semi-discrete method based on Godunov's REA (Reconstruct-Evolve-Average) algorithm [82]. This method is known as the KT method and has numerical diffusion of $\mathcal{O}\left(\Delta x^3\right)$. An extension of the KT method that generalizes the numerical flux using more precise information about the local propagation velocities was proposed in [83] by Kurganov, Noelle and Petrova (KNP). Additionally, the KNP scheme has an upwind nature since it respects wave propagation directions by measuring the one-sided local velocities. Thus, the KNP (and also KT) method enables the use of small steps in time without the excessive refinement of the mesh since the numerical diffusion does not depend on the time step Δt.

Based on those numerical approaches, we propose a novel combination of numerical methods that results in an implicit, stable, accurate, and conservative sequential algorithm to

simulate the gas-liquid flow in a heterogeneous porous medium, including foam and surfactant effects. In this context, we decouple the hydrodynamics from the transport system, resulting in a scheme that uses a locally conservative hybrid mixed finite element method to approximate the total velocity and global pressure fields [84] and a high-order finite volume scheme to solve the transport equations [83]. After discretization in space, the resulting system is integrated in time using an implicit multi-step BDF (Backward Differentiation Formula). A scheme that employs variable order and the time step is used to guarantee convergence of approximated solution in each time step [85]. Furthermore, the hydrodynamics and transport problems are solved in different time scales. The complete problem is solved iteratively, and in each iteration, the velocity and pressure fields are computed (hydrodynamics problem), and the velocity field is used to simultaneously approximate fluid saturations, foam texture, and surfactant concentration (transport problem).

1.4 Objectives

This work aims to analyze numerically how porous media heterogeneity, gravity, and surfactant adsorption affect foam displacement in porous media saturated with gas and water. In order to achieve this objective, the following steps were taken:

- A mathematical foam flow model, formed by six partial differential equations, one ordinary differential equation, and other constitutive relations, was derived. The model includes over thirty parameters, and depending on the foam model adopted (see Sec. 2.5), the number of parameters can increase even more.
- The global pressure concept was used to transform the system of equations into a fractional flow formulation. This modeling technique allows us to rewrite the partial differential equations into conservation relations, which makes it possible to split the mathematical problem into two subsystems of equations: the Darcy system and the transport system. Each sub-problem has specific mathematical properties and is approximated by specific numerical methods.
- Combining the central-upwind KNP method for the transport equations with the hybrid mixed finite element method for the Darcy system, we propose a sequential algorithm that proved less computationally expensive using an implicit temporal discretization with adaptive time steps and adaptive order BDF schemes.
- Based on the proposed sequential algorithm, an extensible, reliable, and flexible in-house simulator called FOSSIL was developed. The simulator is capable of simulating several scenarios, that include: flow through heterogeneous or homogeneous porous media, compressible or incompressible gas flow, with or without foam effects flow, and others.

From the point of view of computational implementation, FOSSIL was developed on top of two open-source libraries, SUNDIALS [85] and deal.II [86].

1.5 Main Contributions and Advances

This thesis employs a proposed sequential algorithm to simulate various two-phase (water and gas) flow problems. In particular, one-dimensional numerical experiments are presented to validate the numerical methodology by reproducing results from the literature. Then, simulations in two spatial dimensions using literature data are performed for more complex cases, assuming heterogeneous porous media, gravity, gas compressibility, and surfactant adsorption. In this direction, mathematical and numerical methodologies are used to study the foam flow in porous media, considering different foam models with Newtonian and non-Newtonian behavior. In this context, we summarize the main advances and contributions obtained in this work, which were partially published in [15, 70, 87]:

- The implicit time integration, BDF method, proved to be stable and with reduced computational cost compared to the Runge-Kutta method, usually adopted in this approach [81, 83, 88, 89].
- The KT method (a central scheme) fails to simulate certain types of problems, while the KNP method (a central-upwind scheme) proved itselft to be stable in all tested cases due to its upwind nature.
- Simulations with and without foam highlight the remarkable ability of foam to increase reservoir sweep efficiency by reducing gravity override and viscous fingering effects. This behavior can be credited to the foam effect of reducing foamed gas mobility.
- Numerical comparisons using water-gas-surfactant co-injection and surfactant-alternating-gas (SAG) injection demonstrate that the SAG method is more efficient and yields higher production than co-injection, in agreement with field applications developed by the FAWAG project and described by [23].
- The numerical results of water-gas-surfactant co-injection in a porous medium saturated with water only indicate that the lower the foam quality, the higher the sweep efficiency. This is due to the reduction of f_g in the injection favoring the influx and propagation of more surfactant in the porous medium, which leads to higher foam generation and lower gas mobility.
- The results show that at a certain point, it is no longer advantageous to increase the concentration of surfactant, as there is no significant productivity improvement. Therefore, there is an optimal surfactant concentration value to obtain the highest possible production, using a relatively low amount of surfactant.

- Numerical simulations, including surfactant adsorption, show that the adsorption phenomena can play an important role in foam flow. This phenomenon is responsible for reducing the amount of surfactant in the aqueous phase, and consequently, foam generation is reduced, ultimately impacting the production of the EOR processes.
- Cartesian and hybrid grid partitioning are studied to circumvent the injectivity estimate issue. The Cartesian is characterized by increasing the number of Cartesian grid blocks around the wells (therefore, using smaller blocks). The hybrid grid method is based on the definition of a cylindrical grid in the near-well region that can better capture the radial flow nature of the well injection/production flow. These approaches significantly improve bottom-hole pressure (BHP) estimation, especially using the hybrid grid.

In the end, we provide a better understanding of the foam flow in porous media, and a more accurate and realistic simulation framework.

1.6 Organization of the Thesis

This work is divided, in addition to this introductory chapter, into 7 chapters in the following way:

- In Chapter 2, the equations that model the foam flow in porous media are presented in conjunction with the physical concepts related to such phenomenon and the simplifying hypotheses adopted for the problem. The foam models used in this work are also presented.
- In Chapter 3, it is introduced the numerical methodology to solve the mathematical model. The two numerical methods are applied in each subsystem of equations, and a sequential algorithm employed to couple the methods are also presented.
- In Chapter 4, simulation results obtained using the linear kinetic foam model are presented. First, several one-dimensional results reproduced from literature using the sequential algorithm proposed are shown. The goal is to validate the implementation of the numerical model. Then, simulation solutions are presented; those aim to assess the influence of foam and gravity effects in in a simple incompressible two-phase flow without adsorption using a Newtonian foam model.
- In Chapter 5, it is studied the stochastic bubble population foam model. Initially, the mathematical and numerical models are validated by reproducing results from the literature. Next, in order to assess the behavior of the foam displacement in a highly heterogeneous porous medium using a non-Newtonian foam model, a series of numerical experiments are performed. Then, simulations that use the numerical methodology capability of handling gas compressibility and gravitational phenomena using the stochastic bubble population foam model are presented.

- In Chapter 6, it is investigated the surfactant's ability to generate and stabilize foam through two injection techniques (co-injection and SAG) in order to undermine the viscous fingering phenomena and the high permeability channeling. Furthermore, the influence of foam and surfactant adsorption on two-phase flow in heterogeneous porous media is studied.
- In Chapter 7 is dedicated to study numerical treatments to circumvent the injectivity issues caused by the use of the Peaceman equation in the numerical simulation of chemically enhanced oil recovery (EOR) processes aimed at reducing fluid mobility, such as foam injection, on coarse grids.
- In Chapter 8, concluding remarks and future works are presented.

2 MATHEMATICAL MODELING

The current chapter presents the system of equations that model two-phase flow in porous media, including the effects of foam, surfactant, adsorption, gas compressibility, and gravity. Then, the mathematical model is reformulated in terms of the global pressure to prepare the equations for numerical discretization and computational implementation. In addition, several models that describe the foam behavior are presented.

2.1 Model

Consider a domain $\Omega \subset \mathbb{R}^{\mathfrak{d}}$, $\mathfrak{d} = 1, 2$ or 3, with Lipschitz boundary $\Gamma = \partial\Omega$ for $\mathfrak{d} = 2$ and 3, and the time interval $(0, T]$. Additionally, it is assumed that the porous medium is rigid and always fully saturated, the liquid phase is incompressible, and the thermal effects are negligible. Based on the previous definitions, we introduce the equations to describe immiscible and compressible two-phase flow including foam displacement in a rigid porous medium [48, 51]

$$\phi\frac{\partial}{\partial t}(S_{\mathrm{w}}\, C_{\mathrm{s}}) + (1-\phi)\rho\frac{\partial}{\partial t}\left(C_{\mathrm{s}}^{\mathrm{eq}}\right) + \nabla\cdot(\mathbf{u}_{\mathrm{w}}\, C_{\mathrm{s}}) = -f_{\mathrm{w}\to\mathrm{s}}^{\mathrm{kin}} + q_{\mathrm{s}} \quad \text{in } \Omega\times(0,T], \tag{2.1}$$

$$\phi\frac{\partial}{\partial t}(S_{\mathrm{g}}\, n_{\mathrm{D}}) + \nabla\cdot(\mathbf{u}_{\mathrm{g}}\, n_{\mathrm{D}}) = \frac{\phi S_{\mathrm{g}}(r_{\mathrm{g}} - r_{\mathrm{c}})}{n_{\max}} + q_{\mathrm{f}} \quad \text{in } \Omega\times(0,T], \tag{2.2}$$

$$\frac{\partial}{\partial t}(\phi\rho_\beta S_\beta) + \nabla\cdot\left(\rho_\beta\mathbf{u}_\beta\right) = q_\beta \quad \text{in } \Omega\times(0,T], \tag{2.3}$$

$$\mathbf{u}_\beta = -\mathbb{K}\lambda_\beta\left(\nabla p_\beta - \rho_\beta\mathbf{g}\right) \quad \text{in } \Omega\times(0,T], \tag{2.4}$$

with proper initial and boundary conditions. In this system, (2.1) is the surfactant transport equation, (2.2) is a population balance equation for foam texture [47] and (2.3)–(2.4) account for the transport of phases and hydrodynamics, respectively. We define ϕ as the porosity of the medium, that can vary throughout the domain, and ρ_β, S_β, $\mathbf{u}_\beta$, q_β, and p_β denote density, saturation, superficial velocity, mass source/sink, and pressure, respectively, of phase β (with $\beta = \mathrm{g}$ for the gas phase and $\beta = \mathrm{w}$ for the aqueous phase). The normalized foam texture is defined as $n_{\mathrm{D}} = n_{\mathrm{f}}/n_{\max}$, where n_{f} if dimensional foam texture, $n_{\max}$ is the maximum foam texture. The source/sink for surfactant and foam texture are referred to as q_{s} and q_{f}, respectively. C_{s} is the surfactant concentration in the water phase, $C_{\mathrm{s}}^{\mathrm{eq}}$ is the concentration of surfactant adsorbed at equilibrium in porous medium sites, $\rho = \rho_s/\rho_{\mathrm{w}}$ is the non-dimensional density, with ρ_s being the rock density and ρ_{w} being the water density. For simplicity, densities of water and surfactant component are assumed equal. $f_{\mathrm{w}\to\mathrm{s}}^{\mathrm{kin}}$ is the net rate of mass transfer from the aqueous phase to the solid phase via time-dependent (kinetic) adsorption, to be defined later. Also, $\mathbf{g}$ is the gravity vector pointing in the opposite direction of the vertical axis, and $\mathbb{K} = \kappa(\mathbf{x})\mathbb{I}$ is the intrinsic isotropic permeability tensor, where $\kappa(\mathbf{x})$ is the permeability and $\mathbb{I}$ is the identity tensor.

From the fractional flow theory [90],

$$\lambda_{\mathrm{w}} = \frac{k_{\mathrm{rw}}}{\mu_{\mathrm{w}}}, \quad \lambda_{\mathrm{g}} = \frac{k_{\mathrm{rg}}}{\mu_{\mathrm{g}}^{\mathrm{f}}}, \quad \text{and} \quad \lambda = \lambda_{\mathrm{w}} + \lambda_{\mathrm{g}}, \tag{2.5}$$

denote, respectively, the mobility of water, gas, and total mobility. Moreover, μ_{w} is the viscosity of water, $\mu_{\mathrm{g}}^{\mathrm{f}}$ is the viscosity of gas in the presence of foam, k_{rw} and k_{rg} are relative permeabilities of water and gas, respectively. The foam generation and coalescence functions are given respectively by r_{g} and r_{c}. In Section 2.5, several foam models that propose different generation and coalescence functions are presented.

The capillary pressure P_{c} is considered in the model and is assumed to be a function of S_{w} only, being defined as [73, 91]

$$P_{\mathrm{c}} = P_{\mathrm{c}}\left(S_{\mathrm{w}}\right) = p_{\mathrm{g}} - p_{\mathrm{w}}. \tag{2.6}$$

Under the previous hypotheses, in the next Section, we rewrite equations (2.2)–(2.4) in a fractional flow formulation using the concept of global pressure [72, 73]. This alternative formulation is more suitable to be solved using advanced numerical methods, being far less computationally expensive than the original two-pressure approach [71, 72, 73, 91].

2.2 The Global Pressure Concept

In order to rewrite the two-phase flow equations (2.2)–(2.4) as a system of transport equations coupled with a pressure equation, we adopt the global pressure concept. This approach replaces the two pressure unknowns (one per phase) with only one pressure unknown, called the global pressure, which is defined physically as the pressure that produces the flow of a certain fluid (with mobility λ) related to the sum of water and gas flows (with their respective mobilities) [73]. The new pressure variable is a function of S_{w}, n_{D}, p_{w} and p_{g}, so the water-gas total flow velocity $\mathbf{u} = \mathbf{u}_{\mathrm{w}} + \mathbf{u}_{\mathrm{g}}$ can be written in terms of S_{w}, n_{D}, p and ∇p only. Hence, the number of unknowns for the hydrodynamics problem (2.3)–(2.4) is reduced to two (global pressure p and total Darcy velocity $\mathbf{u}$).

Mathematically, the global pressure p is defined as [72, 73]

$$p = \frac{1}{2}\left(p_{\mathrm{w}} + p_{\mathrm{g}}\right) + \gamma\left(S_{\mathrm{w}}, n_{\mathrm{D}}\right), \tag{2.7}$$

where the function $\gamma\left(S_{\mathrm{w}}, n_{\mathrm{D}}\right)$ is based on [71, 92] and given by

$$\gamma\left(S_{\mathrm{w}}, n_{\mathrm{D}}\right) = \int_{1-S_{\mathrm{gr}}}^{S_{\mathrm{w}}} \left(\frac{1}{2} - f_{\mathrm{w}}\right) \frac{\mathrm{d}P_{\mathrm{c}}}{\mathrm{d}\eta}\mathrm{d}\eta + \int_{\Omega} \psi^{n_{\mathrm{D}}} \left(\frac{\partial n_{\mathrm{D}}}{\partial x}\mathrm{d}x + \frac{\partial n_{\mathrm{D}}}{\partial y}\mathrm{d}y\right), \tag{2.8}$$

with

$$\psi^{n_{\mathrm{D}}} = \int_{1-S_{\mathrm{gr}}}^{S_{\mathrm{w}}} \frac{\partial f_{\mathrm{w}}}{\partial n_{\mathrm{D}}} \frac{\mathrm{d}P_{\mathrm{c}}}{\mathrm{d}\eta}\mathrm{d}\eta, \tag{2.9}$$

and

$$f_{\mathrm{w}} = \frac{\lambda_{\mathrm{w}}}{\lambda} = \frac{\lambda_{\mathrm{w}}}{\lambda_{\mathrm{w}} + \lambda_{\mathrm{g}}}. \tag{2.10}$$

Using (2.6) and (2.7), it is possible to recover the phase pressures as follows:

$$p_{\mathrm{w}} = p - \left[\gamma\left(S_{\mathrm{w}}, n_{\mathrm{D}}\right) + \frac{1}{2}P_{\mathrm{c}}\right], \tag{2.11}$$

$$p_{\mathrm{g}} = p - \left[\gamma\left(S_{\mathrm{w}}, n_{\mathrm{D}}\right) - \frac{1}{2}P_{\mathrm{c}}\right]. \tag{2.12}$$

The introduction of the global pressure as a variable weakens the non-linearity and coupling between the pressure and saturation equations (2.3)–(2.4), resulting in a more numerically tractable form [72]. From definition (2.7), it is possible to observe that the global pressure is not affected by possible variations in absolute permeability and porosity and is, therefore, applicable to heterogeneous porous media.

2.3 Fractional Flow Formulation

To build a fractional flow model for the water-gas-foam flow in porous media, we use the global pressure concept [72] presented in Section 2.2. This approach allows efficient numerical methods to be devised to take advantage of the mathematical characteristics of the alternative fractional flow system of equations.

2.3.1 Pressure Equation

To derive the Darcy law in terms of the global pressure, we first rewrite the phase pressure formulation (2.4) in terms of the global pressure and total velocity by taking the gradient of definition (2.7):

$$\nabla p = \frac{1}{2}\nabla\left(p_{\mathrm{w}} + p_{\mathrm{g}}\right) + \nabla\gamma\left(S_{\mathrm{w}}, n_{\mathrm{D}}\right).$$

Applying algebraic operations, the term $\nabla\gamma\left(S_{\mathrm{w}}, n_{\mathrm{D}}\right)$ is simplified, leading to [71, 92]:

$$\nabla p = \frac{1}{2}\nabla\left(p_{\mathrm{w}} + p_{\mathrm{g}}\right) + \left(\frac{1}{2} - f_{\mathrm{w}}\right)\nabla\left(p_{\mathrm{g}} - p_{\mathrm{w}}\right).$$

Then, we can rewrite the equations above using (2.10), resulting in

$$\lambda\nabla p = \lambda_{\mathrm{w}}\nabla p_{\mathrm{w}} + \lambda_{\mathrm{g}}\nabla p_{\mathrm{g}}. \tag{2.13}$$

Relation (2.13) shows the physical interpretation of the global pressure mathematically: it is the driving pressure of a flow that is equivalent to the combined flow of water and gas.

The next step is, assuming isotropic permeability, to sum the water and gas pressure equations (2.4), which results in:

$$\mathbf{u}_{\mathrm{w}} + \mathbf{u}_{\mathrm{g}} = \mathbf{u} = -\kappa\lambda_{\mathrm{g}}\nabla p_{\mathrm{g}} - \kappa\lambda_{\mathrm{w}}\nabla p_{\mathrm{w}} + \kappa\lambda_{\mathrm{g}}\rho_{\mathrm{g}}\mathbf{g} + \kappa\lambda_{\mathrm{w}}\rho_{\mathrm{w}}\mathbf{g}. \tag{2.14}$$

Using (2.13), we rewrite (2.14) as follows:

$$\mathbf{u} = -\kappa\lambda\left(\nabla p - \mathbf{G}\left(S_{\mathrm{w}}, n_{\mathrm{D}}, p\right)\right), \tag{2.15}$$

where the gravity term $\mathbf{G}\left(S_{\mathrm{w}}, n_{\mathrm{D}}, p\right)$ is given by

$$\mathbf{G}\left(S_{\mathrm{w}}, n_{\mathrm{D}}, p\right) = \frac{\rho_{\mathrm{g}}\lambda_{\mathrm{g}} + \rho_{\mathrm{w}}\lambda_{\mathrm{w}}}{\lambda}\mathbf{g}. \tag{2.16}$$

Next, we write the continuity equation for the total velocity related to the global pressure.

2.3.2 Continuity Equation

In order to write an equation for the total mass balance, the equations describing transport of water and gas phases (2.3) are summed up, resulting in

$$\nabla\cdot\mathbf{u} = -\sum_{\alpha=\mathrm{w},\,\mathrm{g}}\frac{1}{\rho_\beta}\left[\phi S_\beta\frac{\partial\rho_\beta}{\partial t} + \mathbf{u}_\beta\cdot\nabla\rho_\beta - q_\beta\right].$$

Then, under the hypotheses that the capillary pressure is small enough, so that the phase densities are assumed to depend on the global pressure only [72, 73, 91], it is assumed that $\rho_\beta = \rho_\beta\left(p\right)$, and, applying the water incompressibility assumption, we have

$$\nabla\cdot\mathbf{u} = -\frac{\phi\left(1-S_{\mathrm{w}}\right)}{\rho_{\mathrm{g}}}\frac{\mathrm{d}\rho_{\mathrm{g}}}{\mathrm{d}p}\frac{\partial p}{\partial t} - \left(\frac{\mathbf{u}_{\mathrm{g}}}{\rho_{\mathrm{g}}}\right)\cdot\left(\frac{\mathrm{d}\rho_{\mathrm{g}}}{\mathrm{d}p}\nabla p\right) + \frac{q_{\mathrm{w}}}{\rho_{\mathrm{w}}} + \frac{q_{\mathrm{g}}}{\rho_{\mathrm{g}}}. \tag{2.17}$$

Using equations (2.4) and (2.6), and the fact that $\mathbf{u} = \mathbf{u}_{\mathrm{w}} + \mathbf{u}_{\mathrm{g}}$, the phase velocities $\mathbf{u}_{\mathrm{w}}$ and $\mathbf{u}_{\mathrm{g}}$ can be written in a fractional flow formulation as follows:

$$\mathbf{u}_{\mathrm{w}} = f_{\mathrm{w}}\mathbf{u} + \kappa\lambda_{\mathrm{g}}f_{\mathrm{w}}\left(\nabla P_{\mathrm{c}} - \tilde{\boldsymbol{\rho}}\right), \tag{2.18}$$

$$\mathbf{u}_{\mathrm{g}} = \left(1-f_{\mathrm{w}}\right)\mathbf{u} - \kappa\lambda_{\mathrm{g}}f_{\mathrm{w}}\left(\nabla P_{\mathrm{c}} - \tilde{\boldsymbol{\rho}}\right), \tag{2.19}$$

where

$$\tilde{\boldsymbol{\rho}} = \left(\rho_{\mathrm{g}} - \rho_{\mathrm{w}}\right)\mathbf{g}. \tag{2.20}$$

Substituting equation (2.19) in (2.17) and using relation (2.15), we have

$$\begin{aligned}\nabla\cdot\mathbf{u} = &-\frac{\phi\left(1-S_{\mathrm{w}}\right)}{\rho_{\mathrm{g}}}\frac{\mathrm{d}\rho_{\mathrm{g}}}{\mathrm{d}p}\frac{\partial p}{\partial t}\\ &-\frac{1}{\rho_{\mathrm{g}}}\frac{\mathrm{d}\rho_{\mathrm{g}}}{\mathrm{d}p}\left[\left(1-f_{\mathrm{w}}\right)\mathbf{u} - \kappa\lambda_{\mathrm{g}}f_{\mathrm{w}}\left(\nabla P_{\mathrm{c}} - \tilde{\boldsymbol{\rho}}\right)\right]\cdot\left[-\frac{\mathbf{u}}{\lambda}\kappa^{-1} + \mathbf{G}\left(S_{\mathrm{w}}, n_{\mathrm{D}}, p\right)\right]\\ &+\frac{q_{\mathrm{w}}}{\rho_{\mathrm{w}}} + \frac{q_{\mathrm{g}}}{\rho_{\mathrm{g}}}.\end{aligned} \tag{2.21}$$

Rearranging and manipulating the terms, we have the following continuity equation in terms of p, S_{w}, n_{D} and $\mathbf{u}$:

$$\begin{aligned}
&\frac{\phi\left(1-S_{\mathrm{w}}\right)}{\rho_{\mathrm{g}}}\frac{\mathrm{d}\rho_{\mathrm{g}}}{\mathrm{d}p}\frac{\partial p}{\partial t}+\nabla\cdot\mathbf{u}=\frac{\left(1-f_{\mathrm{w}}\right)\kappa^{-1}}{\lambda\rho_{\mathrm{g}}}\frac{\mathrm{d}\rho_{\mathrm{g}}}{\mathrm{d}p}\left(\mathbf{u}\cdot\mathbf{u}\right)\\
&-\frac{\left(1-f_{\mathrm{w}}\right)}{\rho_{\mathrm{g}}}\frac{\mathrm{d}\rho_{\mathrm{g}}}{\mathrm{d}p}\left[\mathbf{G}\left(S_{\mathrm{w}},n_{\mathrm{D}},p\right)+f_{\mathrm{w}}\left(\nabla P_{\mathrm{c}}-\tilde{\boldsymbol{\rho}}\right)\right]\cdot\mathbf{u}\\
&+\frac{\lambda_{\mathrm{g}}f_{\mathrm{w}}}{\rho_{\mathrm{g}}}\frac{\mathrm{d}\rho_{\mathrm{g}}}{\mathrm{d}p}\kappa\left(\nabla P_{\mathrm{c}}-\tilde{\boldsymbol{\rho}}\right)\cdot\mathbf{G}\left(S_{\mathrm{w}},n_{\mathrm{D}},p\right)+\frac{q_{\mathrm{w}}}{\rho_{\mathrm{w}}}+\frac{q_{\mathrm{g}}}{\rho_{\mathrm{g}}}.
\end{aligned}\tag{2.22}$$

2.3.3 Phase Transport Equation

Assuming the incompressibility of the water phase (ρ_{w} is constant) in equation (2.3), we can write the equation for the transport of the aqueous phase as

$$\phi\frac{\partial}{\partial t}\left(S_{\mathrm{w}}\right)+\nabla\cdot\mathbf{u}_{\mathrm{w}}=\frac{q_{\mathrm{w}}}{\rho_{\mathrm{w}}}.\tag{2.23}$$

Next, replacing relation (2.18) in (2.23) and manipulating the terms, we obtain

$$\phi\frac{\partial}{\partial t}\left(S_{\mathrm{w}}\right)+\nabla\cdot\left[f_{\mathrm{w}}\mathbf{u}-\lambda_{\mathrm{g}}f_{\mathrm{w}}\kappa\tilde{\boldsymbol{\rho}}+\kappa\lambda_{\mathrm{g}}f_{\mathrm{w}}\frac{\mathrm{d}P_{\mathrm{c}}}{\mathrm{d}S_{\mathrm{w}}}\nabla S_{\mathrm{w}}\right]=\frac{q_{\mathrm{w}}}{\rho_{\mathrm{w}}}.\tag{2.24}$$

Equation (2.24) presents five terms: accumulation, convection, gravitational, diffusion, and source.

Additionally, the equations (2.1) and (2.2) can be rewritten using the relations (2.18) and (2.19) in the following way:

$$\begin{aligned}
&\phi\frac{\partial}{\partial t}(S_{\mathrm{w}}\,C_{\mathrm{s}})+(1-\phi)\rho\frac{\partial}{\partial t}\left(C_{\mathrm{s}}^{\mathrm{eq}}\right)\\
&\qquad+\nabla\cdot\left(C_{\mathrm{s}}\left[f_{\mathrm{w}}\mathbf{u}-\lambda_{\mathrm{g}}f_{\mathrm{w}}\kappa\tilde{\boldsymbol{\rho}}+\kappa\lambda_{\mathrm{g}}f_{\mathrm{w}}\frac{\mathrm{d}P_{\mathrm{c}}}{\mathrm{d}S_{\mathrm{w}}}\nabla S_{\mathrm{w}}\right]\right)=-f_{\mathrm{w}\to\mathrm{s}}^{\mathrm{kin}}+q_{\mathrm{s}}
\end{aligned}\tag{2.25}$$

$$\begin{aligned}
&\phi\frac{\partial}{\partial t}(S_{\mathrm{g}}\,n_{\mathrm{D}})+\nabla\cdot\left(n_{\mathrm{D}}\left[(1-f_{\mathrm{w}})\mathbf{u}+\lambda_{\mathrm{g}}f_{\mathrm{w}}\kappa\tilde{\boldsymbol{\rho}}-\kappa\lambda_{\mathrm{g}}f_{\mathrm{w}}\frac{\mathrm{d}P_{\mathrm{c}}}{\mathrm{d}S_{\mathrm{w}}}\nabla S_{\mathrm{w}}\right]\right)\\
&\qquad=\frac{\phi S_{\mathrm{g}}(r_{\mathrm{g}}-r_{\mathrm{c}})}{n_{\max}}+q_{\mathrm{f}}.
\end{aligned}\tag{2.26}$$

Grouping equations (2.15), (2.22), (2.24), (2.25), and (2.26), in the next section we present a system of PDEs that models the two-phase flow in porous media, including foam displacement, as a function of the variables: total fluid velocity $\mathbf{u}$, global pressure p, water saturation S_{w}, surfactant concentration C_{s} and foam texture n_{D}.

2.4 Two-Phase Flow in Porous Media Including Foam Displacement Model

From the developed relations (2.15), (2.22), (2.24), (2.25), (2.26), and the following definitions

$$D\left(S_{\mathrm{w}}, n_{\mathrm{D}}, p\right) = \frac{\left(1-f_{\mathrm{w}}\right)\kappa^{-1}}{\lambda\rho_{\mathrm{g}}}\frac{\mathrm{d}\rho_{\mathrm{g}}}{\mathrm{d}p}, \tag{2.27}$$

$$c\left(S_{\mathrm{w}}, p\right) = \frac{\phi\left(1-S_{\mathrm{w}}\right)}{\rho_{\mathrm{g}}}\frac{\mathrm{d}\rho_{\mathrm{g}}}{\mathrm{d}p}, \tag{2.28}$$

$$\mathbf{B}\left(S_{\mathrm{w}}, n_{\mathrm{D}}, p\right) = \frac{\left(1-f_{\mathrm{w}}\right)}{\rho_{\mathrm{g}}}\frac{\mathrm{d}\rho_{\mathrm{g}}}{\mathrm{d}p}\left[\mathbf{G}\left(S_{\mathrm{w}}, n_{\mathrm{D}}, p\right) + f_{\mathrm{w}}\left(\nabla P_{\mathrm{c}} - \tilde{\boldsymbol{\rho}}\right)\right], \tag{2.29}$$

$$F\left(S_{\mathrm{w}}, n_{\mathrm{D}}, p\right) = \frac{1}{\rho_{\mathrm{g}}}\frac{\mathrm{d}\rho_{\mathrm{g}}}{\mathrm{d}p}\lambda_{\mathrm{g}} f_{\mathrm{w}}\left[\kappa\left(\nabla P_{\mathrm{c}} - \tilde{\boldsymbol{\rho}}\right)\right]\cdot\mathbf{G}\left(S_{\mathrm{w}}, n_{\mathrm{D}}, p\right) + \frac{q_{\mathrm{w}}}{\rho_{\mathrm{w}}} + \frac{q_{\mathrm{g}}}{\rho_{\mathrm{g}}}, \tag{2.30}$$

the total fluid velocity $\mathbf{u}$, the global pressure p, the water saturation S_{w}, the foam texture n_{D}, and the surfactant concentration C_{s} satisfy, in $\Omega\times(0,T]$, the following system of equations:

$$\mathbf{u} = -\kappa\lambda\left(\nabla p - \mathbf{G}\left(S_{\mathrm{w}}, n_{\mathrm{D}}, p\right)\right), \tag{2.31}$$

$$c\left(S_{\mathrm{w}}, p\right)\frac{\partial p}{\partial t} + \nabla\cdot\mathbf{u} = D\left(S_{\mathrm{w}}, n_{\mathrm{D}}, p\right)\left(\mathbf{u}\cdot\mathbf{u}\right) + \mathbf{B}\left(S_{\mathrm{w}}, n_{\mathrm{D}}, p\right)\cdot\mathbf{u} + F\left(S_{\mathrm{w}}, n_{\mathrm{D}}, p\right), \tag{2.32}$$

$$\phi\frac{\partial\mathbf{S}}{\partial t} + (1-\phi)\rho\frac{\partial\mathbf{A}}{\partial t} + \sum_{i=1}^{\mathfrak{d}}\frac{\partial\mathbf{f}_i}{\partial x_i} - \nabla\cdot\left(\mathbb{C}\nabla\mathbf{S}\right) = \mathbf{\Phi}, \tag{2.33}$$

$$f_{\mathrm{w}\to\mathrm{s}}^{\mathrm{kin}} = (1-\phi)\rho\frac{\mathrm{d}C_{\mathrm{s}}^{\mathrm{kin}}}{\mathrm{d}t}, \tag{2.34}$$

where i denotes a spatial direction index, $C_{\mathrm{s}}^{\mathrm{kin}}$ is the concentration of surfactant adsorbed onto kinetic sites on porous medium, and

$$\begin{gathered}
\mathbf{S} = \begin{bmatrix} S_{\mathrm{w}} \\ S_{\mathrm{g}} n_{\mathrm{D}} \\ S_{\mathrm{w}} C_{\mathrm{s}} \end{bmatrix}, \qquad \mathbf{A} = \begin{bmatrix} 0 \\ 0 \\ C_{\mathrm{s}}^{\mathrm{eq}} \end{bmatrix}, \qquad \mathbf{f}_i = \begin{bmatrix} f_{\mathrm{w}} u_i - b_i \\ n_{\mathrm{D}} f_{\mathrm{g}} u_i + n_{\mathrm{D}} b_i \\ C_{\mathrm{s}} f_{\mathrm{w}} u_i - C_{\mathrm{s}} b_i \end{bmatrix}, \\
\mathbb{C} = \kappa\lambda_{\mathrm{g}} f_{\mathrm{w}}\frac{\mathrm{d}P_{\mathrm{c}}}{\mathrm{d}S_{\mathrm{w}}}\begin{bmatrix} -1 & 0 & 0 \\ n_{\mathrm{D}} & 0 & 0 \\ -C_{\mathrm{s}} & 0 & 0 \end{bmatrix}, \qquad \mathbf{\Phi} = \begin{bmatrix} \dfrac{q_{\mathrm{w}}}{\rho_{\mathrm{w}}} \\ \dfrac{\phi S_{\mathrm{g}}(r_{\mathrm{g}} - r_{\mathrm{c}})}{n_{\max}} + q_{\mathrm{f}} \\ -f_{\mathrm{w}\to\mathrm{s}}^{\mathrm{kin}} + q_{\mathrm{s}} \end{bmatrix},
\end{gathered} \tag{2.35}$$

where $\mathbf{b} = \kappa\lambda_{\mathrm{g}} f_{\mathrm{w}}\tilde{\boldsymbol{\rho}}$.

The terms $C_{\mathrm{s}}^{\mathrm{eq}}$ and $f_{\mathrm{w}\to\mathrm{s}}^{\mathrm{kin}}$ are defined using the Langmuir model [93, 94], as follows:

$$C_{\mathrm{s}}^{\mathrm{eq}} = \frac{K_1^{\mathrm{eq}} C_{\mathrm{s}}}{1 + K_2^{\mathrm{eq}} C_{\mathrm{s}}}, \qquad\qquad f_{\mathrm{w}\to\mathrm{s}}^{\mathrm{kin}} = \frac{K_1^{\mathrm{kin}} C_{\mathrm{s}}}{1 + K_2^{\mathrm{kin}} C_{\mathrm{s}}} - K_{\mathrm{des}} C_{\mathrm{s}}^{\mathrm{kin}}, \tag{2.36}$$

where K_1^{eq}, K_2^{eq}, K_1^{kin} and K_2^{kin} are empirical parameters, and K_{des} is the rate of desorption. The use of Langmuir curves allows the definition of a limit for the amount of adsorbed surfactant on the medium.

The boundary and initial conditions for the hydrodynamics given by equations (2.31)–(2.32) are given by

$$\mathbf{u}\cdot\mathbf{n}=\bar{u} \qquad \text{on } \Gamma_N\times(0,T], \qquad p=\bar{p} \quad \text{on } \Gamma_D\times(0,T], \tag{2.37}$$

$$p\left(\mathbf{x},0\right)=p^0 \quad \text{in } \Omega, \tag{2.38}$$

where $\Gamma=\Gamma_N\cup\Gamma_D$, $\Gamma_N\cap\Gamma_D=\emptyset$, with Γ_N denoting the boundary region with Neumann condition (specified injection velocity), Γ_D defining the boundary region with Dirichlet condition on the potential, and $\mathbf{n}$ being the unit outer normal vector to Γ. Also, the terms $\bar{u}$ and $\bar{p}$ are the prescribed velocity and pressure for the Dirichlet boundary condition, respectively, and p^0 is the initial condition for pressure. For the transport subsystem (2.33)–(2.34) the boundary and initial conditions become

$$\mathbf{S}=\begin{bmatrix}\bar{S}_{\mathrm{w}}\\ \bar{n}_{\mathrm{D}}\\ \bar{C}_{\mathrm{s}}\end{bmatrix} \quad \text{on } \Gamma_{inj}^{D}\times(0,T], \qquad \begin{bmatrix}\mathbf{u}_{\mathrm{w}}\cdot\mathbf{n}\\ \left(\mathbf{u}_{\mathrm{g}}\cdot\mathbf{n}\right)n_{\mathrm{D}}\\ \left(\mathbf{u}_{\mathrm{w}}\cdot\mathbf{n}\right)C_{\mathrm{s}}\end{bmatrix}=\begin{bmatrix}\bar{u}_{\mathrm{w}}\\ \bar{u}_{n_{\mathrm{D}}}\\ \bar{u}_{C_{\mathrm{s}}}\end{bmatrix} \quad \text{on } \Gamma_{inj}^{N}\times(0,T], \tag{2.39}$$

$$\mathcal{D}\nabla S_{\mathrm{w}}\cdot\mathbf{n}=0 \quad \text{on } \Gamma^{-}\times(0,T],$$

$$\mathbf{S}\left(\mathbf{x},0\right)=\begin{bmatrix}S_{\mathrm{w}}^{0}\\ S_{\mathrm{g}}^{0}n_{\mathrm{D}}^{0}\\ S_{\mathrm{w}}^{0}C_{\mathrm{s}}^{0}\end{bmatrix} \quad \text{in } \Omega, \qquad C_{\mathrm{s}}^{\mathrm{kin}}(\mathbf{x},0)=C_{\mathrm{s}}^{\mathrm{kin},0} \ \text{ in } \ \Omega \tag{2.40}$$

where $\mathcal{D}=\kappa\lambda_{\mathrm{g}}f_{\mathrm{w}}\left(\mathrm{d}P_{\mathrm{c}}/\mathrm{d}S_{\mathrm{w}}\right)$, $\Gamma=\Gamma_{inj}^{D}\cup\Gamma_{inj}^{N}\cup\Gamma^{-}$, $\Gamma_{inj}^{D}\cap\Gamma_{inj}^{N}=\emptyset$, $\Gamma_{inj}^{N}\cap\Gamma^{-}=\emptyset$, with Γ_{inj}^{N} denoting the Neumann boundary region, Γ_{inj}^{D} representing the boundary region with Dirichlet condition on S_{w} and n_{D}, and $\Gamma^{-}=\Gamma\setminus(\Gamma_{inj}^{D}\cup\Gamma_{inj}^{N})$ denoting the boundary region with no diffusion (usually the outflow and no-flow boundaries). Additionally, for the boundary condition, $\bar{S}_{\mathrm{w}}$ is the Dirichlet boundary value for water saturation, $\bar{n}_{\mathrm{D}}$ is the prescribed foam texture, and $\bar{C}_{\mathrm{s}}$ is the boundary condition for the surfactant concentration. Related to the initial condition, S_{w}^{0} is the initial condition for water saturation, n_{D}^{0} is the initial condition for foam texture, C_{s}^{0} is the initial condition for the surfactant concentration, and $C_{\mathrm{s}}^{\mathrm{kin},0}$ is the initial concentration of surfactant adsorbed onto kinetic sites.

Equations (2.31)–(2.32) define a hydrodynamics problem, while Equations (2.33)–(2.34) defines a transport problem that can be associated with the conservation law and the balance equation. In this work, due to the significant mathematical difference between those two types of problems, each sub-system is solved with a distinct numerical method constructed to fit the characteristics of each problem. Numerical approaches to each problem will be presented in the Chapter 3.

Notice that the complete system of equations that models foam flow in porous media (2.31)–(2.34) contains six partial differential equations, one ordinary differential equation (2.34), and other constitutive relations. Additionally, there are over thirty parameters to be entered to solve this system, and depending on the foam model adopted, the number of parameters can

increase even more. So far, the foam model has not been defined. A variety of models can be plugged into the equations (2.31)–(2.34). In Section 2.5, we present models from the literature to represent foam flow in porous media.

Several foam models were proposed in the literature over the years [21, 48, 52, 34, 50, 39, 95]. In the next section, some foam models are presented, and the functions r_{g} and r_{c}, and the foamed gas viscosity $\mu_{\mathrm{g}}^{\mathrm{f}}$ are defined according to the different approaches to model foam flow in porous media.

2.5 Foam Flow Models

The functions r_{g} and r_{c} present in the source/sink term Φ model the physics of the foam generation and coalescence, respectively, in porous media, where r_{g} is the foam generation function, and r_{c} is the foam coalescence function. In general, the gas mobility reduction effect caused by the foam presence in the flow is represented in models by the changing of gas viscosity [48, 52] and/or gas relative permeability [50], depending on the model.

Models representing foam flow through porous media consider foam texture explicitly or implicitly [21, 39]. For the explicit foam texture models, it is possible to make a further sub-classification: population balance models, local equilibrium models, and semi-empirical models. In the case of implicit foam texture, the models are also known as empirical models. Figure 2 shows a hierarchical representation of the modeling of foam flow in porous media.

Figure 2 – Classification of foam models.

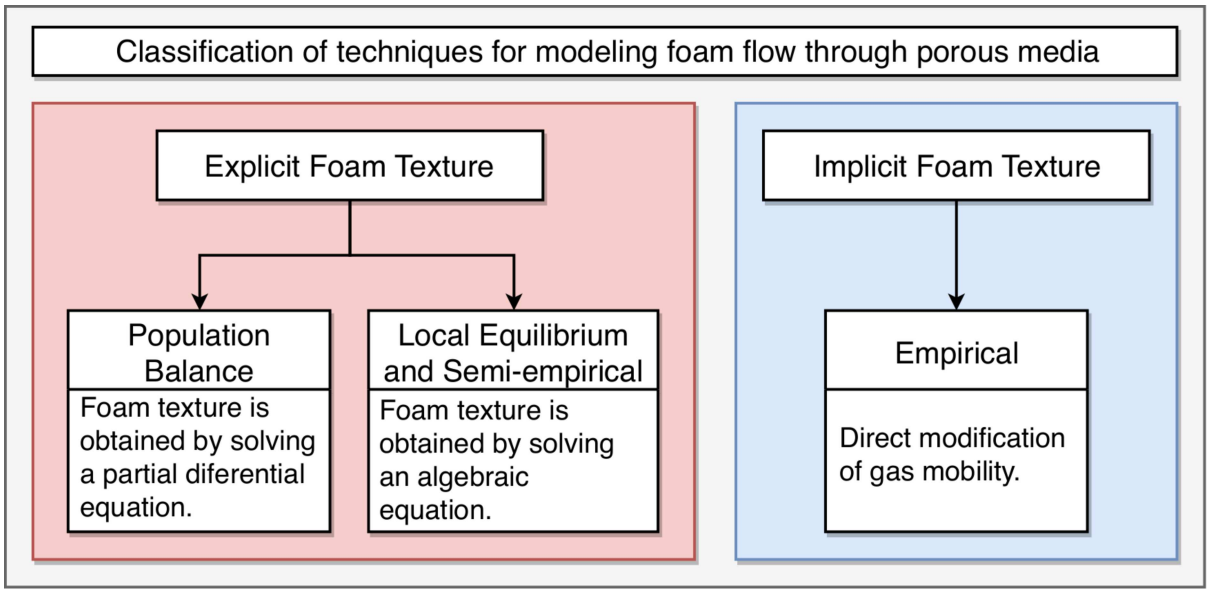

Source: Prepared by the author.

In this context, the foam models classifications described previously can be further

characterized as follows:

- **Population balance:** In the population balance models, foam texture is a variable of the model. Usually, it is obtained from a Partial Differential Equation (PDE), called a population balance equation, for the lamellae. The generation and coalescence functions are provided as source/sink terms for the PDE.
- **Semi-empirical and local equilibrium:** There is an explicit representation of the foam texture, but it is computed from algebraic expressions with parameters adjusted by laboratory experiments. The generation and coalescence function of the population balance models can be used to obtain an equilibrium expression by doing $r_{\mathrm{g}} = r_{\mathrm{c}}$.
- **Empirical:** Foam texture is implicit and not part of the model, i.e., the foam effects on the fluid flow are represented by a mobility reduction factor that depends directly on flow parameters, such as the saturation of the phases. The relation between mobility reduction and saturation is usually defined by foam quality vs. saturation curve fitting. Models in this category are typically assumed to be in local equilibrium.

For the semi-empirical, local equilibrium, and empirical foam models equation (2.2) is discarded, and the mathematical model is simplified. Below we present some mathematical foam flow models [4, 48, 50, 52] adopted in the simulations and comparisons of this work.

2.5.1 STARS Model

In the STARS [4] commercial simulator, the effects of foam are mathematically modeled by an implicit foam model that considers a mobility reduction factor that affects gas mobility. In the general case, the mobility reduction factor, denoted by MRF, involves parameters related to the effects of surfactant in water (F_1), the action of water saturation in foam behavior (F_2), the presence of oil (F_3), the gas velocity (F_4), and the balance between viscous forces and surface tension forces (i.e., capillary number) (F_5), that can be written as

$$\mathrm{MRF} = 1 + fmmob\, F_1 F_2 F_3 F_4 F_5. \tag{2.41}$$

In this work, we adopt only the water saturation (F_2) effects of the STARS mathematical model as follows:

$$\lambda_{\mathrm{g}} = \frac{k_{\mathrm{rg}}}{\mathrm{MRF}\,\mu_{\mathrm{g}}}, \tag{2.42}$$

$$\mathrm{MRF} = 1 + fmmob\, F_2, \tag{2.43}$$

where λ_{g} is the gas mobility (in the presence of foam for MRF > 1), $fmmob$ is the maximum mobility reduction possible . The F_2 term is given by:

$$F_2 = \frac{1}{2} + \frac{1}{\pi}\arctan\left[sfbet(S_{\mathrm{w}} - SF)\right], \tag{2.44}$$

where $sfbet$ and SF are parameters of the model. The SF term is the critical water saturation, that marks the transition between high-quality foam and low-quality foam, while the $sfbet$ parameter controls the sharpness of that transition.

Appendix A presents simulations using the STARS model to reproduce experimental data such as pressure drop and accumulated water production. These laboratory experiments were performed at LASURF[1] and published in [8]. Comparisons with other models are also presented. The STARS foam model was used because it assumes local equilibrium, simplifying the fitting of the model parameters to the experimental data.

In Chapter 7, we study injectivity issues caused by the use of the Peaceman equation in the numerical simulation of chemically enhanced oil recovery processes aimed at reducing fluid mobility, such as foam injection, on coarse grids. Analytical and numerical results were presented using the STARS foam model. Additionally, Appendix C shows comparisons, using the STARS model, between the CMG-STARS commercial simulator and the in-house simulator developed using the numerical methodology proposed in this work (see Chapter 3).

2.5.2 Linear Kinetic Model

The Linear Kinetic foam model, proposed in [50], considers a significant and nearly constant reduction in gas mobility at regions of high water saturation and an abrupt weakening or collapse of foam at the limiting capillary pressure (or, equivalently, at the limiting water saturation). In this approach, foam texture in local equilibrium ($n_{\mathrm{D}}^{\mathrm{LE}}$) depends on the water saturation (S_{w}) as:

$$n_{\mathrm{D}}^{\mathrm{LE}}\left(S_{\mathrm{w}}\right)=\begin{cases}\tanh\left[A\left(S_{\mathrm{w}}-S_{\mathrm{w}}^{*}\right)\right], & S_{\mathrm{w}}>S_{\mathrm{w}}^{*}\\ 0, & S_{\mathrm{w}}\leq S_{\mathrm{w}}^{*},\end{cases} \tag{2.45}$$

where S_{w}^{*} is the limiting water saturation and A is a constant that controls the sharpness of the transition from weak to strong foam. The dynamic foam net generation is given by a first-order approach to local-equilibrium bubble texture at any saturation [52], with a time constant of $1/K_{\mathrm{c}}$, as follows:

$$\left[r_{\mathrm{g}}-r_{\mathrm{c}}\right]=K_{\mathrm{c}}n_{\max}\left[n_{\mathrm{D}}^{\mathrm{LE}}\left(S_{\mathrm{w}}\right)-n_{\mathrm{D}}\right]. \tag{2.46}$$

The linear kinetic model reflects the foam effects in the gas mobility reduction by modifying the gas relative permeability k_{rg} as follows:

$$k_{\mathrm{rg}}\left(S_{\mathrm{w}},n_{\mathrm{D}}\right)=\frac{k_{\mathrm{rg}}^{0}\left(S_{\mathrm{w}}\right)}{18500n_{\mathrm{D}}+1}, \tag{2.47}$$

where k_{rg}^{0} is the gas relative permeability in absence of foam, and the number 18500 is a value that reflects the maximum mobility reduction (C_{mrf}) due to the presence of foam in the flow.

[1] `https://www.lasurf-rio.com`

Relation (2.47) can be expressed in a more general approach to allow maximum mobility reduction factor as follows:

$$k_{\mathrm{rg}}\left(S_{\mathrm{w}}, n_{\mathrm{D}}\right) = \frac{k_{\mathrm{rg}}^{0}\left(S_{\mathrm{w}}\right)}{C_{\mathrm{mrf}} n_{\mathrm{D}} + 1}. \tag{2.48}$$

Notice that, in this model, the foamed gas is treated as a Newtonian fluid, because the gas relative permeability is linearly altered by the presence of foam, as shown (2.47) and (2.48).

To study the capability of foam to reduce gravity override and viscous fingering, the linear kinetic foam model is adopted in Chapter 4. Moreover, a local equilibrium version of the model (2.45) is used in Appendix A to reproduce experimental results.

2.5.3 Stochastic Bubble Population Model

In the Stochastic Bubble Population foam model, proposed in [52], the foam flow is described as a fluid obeying the Herschel–Bulkley rheological model that proposes that there exists yield stress τ_{y}, below which foam does not shear and above which foam flows with a power-law behavior [39]. Therefore it has a non-Newtonian fluid behavior given by:

$$\begin{cases} \mathbf{u}_{\mathrm{g}} = 0, & \tau \leq \tau_{\mathrm{y}} \\ \mu_{\mathrm{g}}^{\mathrm{f}} = \mu_{\mathrm{g}} + \dfrac{K_1}{|\mathbf{v}_{\mathrm{g}}|^{d}} + K_2 \dfrac{\tau_{\mathrm{y}}}{|\mathbf{v}_{\mathrm{g}}|}, & \tau > \tau_{\mathrm{y}}, \end{cases} \tag{2.49}$$

where $|\cdot|$ is the l^2-norm, τ is the stress acting on the fluid, τ_{y} is the yield stress, $\mu_{\mathrm{g}}^{\mathrm{f}}$ is the foamed gas viscosity, μ_{g} is the gas viscosity in absence of foam, $\mathbf{v}_{\mathrm{g}} = \mathbf{u}_{\mathrm{g}}/(\phi S_{\mathrm{g}})$ is the foamed gas interstitial velocity, and K_1, K_2 and d are model parameters. As discussed in [96], in a transient flow, the yield stress is negligible, reducing relation (2.49) to

$$\mu_{\mathrm{g}}^{\mathrm{f}} = \mu_{\mathrm{g}} + \alpha n_{\max} \frac{n_{\mathrm{D}}}{|\mathbf{v}_{\mathrm{g}}|^{d}}, \tag{2.50}$$

with $K_1 = \alpha n_{\max} n_{\mathrm{D}}$ [52], and α being an empirical parameter. For $d = 1/3$, the relation (2.50) reduces to the Hirasaki-Lawson model [53].

The net bubble generation and coalescence rate are expressed as

$$[r_{\mathrm{g}} - r_{\mathrm{c}}] = K_{\mathrm{g}}(1 - n_{\mathrm{D}}) - K_{\mathrm{d}} n_{\mathrm{D}}, \tag{2.51}$$

where K_{g} and K_{d} are the bubble generation and bubble destruction rate coefficients, respectively. It is important to note that $n_{\mathrm{D}} \to 1$ (or equivalently $n_{\mathrm{f}} \to n_{\max}$) is obtained when $K_{\mathrm{d}} \to 0$ and $t \to \infty$.

The non-Newtonian foamed gas behavior modeled by (2.50) and generation and coalescence governed by (2.51) is adopted in Chapter 5. Using this foam model, we present a computational validation from comparisons between the results of laboratory experiments and numerical solutions. Furthermore, two-dimensional problems are studied to evaluate the sweeping efficiency in highly heterogeneous porous media, including gravity and gas compressibility.

2.5.4 Kovscek's Model

The foam model proposed in [48] treats foam as a non-Newtonian fluid by using the foam viscosity model given by relation (2.50) and adopting $d = 1/3$, resulting in the viscosity model proposed in [53]. However, the gas interstitial velocity is computed in the following way

$$\mathbf{v}_{\mathrm{g}} = \frac{\mathbf{u}_{\mathrm{g}}}{\phi S_{\mathrm{g}} X_{\mathrm{f}}}, \tag{2.52}$$

where X_{f} is the gas flowing fraction (defined as $X_{\mathrm{f}} = 1 - X_{\mathrm{t}}$, where X_{t} is the fraction of trapped gas). In this foam model presented by Kovscek et al., the surfactant concentration, different from the previous models, is taken into account, and equation (2.1) is adopted to model the transport of the surfactant.

Regarding the r_{g} and r_{c} terms, the model incorporates into the generation function r_{g} the dependence on aqueous and gas phase velocities. The foam coalescence function r_{c} is modeled as directly dependent on foam velocity and texture. It is also affected by the surfactant concentration, which contributes to foam coalescence in terms of the change in limiting capillary pressure P_{c}^{*}. Therefore, the foam generation and coalescence functions are respectively given by [48, 51]

$$r_{\mathrm{g}} = k_1(n_{\mathrm{D}})|\mathbf{v}_{\mathrm{g}}|^{\frac{1}{3}}|\mathbf{v}_{\mathrm{w}}|n_{\max}^{-1}, \quad \text{and} \quad r_{\mathrm{c}} = k_{-1}(S_{\mathrm{w}}, C_{\mathrm{s}})|\mathbf{v}_{\mathrm{g}}|n_{\mathrm{D}}, \tag{2.53}$$

where $\mathbf{v}_{\mathrm{w}} = \mathbf{u}_{\mathrm{w}}/(\phi S_{\mathrm{w}})$ is the water interstitial velocity. Initially, in the works [48, 55], the coefficient k_1 in the r_{g} function was taken as a constant. However, Chen et al. [2] incorporated the effect of increasing bubble texture on foam-generation sites on the change in k_1:

$$k_1(n_{\mathrm{D}}) = k_1^0\left(1 - n_{\mathrm{D}}^{\omega}\right), \tag{2.54}$$

with constants k_1^0 and ω [51]. Also,

$$k_{-1}(S_{\mathrm{w}}, C_{\mathrm{s}}) = k_{-1}^0\left(\frac{P_{\mathrm{c}}}{P_{\mathrm{c}}^{*} - P_{\mathrm{c}}}\right)^2, \quad \text{with} \quad P_{\mathrm{c}}^{*} = P_{\mathrm{c,\,max}}^{*}\tanh\left(\frac{C_{\mathrm{s}}}{C_{\mathrm{s}}^{\mathrm{ref}}}\right), \tag{2.55}$$

k_{-1}^0 is a constant [51], $P_{\mathrm{c,\,max}}^{*}$ is the maximum value for limiting capillary pressure P_{c}^{*}, $C_{\mathrm{s}}^{\mathrm{ref}}$ is a reference surfactant concentration for strong net foam generation, and P_{c} is the capillary pressure (assumed to be a function of S_{w} only).

A simplified model in local equilibrium ($r_{\mathrm{g}} = r_{\mathrm{c}}$) to relate the normalized foam texture n_{D} with S_{w}, C_{s}, and the total velocity $\mathbf{u}$ was proposed by [2]:

$$n_{\mathrm{D}}^{\omega} + \frac{k_{-1}|\mathbf{v}_{\mathrm{g}}|^{\frac{2}{3}} n_{\max}}{k_1^0|\mathbf{v}_{\mathrm{w}}|} n_{\mathrm{D}} - 1 = 0. \tag{2.56}$$

Choosing $\omega = 3$ and neglecting that $\mathbf{v}_{\mathrm{g}}$ is dependent on n_{D}, as proposed by [2], a cubic equation with a single real root is obtained. Thus, given the liquid velocity, gas velocity, and capillary pressure, it is possible to obtain n_{D} analytically.

To allow for simulating scenarios where the capillary pressure in the pore P_{c} is greater than the limiting capillary pressure P_{c}^{*} (in which case the bubbles become unstable and instantly coalesce [97]), we propose the following adaptation of (2.56):

$$\begin{cases} n_{\mathrm{D}}^{\omega} + \dfrac{k_{-1}|\mathbf{v}_{\mathrm{g}}|^{\frac{2}{3}} n_{\max}}{k_1^0 |\mathbf{v}_{\mathrm{w}}|} n_{\mathrm{D}} - 1 = 0, & P_{\mathrm{c}} < P_{\mathrm{c}}^{*}, \\ n_{\mathrm{D}} = 0, & P_{\mathrm{c}} \geq P_{\mathrm{c}}^{*}. \end{cases} \tag{2.57}$$

Choosing $\omega = 3$ in (2.57) and solving the resulting cubic equation, the following relation, that provides the single real root, is obtained:

$$n_{\mathrm{D}} = \begin{cases} \dfrac{\sqrt[3]{z}}{\sqrt[3]{18}} - \dfrac{\sqrt[3]{\frac{2}{3}}a}{\sqrt[3]{z}}, & P_{\mathrm{c}} < P_{\mathrm{c}}^{*}, \\ 0, & P_{\mathrm{c}} \geq P_{\mathrm{c}}^{*}, \end{cases} \tag{2.58}$$

where $z = \sqrt{12a^3 + 81} + 9$ and $a = \dfrac{k_{-1}|\mathbf{v}_{\mathrm{g}}|^{\frac{2}{3}} n_{\max}}{k_1^0 |\mathbf{v}_{\mathrm{w}}|}$.

The model proposed by Kovscek and Radke is used in Chapter 6 to study the influence of the co-injection and SAG techniques on the sweep efficiency in heterogeneous porous media. This model is also applied to investigate the surfactant adsorption effect on foam flow in heterogeneous porous media. In those simulations, the local equilibrium assumption is adopted, and relation (2.58) is used instead of equation (2.2).

3 NUMERICAL METHODOLOGY

In this chapter, we introduce a numerical methodology to solve the system (2.31)–(2.34) derived in Chapter 2. These equations, that model the foam flow in porous media, exhibit different mathematical properties: the transport system is formed of hyperbolic type equations and the hydrodynamics problem is of elliptic nature. In this context, we propose a sequential algorithm that combines finite element and finite volume methods for spatial discretization and the finite difference method for time integration.

The hydrodynamics problem (2.31)–(2.32) is approximated using a naturally stable mixed finite element method introduced in [76]. This method is locally conservative, relying on the strong imposition of the continuity of normal fluxes and a discontinuous pressure field. In order to obtain a reduction of the degrees of freedom and generate a positive-definite system of equations, we adopt the hybrid formulation to solve the problem [84]. In cases where we assume compressibility effects, the time derivative term in (2.32) is approximated using an implicit first-order finite difference scheme.

The transport system (2.33) is solved using the KNP method, a conservative, high-order, central-upwind finite volume scheme introduced in [83] that shows reduced numerical diffusion effects. The KNP scheme is an extension of the KT method [81] that generalizes the numerical flux using more precise information about the local propagation velocities. At the same time, the KNP scheme has an upwind nature since it respects wave propagation directions by measuring the one-sided local velocities. KNP is a semi-discrete method based on the REA (Reconstruct Evolve Average) algorithm of Godunov [82]. Furthermore, the KNP scheme allows for using small steps in time without requiring an excessive refinement of the spatial mesh since the numerical diffusion does not depend on the time step. After discretization in space, the resulting system of ODEs (Ordinary Differential Equations) is integrated in time using a BDF (Backward Differentiation Formula), which is an implicit, multi-step method that is especially indicated to solve stiff equations [98].

Finally, the computer simulator developed to accommodate the proposed sequential algorithm is presented. Named FOSSIL (FOam diSplacement SImuLator), this in-house simulator combines two open-source libraries, SUNDIALS [85] and deal.II [86].

3.1 The Sequential Algorithm

We use a staggered algorithm to decouple the system of equations (2.31)-(2.34) into two sub-systems: a hydrodynamics one, with time step Δt_{u}, and a transport one, with time step Δt_{s}, with $\Delta t_{\mathrm{u}} \gg \Delta t_{\mathrm{s}}$, because the time scale of the hydrodynamics is usually much slower than of the transport [91, 88, 89]. Algorithm 1 describes the sequential method to solve each problem separately. For the transport problem, adaptive time steps (Δt_{s}) are used as needed to bound the

error in the approximations under a certain combination of relative and absolute tolerances. A general idea of the sequential scheme is shown in Figure 3.

Considering a time instant n, when the solution is known, and the next instant in time $n+1$, when the solution is yet to be computed, in each iteration, approximations for velocity $\mathbf{u}^{n+1}$ and pressure p^{n+1} at $t = t^{n+1}$ are computed from system (2.31)-(2.32) as follows

$$\mathbf{u}^{n+1} = -\kappa\lambda^n \left[\nabla p^{n+1} - \mathbf{G}\left(S_{\mathrm{w}}^n, n_{\mathrm{D}}^n, p^n\right)\right], \tag{3.1a}$$

$$c\left(S_{\mathrm{w}}^n, p^n\right)\frac{p^{n+1}}{\Delta t_{\mathrm{u}}} + \nabla\cdot\mathbf{u}^{n+1} = D\left(S_{\mathrm{w}}^n, n_{\mathrm{D}}^n, p^n\right)(\mathbf{u}^n\cdot\mathbf{u}^n) + \mathbf{B}\left(S_{\mathrm{w}}^n, n_{\mathrm{D}}^n, p^n\right)\mathbf{u}^n + F\left(S_{\mathrm{w}}^n, n_{\mathrm{D}}^n, p^n\right) + c\left(S_{\mathrm{w}}^n, p^n\right)\frac{p^n}{\Delta t_{\mathrm{u}}}, \tag{3.1b}$$

supplemented by the boundary (2.37) and initial conditions (2.38). It is worth noticing that in equation (3.1b) the time derivative was discretized using an implicit first-order finite difference, and a linearization was performed by computing the coefficients $c\left(S_{\mathrm{w}}, p\right)$, $D\left(S_{\mathrm{w}}, n_{\mathrm{D}}, p\right)$, $\mathbf{B}\left(S_{\mathrm{w}}, n_{\mathrm{D}}, p\right)$ and $F\left(S_{\mathrm{w}}, n_{\mathrm{D}}, p\right)$ at a previous time step, and also using the previous solution value for $\mathbf{u}$ in the right-hand side of (3.1b). Since the pressure initial condition is prescribed as a scalar value p^0, the initial condition for $\mathbf{u}$ is, then, taken as zero.

Figure 3 – Sequential scheme to decouple the hydrodynamics and transport problems.

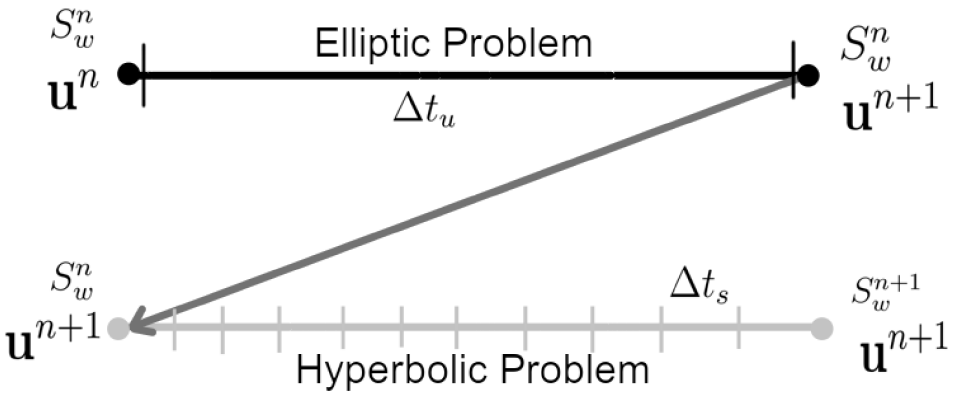

Source: Prepared by the author.

Then, an iterative algorithm is used to find approximations for water saturation (S_{w}^{n+1}), foam texture (n_{D}^{n+1}), surfactant concentration (C_{s}^{n+1}), and surfactant concentration adsorbed onto kinetic sites on porous medium ($C_{\mathrm{s}}^{\mathrm{kin}}$) by solving the following system of PDEs in $\Omega\times(t^n, t^{n+1}]$:

$$\phi\frac{\partial\mathbf{S}^{n+1}}{\partial t} + (1-\phi)\rho\frac{\partial\mathbf{A}^{n+1}}{\partial t} + \sum_{i=1}^{\mathfrak{d}}\frac{\partial\mathbf{f}_i^{n+1}}{\partial x_i} - \nabla\cdot\left(\mathbb{C}^{n+1}\nabla\mathbf{S}^{n+1}\right) = \mathbf{\Phi}^{n+1}, \tag{3.2}$$

$$f_{\mathrm{w}\to\mathrm{s}}^{\mathrm{kin},n+1} = (1-\phi)\rho\frac{\mathrm{d}C_{\mathrm{s}}^{\mathrm{kin},n+1}}{\mathrm{d}t}, \tag{3.3}$$

with boundary and initial conditions given by (2.39) and (2.40), respectively.

Algorithm 1: Sequential algorithm to solve (3.1)–(3.3). The term T is the final simulation time, t is the elapsed time related to the hydrodynamics problem, t_s is the elapsed time related to the transport problem, n is the index for the time instant of the last known solution, $n+1$ is the index for the time instant of the unknown solution yet to be computed, m and $m+1$ are the indexes for the time instants of the known and unknown solution related to the transport sub-problem iterations.

Set initial conditions $\mathbf{u}^0$, p^0, S_{w}^0, n_{D}^0, C_{s}^0 and $C_{\mathrm{s}}^{\mathrm{kin},0}$;
$n \leftarrow 0$; $t \leftarrow 0$; $t_{\mathrm{s}} \leftarrow 0$;
do
  Compute velocity $\mathbf{u}^{n+1}$ and pressure p^{n+1} fields using (3.1);
  $t = t + \Delta t_{\mathrm{u}}$;
  $m \leftarrow 0$;
  $\left(\mathbf{S}^{n+1}\right)^m \leftarrow \mathbf{S}^n$;
  $\left(C_{\mathrm{s}}^{\mathrm{kin},n+1}\right)^m \leftarrow C_{\mathrm{s}}^{\mathrm{kin,n}}$;
  do
    Update $C_{\mathrm{s}}^{\mathrm{eq}}$ using $\left(C_{\mathrm{s}}^{n+1}\right)^m$;
    Compute $\left(\mathbf{S}^{n+1}\right)^{m+1}$ and $\left(C_{\mathrm{s}}^{\mathrm{kin},n+1}\right)^{m+1}$ using (3.2) and (3.3) with $\mathbf{u}^{n+1}$;
    $t_{\mathrm{s}} = t_{\mathrm{s}} + \Delta t_{\mathrm{s}}$;
    $m = m + 1$;
  while $t_s < t$;
  $\mathbf{S}^{n+1} \leftarrow \left(\mathbf{S}^{n+1}\right)^m$, $\left(C_{\mathrm{s}}^{\mathrm{kin}}\right)^{n+1} \leftarrow \left(C_{\mathrm{s}}^{\mathrm{kin},n+1}\right)^m$;
  Update $C_{\mathrm{s}}^{\mathrm{eq}}$ using C_{s}^{n+1};
  $n \leftarrow n + 1$;
while $t < T$;

In the following sections, we present the numerical methods used to discretize each problem in space.

3.2 Hybrid Mixed Finite Element Method for Hydrodynamic Flow

When a mixed finite element formulation is used to approximate the Darcy system (3.1), it is necessary to fulfill the compatibility condition between velocity and pressure spaces simultaneously and to impose the continuity of the normal vector across interelement edges. In addition, the employ of classical finite element methods, that simultaneously approximate the velocity and pressure fields, results in an indefinite linear system or saddle-point system, which can restrict the numerical solvers that could be applied [76, 84, 99, 100]. By using a hybrid formulation, the continuity requirement is imposed via Lagrange multipliers, defined on the interelement edges, and by choosing a stable approximation space, such as Raviart-Thomas approximation spaces for velocity, the compatibility between pressure and velocity is achieved [84]. Furthermore, suppose the local problems are solvable. In that case, it is possible to eliminate

all degrees of freedom related to local problems using a static condensation technique, resulting in a considerable reduction of the computational cost since the global system is positive-definite and involves only the degrees of freedom of the Lagrange multiplier [15, 84, 101]. Once the approximation for the Lagrange multipliers is found, the original degrees of freedom (associated with velocity and pressure) can be computed in local and independent problems.

3.2.1 Fundamental Definitions

In this section, fundamental definitions related to the hybrid mixed finite element method are presented. Let a square-integrable function space be defined as

$$L^2(\Omega) = \left\{ q : \int_\Omega |q|^2 \, d\mathbf{x} < \infty \right\}, \tag{3.4}$$

that induces the following norm

$$\|q\|_0 = \|q\|_{L^2(\Omega)} = \left[\int_\Omega |q|^2 \, d\mathbf{x} \right]^{1/2}. \tag{3.5}$$

Constraining the domain Ω to two-dimensions ($\mathfrak{d} = 2$) and given a scalar $q \in \mathbb{R}$ and a vector $\mathbf{v} \in \mathbb{R}^2$, we can define the gradient (∇) and divergent (div) operators as follows,

$$\text{div}(\mathbf{v}) = \left(\frac{\partial v_1}{\partial x_1} + \frac{\partial v_2}{\partial x_2} \right), \qquad \nabla q = \left(\frac{\partial q}{\partial x_1}, \frac{\partial q}{\partial x_2} \right), \qquad \nabla \mathbf{v} = \begin{bmatrix} \dfrac{\partial v_1}{\partial x_1} & \dfrac{\partial v_1}{\partial x_2} \\ \dfrac{\partial v_2}{\partial x_1} & \dfrac{\partial v_2}{\partial x_2} \end{bmatrix}.$$

Based on the space $L^2(\Omega)$ and the definitions above, we can define the following Sobolev spaces,

$$H^1(\Omega) = \left\{ q \in L^2(\Omega) : \nabla q \in \left[L^2(\Omega) \right]^2 \right\}, \tag{3.6}$$

with norm and semi-norm given, respectively, by

$$\|q\|_1^2 = \|q\|_{H^1(\Omega)}^2 = \|q\|_0^2 + \|\nabla q\|_0^2, \tag{3.7}$$

$$|q|_1^2 = |q|_{H^1(\Omega)}^2 = \|\nabla q\|_0^2. \tag{3.8}$$

We also define the following space:

$$H(\text{div}, \Omega) = H(\text{div}) = \left\{ \mathbf{v} \in \left[L^2(\Omega) \right]^2 : \text{div}(\mathbf{v}) \in L^2(\Omega) \right\}, \tag{3.9}$$

with its respective norm

$$\|q\|_{H(\text{div})}^2 = \|\mathbf{v}\|_0^2 + \|\text{div}(\mathbf{v})\|_0^2, \tag{3.10}$$

Let $\Omega_h = \{K\}$ a regular mesh of finite elements in $\Omega \subset \mathbb{R}^2$ formed by elements K, where two neighboring elements K_1 e K_2 share the same edge e, as shown in Figure 4. We can define the set of edges e of the elements $K \in \Omega_h$, as

$$\mathcal{E}_h = \{e;\ e \text{ is an edge of } K,\ \forall K \in \Omega_h\}\,, \tag{3.11}$$

the set of interior edges as

$$\mathcal{E}_h^0 = \{e \in \mathcal{E}_h;\ e = K_1 \cap K_2,\ \forall K_1, K_2 \in \Omega_h\} \tag{3.12}$$

and the set of edges at the boundary as

$$\mathcal{E}_h^\partial = \{e \in \mathcal{E}_h;\ e \subset \partial\Omega\}\,. \tag{3.13}$$

Figure 4 – Representation of edges of neighboring elements.

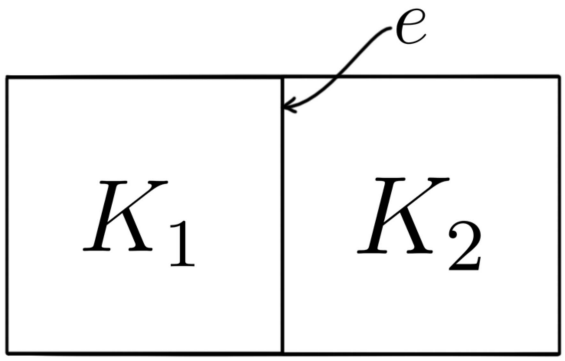

Source: Prepared by the author.

Based on the previous definitions, we present the (discontinuous) $\mathcal{RT}$ spaces of order of polynomial interpolation k [76] used to approximate the problem, here denoted by $\mathcal{U}_h^k \times \mathcal{P}_h^k$, and defined as:

$$\mathcal{U}_h^k = \left\{\mathbf{v}_h \in [L^2(\Omega)]^2; \mathbf{v}_h|_K \in \mathbf{P}_{\hat{K}\to K}\left(\mathbb{Q}_{k,k-1}\left(\hat{K}\right) \times \mathbb{Q}_{k-1,k}\left(\hat{K}\right)\right), \forall K \in \Omega_h\right\}, \tag{3.14}$$

$$\mathcal{P}_h^k = \left\{q_h \in L^2(\Omega)\,; q_h|_K \in P_{\hat{K}\to K}\left(\mathbb{Q}_{k,k}\left(\hat{K}\right)\right), \forall K \in \Omega_h\right\}, \tag{3.15}$$

where $\mathbb{Q}_{i,j}$ denotes the space of the polynomial functions of degree less than or equal to i for the first component of the variable and less than or equal to j for the second component of the variable, $\hat{K}$ is the reference element and the operators $\mathbf{P}_{\hat{K}\to K}$ and $P_{\hat{K}\to K}$ are transformed that takes a function in $\hat{K}$ to a related function in K. Due to the vector nature of the Raviart-Thomas bases, the mapping of the reference element $\hat{K}$ to the physical elements $K \in \Omega_h$ is done by the Piola's transform $\mathbf{P}_{\hat{K}\to K}$, which preserves the divergent and normal components of the vectors. Defining a mapping $F_K = F_{\hat{K}\to K}$, a vector function $\hat{\boldsymbol{\varphi}}$ in $\hat{K}$ is transformed into the function $\boldsymbol{\varphi}$ in K using the Piola's transformation [102]:

$$\boldsymbol{\varphi}(\mathbf{x}) = \mathbf{P}_{\hat{K}\to K}\left(\hat{\boldsymbol{\varphi}}(\hat{\mathbf{x}})\right) = \frac{1}{\det\left|D\mathbf{F}_K(\hat{\mathbf{x}})\right|}\left[D\mathbf{F}_K(\hat{\mathbf{x}})\right]\hat{\boldsymbol{\varphi}}(\hat{\mathbf{x}}), \tag{3.16}$$

where $\mathbf{x} = \mathbf{F}_K(\hat{\mathbf{x}})$ and $D\mathbf{F}_K(\hat{\mathbf{x}})$ is the Jacobian matrix of the transformation $\mathbf{F}_K$. The transform $P_{\hat{K}\to K}$ is a composition of the type $\varphi(\mathbf{x}) = P_{\hat{K}\to K}(\hat{\varphi}(\hat{\mathbf{x}})) = \hat{\varphi}(\hat{\mathbf{x}})$, that allows for the continuity of the transformed function on each edge of the mesh. We also define the following sets of functions on the mesh skeleton:

$$\mathcal{M}_h^k = \left\{\mu_h \in L^2(\mathcal{E}_h);\ \mu_h|_e \in p_k(e),\ \forall e \in \mathcal{E}_h^0,\ \mu_h|_e = \bar{p}, \forall e \in \mathcal{E}_h^\partial \cap \Gamma_D\right\}, \tag{3.17}$$

$$\bar{\mathcal{M}}_h^k = \left\{\mu_h \in L^2(\mathcal{E}_h);\ \mu_h|_e \in p_k(e),\ \forall e \in \mathcal{E}_h^0,\ \mu_h|_e = 0, \forall e \in \mathcal{E}_h^\partial \cap \Gamma_D\right\}, \tag{3.18}$$

where $p_k(e)$ denotes the set of polynomial functions of degree up to k on e. In the simulations, we adopt the standard lowest order index $\mathcal{RT}$ space ($k = 0$), a low computational cost choice (compared to $k > 0$) that is extensively employed in fluid mechanics computations [102].

3.2.2 Hybrid Mixed Formulation

Hybrid methods solve a global problem in Ω_h that is constructed based on discontinuous local problems defined in each element $K \in \Omega_h$. The Lagrange multipliers link the global problem to the local problems. The multiplier is defined on the edges e of an element K, aiming to impose the interface conditions weakly on each element of the mesh. An advantage of the hybrid methods is the computational cost reduction to obtain the numerical solution, which is reached by reducing the size of the global problem to be solved [77, 84]. This reduction happens due to the static condensation that condenses the problem in the Lagrange multipliers, resulting in a reduction in the number of degrees of freedom [15, 84, 101]. The local problems are considered computationally negligible compared to the global problem. In addition, due to the discontinuous characteristics, the existence of local problems allows the use of parallelization techniques, especially when high-order approximations are used [103].

In this context, we adopt a hybrid mixed formulation employing Raviart-Thomas spaces to solve the hydrodynamics. In this formulation, the Lagrange multiplier is associated with the trace of the pressure field $\lambda = p|_e$ on each edge $e \in \mathcal{E}_h$ belonging to space $\mathcal{M}_h^k$. Then, to present the hybrid formulation for Darcy's problem we first consider the equations (3.1a) and (3.1b) multiplied by $\mathbf{v}_h \in \mathcal{U}_h^k$ and $q_h \in \mathcal{P}_h^k$ respectively, and using integration by parts, we generate the following approximation in each element $K \in \Omega_h$:

$$\int_K \mathbb{A}(S_{\mathrm{w}}^n, n_{\mathrm{D}}^n)\mathbf{u}_h^{n+1} \cdot \mathbf{v}_h \mathrm{d}\mathbf{x} - \int_K p_h^{n+1}\, \nabla \cdot \mathbf{v}_h \mathrm{d}\mathbf{x} + \int_{\partial K} \lambda_h^{n+1} \mathbf{v}_h \cdot \mathbf{n}_K \mathrm{d}s = 0 \tag{3.19}$$

$$\begin{aligned}\int_K c\left(S_{\mathrm{w}}^n, p^n\right) \frac{p^{n+1}}{\Delta t_{\mathrm{u}}}\, q_h \mathrm{d}\mathbf{x} - \int_K q_h\, \nabla \cdot \mathbf{u}_h^{n+1} \mathrm{d}\mathbf{x} &= \int_K c\left(S_{\mathrm{w}}^n, p^n\right) \frac{p^n}{\Delta t_{\mathrm{u}}}\, q_h \mathrm{d}\mathbf{x} \\ &+ \int_K \mathbf{G}\left(S_{\mathrm{w}}^n, n_{\mathrm{D}}^n, p^n\right) \cdot \mathbf{v}_h \mathrm{d}\mathbf{x} + \int_K D\left(S_{\mathrm{w}}^n, n_{\mathrm{D}}^n, p^n\right)(\mathbf{u}^n \cdot \mathbf{u}^u)\, q_h \mathrm{d}\mathbf{x} \\ &+ \int_K \mathbf{B}\left(S_{\mathrm{w}}^n, n_{\mathrm{D}}^n, p^n\right) \cdot \mathbf{u}^n\, q_h \mathrm{d}\mathbf{x} - \int_K F\left(S_{\mathrm{w}}^n, n_{\mathrm{D}}^n, p^n\right) q_h \mathrm{d}\mathbf{x},\end{aligned} \tag{3.20}$$

where $\mathbb{A}(S_{\mathrm{w}}^n, n_{\mathrm{D}}^n) = \left[\kappa\lambda(S_{\mathrm{w}}^n, n_{\mathrm{D}}^n)\right]^{-1}$ and $\lambda_h = p_h|_e$ the trace of the pressure field defined on each edge $e \in \mathcal{E}_h$ belonging to space $\mathcal{M}_h^k$. To close the system, we introduce the multiplier

equation

$$\int_{\partial K} \mu_h \mathbf{u}_h \cdot \mathbf{n}_K \mathrm{d}s = \int_{\Gamma_N} \bar{u}\, \mu_h \mathrm{d}s, \tag{3.21}$$

for all μ_h belonging to space $\bar{\mathcal{M}}_h^k$. The Equation (3.21) naturally imposes the continuity condition on the edges of K and the Neumann boundary condition (2.37) on Γ_N.

Adding the local problems (3.19) and (3.20) with the global problem (3.21) and summing on all elements $K \in \Omega_h$, we can write the following hybrid mixed formulation for the hydrodynamic problem (3.1):

Given S_w^n, n_D^n, C_s^n, p^n and $\mathbf{u}^n$, find the pair $[\mathbf{u}_h^{n+1}, p_h^{n+1}] \in \mathcal{U}_h^k \times \mathcal{P}_h^k$ and the Lagrange multiplier $\lambda_h^{n+1} \in \mathcal{M}_h^k$ such that, for all $[\mathbf{v}_h, q_h, \mu_h] \in \mathcal{U}_h^k \times \mathcal{P}_h^k \times \bar{\mathcal{M}}_h^k$,

$$\sum_{K \in \mathcal{T}_h} a_K([\mathbf{u}_h^{n+1}, p_h^{n+1}]; [\mathbf{v}_h, q_h]) + \sum_{K \in \mathcal{T}_h} b_K(\lambda_h^{n+1}, \mathbf{v}_h) = \sum_{K \in \mathcal{T}_h} f_K([\mathbf{v}_h, q_h]), \tag{3.22}$$

$$\sum_{K \in \mathcal{T}_h} b_K(\mu_h, \mathbf{u}_h^{n+1}) = \int_{\Gamma_N} \bar{u}\, \mu_h \mathrm{d}s, \tag{3.23}$$

with

$$\begin{aligned} a_K([\mathbf{u}_h^{n+1}, p_h^{n+1}]; [\mathbf{v}_h, q_h]) = & \int_K \mathbb{A}(S_{\mathrm{w}}^n, n_{\mathrm{D}}^n)\mathbf{u}_h^{n+1} \cdot \mathbf{v}_h \mathrm{d}\mathbf{x} - \int_K p_h^{n+1} \nabla \cdot \mathbf{v}_h \mathrm{d}\mathbf{x} \\ & - \int_K q_h \nabla \cdot \mathbf{u}_h^{n+1} \mathrm{d}\mathbf{x} + \int_K c\left(S_{\mathrm{w}}^n, p^n\right) \frac{p^{n+1}}{\Delta t_{\mathrm{u}}} q_h \mathrm{d}\mathbf{x}, \end{aligned} \tag{3.24}$$

$$b_K\left(\lambda_h^{n+1}, \mathbf{v}_h\right) = \int_{\partial K} \lambda_h^{n+1} \mathbf{v}_h \cdot \mathbf{n}_K \mathrm{d}s, \tag{3.25}$$

$$\begin{aligned} f_K\left([\mathbf{v}_h, q_h]\right) = & \int_K c\left(S_{\mathrm{w}}^n, p^n\right) \frac{p^n}{\Delta t_{\mathrm{u}}} q_h \mathrm{d}\mathbf{x} + \int_K \mathbf{G}\left(S_{\mathrm{w}}^n, n_{\mathrm{D}}^n, p^n\right) \cdot \mathbf{v}_h \mathrm{d}\mathbf{x} \\ & + \int_K D\left(S_{\mathrm{w}}^n, n_{\mathrm{D}}^n, p^n\right) \left(\mathbf{u}^n \cdot \mathbf{u}^u\right) q_h \mathrm{d}\mathbf{x} \\ & + \int_K \mathbf{B}\left(S_{\mathrm{w}}^n, n_{\mathrm{D}}^n, p^n\right) \cdot \mathbf{u}^n q_h \mathrm{d}\mathbf{x} - \int_K F\left(S_{\mathrm{w}}^n, n_{\mathrm{D}}^n, p^n\right) q_h \mathrm{d}\mathbf{x}. \end{aligned} \tag{3.26}$$

To solve the hybrid formulation (3.22)–(3.23) we apply the static condensation technique.

3.2.3 Static Condensation

The static condensation technique [15, 84, 101] consists in a set of algebraic operations, done at the element level, to eliminate all degrees of freedom corresponding to the variables $\mathbf{u}_h$ and p_h, leading to a global system with the degrees of freedom associated with the multipliers only. To apply this technique to solve (3.22)–(3.23), we consider the matrices $\mathbf{A}_K$, generated by the bilinear form $a_K(\cdot,\cdot)$ (3.24), and $\mathbf{B}_K$, generated by the bilinear form $b_K(\cdot,\cdot)$ (3.25), and also the vectors $\mathbf{F}_K$, constructed by the functional $f_K(\cdot)$ (3.26), and $\bar{\mathbf{U}}$, defined only in the boundary, resulting from the Neumann boundary condition in (3.23). Thus, the local problems (3.22) and the global problem (3.23) are rewrite in the following matrix form:

$$\mathbf{A}_K \mathbf{U}_K + \mathbf{B}_K \mathbf{\Lambda}_K = \mathbf{F}_K, \ \forall K \in \Omega_h, \tag{3.27}$$

$$\sum_{K \in \Omega_h} \mathbf{B}_K^T \mathbf{U}_K = \bar{\mathbf{U}}, \tag{3.28}$$

where the vector $\mathbf{U}_K$ contains the local degrees of freedom associated with the variables $\mathbf{u}_h^{n+1}$ and p_h^{n+1} in K and the vector $\mathbf{\Lambda}_K$ is formed by the degrees of freedom associated with the Lagrange multipliers on the edges of K.

Since $\mathbf{A}_K$ is invertible, we can write an equation for $\mathbf{U}_K$:

$$\mathbf{U}_K = \mathbf{A}_K^{-1}\left(\mathbf{F}_K - \mathbf{B}_K\mathbf{\Lambda}_K\right), \ \forall K \in \Omega_h. \tag{3.29}$$

Using (3.29) in (3.28), we reach a global system in terms of $\mathbf{\Lambda}_K$ only:

$$\sum_{K\in\mathcal{T}_h} \mathbf{B}_K^T\mathbf{A}_K^{-1}\mathbf{B}_K\mathbf{\Lambda}_K = \sum_{K\in\mathcal{T}_h} \mathbf{B}_K^T\mathbf{A}_K^{-1}\mathbf{F}_K + \bar{\mathbf{U}}. \tag{3.30}$$

After system (3.30) is solved, $\mathbf{\Lambda}_K$ is used in (3.29) to find the vector $\mathbf{U}_K$ in each element $K \in \Omega_h$.

We can observe that static condensation causes a significant reduction in the size of the global problem, which is now rewritten in terms of the multiplier only. Also, the new system of equations is positive-definite, allowing for using simpler and more robust solvers. In the end, a hybrid formulation associated with static condensation reduces the computational cost required to solve the global problem. In this work, the deal.II library [86] is used to solve this hydrodynamics problem.

3.3 High Order Central-Upwind Scheme for the Transport Problem

The numerical methodology used to approximate the water saturation, foam texture, and surfactant concentration equations (3.2) is a high-order non-oscillatory central-upwind finite volume method proposed by Kurganov, Noelle and Petrova (KNP) in [83]. In this thesis, we adopt the modification proposed in [89] to accommodate the variation of the porous medium's porosity. In this section, the numerical method to solve the phase transport equation is presented.

3.3.1 REA Algorithm

Many modern high-order schemes, such as the KNP method, are based on the REA algorithm of [82]. This methodology defines three main steps for solving hyperbolic equations: **R**econstruct, **E**volve and **A**verage:

1. ***Reconstruct***: The objective of the reconstruction step is to reconstruct a piecewise polynomial function in each cell using the known average solution of the cell.

2. ***Evolve***: The hyperbolic equation is evolved over time based on the data calculated in the previous time step. The evolution is done in an alternating mesh computed, taking into account the Riemann fans.

3. ***Average***: In this step, the final solution is calculated using the solution average in each cell, using the polynomial function reconstructed in time.

All these processes are then repeated consecutively for the next step until the final time is reached. In order to implement the REA algorithm procedure, we must be able to solve the hyperbolic equation in step 2 [104]. Figure 5 shows a graphic scheme of the three steps of the REA algorithm.

Figure 5 – Graphical scheme of the REA algorithm.

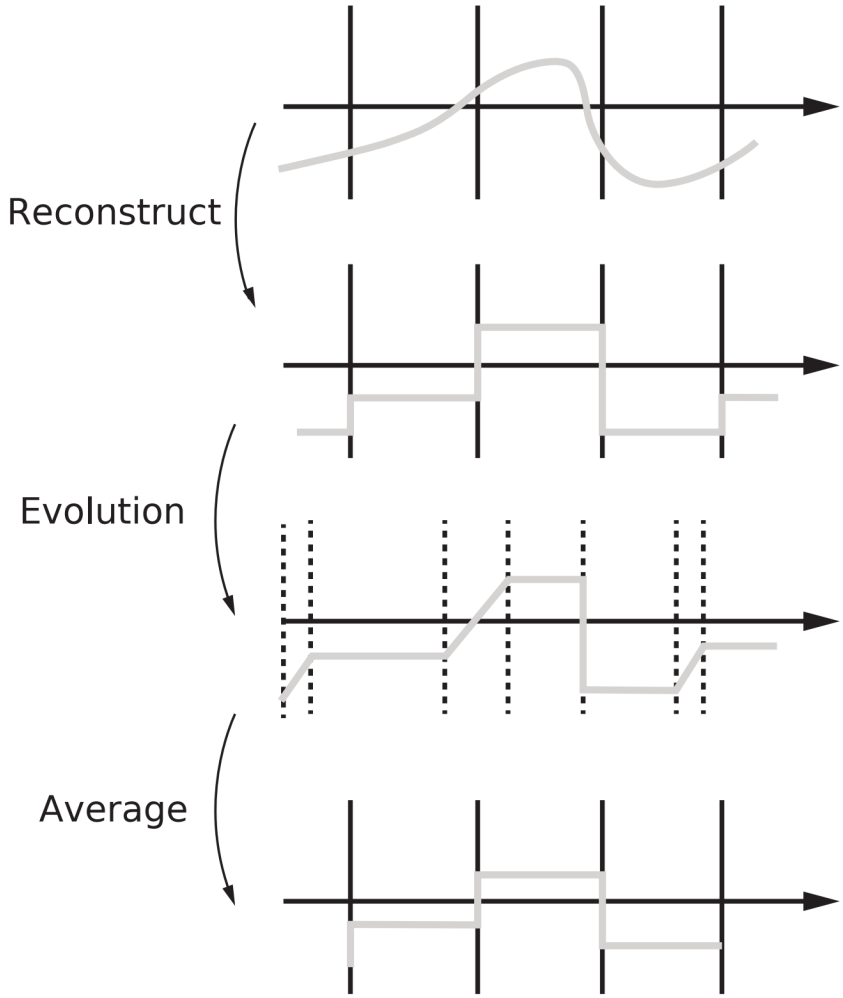

Source: Prepared by the author.

3.3.2 The Kurganov-Noelle-Petrova Method

The KNP method is based on a grid of control volumes (or cells), as shown in Figure 6 for a two-dimensional mesh. The letter l indicates the current cell, $l+1$ the cell to the right (or the cell above), $l-1$ the volume to the left (or the volume down), $l-1/2$ and $l+1/2$ refer to the left and right faces (or the lower and upper faces), respectively. The left and right side of the

same cell face is referenced by $-$ and $+$, respectively, and similarly, the symbol $+$ refers to the upper portion of a face and $-$ to the lower portion of the same face.

Figure 6 – Tow-dimensional finite volume grid
and its notations.

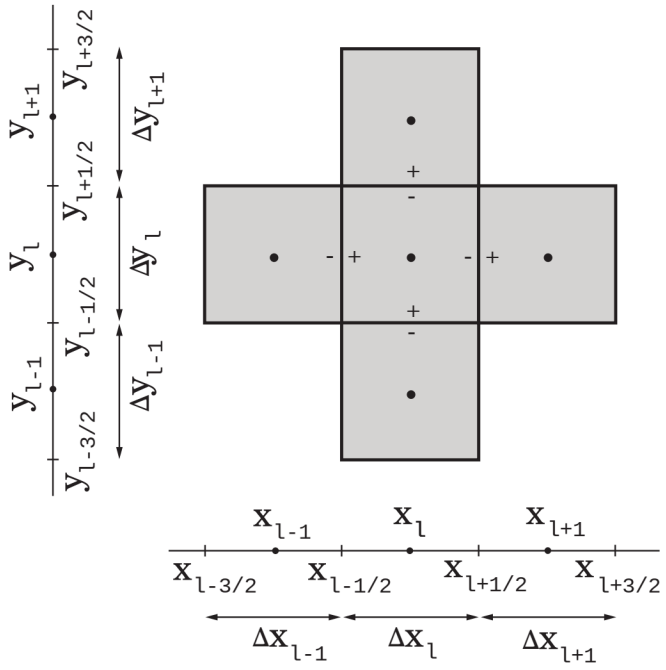

Source: Prepared by the author.

The KNP scheme [83] is a semi-discrete second-order central-upwind scheme that can be derived using the REA algorithm using a MUSCL (Monotonic Upstream-centered Schemes for Conservations Laws) type scheme [105]. The upwind nature of KNP is because it respects the directions of wave propagation by measuring the one-sided local speeds given by

$$a^{\text{max/min}}_{l\pm1/2,i} = \frac{\max / \min_{\boldsymbol{\omega}\in C\left(\mathbf{S}^{-}_{l\pm1/2,i},\mathbf{S}^{+}_{l\pm1/2,i}\right)} \left\{ \Lambda^{\text{max/min}} \left[\dfrac{\partial \mathbf{f}_i}{\partial \mathbf{S}} (\boldsymbol{\omega}) \right], 0 \right\}}{\min\left(\phi_l, \phi_{l\pm1}\right)}, \tag{3.31}$$

on direction i and a cell of index l, where $l+1/2$ is the right (resp. top) face and $j-1/2$ is the left (resp. bottom) face of a cell, $\mathbf{S}^{-}_{l\pm1/2,i}$ is the local reconstruction of $\mathbf{S}$ at the left (resp. bottom) side of a face, and $\mathbf{S}^{+}_{l\pm1/2,i}$ is the local reconstruction of $\mathbf{S}$ at the right (resp. top) side of a face; $\Lambda^{\max}$ and $\Lambda^{\min}$ are the maximum and minimum eigenvalues, respectively, of the Jacobian $\partial \mathbf{f}_i / \partial \mathbf{S}$ and $C\left(\mathbf{S}^{-}_{l\pm1/2,i}, \mathbf{S}^{+}_{l\pm1/2,i}\right)$ is the curve in the phase space that connects the left and right values of the reconstruction at $x = x_{l\pm1/2,i} = x_{l,i} \pm h_i/2$. The terms ϕ_l and $\phi_{l\pm1}$ are the porosity values at the cell of index l or $l \pm 1$, which refers to the porous medium's porosity field. In the genuinely nonlinear or linearly degenerate case, when the fractional flux function is convex, we

can simplify the expression (3.31) in the following way [83]:

$$a_{l\pm1/2,i}^{\text{max/min}} = \max \,/\, \min \left\{ \Lambda^{\text{max/min}} \left[\frac{\partial \mathbf{f}_i}{\partial \mathbf{S}} \left(\mathbf{S}_{l\pm1/2,i}^{-} \right) \right], \Lambda^{\text{max/min}} \left[\frac{\partial \mathbf{f}_i}{\partial \mathbf{S}} \left(\mathbf{S}_{l\pm1/2,i}^{+} \right) \right], 0 \right\}.$$

When the flux function becomes non-convex, a more cautious computation of the local propagation speed is needed. A possible approach is to discretize the interval $\left(\mathbf{S}_{l\pm1/2,i}^{-}, \mathbf{S}_{l\pm1/2,i}^{+}\right)$, and search for the maximum and minimum eigenvalues. Additionally, the terms of the Jacobian matrix are discretized using forward finite difference and then evaluated in the required points for each i direction.

The result of spatial discretization using KNP is the system of ODEs given in the following conservative form:

$$\frac{\mathrm{d}\mathbf{S}_l}{\mathrm{d}t} = \frac{1}{\phi_l} \sum_{i=1}^{\mathfrak{d}} \left(\frac{\mathbf{H}_{l-1/2,i} - \mathbf{H}_{l+1/2,i}}{h_i} + \frac{\mathbf{P}_{l+1/2,i} - \mathbf{P}_{l-1/2,i}}{h_i} \right) + \frac{1}{\phi_l} \mathbf{\Phi}_l, \tag{3.32}$$

where $\mathbf{\Phi}_l = \mathbf{\Phi}\left(\mathbf{S}_l\right)$, h_i is the cell size in the i-th direction, with the convective numerical fluxes given by

$$\begin{aligned} \mathbf{H}_{l+1/2,i} = & \frac{\phi_{l+1} a_{l+1/2,i}^{\max} \mathbf{f}_i \left(\mathbf{S}_{l+1/2,i}^{-} \right) - \phi_l a_{l+1/2,i}^{\min} \mathbf{f}_i \left(\mathbf{S}_{l+1/2,i}^{+} \right)}{\phi_{l+1} a_{l+1/2,i}^{\max} - \phi_l a_{l+1/2,i}^{\min}} \\ & + \frac{\phi_l \phi_{l+1} a_{l+1/2,i}^{\max} a_{l+1/2,i}^{\min}}{\phi_{l+1} a_{l+1/2,i}^{\max} - \phi_l a_{l+1/2,i}^{\min}} \left(\mathbf{S}_{l+1/2,i}^{+} - \mathbf{S}_{l+1/2,i}^{-} \right), \end{aligned} \tag{3.33}$$

$$\begin{aligned} \mathbf{H}_{l-1/2,i} = & \frac{\phi_l a_{l-1/2,i}^{\max} \mathbf{f}_i \left(\mathbf{S}_{l-1/2,i}^{-} \right) - \phi_{l-1} a_{l-1/2,i}^{\min} \mathbf{f}_i \left(\mathbf{S}_{l-1/2,i}^{+} \right)}{\phi_l a_{l+1/2,i}^{\max} - \phi_{l-1} a_{l-1/2,i}^{\min}} \\ & + \frac{\phi_{l-1} \phi_l a_{l-1/2,i}^{\max} a_{l-1/2,i}^{\min}}{\phi_l a_{l-1/2,i}^{\max} - \phi_{l-1} a_{l-1/2,i}^{\min}} \left(\mathbf{S}_{l-1/2,i}^{+} - \mathbf{S}_{l-1/2,i}^{-} \right), \end{aligned} \tag{3.34}$$

where by choosing $a_{l\pm1/2,i}^{\max} = -a_{l\pm1/2,i}^{\min} = a_{l\pm1/2,i} \coloneqq \max\left\{ |\Lambda_{\mathbf{S}_{l\pm1/2,i}^{-}}^{\max,\min}|, |\Lambda_{\mathbf{S}_{l\pm1/2,i}^{+}}^{\max,\min}| \right\}$, we eliminate the upwind nature of convective numerical fluxes (3.33)–(3.34) and recover the KT method proposed in [81]. In addition, the diffusive numerical fluxes are given by

$$\mathbf{P}_{l\pm1/2,i}(t) = \tilde{\mathbb{C}}_{l\pm1/2,i} \frac{\pm \mathbf{S}_{l\pm1,i} \mp \mathbf{S}_{l,i}}{h_i}, \tag{3.35}$$

where $\tilde{\mathbb{C}}_{l\pm1/2,i}$ is defined as the harmonic mean of $\mathbb{C}_l$ and $\mathbb{C}_{l\pm1,i}$. The scheme (3.32)–(3.35), combined with minmod reconstruction of the type

$$\begin{aligned} \tilde{\mathbf{S}}_l(\mathbf{x}) &= \mathbf{S}_l^n + \sum_{i=1}^{\mathfrak{d}} \mathbf{d}_{l,i}^n (x_i - x_{l,i}), \\ \mathbf{d}_{l,i}^n &= \text{minmod} \left(\theta \frac{\mathbf{S}_{l,i}^n - \mathbf{S}_{l-1,i}^n}{h_i}, \frac{\mathbf{S}_{l+1,i}^n - \mathbf{S}_{l-1,i}^n}{2h_i}, \theta \frac{\mathbf{S}_{l+1,i}^n - \mathbf{S}_{l,i}^n}{h_i} \right), \end{aligned}$$

is a TVD scheme if $1 \leq \theta \leq 2$ [83], where $\tilde{\mathbf{S}}_l$ is a piecewise linear approximation to the solution at time t^n, i.e., $\tilde{\mathbf{S}}_l(\mathbf{x}) \approx \mathbf{S}_l^n(\mathbf{x})$. Then we can use the fact that $x_{l\pm1/2,i} = x_{l,i} \pm h_i/2$ to find $\mathbf{S}^{\pm}_{l\pm1/2,i}$. The minmod operator is a flux limiter used to avoid spurious oscillations in high-resolution schemes [81, 83], defined as follows:

$$\text{minmod}(q_1, q_2, \ldots, q_n) = \begin{cases} \min\left\{q_j\right\}, & \text{if} \quad q_j > 0 \quad \forall j, \\ \max\left\{q_j\right\}, & \text{if} \quad q_j < 0 \quad \forall j, \\ 0, & \text{otherwise.} \end{cases} \tag{3.36}$$

The system of ODEs (3.32) can be solved by several numerical methods. Usually, this model is solved by applying explicit-in-time finite difference schemes [34, 58, 60, 62, 106]. However, this thesis adopts an implicit variable order, adaptive step Backward Differentiation Formula (BDF). This stable implicit scheme allows for taking larger time steps than an explicit method would require, which reduces the computational cost. In our numerical simulations, we used the implementation of the BDF scheme from the `CVode` package, available in the SUNDIALS library [85].

3.4 FOSSIL (FOam diSplacement SImuLator)

FOSSIL is an in-house foam simulator developed in LAMAP[1] by a multidisciplinary team whose primary goal is to be a highly extensible, reliable, and flexible software that every researcher in the laboratory could use. The code can run simulations as simple as Buckley-Leverett problems or as complex as highly heterogeneous, compressible flows, including gravitational effects. The main focus of the software is the simulation of multi-phase flows, including foam effects in heterogeneous porous media, using advanced numerical methods. FOSSIL, based on the proposed sequential Algorithm 1, was implemented to be a robust, accurate, and precise simulator. Additionally, the code was validated against several analytical solutions, laboratory experimental data, and commercial software (CMG-STARS). The validations are presented in Chapters 4–6, and also in Appendix C.

The simulator was built based on three steps: definition of the mathematical model, choice of the numerical methods used to approximate the mathematical model and computational implementation of the discretizations generated by the numerical methods. The mathematical model adopted uses the concept of global pressure [72, 73] to rewrite equations (2.1)–(2.4) in a more suitable system of equations for numerical solvers, such as (2.31)–(2.34). The numerical methodology is based on a staggered formulation, in which equations (2.31)–(2.34) are separated into two subsystems of distinct kind: one of hydrodynamic problem (2.31)–(2.32) and the other with transport relations (2.31)–(2.34). Due to this staggered methodology, two different

[1] LAMAP stands for LAboratório de Matemática APlicada or Applied Mathematics Laboratory (more details in `http://lamap.ufjf.br/`).

numerical methods can be applied to each subsystem: a mixed hybrid finite element method [76] to the Darcy problem and a high order non-oscillatory finite volume method [83] to the transport problem. A detailed description of the solution methodology was given in the previous sections. Algorithm 1 summarizes the basic methodology implemented to solve (2.31)–(2.34).

From the point of view of computational implementation, FOSSIL is being developed on top of two open-source libraries, SUNDIALS [85] and deal.II [86]. The SUNDIALS library is a suite of advanced computational codes for solving large-scale problems that can be modeled as a system of ordinary differential equations. The library's architecture is shown in Figure 7. SUNDIALS is divided into six solver packages: CVODE, CVODES, ARKODE, ARKODES, IDA, IDAS and KINSOL and provides both linear and non-linear solvers.

In this context, we selected the CVODE solver to discretize the ODEs that rise from the finite volume method discretization. The package applies Backward Differentiation Formulas (BDF). The scheme used in CVode is variable-order and variable-step multistep methods. Hence, Δt_s varies in the integration process bounded to relative and absolute tolerances. The non-linear problem resulted from (3.2) after space discretization was solved using a quasi-Newton method along with the Scaled, Preconditioned, Generalized Minimum Residual (SPGMR) linear solver. The evaluations of the right-hand side of the ordinary differential equations (3.32) were implemented in parallel, using OpenMP API.

Figure 7 – Internal architecture of Sundials library.

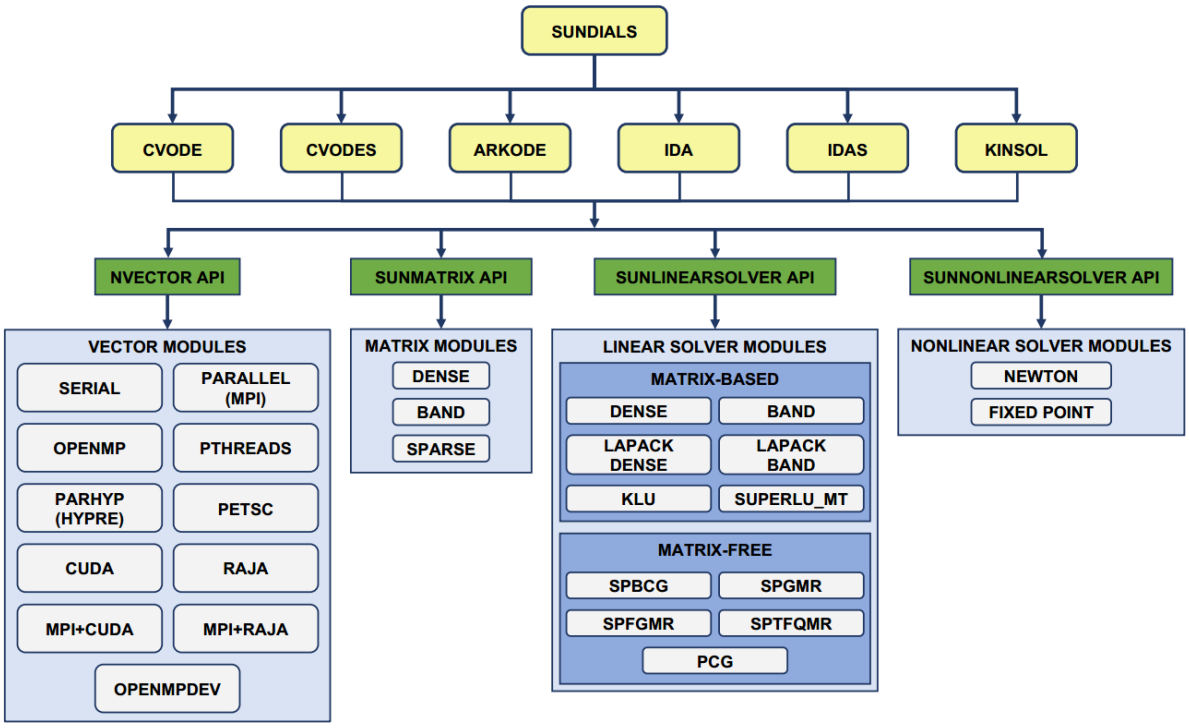

Source: [107]

Deal.II is a C++ objected-oriented library designed to solve systems of partial differential

equations using finite element methods. The classes in the deal.II library are grouped into several modules (see Fig. 8). These modules contain the essential tools to implement any finite element program. The global linear system was solved using the UMFPACK [108], a set of routines using multifrontal LU factorization.

Figure 8 – Modules structure of the deal.II library. Arrows indicate the interaction between modules. The light gray boxes are a subset of optional external libraries, and the light gray ovals are a subset of optional external applications that deal.II can interact with.

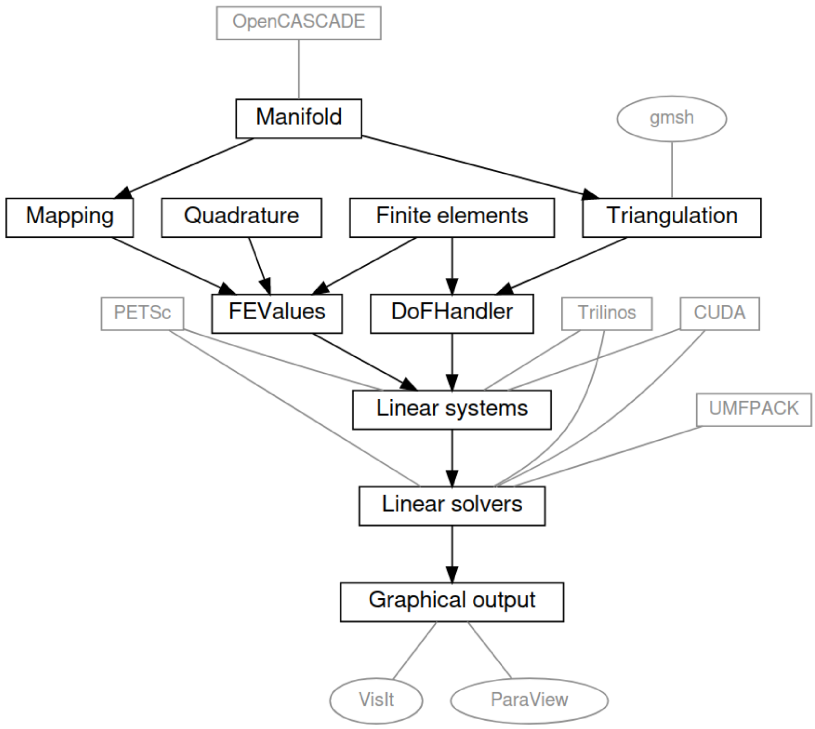

Source: from `https://www.dealii.org/`

Several functionalities were implemented in FOSSIL aiming at constructing a robust and flexible foam displacement simulator. The following (non-exhaustive) list shows some of the simulator features:

- One or Two-dimensional simulations with cartesian grid generation;
- Two-phase flow simulations with or without foam displacement;
- Several empirical, local equilibrium and population balance foam models;
- Equilibrium and kinetic adsorption models;
- Gases can be treated both as compressible or incompressible;
- A variety of boundary conditions can be applied;

- Simulations with or without capillary effects;
- Heterogeneous permeability and porosity fields;
- Gravitational effect;
- Well injection;
- Shared memory parallel computing;
- Outputs both in plain text and VTK formats.

In order to improve the usability of FOSSIL, the simulations are configured through input files, from where the software reads all data needed to run a simulation. The several options in the input file control many aspects of the software's behavior regarding numerical methods, boundary conditions, geometry, rock properties, physical parameters, etc. All input parameters have default values, which allows for omitting any of them in the input file when they are not necessary for the specific simulation being described or when it is intended to use their default values.

4 FOAM MODEL WITH NEWTONIAN BEHAVIOR

The current chapter shows results using the foam model with Newtonian behavior proposed in [50] and presented in Section 2.5.2. First, one-dimensional results reproduced from literature using FOSSIL are shown, aiming at the computational validation of the numerical methodology proposed in this work when applied to the linear kinetic model. Then, a problem involving the gravitational effect in two-dimensional heterogeneous porous media is simulated, to study the capability of foam to reduce gravity override and viscous fingering. These results are published in [15].

4.1 Model Definition

To simulate the linear kinetic foam model, it is adopted the assumptions of water-gas phases incompressibility, the surfactant transport equation (2.1) is neglected, alongside the adsorption effect. It is also assumed that surfactant is readily available in the aqueous phase for foam generation. Hence, the mathematical model presented in Section 2.4 can be reduced as follows:

Find, in $\Omega \times (0, T]$, the total fluid velocity $\mathbf{u}$, the global pressure p, the water saturation S_{w}, and the foam texture n_{D} satisfying

$$\mathbf{u} = -\kappa\lambda \left(\nabla p - \mathbf{G}\left(S_{\mathrm{w}}, n_{\mathrm{D}}, p\right)\right), \tag{4.1}$$

$$\nabla \cdot \mathbf{u} = 0, \tag{4.2}$$

$$\phi \frac{\partial \mathbf{S}}{\partial t} + \sum_{i=1}^{\mathfrak{d}} \frac{\partial \mathbf{f}_i}{\partial x_i} - \nabla \cdot (\mathbb{C} \nabla \mathbf{S}) = \mathbf{\Phi}, \tag{4.3}$$

where

$$\mathbf{S} = \begin{bmatrix} S_{\mathrm{w}} \\ S_{\mathrm{g}} n_{\mathrm{D}} \end{bmatrix}, \qquad \mathbf{f}_i = \begin{bmatrix} f_{\mathrm{w}} u_i - b_i \\ n_{\mathrm{D}} f_{\mathrm{g}} u_i + n_{\mathrm{D}} b_i \end{bmatrix}, \qquad \mathbf{\Phi} = \begin{bmatrix} 0 \\ \phi S_{\mathrm{g}} K_{\mathrm{c}} \left[n_{\mathrm{D}}^{\mathrm{LE}}\left(S_{\mathrm{w}}\right) - n_{\mathrm{D}} \right] \end{bmatrix},$$

$$\mathbb{C} = \kappa\lambda_{\mathrm{g}} f_{\mathrm{w}} \frac{\mathrm{d}P_{\mathrm{c}}}{\mathrm{d}S_{\mathrm{w}}} \begin{bmatrix} -1 & 0 \\ n_{\mathrm{D}} & 0 \end{bmatrix}, \quad n_{\mathrm{D}}^{\mathrm{LE}}\left(S_{\mathrm{w}}\right) = \begin{cases} \tanh\left[A\left(S_{\mathrm{w}} - S_{\mathrm{w}}^{*}\right)\right], & S_{\mathrm{w}} > S_{\mathrm{w}}^{*}, \\ 0, & S_{\mathrm{w}} \leq S_{\mathrm{w}}^{*}. \end{cases} \tag{4.4}$$

where $\mathbf{b} = \kappa\lambda_{\mathrm{g}} f_{\mathrm{w}} \tilde{\boldsymbol{\rho}}$. In addition, the boundary and initial conditions of the model presented above are given in (2.37)-(2.40), neglecting the surfactant concentration and adsorption.

In order to solve the problem (4.1)–(4.3), the numerical methodology presented in Chapter 3 is adapted. In the Algorithm 1, the steps related to compressibility, surfactant transport, and adsorption are neglected.

4.2 Computational Validation for the Linear Kinetic Model

In the work [50], it is investigated the case study of the injection of foam at an injection state (J) into a core with a certain initial state (I). The states I and J are defined by the pair of water saturation and dimensionless bubble texture (Table 1). The resulting solution is a shock that starts on state J and goes to state I, so these two states are also the states upstream and downstream of the shock, respectively. The pair of values for I and J are $(S_{\mathrm{w}}, n_{\mathrm{D}})^I = (0.72, 1.0)^I$ and $(S_{\mathrm{w}}, n_{\mathrm{D}})^J = (0.372, 0.664)^J$. The simulations are carried out using the following relative permeability and capillary pressure functions [50]:

$$k_{\mathrm{rw}} = 0.2\left(\frac{S_{\mathrm{w}} - S_{\mathrm{wc}}}{1 - S_{\mathrm{wc}} - S_{\mathrm{gr}}}\right)^{4.2}, \tag{4.5}$$

$$k^0_{\mathrm{rg}} = 0.94\left(\frac{1 - S_{\mathrm{w}} - S_{\mathrm{gr}}}{1 - S_{\mathrm{wc}} - S_{\mathrm{gr}}}\right)^{1.3}, \tag{4.6}$$

$$P_{\mathrm{c}} = 330\frac{\left(1 - S_{\mathrm{w}} - S_{\mathrm{gr}}\right)^{0.01}}{(S_{\mathrm{w}} - S_{\mathrm{wc}})}, \tag{4.7}$$

where S_{wc} is connate water saturation, the S_{gr} residual gas saturation, and k^0_{rg} is the gas relative permeability in absence of foam. The linear kinetic model modifies the foamed gas mobility altering the gas relative permeability in the following way

$$k_{\mathrm{rg}}\left(S_{\mathrm{w}}, n_{\mathrm{D}}\right) = \frac{k^0_{\mathrm{rg}}\left(S_{\mathrm{w}}\right)}{C_{\mathrm{mrf}} n_{\mathrm{D}} + 1}. \tag{4.8}$$

Other parameters are given in Table 1 and, additionally, the flow is considered to be incompressible and the gravity and adsorption are neglected.

In the simulations, while the states I and J are maintained constant, four values for K_{c} are evaluated. As can be seen in (2.46), the parameter K_{c} controls how fast foam reaches local equilibrium ($r_{\mathrm{g}} = r_{\mathrm{c}}$). Thus, for elevated values of K_{c}, foam achieves local equilibrium rapidly, while for lower values of K_{c}, the foam takes comparatively longer to reach equilibrium. Figure 9 presents solutions for $K_{\mathrm{c}} = 0, 0.01, 1.0$ and 200. The result for $K_{\mathrm{c}} = 200$ (Fig. 9(d)) shows an almost local equilibrium behavior, as expected for a relatively large K_{c} values that, in this case, is in the range of hundreds. It is worth noticing that for $K_{\mathrm{c}} = 200$ the problem becomes stiff. These kinds of equations are characterized by the existence of terms that can lead to a rapid variation of the solution. Moreover, the stiff nature of the problem requires time step reduction (Δt_{s}), in order to make the solution match absolute and relative tolerances error bounds. Additionally, when a central method, such as the proposed by Kurganov and Tamdmor (KT) [81] is adopted, spurious oscillation appears, and there is no convergence to the expected solution, as can be seen in Figure 10. A similar oscillatory behavior was also observed in [109] when the KT method was used to solve a three-phase flow problem. Figure 9(c) is shown the solution for $K_{\mathrm{c}} = 1$, which presents oscillations upstream of the wavefront. As demonstrated in [50, 110], the oscillations are non-spurious, as they are a part of the analytical solution. Nonetheless, the

Table 1 – Simulation parameters for the linear kinetic model.

Parameter	Value	Parameter	Value
Water Viscosity (μ_{w}) [Pa s]	1.0×10^{-3}	C_{mrf}	18500
Gas Viscosity $\left(\mu_{\mathrm{g}}\right)$ [Pa s]	2.0×10^{-5}	A	400
Water residual saturation (S_{wc})	0.2	K_{c} [1/s]	$\{0, 0.01, 1, 200\}$
Gas residual saturation $\left(S_{\mathrm{gr}}\right)$	0.18	Length [m]	0.05
Critical water saturation $\left(S_{\mathrm{w}}^{*}\right)$	0.37	Final time [s]	100
Max foam texture $(n_{\max})$ [m^{-3}]	8.0×10^{13}	Δt_{u} [s]	5.0
Injection velocity $(\bar{u})$ [m s^{-1}]	2.93×10^{-5}	Number of cells	100
Initial water saturation (S_{w}^{0})	0.72	Minmod parameter (θ)	1.0
Injected water saturation $\left(\bar{S}_{\mathrm{w}}\right)$	0.372	Absolute tolerance	1.0×10^{-6}
Initial foam texture (n_{D}^{0})	1.0	Relative tolerance	1.0×10^{-4}
Injected foam texture $(\bar{n}_{\mathrm{D}})$	0.664	$\mathcal{RT}$ index (k)	0
Porosity	0.25		

amount of diffusion (numerical diffusion and/or the diffusion from the capillary pressure) can modify the oscillation pattern. As the K_{c} value decreases and reaches 0.01 (Figure 9(b)), the oscillations are dissipated. In this case, it is possible to see a water saturation decay right before the shock, coinciding with the foam texture transition from I to J becoming less steep. This behavior is accentuated for $K_{\mathrm{c}} = 0$ (see Fig. 9(a)).

The vertical red line in Figure 9 represents the analytical shock front position for the water saturation, which can be obtained using the following expression [50]:

$$x_s = t\frac{u}{\phi}\frac{f_{\mathrm{w}}^{I} - f_{\mathrm{w}}^{J}}{S_{\mathrm{w}}^{I} - S_{\mathrm{w}}^{J}}, \tag{4.9}$$

where x_s is the shock front position, u is the total injection velocity, t is the simulation final time, and the superscripts I and J stand for conditions upstream and downstream of the shock, respectively. With that, it can be seen in Figure 9, that the water saturation numerical shock front position matches the analytical prediction given by the equation (4.9).

Figure 9 – Linear kinetic model results for $K_c = 0, 0.01, 1.0, 200$.

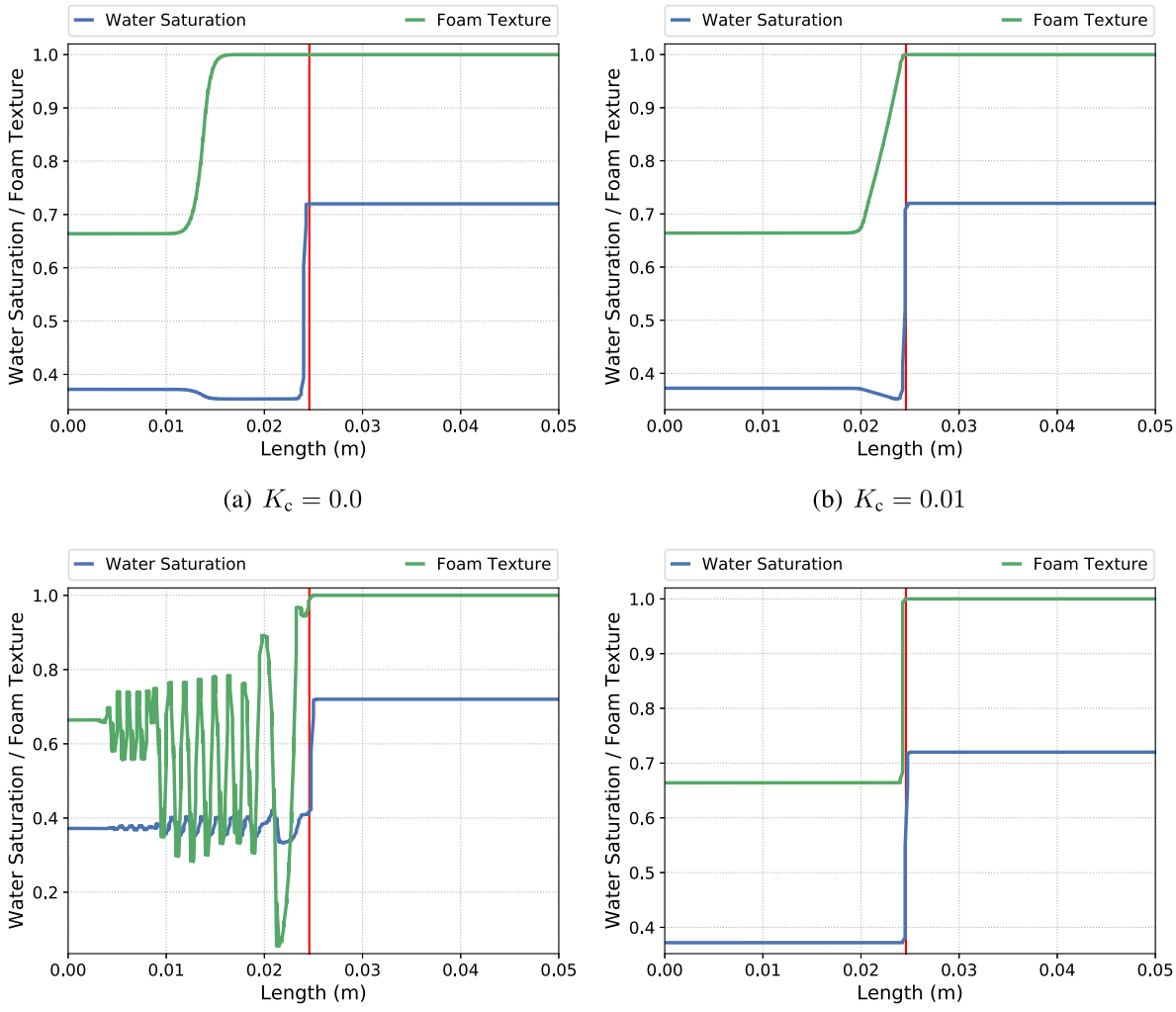

(a) $K_c = 0.0$

(b) $K_c = 0.01$

(c) $K_c = 1.0$

(d) $K_c = 200$

Source: Prepared by the author.

Figure 10 – Comparison between KT and KNP methods for the linear kinetic model with $K_c = 200$.

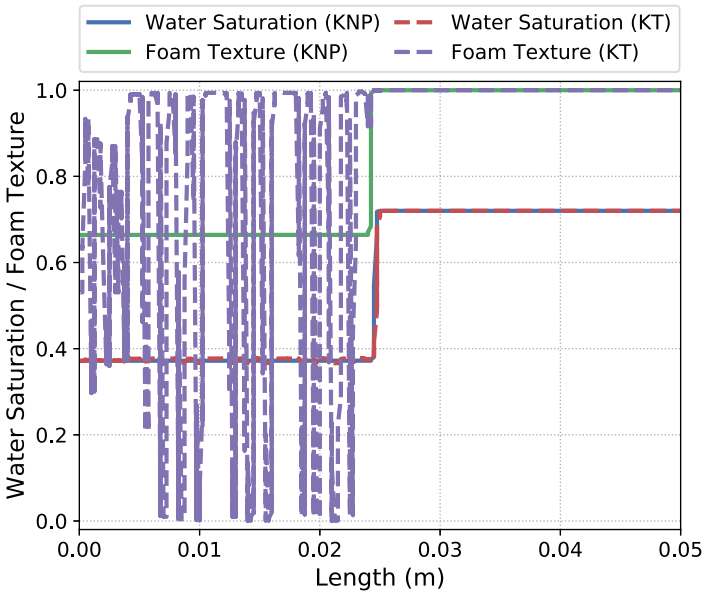

Source: Prepared by the author.

4.3 Influence of Newtonian Foam Flow Model in Gravity Override

We now present results of two-dimensional numerical experiments in a heterogeneous porous medium, published in [15], that aim to assess the influence of foam and gravity effects in incompressible two-phase flow using the Linear kinetic foam model (Section 2.5.2). Flows without and with foam are compared. In both cases, scenarios with gravity and without gravity are considered. In flows without foam, the hydrodynamics and the mobility of the gas phase remain unchanged $\left(k_{\text{rg}} = k_{\text{rg}}^0\right)$, because $n_{\text{D}} = 0$. In flows with foam, we assume that surfactant is readily available in the water phase, allowing for foam creation and changes in the mobility of the gas phase.

In these simulations, the capillary pressure is given in (4.7), and relative permeabilities are defined as

$$k_{\text{rw}} = \left(\frac{S_{\text{w}} - S_{\text{wc}}}{1 - S_{\text{wc}} - S_{\text{gr}}}\right)^4, \qquad k_{\text{rg}}^0 = \left(\frac{1 - S_{\text{w}} - S_{\text{gr}}}{1 - S_{\text{wc}} - S_{\text{gr}}}\right)^2.$$

The permeability fields $\kappa(\mathbf{x})$ are given by layers 1 (case A, Fig. 11(a)) and 36 (case B, Fig. 11(b)) of the 10$^{\text{th}}$ SPE project [1], rotated to the xy plane. The right boundary is chosen to be of the Dirichlet type (Γ_D) with $\bar{p} = 0$, while left, top and bottom boundaries are set to Neumann condition (Γ_N) with $\bar{u} < 0$ for the left boundary and $\bar{u} = 0$ for the top and bottom boundaries. Coefficients and numerical parameters used in the simulations are shown in Table 2.

Table 2 – Simulation parameters aiming to assess the influence of foam in gravity override.

Parameter	Value	Parameter	Value
Water density (ρ_{w}) [kg/m^3]	1000	Porosity	0.25
Gas density $\left(\rho_{\text{g}}\right)$ [kg/m^3]	1.65	C_{mrf}	500
Water Viscosity (μ_{w}) [Pa s]	1.0e-3	A	100
Gas Viscosity $\left(\mu_{\text{g}}\right)$ [Pa s]	2.0e-5	K_{c} [1/s]	1.0×10^{-4}
Water residual saturation (S_{wc})	0.2	Dimensions [m]	3.67×1.0
Gas residual saturation $\left(S_{\text{gr}}\right)$	0.0	Final time [s]	1.0×10^4
Critical water saturation $\left(S_{\text{w}}^*\right)$	0.37	$\Delta t_{\text{u}}[s]$	20.0
Max foam texture ($n_{\max}$) [m^{-3}]	8.0e13	Number of cells	220×60
Gas injection velocity [m s^{-1}]	2.7e-5	minmod parameter (θ)	1.0
Water injection velocity [m s^{-1}]	3.0e-6	Absolute tolerance	1.0×10^{-6}
Initial water saturation (S_{w}^0)	1.0	Relative tolerance	1.0×10^{-4}
Initial foam texture (n_{D}^0)	0.0	$\mathcal{RT}$ index (k)	0
Injected foam texture ($\bar{n}_{\text{D}}$)	0.0		

The water saturation profiles for case A at $t = 2\,000$ s and $t = 10\,000$ s are shown in Figures 12 and 13, respectively. It is visible that the gravity effects are much more pronounced

in the no-foam simulation. Also, as expected, the fluid phase displacement occurs more slowly in the foam presence due to the gas mobility reduction caused by foam. Note that, without foam, the gas breakthrough has already occurred at $t = 10\,000$ s (Fig. 13), which does not occur when the foam is present. Additionally, the foam texture results for the case where foam is not absent are shown in Figures 14. The foam texture solutions show virtually no difference between the case with gravity and the case with no gravity, showing the foam's ability to significantly reduce the gravity override phenomenon. Interestingly, the higher values of foam texture are found in the wavefront, demonstrating a better control of gas front flow. Moreover, for the foam model [50] and simulation data adopted, viscous fingering and gravity override are significantly reduced with foam as time advances. As a result, a better sweep efficiency of the medium is observed when the foam is present, as can be seen in Figure 18(a), which shows the cumulative water production.

Figure 11 – Permeability map of layer 1 (a) and layer 36 (b) of the 10$^{\text{th}}$ SPE project [1].

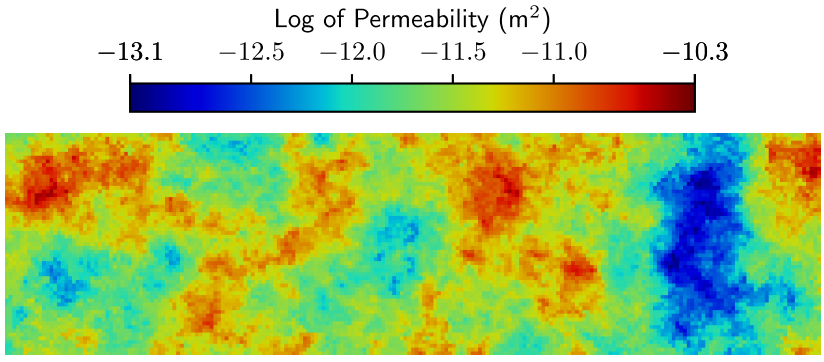

(a) Case A.

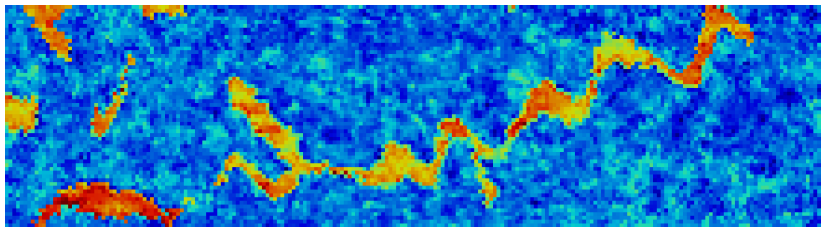

(b) Case B.

Source: Prepared by the author.

In case B, the permeability field has a more evident preferential channel in the lower region (see Fig. 11(b)). The results of this channelized porous formation (Figs. 15–17) reinforce the foam's ability to reduce the effects of gravity override and viscous fingering, according to the model used, even though this case presents a more pronounced preferential path. The water cumulative production curves for case B (Fig. 18(b)) show a similar behavior presented previously in Case A: the presence of foam in the flow in porous media significantly increases the production. It is interesting to note that for the foam flow experiments, the production curves

Figure 12 – Case A: water saturation at $t = 2\,000$ s.

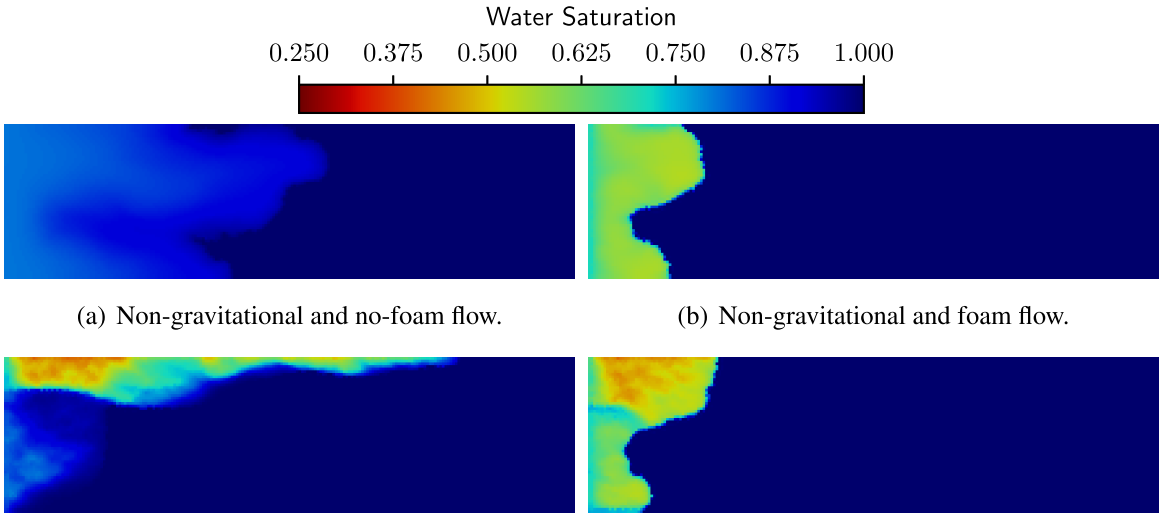

(a) Non-gravitational and no-foam flow.

(b) Non-gravitational and foam flow.

(c) Gravitational and no-foam flow.

(d) Gravitational and foam flow.

Source: Prepared by the author.

Figure 13 – Case A: water saturation at $t = 10\,000$ s.

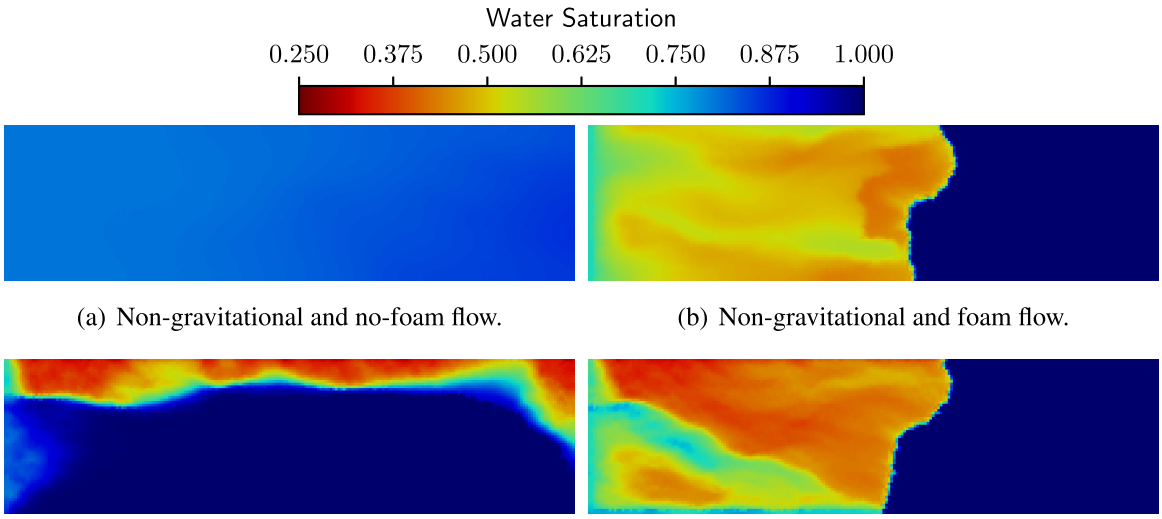

(a) Non-gravitational and no-foam flow.

(b) Non-gravitational and foam flow.

(c) Gravitational and no-foam flow.

(d) Gravitational and foam flow.

Source: Prepared by the author.

(Fig. 18(a) and 18(b)) for the simulations with gravity and without gravity are very similar, especially in Case B.

Figure 14 – Case A: foam texture when the foam is present in the flow.

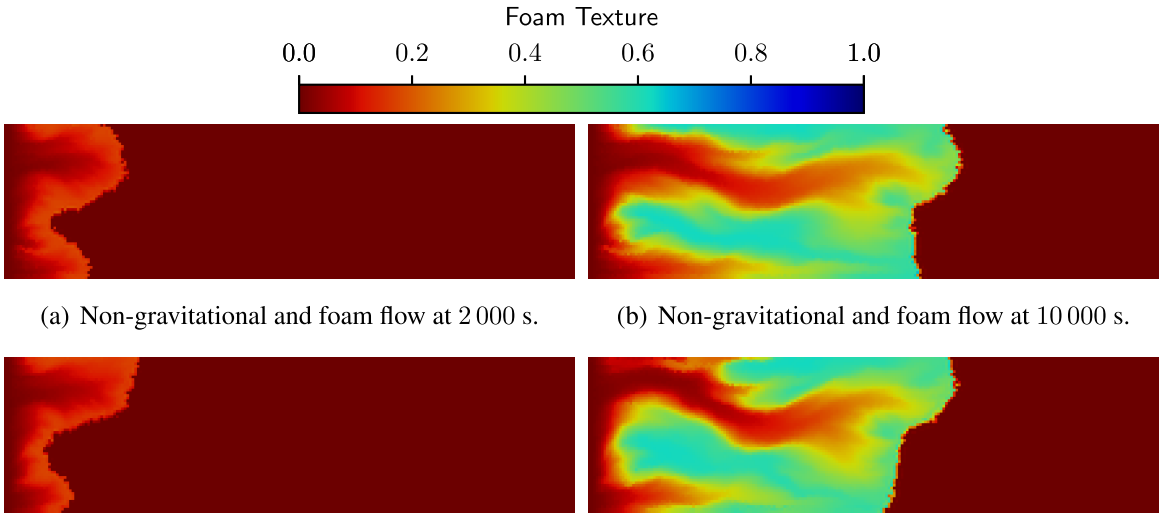

(a) Non-gravitational and foam flow at 2 000 s.

(b) Non-gravitational and foam flow at 10 000 s.

(c) Gravitational and foam flow at 2 000 s.

(d) Gravitational and foam flow at 10 000 s.

Source: Prepared by the author.

Figure 15 – Case B: water saturation at $t = 2\,000$ s.

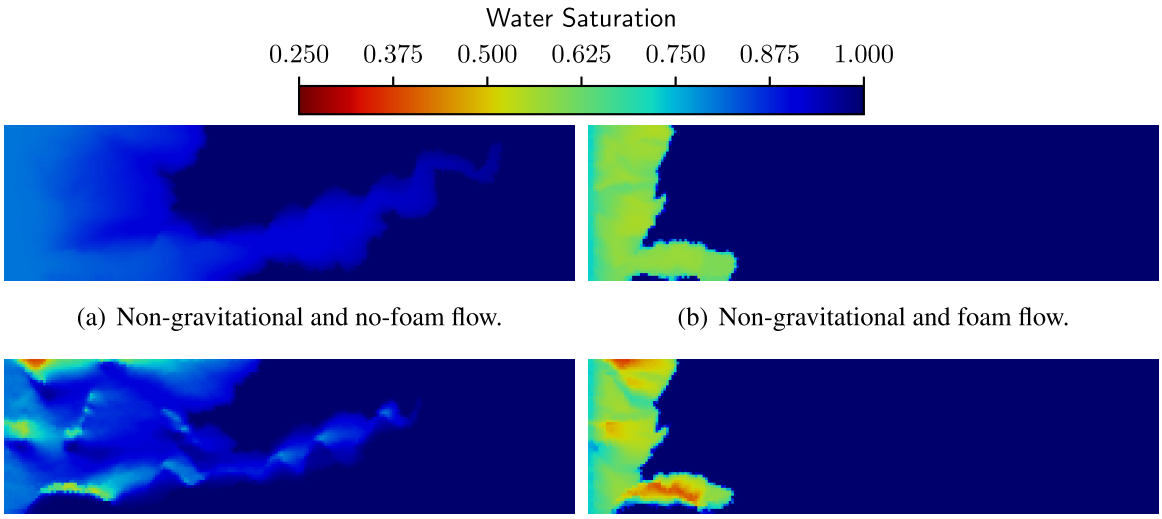

(a) Non-gravitational and no-foam flow.

(b) Non-gravitational and foam flow.

(c) Gravitational and no-foam flow.

(d) Gravitational and foam flow.

Source: Prepared by the author.

4.4 Partial Conclusions

The numerical and computational methodology proposed in Chapter 3 combined with linear kinetic foam flow was successfully applied to reproduce the results presented in [50]. For the case that non-spurious oscillation appears ($K_c = 1$), the numerical solutions were able to reflect that behavior. When the problem becomes stiff ($K_c = 200$), additional numerical difficulties can arise. For example, simulations using the classical KT method [81] (see Sec.

Figure 16 – Case B: water saturation at $t = 10\,000$ s.

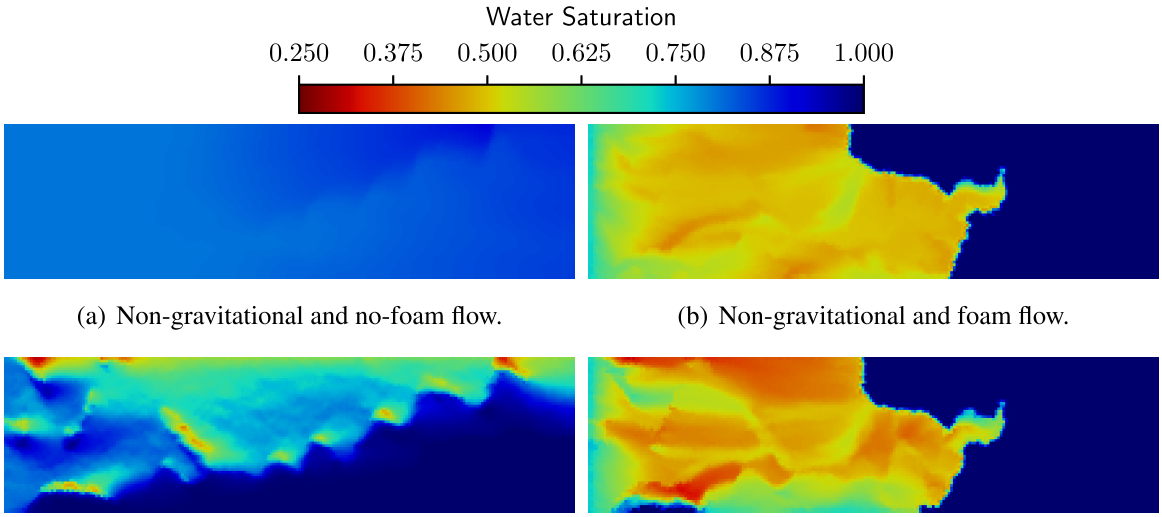

(a) Non-gravitational and no-foam flow.

(b) Non-gravitational and foam flow.

(c) Gravitational and no -foam flow.

(d) Gravitational and foam flow.

Source: Prepared by the author.

Figure 17 – Case B: foam texture when the foam is present in the flow.

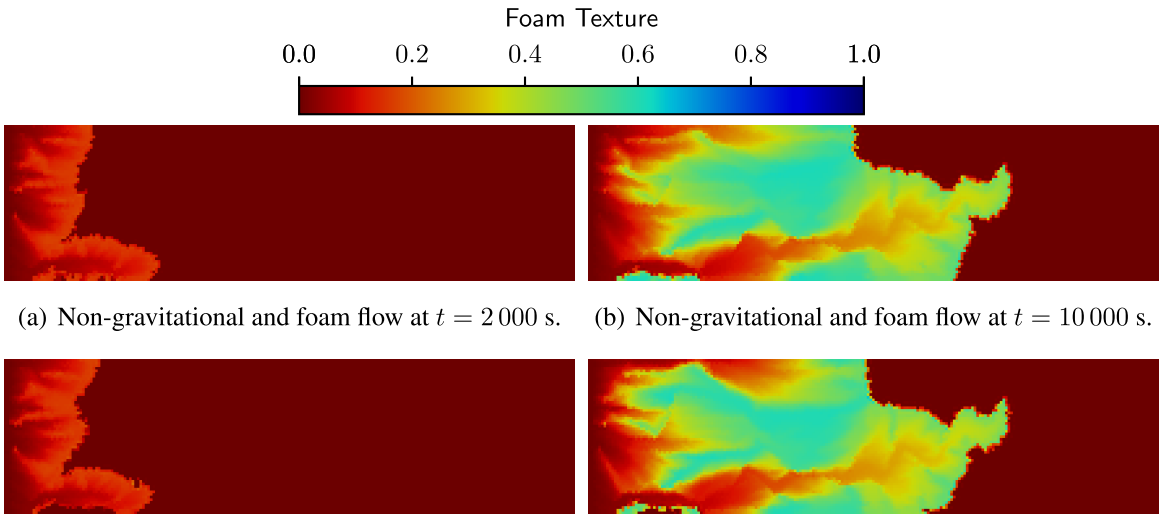

(a) Non-gravitational and foam flow at $t = 2\,000$ s.

(b) Non-gravitational and foam flow at $t = 10\,000$ s.

(c) Gravitational and foam flow at $t = 2\,000$ s.

(d) Gravitational and foam flow at $t = 10\,000$ s.

Source: Prepared by the author.

3.3.2) was not able to converge to the expected solution, as spurious oscillations appear in the results. On the other hand, the numerical experiments using the KNP method [83] (Fig. 9) showed good agreement with the results presented in [50].

Algorithm 1 was also applied to simulate regimes with pure gas-water injection and gas-water-foam flow. In this context, we established a comparison between these two regimes considering two layers of the SPE10 project [1] with different heterogeneous permeability fields. The results, based on the model proposed in [50], point to the remarkable foam's ability to reduce

Figure 18 – Water cumulative production for cases A and B.

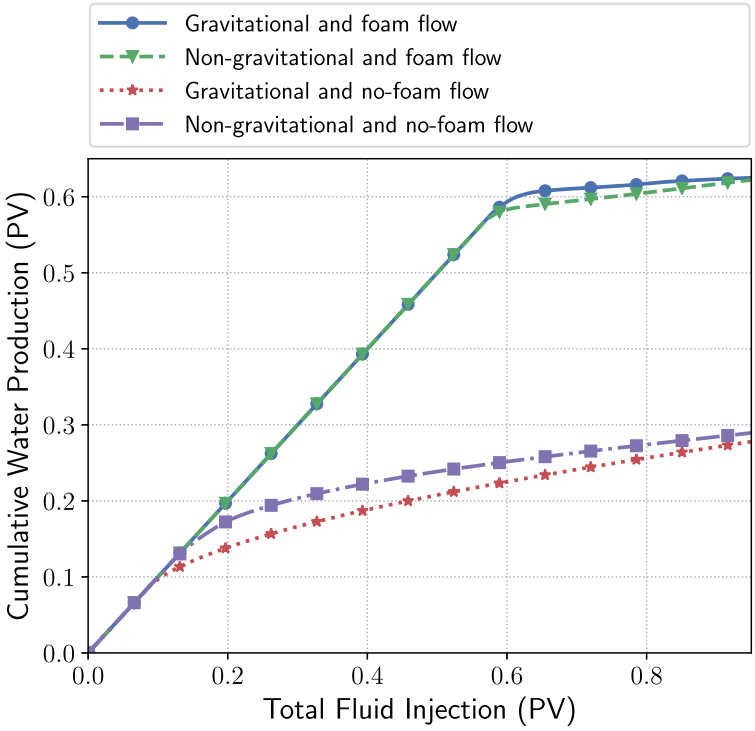

(a) Case A.

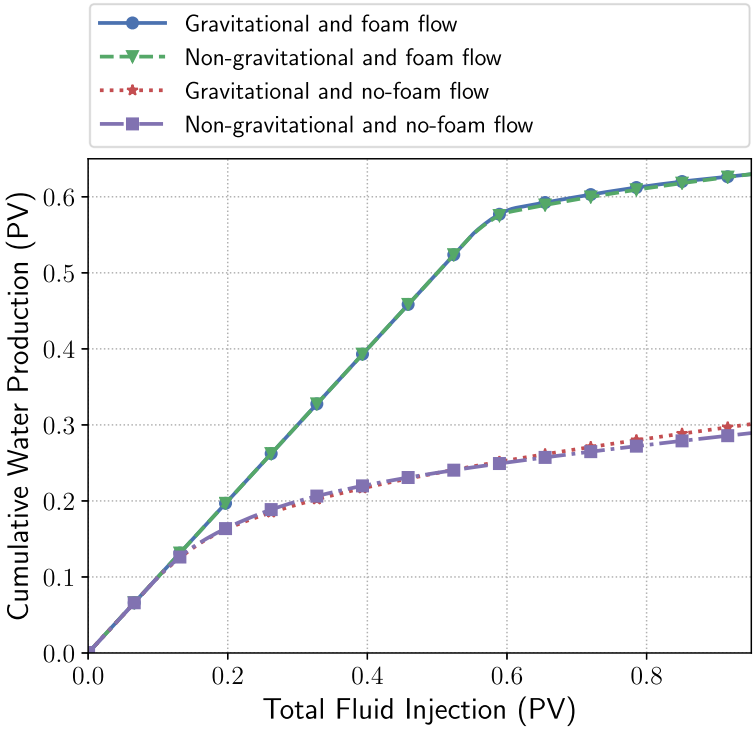

(b) Case B.

Source: Prepared by the author.

the gravity override and viscous fingering even in cases of porous media with rather pronounced preferential channels. The production curves (Fig. 18) show a significant improvement in the results when the foam is present in the flow.

5 FOAM MODEL WITH NON-NEWTONIAN BEHAVIOR

This chapter presents results using the two-phase flow in porous media including foam displacement with non-Newtonian behavior provided by the stochastic bubble population foam model proposed in [52] and shown in Section 2.5.3. Initially, FOSSIL is applied to reproduce computational results from literature and laboratory experiments. These results aim at the computational validation of the Algorithm 1 when the stochastic bubble population model is adopted. Next, two-dimensional problems are simulated to assess the non-Newtonian foam behavior provided by the foam model in heterogeneous porous media under the effects of gravity and gas compressibility.

5.1 Model Definition

The mathematical model adopted in this chapter is derived from the system of equations presented in Section 2.4, neglecting surfactant equation (2.1) and, consequently, the adsorption phenomena and assuming the surfactant concentration in the water phase is high enough such that it does not impact foam coalescence, leading to the choice of zero for the bubble destruction coefficient (K_{d}) in equation (2.51). In this context, the following problem is generated:

Find, in $\Omega \times (0, T]$, the total fluid velocity $\mathbf{u}$, the global pressure p, the water saturation S_{w}, and the foam texture n_{D} satisfying

$$\mathbf{u} = -\kappa\lambda \left(\nabla p - \mathbf{G}\left(S_{\mathrm{w}}, n_{\mathrm{D}}, p\right)\right), \tag{5.1}$$

$$c\left(S_{\mathrm{w}}, p\right)\frac{\partial p}{\partial t} + \nabla \cdot \mathbf{u} = D\left(S_{\mathrm{w}}, n_{\mathrm{D}}, p\right)(\mathbf{u}\cdot\mathbf{u}) + \mathbf{B}\left(S_{\mathrm{w}}, n_{\mathrm{D}}, p\right)\cdot\mathbf{u} + F\left(S_{\mathrm{w}}, n_{\mathrm{D}}, p\right), \tag{5.2}$$

$$\phi\frac{\partial \mathbf{S}}{\partial t} + \sum_{i=1}^{\mathfrak{d}}\frac{\partial \mathbf{f}_i}{\partial x_i} - \nabla\cdot(\mathbb{C}\nabla\mathbf{S}) = \mathbf{\Phi}, \tag{5.3}$$

where

$$\mathbf{S} = \begin{bmatrix} S_{\mathrm{w}} \\ S_{\mathrm{g}} n_{\mathrm{D}} \end{bmatrix}, \qquad \mathbf{f}_i = \begin{bmatrix} f_{\mathrm{w}} u_i - b_i \\ n_{\mathrm{D}} f_{\mathrm{g}} u_i + n_{\mathrm{D}} b_i \end{bmatrix}, \qquad \mathbf{\Phi} = \begin{bmatrix} 0 \\ \phi S_{\mathrm{g}} K_{\mathrm{g}} (1 - n_{\mathrm{D}}) \end{bmatrix},$$

$$\mathbb{C} = \kappa\lambda_{\mathrm{g}} f_{\mathrm{w}} \frac{\mathrm{d}P_{\mathrm{c}}}{\mathrm{d}S_{\mathrm{w}}} \begin{bmatrix} -1 & 0 \\ n_{\mathrm{D}} & 0 \end{bmatrix}, \tag{5.4}$$

where $\mathbf{b} = \kappa\lambda_{\mathrm{g}} f_{\mathrm{w}} \tilde{\boldsymbol{\rho}}$, and the terms $D\left(S_{\mathrm{w}}, n_{\mathrm{D}}, p\right)$, $c\left(S_{\mathrm{w}}, p\right)$, $\mathbf{B}\left(S_{\mathrm{w}}, n_{\mathrm{D}}, p\right)$, and $F\left(S_{\mathrm{w}}, n_{\mathrm{D}}, p\right)$ are given in the definitions (2.27)–(2.30). Additionally, the boundary and initial conditions for this model are given in (2.37)-(2.40), neglecting the surfactant concentration and adsorption.

The foam model proposed in [52] assumes the non-Newtonian foam behavior that is incorporated in the system (5.1)-(5.3) through the Equation (2.49), that in a transient flow, can be reduced to [96]

$$\mu_{\mathrm{g}}^{\mathrm{f}} = \mu_{\mathrm{g}} + \alpha n_{\max}\frac{n_{\mathrm{D}}}{|\mathbf{v}_{\mathrm{g}}|^{d}}. \tag{5.5}$$

For $d = 1/3$, the Equation (5.5) recovers the well-known Hirasaki-Lawson relation [53], where α is an empirical parameter. Moreover, this relation states that the foamed gas viscosity presents a non-linear dependence on the interstitial gas velocity. It is also worth noticing that the foam texture plays an important role in the foam viscosity alteration; as n_{D} increases, viscosity also increases, reducing foamed gas mobility. In addition, the relative permeability and capillary pressure functions used in this chapter are given by

$$k_{\mathrm{rw}} = k'_{\mathrm{rw}} \left(\frac{S_{\mathrm{w}} - S_{\mathrm{wc}}}{1 - S_{\mathrm{wc}}} \right)^{\zeta}, \tag{5.6}$$

$$k_{\mathrm{rg}} = k'_{\mathrm{rg}} \left(1 - \frac{S_{\mathrm{w}} - S_{\mathrm{wc}}}{1 - S_{\mathrm{wc}}} \right)^{\frac{3\zeta + 2}{\zeta}}, \tag{5.7}$$

$$P_{\mathrm{c}} = P_{\mathrm{c},0} \gamma \left(\frac{0.5 - S_{\mathrm{wc}}}{1 - S_{\mathrm{wc}}} \right)^{\frac{1}{\zeta}} \left(\frac{S_{\mathrm{w}} - S_{\mathrm{wc}}}{1 - S_{\mathrm{wc}}} \right)^{-\frac{1}{\zeta}}, \tag{5.8}$$

with

$$P_{\mathrm{c},0} = \frac{2\sigma_{wg}}{r_{\mathrm{p}}} \cos\theta \tag{5.9}$$

where k'_{rw} and k'_{rg} are the end-point relative permeabilities, S_{wc} is the connate water saturation, ζ is a constant, γ is a fitting parameter, σ_{wg} is the surface tension between water and gas, θ is the wetting angle between phases, and r_{p} is the effective pore radius.

The Algorithm 1, alongside the numerical methods, proposed in Chapter 3 are employed to solve the mathematical model given by the equations (5.1)–(5.3). In that sense, the surfactant transport, and adsorption computations are neglected.

5.2 Computational Validation for the Stochastic Bubble Population Model

This section provides a numerical investigation of foam flow using the stochastic bubble population model (see Section 2.5.3), aiming at reproducing the results found in [3]. The model treats foam as a non-Newtonian fluid, using the Hirasaki-Lawson expression (5.5) [53] to modify the foam viscosity using the foamed gas velocity, and foam texture. Based on the data provided in [3], the simulations are performed in a one-dimensional core of length of 0.38 m. Other assumptions are [3]: incompressibility, negligible gravity and adsorption effects. Table 3 shows several other parameters adopted for the numerical simulations. The boundary conditions adopted in these studies prescribe, for the Darcy system, the right boundary as a Dirichlet type (Γ_D) with $\bar{p} = 0$, while left, top and bottom boundaries are set to a Neumann condition (Γ_N), with $\bar{u} < 0$ for the left boundary and $\bar{u} = 0$ for the top and bottom boundaries. For the transport equations, on the left boundary, it is imposed $f_{\mathrm{g}} = 1 - f_{\mathrm{w}}$ for the aqueous phase, whereas right, top, and bottom boundaries are defined with a homogeneous Neumann condition. Additionally,

Table 3 – Simulation parameters stochastic bubble population model.

Parameter	Value	Parameter	Value
Maximum k_{rw} $\left(k'_{\text{rw}}\right)$	0.70	Maximum k_{rg} $\left(k'_{\text{rg}}\right)$	1.0
Exponent ζ	5.0	Model parameter d	$1/3$
Wetting angle (θ)	0.0	Pore radius (r_{p})	5.0×10^{-6}
Water-gas surface tension $\left(\sigma_{wg}\right)$ [N/m]	3.0×10^{-2}	Fitting parameter γ	0.5
Water Viscosity (μ_{w}) [Pa s]	1.0×10^{-3}	Porosity	0.25
Gas Viscosity $\left(\mu_{\text{g}}^{\text{nf}}\right)$ [Pa s]	1.8×10^{-5}	K_{d} $[1/\text{s}]$	0.0
Water residual saturation (S_{wc})	0.1	K_{g} $[1/\text{s}]$	0.1
Gas residual saturation $\left(S_{\text{gr}}\right)$	0.0	Length [m]	0.384
Max foam texture $(n_{\max})$ [mm^{-3}]	$\{250, 500\}$	Final time [s]	2,693
Water injection velocity [m s^{-1}]	1.47×10^{-6}	Δt_{u} [s]	20.0
Gas injection velocity [m s^{-1}]	1.47×10^{-5}	Number of cells	250
Initial foam texture (S_{w}^0)	1.0	minmod parameter (θ)	1.0
Initial foam texture (n_{D}^0)	0.0	Absolute tolerance	1.0×10^{-6}
Injected foam texture $(\bar{n}_{\text{D}})$	0.0	Relative tolerance	1.0×10^{-4}
Foamed gas viscosity constant (α)	5.8×10^{-16}	$\mathcal{RT}$ index (k)	0.0

in the right boundary, flow due to capillary pressure is not considered, and the no diffusion condition is adopted.

Following [3], two sets of simulations were performed: (1) the model parameters K_{g} and $n_{\max}$ were set to be 0.1 s^{-1} and 500 mm^{-3}, respectively; (2) the value for K_{g} was varied in 0.001, 0.01 and 0.1 s^{-1} and $n_{\max}$ fixed in 250 mm^{-3}. In the first case, the numerical simulations were performed for 0.54 injected pore volume (PV) to show the transient behavior of foam flow in the porous medium. Figure 19(a) presents the results for the first set of simulations that shows a good agreement with the solutions in [3]. It can be observed in the water saturation plot (Figure 19(a)) that the value for S_{w} in the inlet is higher, reaching $S_{\text{w}} = 0.43$, but a little further into the core, the water saturation drops to $S_{\text{w}} = 0.38$. This fact can be attributed to a very rapid increase of foam texture (n_{D}) from zero in the core entrance to the maximum foam texture $(n_{\max}$, or equivalently $n_{\text{D}} = 1)$ further into the medium, as can be seen in Figure 19(b). It is interesting to see that in the pressure profiles (Figure 19(c)), there are three main regions: right at the entrance, the pressure drop is not very pronounced, due to the lower but increasing foam texture, that does not impose significantly gas mobility reduction; in the region where $n_{\text{D}} = 1$, the pressure drop is very abrupt, because foam reduces the gas mobility significantly. Ahead of the foam wavefront, a region of single-phase water flow, the pressure drop suffers a great reduction, corresponding to the higher mobility of the water phase.

The results for the second set of numerical experiments, presented in Figure 20, are also

in good agreement with the results shown in [3]. The foam texture profiles (Figure 20(b)) show that the parameter K_{g} affects directly the foam generation rate. For higher values of K_{g}, foam texture reaches its maximum faster than for lower values. Figures 20(a) and 20(b) indicated that the wavefront is also affected by the K_{g} value due to the difference in gas mobility reduction, the difference in foam generation rates causes that. Then, in the case where $K_{\mathrm{g}} = 0.001\ \mathrm{s}^{-1}$, for example, foam texture slowly grows and does not reach $n_{\mathrm{D}} = 1$, leading to a moderate gas mobility reduction, causing a faster foam propagation. Also, the entrance region, where S_{w} decreases until it reaches a plateau, is considerably extended for lower foam generation coefficients. As to the pressure profile (Fig. 20(c)), foam with higher K_{g} exhibits a higher and steeper pressure gradient caused by the mobility reduction variation.

Figure 19 – Stochastic bubble population model results with $K_g = 0.1\ s^{-1}$ and $n_{max} = 500\ mm^{-3}$.

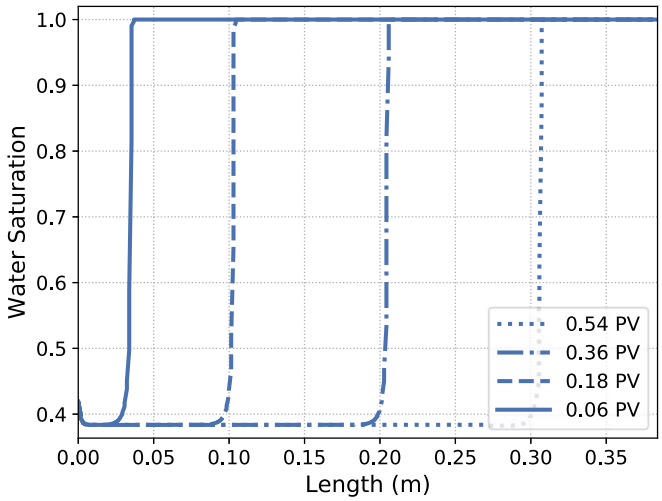

(a) Water Saturation.

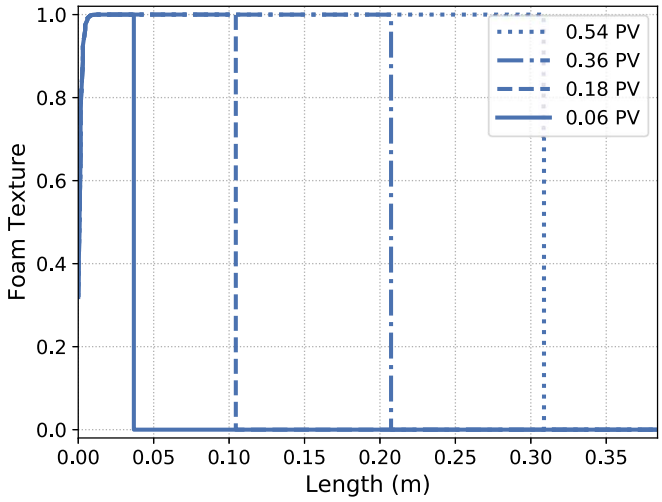

(b) Foam Texture.

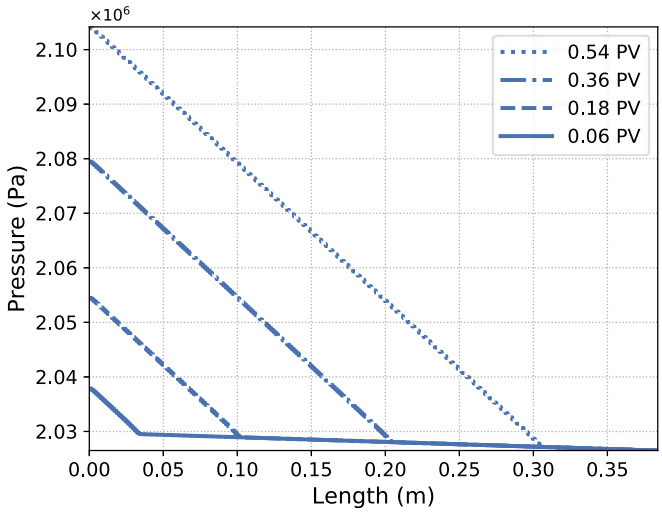

(c) Pressure (Pa).

Source: Prepared by the author.

Figure 20 – Effect of bubble generation parameter on S_{w}, n_{D} and p profiles with $n_{\max} = 250\ \mathrm{mm}^{-3}$.

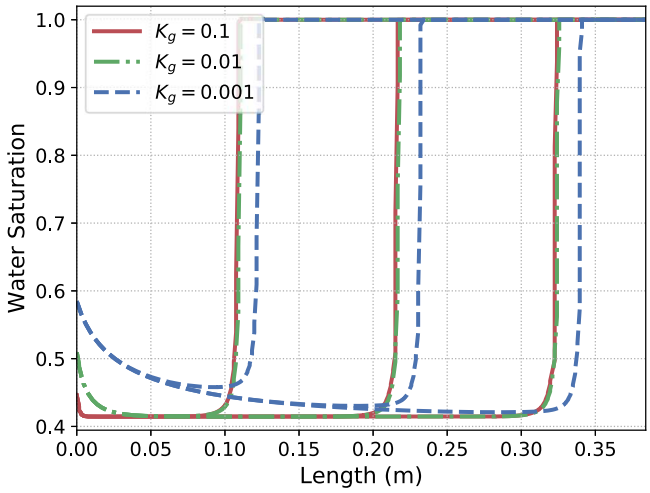

(a) Water Saturation.

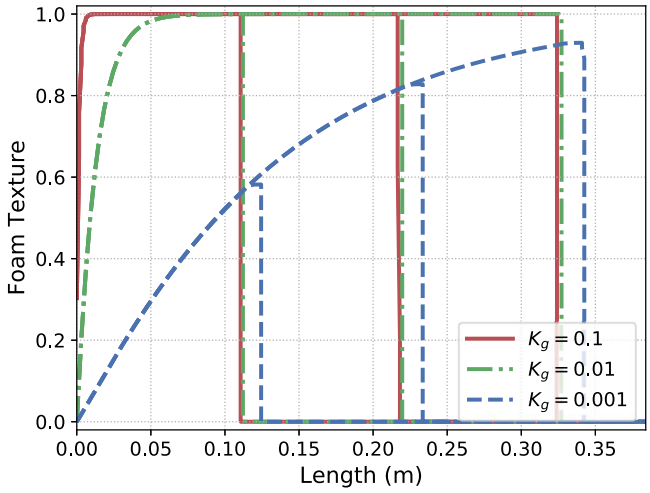

(b) Foam Texture.

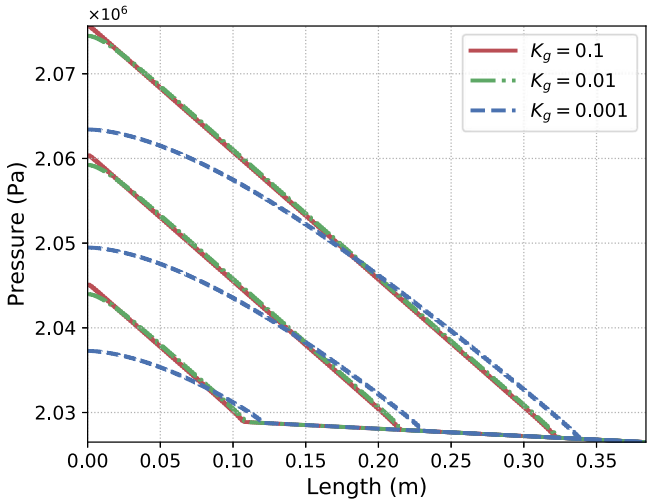

(c) Pressure (Pa).

Source: Prepared by the author.

5.3 Numerical Validation Using Experimental Results

In order to verify the numerical and mathematical modeling's capabilities in reproducing experimental results, two sets of comparisons are presented in this section: a surfactant saturated Bentheimer sandstone core experiment presented in [3] is reproduced, and CT (Computed Tomography) Scan images are processed to obtain data for simulations.

5.3.1 Surfactant Saturated Bentheimer Sandstone Core

A comparison between the experimental results and the computational is presented, reproducing the results developed in [3]. The water saturation experimental results were obtained using a CT (Computed Tomography) scan, an equipment capable of obtaining cross-sectional images of a core. In order to match the experimental data, the simulation parameters are taken from Table 3, with $K_g = 0.1$ s^{-1} and $n_{max} = 250$ mm^{-3} as in [3]. The relative permeability and capillary pressure functions are given by (5.6)–(5.8).

Figure 21 shows the numerical and experimental results for water saturation in several porous volumes (PV). It can be stated that the foam displacement in porous media behaves in a front-like manner. The numerical methodology fully captured that behavior, which could predict the wavefront's positions. However, the water saturation from the simulated results did not match the lower values obtained experimentally.

Figure 21 – Experimental and numerical water saturation profiles during transient foam flow in a surfactant saturated Bentheimer sandstone core. The time frames are PV = 0.10, 0.16, 0.22, 0.30, 0.36, 0.46, 0.52, 0.58.

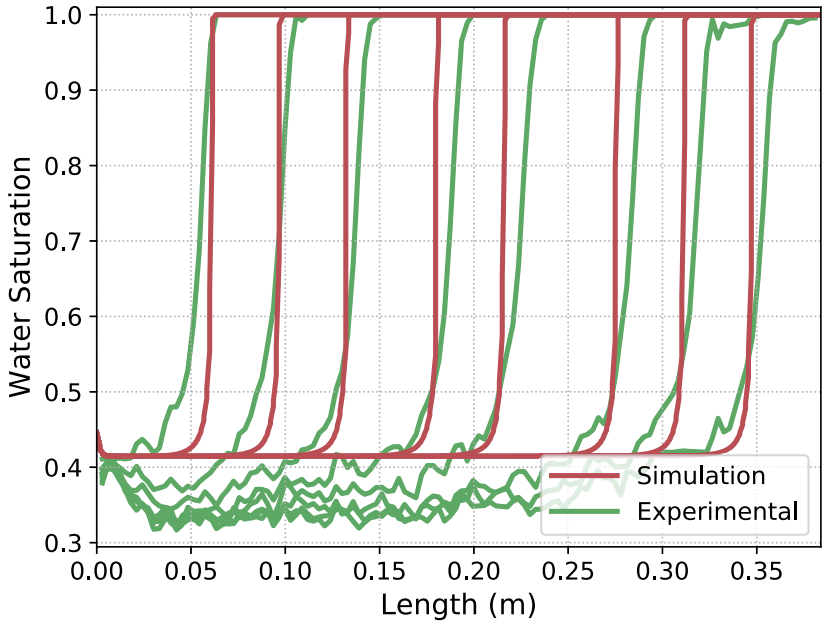

Source: Prepared by the author.

5.3.2 CT Scan Experimental Data Analysis

Computed Tomography (CT) scan is an imaging technique that uses computer-processed combinations of multiple X-ray measurements taken from different angles to produce cross-sectional images of an object. This technology can be applied to the study of foam flow in porous media, allowing for the visualization of cross-sectional images throughout the core (Fig. 22). Figure 23 shows a typical CT scan image. The CT scan data used in the following study were provided by a previous TU Delft research project supported by Shell and published in [3, 111, 112].

In this subsection, we describe an image processing methodology to obtain valuable information from CT data of core samples acquired during foam displacement. We then use the estimated porosity field to simulate foam displacement in the porous medium.

Figure 22 – CT scan schematic.

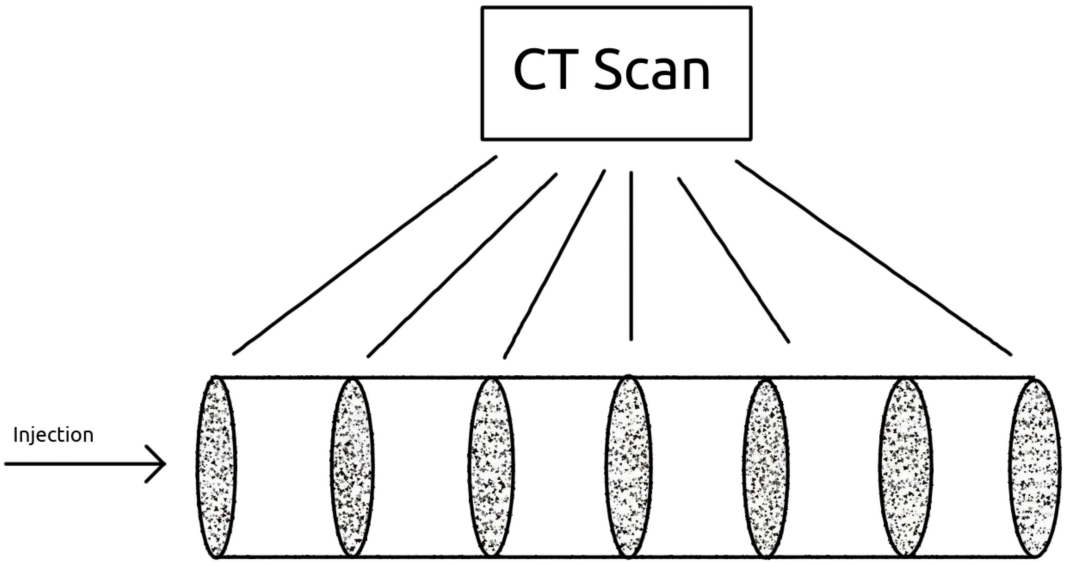

Source: Prepared by the author.

5.3.2.1 Image Processing of CT Scan Data

The CT scan data can be processed to obtain useful information about the rock sample. A methodology was developed to process the CT scan images to get the porosity distribution of the core sample and the water saturation profile during foam flow. The first step is to detect the centers and the radii of the circles representing the core in each figure using an image processing tool. Figure 24 shows a processed image using the circle Hough transform, an algorithm used to find circles in an image. The detected circles are then adjusted to a central line (identified as the axis of the cylindrical core). Finally, a longitudinal section of the core is chosen to obtain a

Figure 23 – A typical CT scan image. The innermost white circle is the core itself.

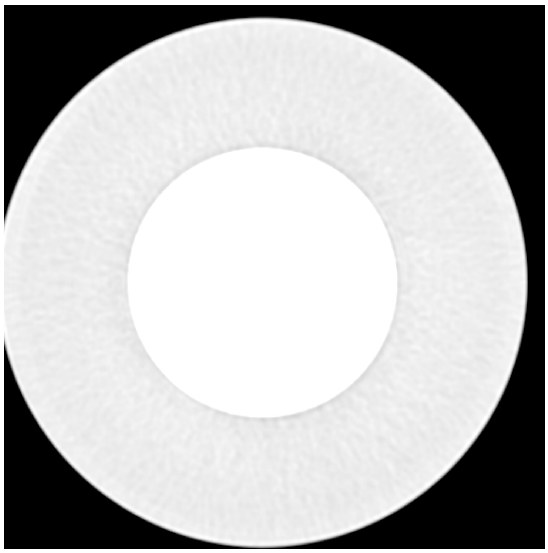

Source: Prepared by the author.

two-dimensional porosity field. For example, a vertical section can be chosen, as indicated by the purple line in Figure 25.

Figure 24 – CT scan image processed using the circle Hough transform.

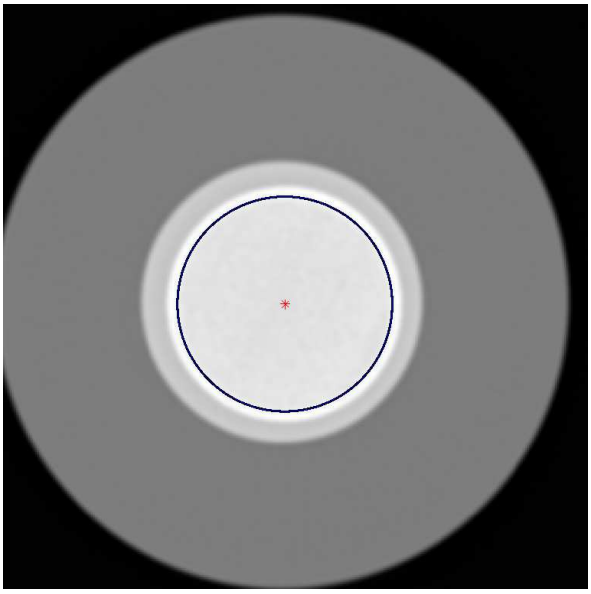

Source: Prepared by the author.

Figure 25 – Vertical section in a processed CT scan image.

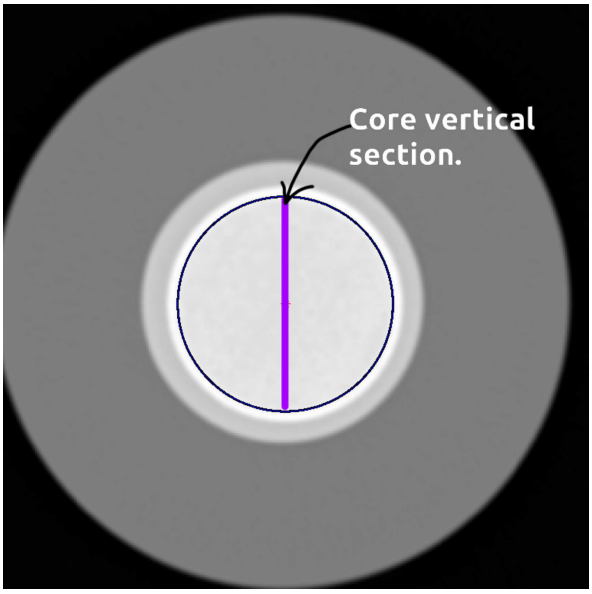

Source: Prepared by the author.

Following [113], a porosity field can be computed from the processed CT scan images using

$$\phi = \frac{HU_{\text{wet}} - HU_{\text{dry}}}{1000},$$

where HU_{wet} and HU_{dry} are the X-ray attenuation coefficients (given in Hounsfield units – HU) measured with a brine-saturated and a dry core, respectively. Then, the porosity values data computed from a longitudinal section of the core are organized throughout a two-dimensional grid as shown in Figure 26.

Figure 26 – Assembly of image sections to compose a single two-dimensional field.

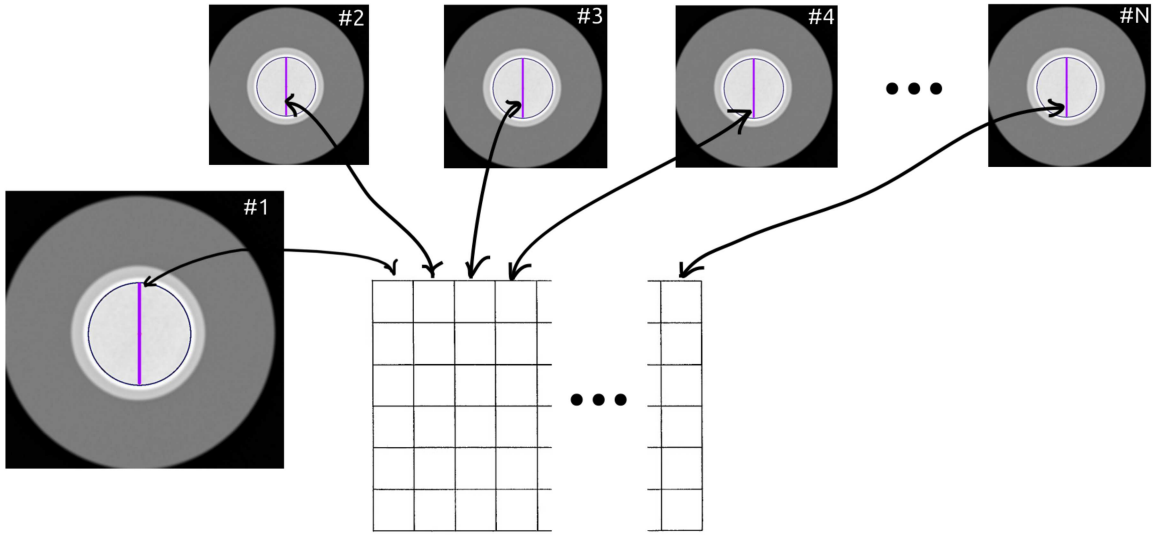

Source: Prepared by the author.

Choosing the vertical longitudinal section of the core for this study, Figure 27 shows the porosity field obtained.

Figure 27 – Porosity of a longitudinal section resulting from the processing of CT scan images.

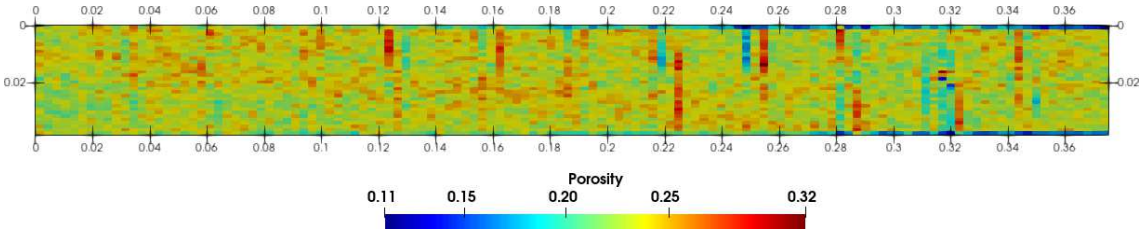

Source: Prepared by the author.

A permeability field can be estimated from the porosity field using the Kozeny-Carman relation [114]

$$\mathbb{K} = \frac{C_0 D_g^2 \phi^3}{(1-\phi)},$$

where C_0 is the Kozeny constant and D_g is the mean grain size. It is used $C_0 = 1/180$ [115] and $D_g = 0.00026$ [114]. The porosity field, obtained via image processing, and the corresponding permeability field, computed using the Kozeny-Carman relation, are shown in Figures 27 and 28.

Figure 28 – Permeability field estimated from the porosity using a Kozeny-Carman relation.

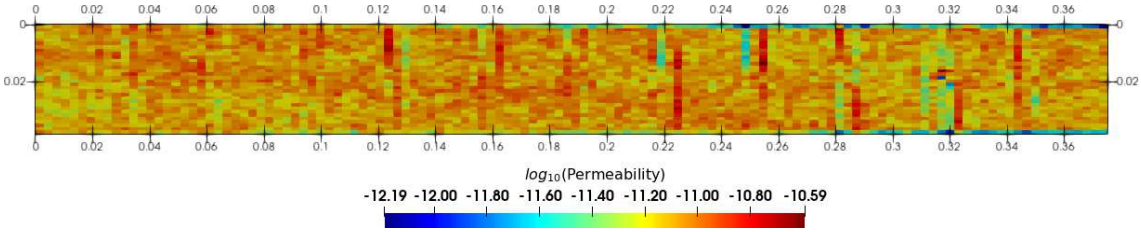

Source: Prepared by the author.

5.3.2.2 Simulation Results

This section provides a comparison between the experimental results and the numerical simulations. For the simulations, we adopt the mathematical model (5.1)-(5.3) assuming incompressibility and neglecting gravity and adsorption effects. The simulation parameters are given in Table 4, and the boundary conditions are set as: for the Darcy system, the right boundary is set as Dirichlet, while the left boundary is taken as injection Neumann condition, and the top and bottom boundaries are set to a homogeneous Neumann condition. For the transport equations, on the left boundary, is imposed injection Neumann condition, whereas the right, top, and bottom boundaries are defined with a no diffusion condition.

Table 4 – Parameters used in the simulation of foam displacement in a porous medium taken from [3].

Parameter	Value	Parameter	Value
Water Viscosity (μ_{w}) [Pa s]	1×10^{-3}	Pore radius (r_{p})	5.0×10^{-6}
Gas Viscosity $\left(\mu_{\mathrm{g}}\right)$ [Pa s]	1.8×10^{-5}	Model parameter d	$1/3$
Water residual saturation (S_{wc})	0.1	K_{d} [1/s]	0.0
Gas residual saturation $\left(S_{\mathrm{gr}}\right)$	0.0	K_{g} [1/s]	0.1
Max foam texture $(n_{\max})$ [m^{-3}]	5×10^{11}	Dimensions [m]	0.038×0.378
Initial water saturation $(S_{\mathrm{w}}^{\mathrm{init}})$	1.0	Final time [s]	3320.86
Initial foam texture $(n_{\mathrm{D}}^{\mathrm{init}})$	0.0	$\Delta t_{\mathrm{u}}[s]$	1.0
Injected water velocity [m s^{-1}]	1.47×10^{-6}	Mesh size	32×126
Injected gas velocity [m s^{-1}]	1.47×10^{-5}	minmod parameter (θ)	1.0
Injected foam texture $(n_{\mathrm{D}}^{\mathrm{inj}})$	0.0	Absolute tolerance	1×10^{-6}
Foamed gas viscosity constant (α)	5.8×10^{-16}	Relative tolerance	1×10^{-4}
Maximum k_{rw} $\left(k'_{\mathrm{rw}}\right)$	0.75	$\mathcal{RT}$ index (k)	0
Maximum k_{rg} $\left(k'_{\mathrm{rg}}\right)$	1.0	Exponent ζ	5.0
σ_{wg} [N/m]	3×10^{-3}	Fitting parameter γ	0.5

Following [116], the water saturation profiles can be obtained from the CT scan data using

$$S_{\mathrm{w}} = \frac{HU_{\mathrm{foam}} - HU_{\mathrm{dry}}}{HU_{\mathrm{surf}} - HU_{\mathrm{dry}}},$$

where HU_{foam} and HU_{surf} stand for the normalized CT numbers measured in a core saturated with foam and with the surfactant solution, respectively.

A comparison between the water saturation obtained from the simulation and the CT data is presented in Figure 29 at various PV instants. We can observe that the numerical results show that foam displaces the initial aqueous (surfactant solution) phase in a characteristic front-like manner, in good agreement with the experimental results. The simulation shows a good representation of the position of the wavefronts, providing a good match of the foam propagation rate observed experimentally. However, the wavefront instabilities shown in the CT data are not present in the simulation results: the heterogeneity in the porosity and permeability fields did not play a significant role in the foam displacement, leading to computational results much similar to those that would be obtained using homogeneous porosity and permeability fields. That behavior can be attributed to the very low heterogeneity of the core sample (see Figure 30).

Figure 29 – Water saturation obtained via numerical simulation (top) and from the processing of CT images (bottom).

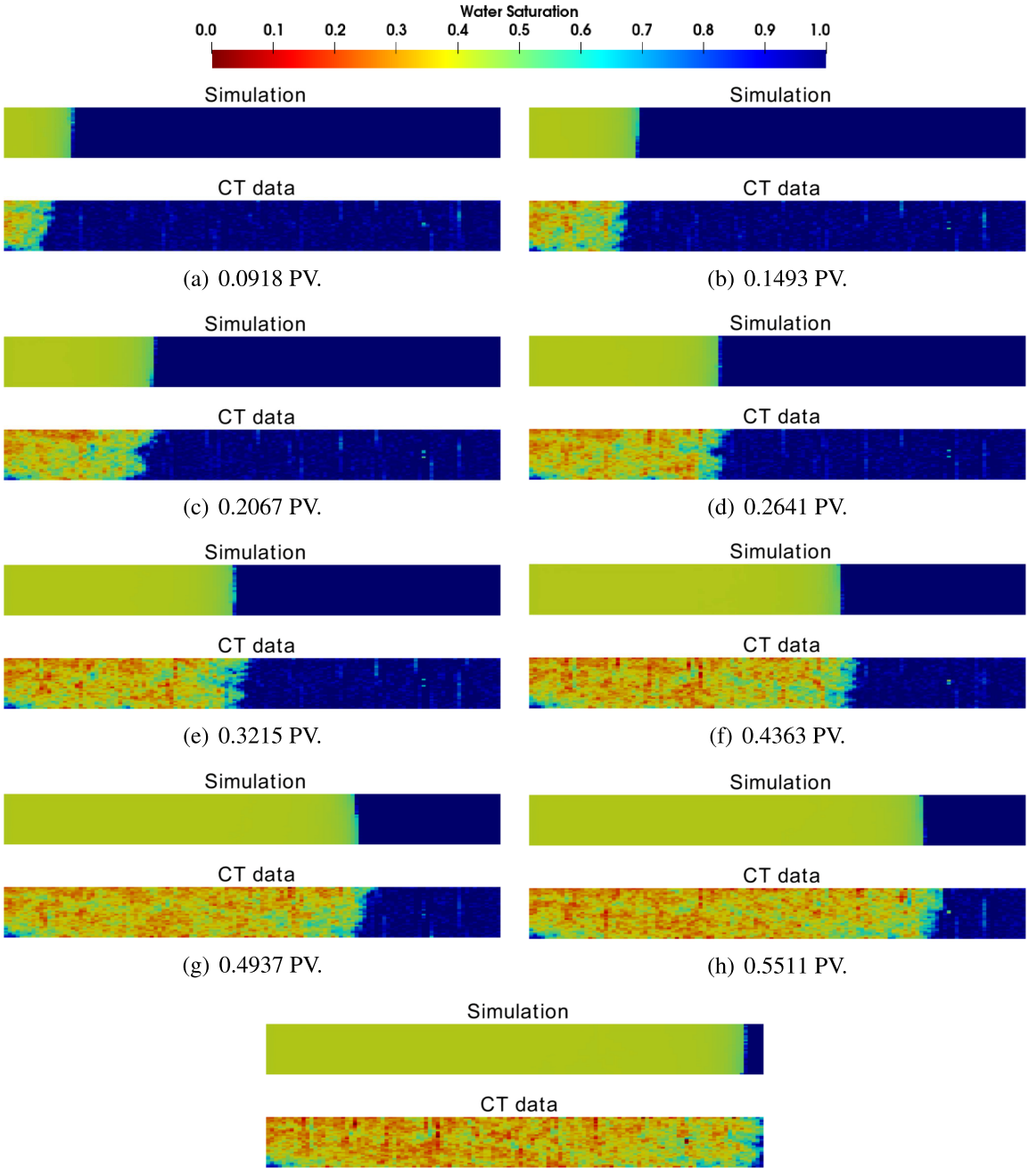

(a) 0.0918 PV. (b) 0.1493 PV.

(c) 0.2067 PV. (d) 0.2641 PV.

(e) 0.3215 PV. (f) 0.4363 PV.

(g) 0.4937 PV. (h) 0.5511 PV.

(i) 0.6659 PV.

Source: Prepared by the author.

Figure 30 – Analysis of the porosity field in Figure 27 showing that the porosity throughout the core sample does not deviate much from an average value. (a) Plot over a horizontal line passing through the longitudinal center line (i.e., the core axis) of the field; (b) Histogram.

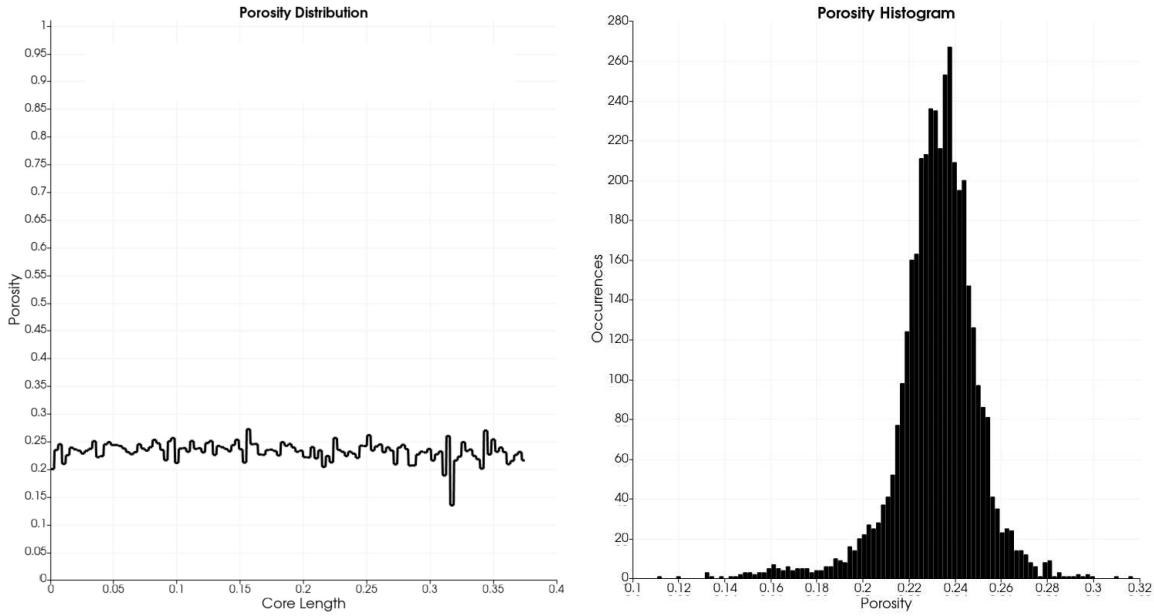

(a) (b)

Source: Prepared by the author.

5.4 Two-Dimensional Foam Flow in Heterogeneous Porous Media

In order to assess the behavior of the foam displacement in a heterogeneous porous media, we simulate a series of numerical experiments using the model (5.1)-(5.3) assuming incompressibility and neglecting gravity and adsorption effects. In this context, two different permeability fields are used: Case C refers to 11(a) and Case D to 11(b). Simulations run for $30\,000$ s on a grid of 220×60 size 3.67 m $\times$ 1.0 m. The relative permeability and capillary pressure functions are given by (5.6)–(5.8) and several parameters are shown in Table 3, where we choose $n_{\max} = 250$ mm^{-3} and $K_{\mathrm{g}} = 0.1$ s^{-1}. The boundary conditions for the simulations are imposed in the following way:

- For the Darcy problem (5.1)–(5.2), the right boundary is a Dirichlet-type, while the left is taken as injection Neumann condition, and top and bottom boundaries are set to Neumann condition.
- For the transport equations (5.3), on the left boundary is imposed injection Neumann condition, whereas the top, bottom, and the right border are set to the no diffusion condition.

Figures 31 and 32 show the water saturation simulation solutions for Case C and D,

respectively, where the left column presents the results in the absence of foam, the right column presents the results with foam displacement and each row, from top to bottom, corresponds to the time instants $t = 5\,000$ s, $t = 15\,000$ s and $t = 30\,000$ s. In Case C (Figure 31), the non-foam flow breakthrough occurs in approximately $15\,000$ s, which is much faster than the foam flow case, which occurs around $30\,000$ s. That early breakthrough, mainly due to high gas mobility, leads to a poor reservoir sweep efficiency, which can be verified by the higher water saturation values, especially in the lower permeability regions, in the medium for the non-foam results compared to the foam ones. More clearly, Figures 33 shows the foam effect in the flow. Foam generation occurs in the region where the injected gas phase becomes available for bubble formation (Fig. 33). The improved sweep efficiency due to foam injection is more evident in Figure 35(a), where cumulative water production curves are plotted, showing a higher production when the foam is present in the flow. It is also interesting to note that the solutions for the foam displacement (right column) show an efficient gas mobility control, reducing the fingering and maximizing the water displacement.

The permeability field of Case D (Figure 11(b)) presents a channel of higher permeability that tends to form a preferential path for the high mobility gas phase, leading to an early breakthrough, as can be seen in the left column of Figure 32. However, when the foam is generated (right column of Fig. 32), the gas flowing through the higher permeability channel is contained, and preferential paths do not occur. This behavior leads to a late breakthrough and higher reservoir sweep efficiency, as can be seen in Figure 35(b). Figures 34 show the foam texture of the fluid flow. These results are similar to Case C: foam generates rapidly in the region where the injected gas is flowing.

Figure 31 – Case C: water saturation results.

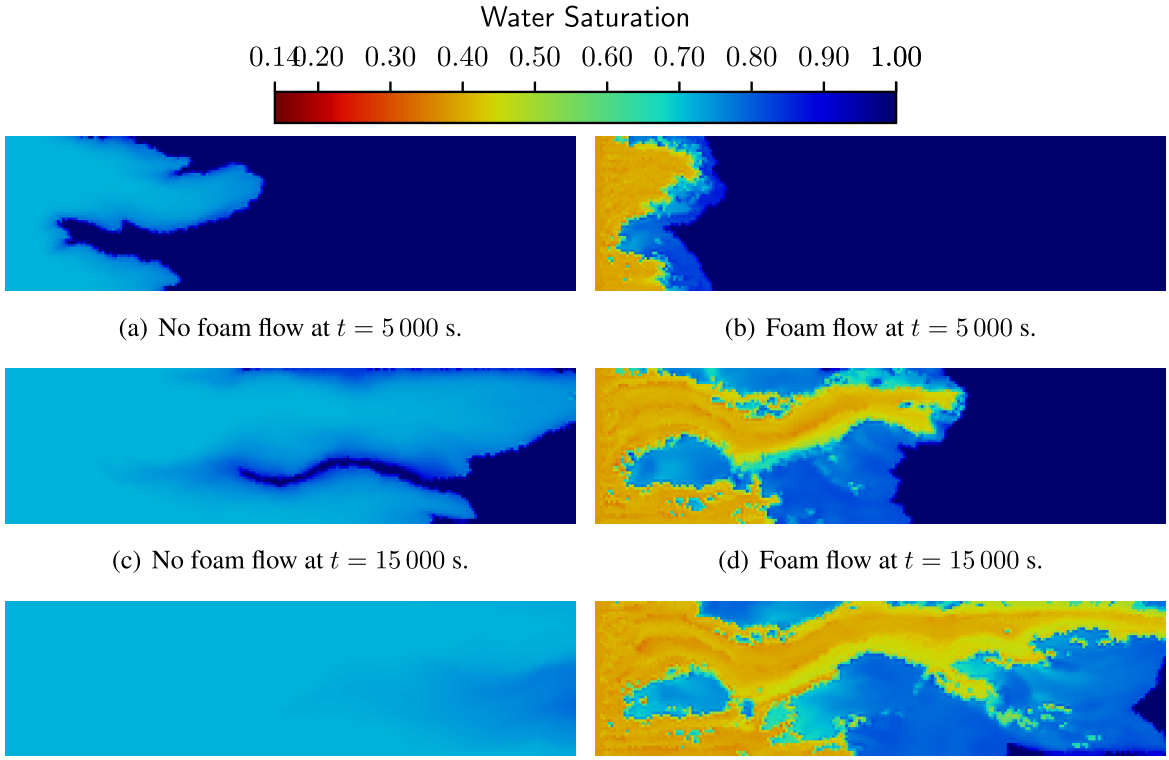

(a) No foam flow at $t = 5\,000$ s.

(b) Foam flow at $t = 5\,000$ s.

(c) No foam flow at $t = 15\,000$ s.

(d) Foam flow at $t = 15\,000$ s.

(e) No foam flow at $t = 30\,000$ s.

(f) Foam flow at $t = 30\,000$ s.

Source: Prepared by the author.

Figure 32 – Case D: water saturation results.

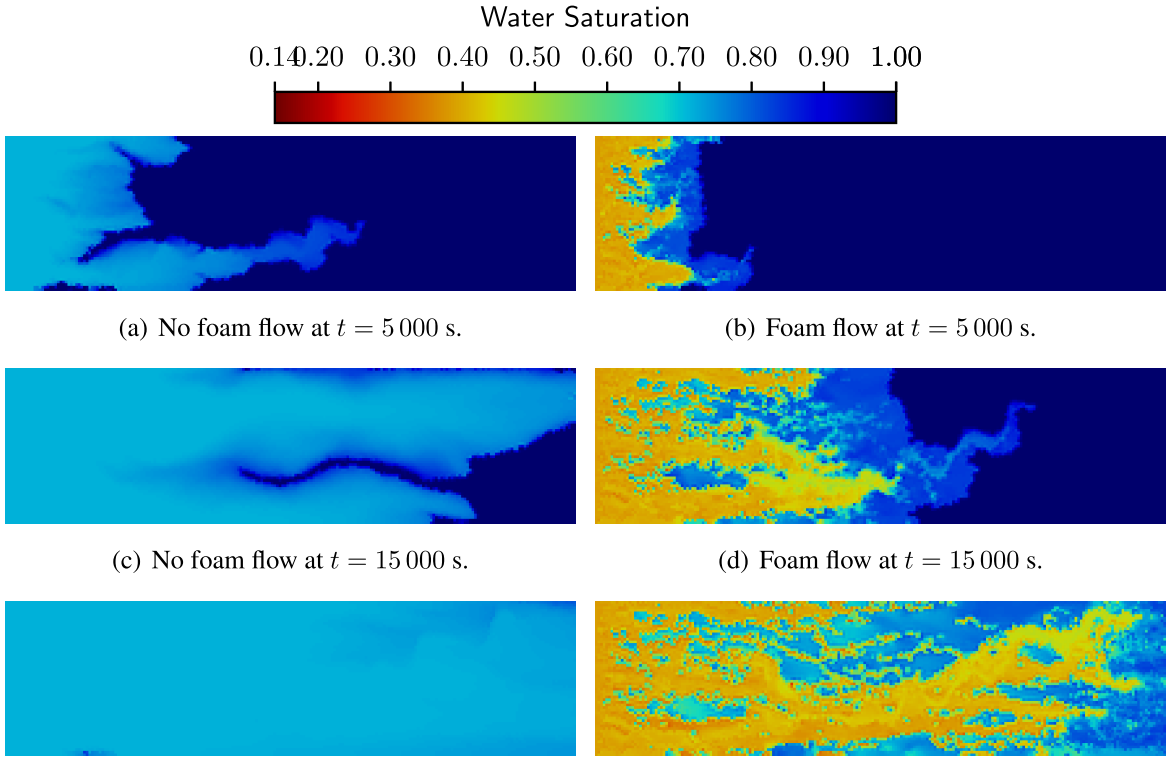

(a) No foam flow at $t = 5\,000$ s.

(b) Foam flow at $t = 5\,000$ s.

(c) No foam flow at $t = 15\,000$ s.

(d) Foam flow at $t = 15\,000$ s.

(e) No foam flow at $t = 30\,000$ s.

(f) Foam flow at $t = 30\,000$ s.

Source: Prepared by the author.

Figure 33 – Case C: foam texture results when foam is present in the flow.

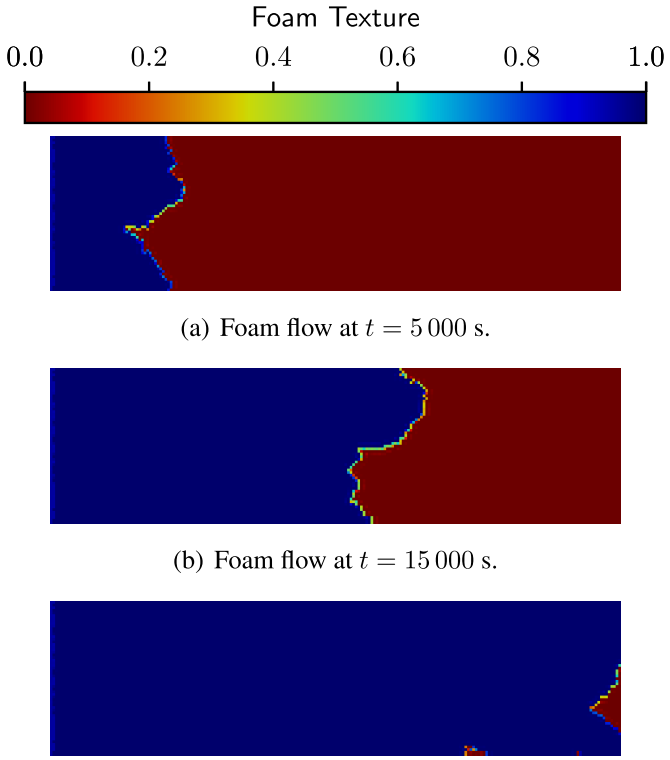

(a) Foam flow at $t = 5\,000$ s.

(b) Foam flow at $t = 15\,000$ s.

(c) Foam flow at $t = 30\,000$ s.

Source: Prepared by the author.

Figure 34 – Case D: foam texture results when the foam is present in the flow.

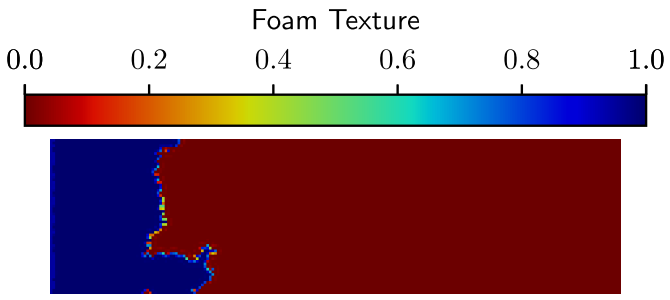

(a) Foam flow at $t = 5\,000$ s.

(b) Foam flow at $t = 15\,000$ s.

(c) Foam flow at $t = 30\,000$ s.

Source: Prepared by the author.

Figure 35 – Water cumulative production for cases C and D.

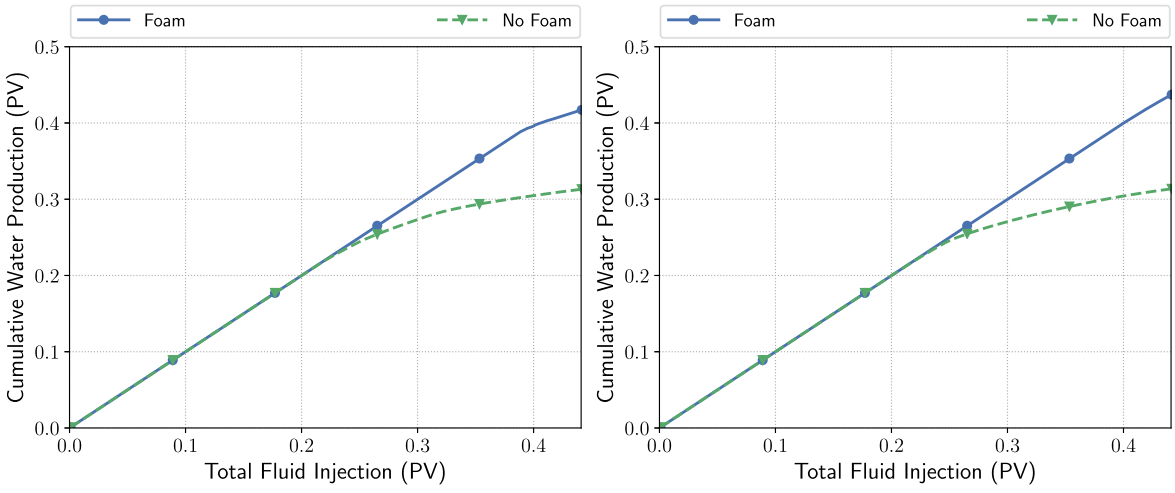

(a) Case C.

(b) Case D.

Source: Prepared by the author.

5.5 Compressible and Gravitational Foam Flow in Highly Heterogeneous Porous Media

In the simulations presented in this section, we adopt the complete mathematical model (5.1)-(5.2). Moreover, the porous medium is taken as highly heterogeneous, and, therefore, the permeability and porosity are variables within the domain. In that way, the permeability field is the one presented in Figure 11(a) and the porosity field is shown in Figure 36. As the flow is treated as compressible, Table 5 presents tuples that describe the relation of gas density and pressure used in the simulations. The gas compressibility data, plotted in Figure 37, is taken from the STARS simulator [4] Figure 37.

Figure 36 – Porosity map of layer 1 of the SPE10.

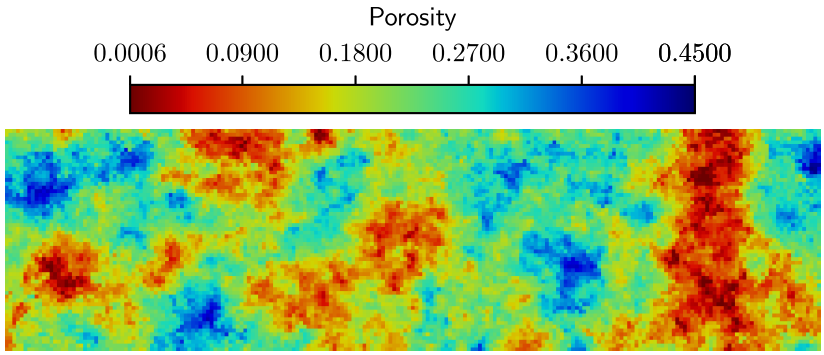

Source: Prepared by the author.

Table 5 – Gas density as a function of pressure taken from STARS simulator [4].

Pressure (kPa)	Density (kg/m^3)	Pressure (kPa)	Density (kg/m^3)
500	5.66084	42200	389.419
7450	85.3543	49150	427.91
14400	162.525	56100	461.482
21350	232.3	63050	491.096
28300	292.924	70000	517.312
35250	344.87		

The relative permeability and capillary pressure functions are given by (5.6)–(5.8) and other parameters are show in Table 3, where we take $n_{\max} = 500\ \text{mm}^{-3}$ and $K_{\text{g}} = 0.1\ \text{s}^{-1}$. Similarly to the experiments of Section 5.4, the simulations run for $30\,000$ s in a 220×60 grid of size 3.67 m $\times$ 1.0 m, and the boundary conditions are set as follows:

- For the Darcy problem (2.31)–(2.32), the right boundary is a Dirichlet-type, while the left is taken as injection Neumann condition, and top and bottom boundaries are set to Neumann condition.

Figure 37 – Variation of gas density as a function of pressure.

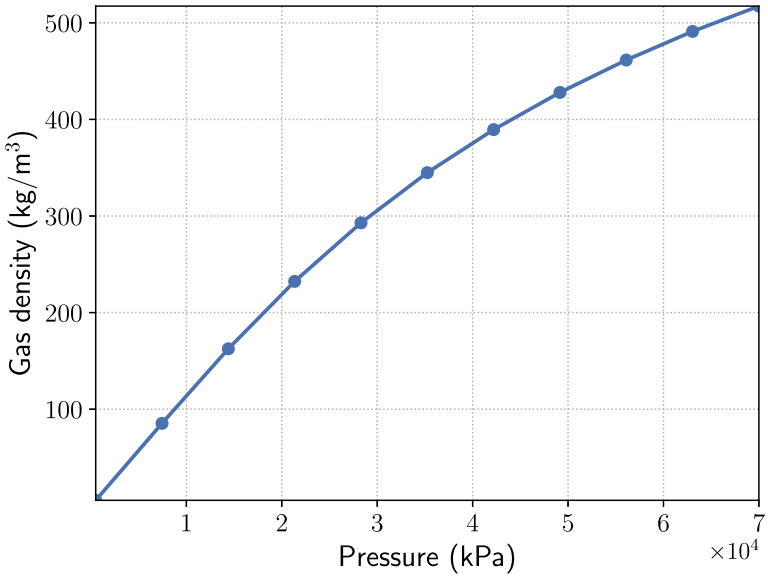

Source: Prepared by the author.

- For the transport equations (2.33), on the left boundary is imposed injection Neumann condition, whereas the top, bottom, and the right border are set to the no diffusion condition.

It is shown in Figures 38–39 the simulation results, where the left column is the solutions without foam, and the right column are results where foam is present in the flow. Each row, from top to bottom, corresponds to the time instants $t = 5\,000$ s, $t = 15\,000$ s and $t = 30\,000$ s. The water saturation solutions (Fig. 38) show that gravity plays an important role in two-phase flow in porous media, especially when the foam is absent. The gravity override in the case without foam in the flow is very pronounced, as it leads to excessive gas accumulation in the top region of the reservoir. As a practical result, a significant part of the domain is not swept, and an expressive amount of the initial water is not displaced. On the other hand, the capability of reducing viscous fingering and gravity override by reducing gas mobility is verified in Figure 38. It is also possible to see in the water saturation results that the sweep efficiency is increased when the foam is present in the flow, as the domain presents an overall lower water saturation, meaning that the injected gas was able to displace the resident aqueous fluid more effectively.

Figure 39 presents the foam texture results for the case where foam is generated in the two-phase flow. The presence of foam in the flow, as in Figure 39, characterize an overall higher foamed gas viscosity (see (5.5)), increasing drastically gas mobility. With that, the reservoir sweep efficiency is improved. As expected, the previously mentioned solutions reflect ultimately in the cumulative water production results presented in Figure 40, which shows a clear gain in production in the case where foam is formed in the porous medium.

Figure 38 – Water saturation results. The first, second, and third rows correspond to the time instants $t = 5\,000$ s, $t = 15\,000$ s and $t = 30\,000$ s, respectively. Left column: no foam effects; right column: foam effects.

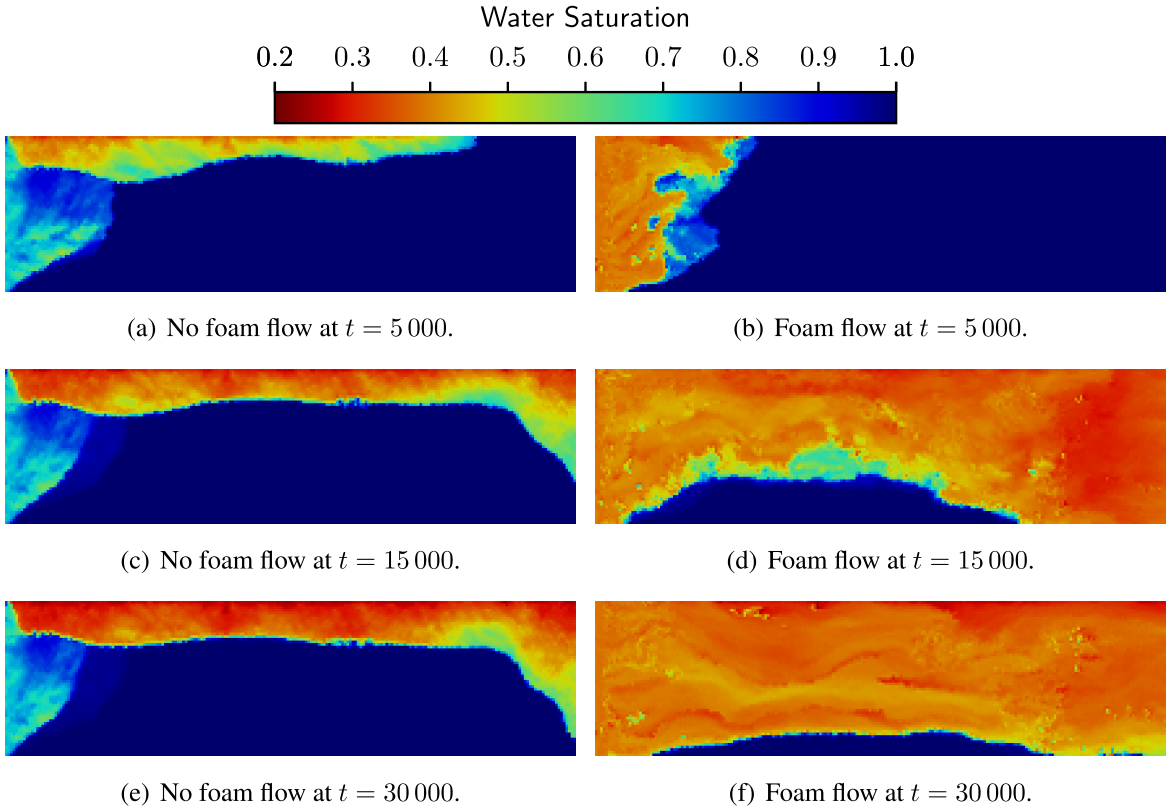

(a) No foam flow at $t = 5\,000$.

(b) Foam flow at $t = 5\,000$.

(c) No foam flow at $t = 15\,000$.

(d) Foam flow at $t = 15\,000$.

(e) No foam flow at $t = 30\,000$.

(f) Foam flow at $t = 30\,000$.

Source: Prepared by the author.

5.6 Preliminary Conclusions

The numerical and computational methodology presented in Chapter 3 handled complex mathematical features of the model, such as gravity, gas compressibility, and non-Newtonian behavior. Results from the literature, both numerical and experimental, were reproduced successfully using FOSSIL. In addition, a method to process CT scan raw data images to obtain permeability and porosity distribution in the porous medium was presented. That technique allows the acquisition of multi-dimensional data from a core flood experiment equipped with a CT scan machine. The results obtained using a heterogeneous porous medium demonstrated a good agreement with the experimental data. However, the heterogeneity in the porosity and permeability fields seemed not to play a significant role in the foam displacement, leading to computational results much similar to those that would be obtained using a homogeneous porous medium. The low variation of the core sample porosity can cause that behavior.

Simulations using two different two-dimensional heterogeneous porous media were conducted to assess the foam's capability to reduce viscous fingering and increase water displacement. In this case, scenarios with foam generation and without foam present in the flow

Figure 39 – Foam texture results. The first, second, and third rows correspond to the time instants $t = 5\,000$ s, $t = 15\,000$ s and $t = 30\,000$ s, respectively.

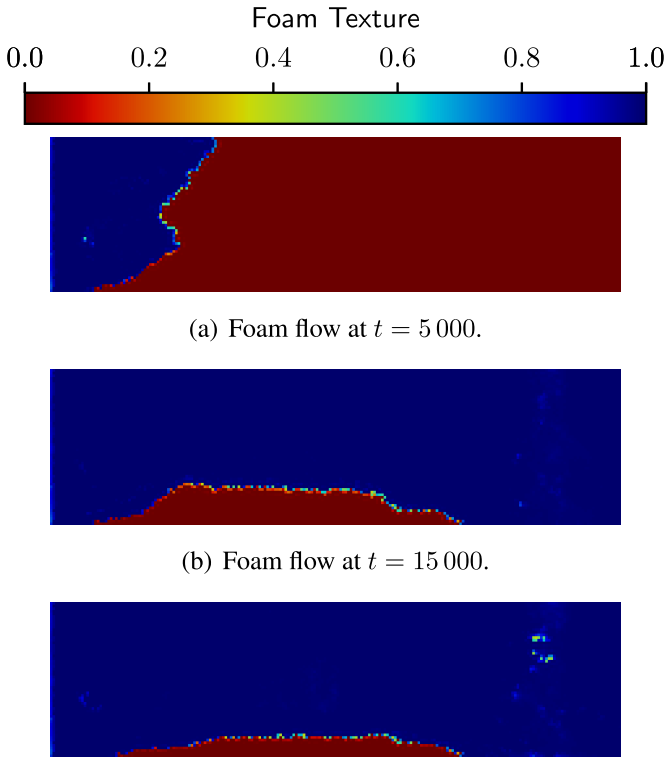

(a) Foam flow at $t = 5\,000$.

(b) Foam flow at $t = 15\,000$.

(c) Foam flow at $t = 30\,000$.

Source: Prepared by the author.

were compared. The results show an early gas breakthrough in the no-foam simulations due to the high gas mobility. When the foam was injected into the medium, the gas breakthrough was significantly delayed compared to the no-foam flow case. Moreover, it is interesting to note that the water saturation results presented an efficient gas mobility control, reducing the fingering and maximizing the water displacement.

A more complex two-dimensions simulation is also performed in a heterogeneous porous medium that includes gas compressibility and gravity. The results for the scenario without foam show an excessive gas gravitational segregation in the higher parts of the reservoir. That gas accumulation on the top regions of the porous medium is especially harmful when dealing with deep reservoirs. As seen in the results, the foam generation in the flow can actively reduce that gravity phenomenon, mainly due to a better gas phase mobility control [15, 24, 58, 117]. Thus, foam usage can present several advantages in improving reservoir sweep efficiency, leading to higher production rates.

Figure 40 – Cumulative water production.

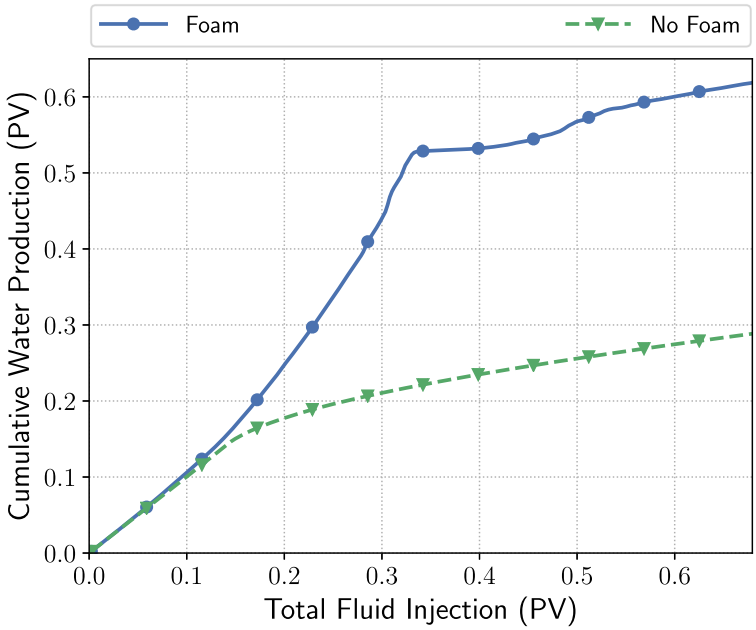

Source: Prepared by the author.

6 FOAM MODEL WITH NON-NEWTONIAN BEHAVIOR INCLUDING SURFACTANT EFFECTS

To simulate the foam flow with non-Newtonian behavior and surfactant effects in this chapter, we adopt Kovscek's foam model [2, 48] presented in Section 2.5.4. The numerical results are obtained through the simulation of the system of equations (2.31)-(2.34) assuming local equilibrium, incompressibility and neglecting the gravity. In this context, we validate the proposed numerical methodology by comparing it with computational and experimental literature results in a one-dimensional domain. Then, several two-dimensional simulations are presented to compare co-injection and SAG techniques and the adsorption effect in foam flow in porous media. Part of these results are being published in [87] and [118].

6.1 Model Definition

The simulations developed in the current chapter are assumed to be in local equilibrium; therefore, equation (2.2) is neglected. In addition, gravity and compressibility are also neglected. From these assumptions, the mathematical model described in Section 2.4 is reduced to:

$$\mathbf{u} = -\kappa\lambda\nabla p, \tag{6.1}$$

$$\nabla\cdot\mathbf{u} = 0, \tag{6.2}$$

$$\phi\frac{\partial \mathbf{S}}{\partial t} + (1-\phi)\rho\frac{\partial \mathbf{A}}{\partial t} + \sum_{i=1}^{\mathfrak{d}}\frac{\partial \mathbf{f}_i}{\partial x_i} + \nabla\cdot(\mathbb{C}\nabla\mathbf{S}) = \mathbf{\Phi}, \tag{6.3}$$

$$f_{\mathrm{w}\to\mathrm{s}}^{\mathrm{kin}} = (1-\phi)\rho\frac{\mathrm{d}C_{\mathrm{s}}^{\mathrm{kin}}}{\mathrm{d}t}, \tag{6.4}$$

where

$$\mathbf{S} = \begin{bmatrix} S_{\mathrm{w}} \\ S_{\mathrm{w}}C_{\mathrm{s}} \end{bmatrix}, \qquad \mathbf{A} = \begin{bmatrix} 0 \\ C_{\mathrm{s}}^{\mathrm{eq}} \end{bmatrix}, \quad \mathbf{f}_i = \begin{bmatrix} f_{\mathrm{w}}u_i - b_i \\ C_{\mathrm{s}}f_{\mathrm{w}}u_i - C_{\mathrm{s}}b_i \end{bmatrix}, \quad \mathbf{\Phi} = \begin{bmatrix} 0 \\ -f_{\mathrm{w}\to\mathrm{s}}^{\mathrm{kin}} \end{bmatrix},$$

$$\mathbb{C} = \kappa\lambda_{\mathrm{g}}f_{\mathrm{w}}\frac{\mathrm{d}P_{\mathrm{c}}}{\mathrm{d}S_{\mathrm{w}}}\begin{bmatrix} 1 & 0 \\ C_{\mathrm{s}} & 0 \end{bmatrix}. \tag{6.5}$$

where $\mathbf{b} = \mathbb{K}\lambda_{\mathrm{g}}f_{\mathrm{w}}\tilde{\boldsymbol{\rho}}$. The terms $C_{\mathrm{s}}^{\mathrm{eq}}$ and $f_{\mathrm{w}\to\mathrm{s}}^{\mathrm{kin}}$ are defined using the Langmuir model [93, 94], as follows:

$$C_{\mathrm{s}}^{\mathrm{eq}} = \frac{K_1^{\mathrm{eq}}C_{\mathrm{s}}}{1+K_2^{\mathrm{eq}}C_{\mathrm{s}}}, \qquad f_{\mathrm{w}\to\mathrm{s}}^{\mathrm{kin}} = \frac{K_1^{\mathrm{kin}}C_{\mathrm{s}}}{1+K_2^{\mathrm{kin}}C_{\mathrm{s}}} - K_{\mathrm{des}}C_{\mathrm{s}}^{\mathrm{kin}}, \tag{6.6}$$

where K_1^{eq}, K_2^{eq}, K_1^{kin} and K_2^{kin} are empirical parameters, and K_{des} is the rate of desorption. Moreover, this model's boundary and initial conditions are given in (2.37)-(2.40), neglecting the foam texture variable.

As the population balance is assumed to be in local equilibrium, to calculate n_{D} we adopt the following algebraic system:

$$n_{\mathrm{D}} = \begin{cases} \dfrac{\sqrt[3]{z}}{\sqrt[3]{18}} - \dfrac{\sqrt[3]{\frac{2}{3}}a}{\sqrt[3]{z}}, & P_{\mathrm{c}} < P_{\mathrm{c}}^{*}, \\ 0, & P_{\mathrm{c}} \geq P_{\mathrm{c}}^{*}, \end{cases} \tag{6.7}$$

where $z = \sqrt{12a^3 + 81} + 9$, $a = \dfrac{k_{-1}|\mathbf{v}_{\mathrm{g}}|^{\frac{2}{3}} n_{\max}}{k_1^0 |\mathbf{v}_{\mathrm{w}}|}$, P_{c}^{*} is defined in (2.55) and P_{c} is introduced below in Equation (6.10). The relation for foam texture in local equilibrium (6.7) is the single real root of the Equation (2.56) (more details in Section 2.5.4). Furthermore, as in the previous chapter, we adopt the Hirasaki-Lawson relation [53]

$$\mu_{\mathrm{g}}^{\mathrm{f}} = \mu_{\mathrm{g}} + \alpha n_{\max} \frac{n_{\mathrm{D}}}{|\mathbf{v}_{\mathrm{g}}|^{1/3}}. \tag{6.8}$$

to compute the viscosity of gas in the presence of foam.

The problem given by the equations (6.1)–(6.4) is solved using the methodology proposed in the Chapter 3. The Algorithm 1 is simplified by neglecting the computations related to compressibility, gravity, and population balance equation. In this case, the Equations (6.7) and (6.8) are evaluated at each time step of Hydrodynamics and transport.

6.2 Computational Validation for the Kovscek's Model

In this section, we study the influence of foam and surfactant concentration on incompressible two-phase flow without gravity and adsorption in porous media. The results published by [2, 5] are used to validate and verify the capabilities of the proposed sequential algorithm.

The relative permeabilities for aqueous and gas phases are calculated from the equations

$$k_{\mathrm{rw}} = k'_{\mathrm{rw}} \left(\frac{S_{\mathrm{w}} - S_{\mathrm{wc}}}{1 - S_{\mathrm{wc}} - S_{\mathrm{gr}}} \right)^{n_{\mathrm{w}}}, \quad \text{and} \quad k_{\mathrm{rg}} = k'_{\mathrm{rg}} \left(X_{\mathrm{f}} \frac{1 - S_{\mathrm{w}} - S_{\mathrm{gr}}}{1 - S_{\mathrm{wc}} - S_{\mathrm{gr}}} \right)^{n_{\mathrm{g}}}, \tag{6.9}$$

where S_{wc} denotes the connate water saturation, S_{gr} is the residual gas saturation, and k'_{rw} and k'_{rg} are the endpoint relative permeabilities of water and gas, respectively, and n_{w} and n_{g} are empirical constants. The capillary pressure (assumed to be a function of S_{w} only), is defined as [55]

$$P_{\mathrm{c}} = P_{\mathrm{c}}\left(S_{\mathrm{w}}\right) = p_{\mathrm{g}} - p_{\mathrm{w}} = \sigma_{\mathrm{wg}} \sqrt{\frac{\phi}{\kappa(\mathbf{x})}} \left(\frac{0.022}{S_{\mathrm{w}} - 0.15} \right)^{0.2}, \tag{6.10}$$

with σ_{wg} denoting the gas-liquid interface tension.

Following the numerical experiments of [2, 5],we present comparisons with other approaches of approximation of convective flows and integration in time, demonstrating a better efficiency of the proposed methodology.The simulations are ran for a 0.6 m one-dimensional

Table 6 – Simulation parameters for the Kovscek's model adapted from [2, 5].

Parameter	Value	Parameter	Value
Water Viscosity (μ_{w}) [Pa s]	1.0×10^{-3}	Permeability [mD]	300
Gas Viscosity (μ_{g}) [Pa s]	1.8×10^{-5}	Interface tension (σ) [N/m]	0.033
Water residual saturation (S_{wc})	0.38	k_1^0 [$\mathrm{s}^{1/3}\mathrm{m}^{-13/3}$]	1.65×10^{15}
Gas residual saturation (S_{gr})	0.0	k_{-1}^0 [m^{-1}]	10.0
Maximum k_{rg} (k'_{rg})	1.0	$P^*_{\mathrm{c,\,max}}$ [Pa]	3.0×10^4
Maximum k_{rw} (k'_{rw})	0.7	α [$\mathrm{Pa\ s}^{2/3}\mathrm{m}^{1/3}$]	7.4×10^{12}
Exponent for k_{rg} (n_{g})	3	Trapped gas fraction (X_{t})	0.78
Exponent for k_{rw} (n_{w})	3	Reference C_{s} ($C_{\mathrm{s}}^{\mathrm{ref}}$) [wt.%]	0.083
Max. foam texture ($n_{\max}$) [m^{-3}]	1.0×10^{12}	$\Delta t_{\mathrm{u}}[s]$	10.0
Injection velocity ($\bar{u}$) [$\mathrm{m\ s}^{-1}$]	1.41×10^{-5}	minmod parameter (θ)	1.0
Injection C_{s} [wt.%]	1.0	Absolute tolerance	1.0×10^{-6}
Initial water saturation (S_{w}^0)	1.0	Relative tolerance	1.0×10^{-6}
Porosity (ϕ)	0.18	$\mathcal{RT}$ index (k)	0

domain, for 1.0 PV, for a initial surfactant concentration of $1.0\,\mathrm{wt.\%}$. The remaining parameters can be found in Table 6.

Figure 41 presents a comparison between numerical results and experimental data (taken from [2]) for water saturation profiles at different injected porous volume (PV). The simulation was carried out with 200 cells, and the entry boundary condition for water saturation was prescribed as $S_{\mathrm{w}} = 0.55$. The injected PV is computed as the product between elapsed time and injection velocity divided by the product between core length and porosity. The experimental data are marked as filled circles and connected by lines to facilitate the reading, and the non-marked lines represent the numerical solutions. In the horizontal axis, the results are plotted using the dimensionless distance, the distance position divided by the domain length. The validation results are consistent with the literature [2, 5] and show a good match between experimental data and numerical solution, as the simulation results could predict the wavefronts' positions. In addition, the foam propagation in porous media behaves in a front-like manner, leading to a very efficient displacement of the aqueous phase.

It is presented in Figure 42 results for foam texture when the simulation's grid size is varied. It is interesting noticing that the foam texture solutions present a peak reaching $n_{\max}$ right behind the shock wave. It is also evident in Figure 42, the difference in the solutions for each grid size, showing the dependence of the foam texture resolution with the grid size as the peak region of the foam texture becomes more slender. The previous grid size dependence behavior can be credited to the intermediary values of S_{w} between the injection state **J** and the initial state **I** (see Fig. 43). The numerical diffusion and the diffusion from the capillary pressure term yield

Figure 41 – Experimental data [2] and numerical solution for water saturation profiles during co-injection of water, gas, and surfactant. It was prescribed $S_w = 0.55$ at the entry boundary condition.

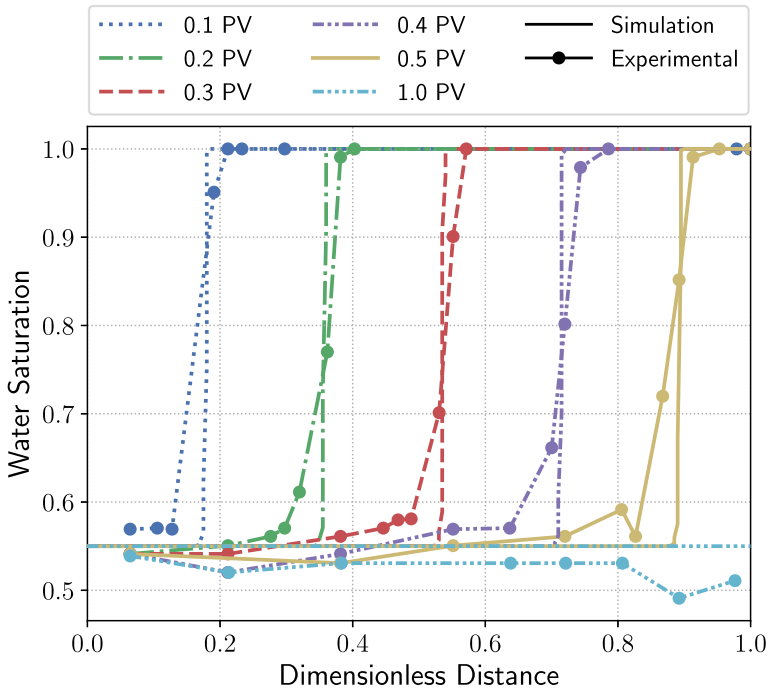

Source: Prepared by the author.

intermediate water saturation values (between states **I** and **J**), that correspond to high n_D values (See Fig. 43), resulting in the foam texture peaks observed in Figure 42. Notice that the presence of the peaks in the foam texture is not entirely a numerical artifact [62]. For similar models, it was proven to be part of mathematical solutions [119].

Figure 43 shows the foam texture n_D as a function of the water saturation S_w, for fixed values of surfactant concentration C_s. To simulate the curves in Figure 43, we use Eq. (2.58) with parameters values from Table 6. Fixing a total injection velocity $\bar{u} = 1.41 \times 10^{-5}$ m s^{-1}, we find the phase velocities $\mathbf{v}_g$ and $\mathbf{v}_w$, which are inter-dependent with μ_g^f, using a technique similar to one proposed in [34]. This process initially assumes an approximation for $\mathbf{v}_g$ and $\mathbf{v}_w$. Then, the f_w is computed using those approximations. New values for f_g and $\mathbf{v}_w$ are computed using the last evaluated f_w. These steps are iterated until convergence. Elevated gradient (see Figure 43) causes a small variation in the injection water saturation (point **J**) leading to a relatively high variation in the injection foam texture. Notice that, the injection state of the previously presented solutions (point **J**) falls in that steep region of Figure 43 (for $C_s = 1.0\,\text{wt.}\%$, $0.5 \lessapprox S_w \lessapprox 0.6$).

6.2.1 Stability, Numerical Dissipation and Computational Cost

Results comparing the proposed methodology with other numerical approaches to approximate convective fluxes are shown in Figure 44. Figures 44(a) and 44(b) present an approximation

Figure 42 – Foam texture for different grid sizes during co-injection of water, gas, and surfactant, with $f_g = 0.9$.

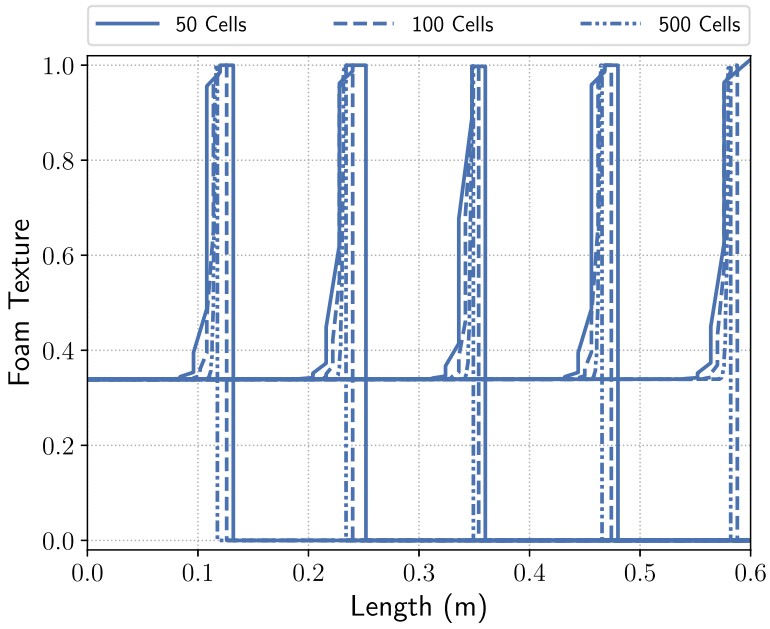

Source: Prepared by the author.

Figure 43 – Foam texture (n_D) as a function of water saturation (S_w) for selected surfactant concentrations. The symbol **J** is the injection state and **I** is the initial state.

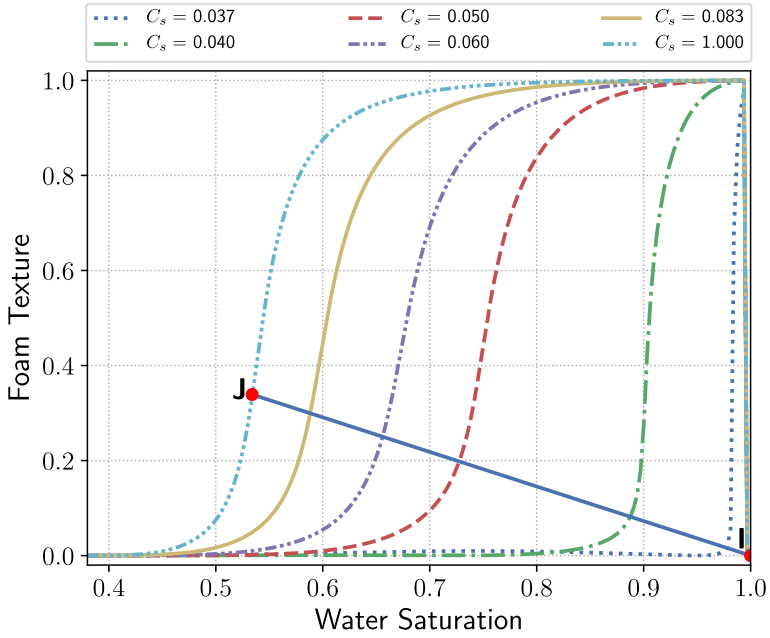

Source: Prepared by the author.

for the water saturation and foam texture at 0.3 PV comparing the KNP method with the KT (a central scheme [81]) and the classical upwind methods using 100 cells. In order to use the KT and upwind method in the simulations, the convective fluxes (3.33)-3.34 are adapted to these methodologies. The results for the foam texture (Fig. 44(b)) show a lower accuracy and greater numerical dissipation of the upwind method compared to the KNP method since the more accurate the solution, the thinner the peak region (see Fig. 42). Moreover, the KT method presents spurious oscillations and fails to approach this model with this mesh refinement, as can be seen in Figures 44(a) and 44(b). These oscillations when the KT method is adopted was also observed in Sections 4.2 and in [109]. In the simulated case, where $C_{\mathrm{s}} = 1.0\,\mathrm{wt.\%}$, the P_{c} does not exceed P_{c}^{*}. According to Figure 43, the spurious oscillations in the KT method, due to the scheme instability, appear specifically in the region for $S_w \lesssim 0.45$ (see Fig. 44(a)) and $C_{\mathrm{s}} = 1.0\,\mathrm{wt.\%}$, where foam texture approaches zero ($n_{\mathrm{D}} = 0$). The foam generation model is a power-law expression proportional to the magnitude of the phase velocities (more details in [48, 55]). Therefore, as water saturation reduces its value, the water velocity $\mathbf{v}_{\mathrm{w}}$ tends to zero, yielding the foam collapse. In this case, to obtain a stable solution using the KT method, as shown in Figures 44(c) and 44(d), excessive mesh refinement is required, which highlights the stability of upwind approaches, especially the KNP method for this type of problem.

In addition, a computational cost study comparing the implicit time-integration strategy adopted with the explicit approach commonly applied to these central finite volume methods [81, 83] is presented in Figure 45. The physical and numerical data used in these simulations are provided in Tables 6, varying only the number of processor cores used in the computation. The stability of the adaptive process of approximation in time is guaranteed by the SUNDIALS library [85], which meets the solution convergence criteria at each time step. Thus, both the solutions using the implicit and the explicit scheme converge to a unique solution since the solutions are obtained using the same convergence criterion. The figure relates the resolution time in seconds to the grid size and is presented on the log scale. The results show a lower computational cost of the implicit strategy (BDF) adopted compared to the Runge-Kutta (RK) method. This cost can be reduced by increasing the number of processing cores. This is because the SUNDIALS library algorithm requires smaller time steps for the explicit method, demonstrating a greater CFL condition restriction.

6.3 Comparison Between Co-injection and SAG

In this section, we investigate the surfactant's ability to generate and stabilize foam through two injection techniques in order to reduce the viscous fingering phenomena and the high permeability channeling. In order to achieve these goals, we use the heterogeneous, isotropic permeability field of layer 36 of the 10^{th} SPE project [1]. This layer clearly presents a high permeability channel, as shown in Figure 11(b). In this context, we compared the water-surfactant-gas co-injection technique with the injection of the water-surfactant solution

Figure 44 – Approximation of n_D in 0.3 PV comparing different numerical methods with 100 cells (a) and with different grid refinements for KT method (b).

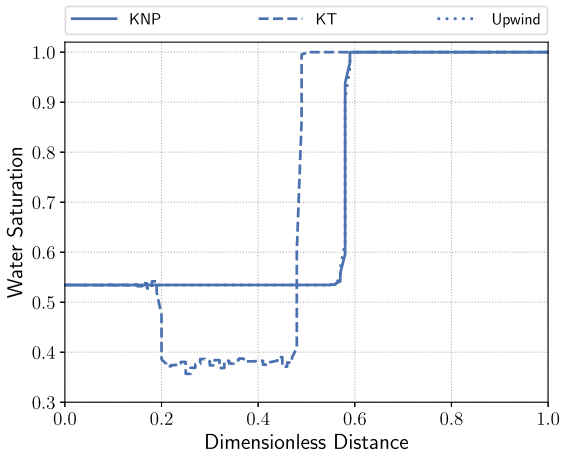

(a) Water saturation results for KNP, KT, and upwind methods.

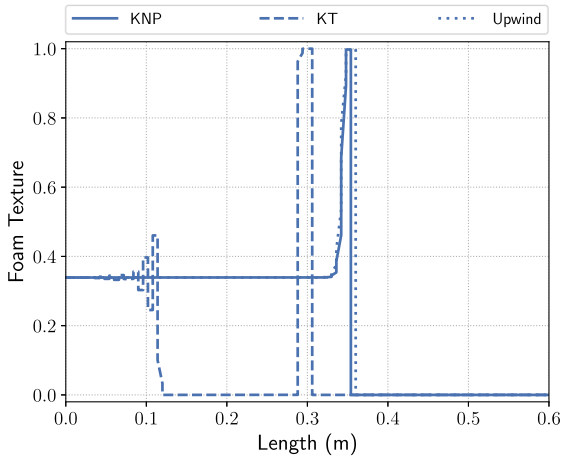

(b) Foam texture results for KNP, KT and upwind methods.

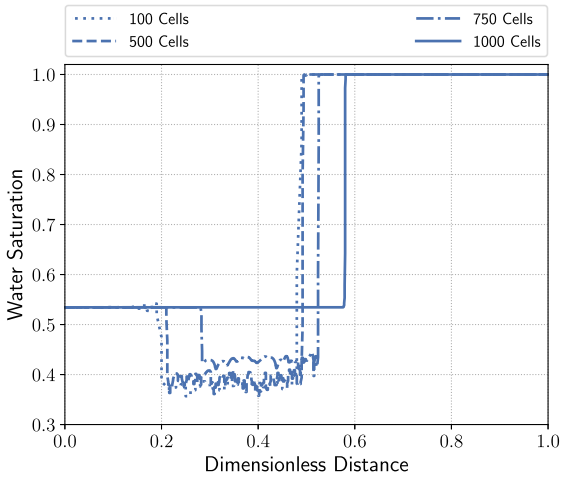

(c) Water saturation results for several grid sizes for KT method.

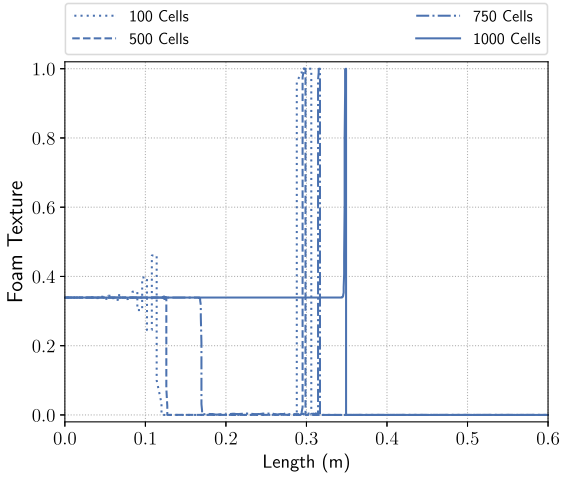

(d) Foam texture results for several grid sizes for KT method .

Source: Prepared by the author.

Figure 45 – The computational cost depends on the method used to solve the system of ODEs (BDF or RK), the grid size and the number of processing cores.

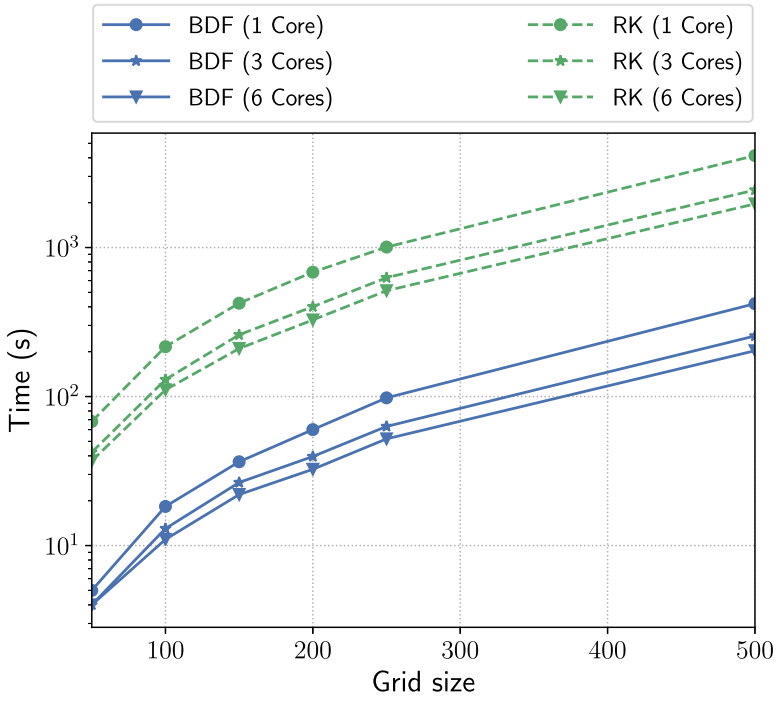

Source: Prepared by the author.

alternating with gas. Co-injection is a characteristic approach of laboratory experiments and SAG is associated with remediation and EOR strategies in field applications.

The relative permeability and capillary pressure functions are given by the expressions (6.9) and (6.10). The boundary conditions adopted in these studies prescribe, for the Darcy system, the right boundary as a Dirichlet type (Γ_D) with $\bar{p} = 0$, while left, top and bottom boundaries are set to a Neumann condition (Γ_N) with $\bar{u} < 0$ for the left boundary and $\bar{u} = 0$ for the top and bottom boundaries. For the transport equations, on the left boundary, it is imposed f_{g} for the aqueous phase and $C_{\mathrm{s}}(1 - f_{\mathrm{g}})$ for the surfactant transport equation, whereas right, top and bottom boundaries are defined with a homogeneous Neumann condition. The surfactant pore volume (e.g., Fig. 46) is computed by multiplying the surfactant concentration by the water pore volume since the densities of surfactant and water components are considered equal.

The simulations were carried out for $20{,}000$ seconds in a two-dimensional domain of 3.67×1.0, with a mesh of 220×60 cells. This porous medium is pre-saturated with pure water ($S_{\mathrm{w}}^0 = 1.0$ and $C_{\mathrm{s}}^0 = 0.0$), the effects of the trapped gas fraction are neglected ($X_{\mathrm{t}} = 0$). The remaining parameters can be found in Table 6.

To simulate co-injection, we carried out 4 experiments by simulating the injection of an aqueous solution with $1.0\,\mathrm{wt.\%}$ surfactant, using different foam qualities (shown in Table 7). On the other hand, for the surfactant alternating gas technique, setting $f_{\mathrm{w}} = 1.0$ we inject $t_{C_{\mathrm{s}}} = 0.0438$ PV, $t_{C_{\mathrm{s}}} = 0.0875$ PV, $t_{C_{\mathrm{s}}} = 0.1313$ PV, $t_{C_{\mathrm{s}}} = 0.1751$ PV of water with $1.0\,\mathrm{wt.\%}$

Table 7 – Co-injection study: injected foam qualities and corresponding total injected surfactant solution.

Co-injection – f_g	**SAG – Injected surfactant**
0.6	1.751×10^{-3} PV
0.7	1.313×10^{-3} PV
0.8	0.875×10^{-3} PV
0.9	0.438×10^{-3} PV

surfactant, which introduces the same amount of surfactant into the porous medium as in the co-injection cases studied (see Fig. 46(b)). Then, a gas slug was injected ($f_g = 1.0$) until the end of the simulation.

Figure 47 shows the results for surfactant concentration comparing the water-gas co-injection with $1.0\,\mathrm{wt.\%}$ of surfactant concentration for different foam qualities ($f_g = 60$, 70, 80, 90%) with SAG injection for different slug sizes of surfactant solution ($t_{C_s} = 0.1751$, 0.1313, 0.0875, 0.0438 PV). Although in both injection strategies, there is the same amount of surfactant for each case studied, the SAG technique presents a better propagation of the surfactant in the porous medium, mainly percolating through the preferential channel. This behavior of the SAG injection induces a greater formation of foam in the preferential channels, unlike the co-injection that maintains the maximum value of the foam texture in the entrance region of the domain, as can be seen in the Figure 48. Notice that the foam collapses upstream (reflecting in the lower foam texture) near the entrance region, mainly due to the reduction of the water saturation during the gas injection in SAG.

Due to the dependence of the apparent viscosity on the foam texture and gas velocity (2.50), it is possible to notice in Figure 49 that the behavior of the apparent viscosity for the co-injection is similar to the foam texture, with higher values at the entrance of the domain. However, the SAG strategy presents higher values in the region of the preferential channel, especially when there is a greater amount of surfactant injected, and in the rest of the domain, the apparent viscosity is lower than in the co-injection case. This is due to the fact that during gas injection the gas velocity is higher in SAG than in co-injection due to the imposition of $f_g = 1.0$. Despite this, the effects of apparent viscosity on the gas mobility reduction of the SAG present better sweeping efficiency than co-injection, reducing water saturation both at the entrance to the domain and in the preferential channel, as shown in Figure 50.

A better comparison of the sweep efficiency between SAG and co-injection is shown in Figure 51, where the cumulative water production to each foam quality and surfactant slug size simulated is presented, in addition to the case without surfactant (no foam). In the co-injection results, it is possible to observe that as f_g decreases there is an increase in cumulative water production, especially when there is a surfactant in the medium to induce foam generation (Fig. 51(a)). The greater amount of surfactant injected due to the reduction of f_g (Fig. 46(a)), increases the cumulative water production difference in relation to the case without surfactant.

Figure 46 – Cumulative surfactant injection for co-injection and SAG techniques.

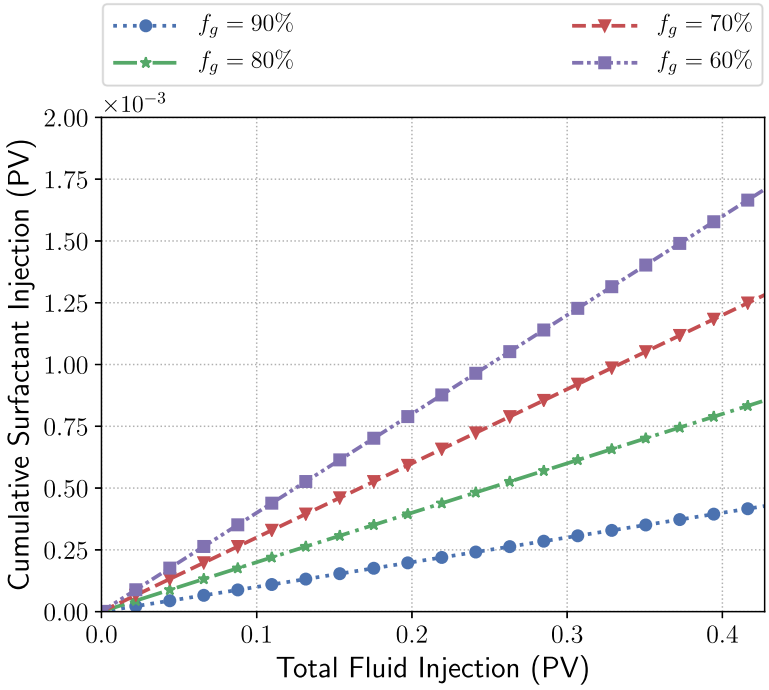

(a) Co-injection

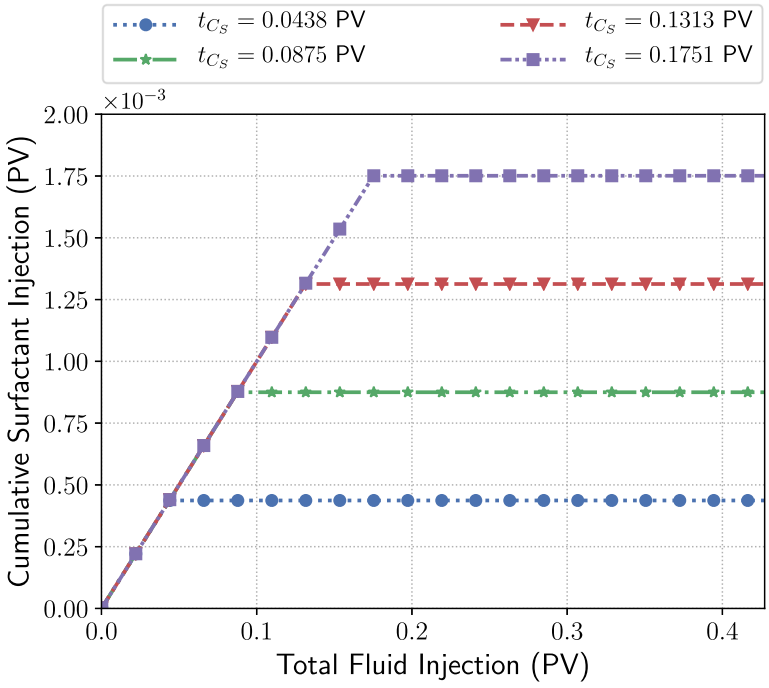

(b) SAG

Source: Prepared by the author.

Figure 47 – Surfactant concentration C_s computed at $t = 20\,000$ s. Left: co-injection, varying the foam quality f_g. Right: SAG, varying slug sizes of surfactant solution t_{C_s}.

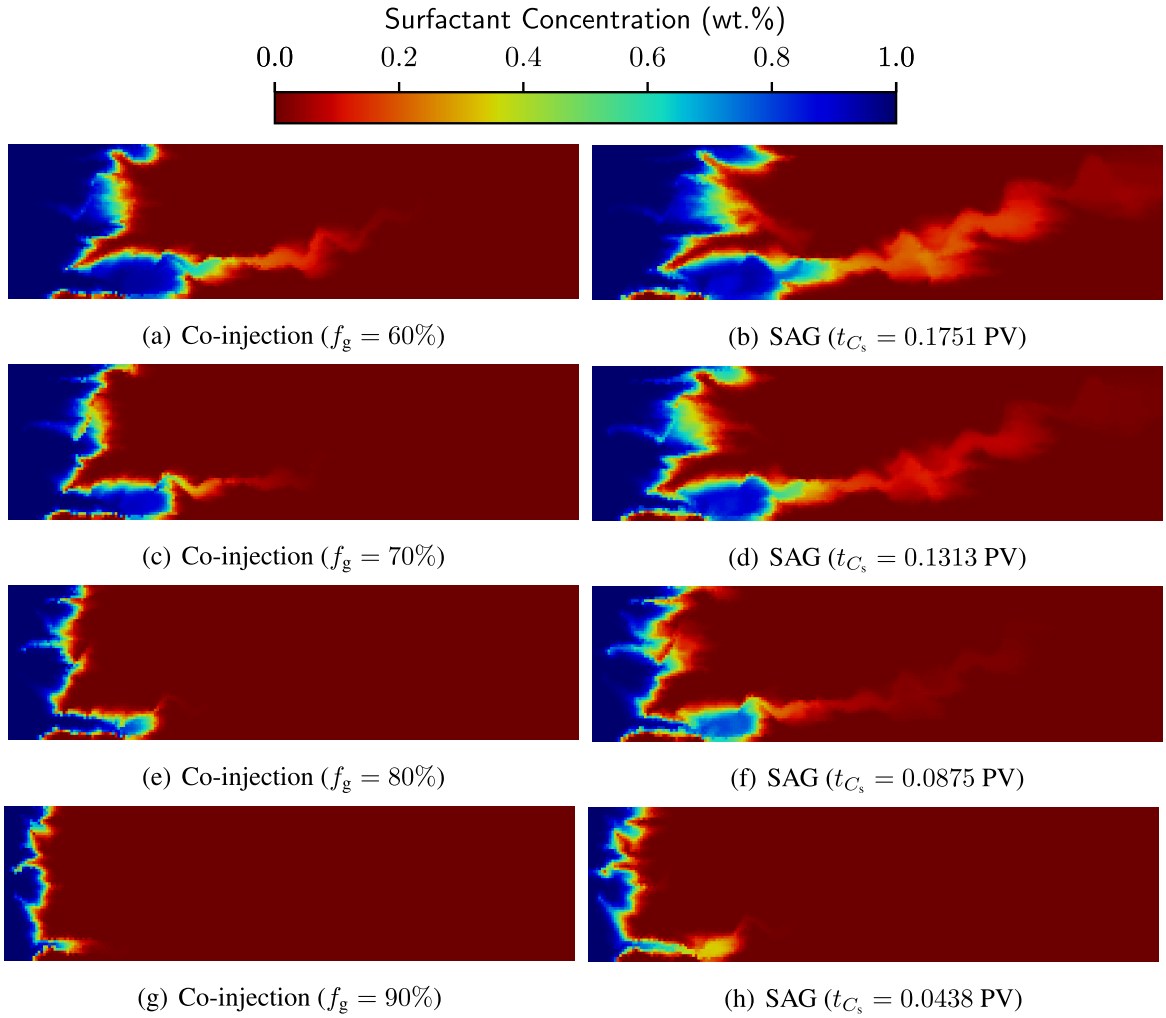

(a) Co-injection ($f_g = 60\%$)

(b) SAG ($t_{C_s} = 0.1751$ PV)

(c) Co-injection ($f_g = 70\%$)

(d) SAG ($t_{C_s} = 0.1313$ PV)

(e) Co-injection ($f_g = 80\%$)

(f) SAG ($t_{C_s} = 0.0875$ PV)

(g) Co-injection ($f_g = 90\%$)

(h) SAG ($t_{C_s} = 0.0438$ PV)

Source: Prepared by the author.

In addition, the reduction of f_g decreases the gas injection velocity and, therefore, the aqueous phase that contains the surfactant species presents a greater propagation. Consequently, more foam is generated, which leads to greater sweep efficiency. On the other hand, Figure 51(b) presents the SAG results for different surfactant slug sizes, adopting the same surfactant amounts as in the co-injection cases. It is also presented the WAG (Water Alternating Gas) injection strategy for different water slug sizes ($t_{S_w} = 0.0438, 0.0875, 0.1313, 0.1751$ PV), for the case when the foam is not present in the flow. The results show that SAG injection generates a higher water production than WAG strategy [120]. In comparison, SAG can also achieve better water production when compared to the co-injection strategy. In addition, it is evident in Figure 51(b) that the more surfactant injected, the more delayed the gas phase breakthrough.

We proceed with the same scenario as the previous simulation with different percentages of surfactant in the injected aqueous solution. In Figure 52, we present a comparison relating

Figure 48 – Foam texture n_{D} computed at $t = 20\,000$ s. Left: co-injection, varying the foam quality f_{g}. Right: SAG, varying slug sizes of surfactant solution $t_{C_{\mathrm{s}}}$.

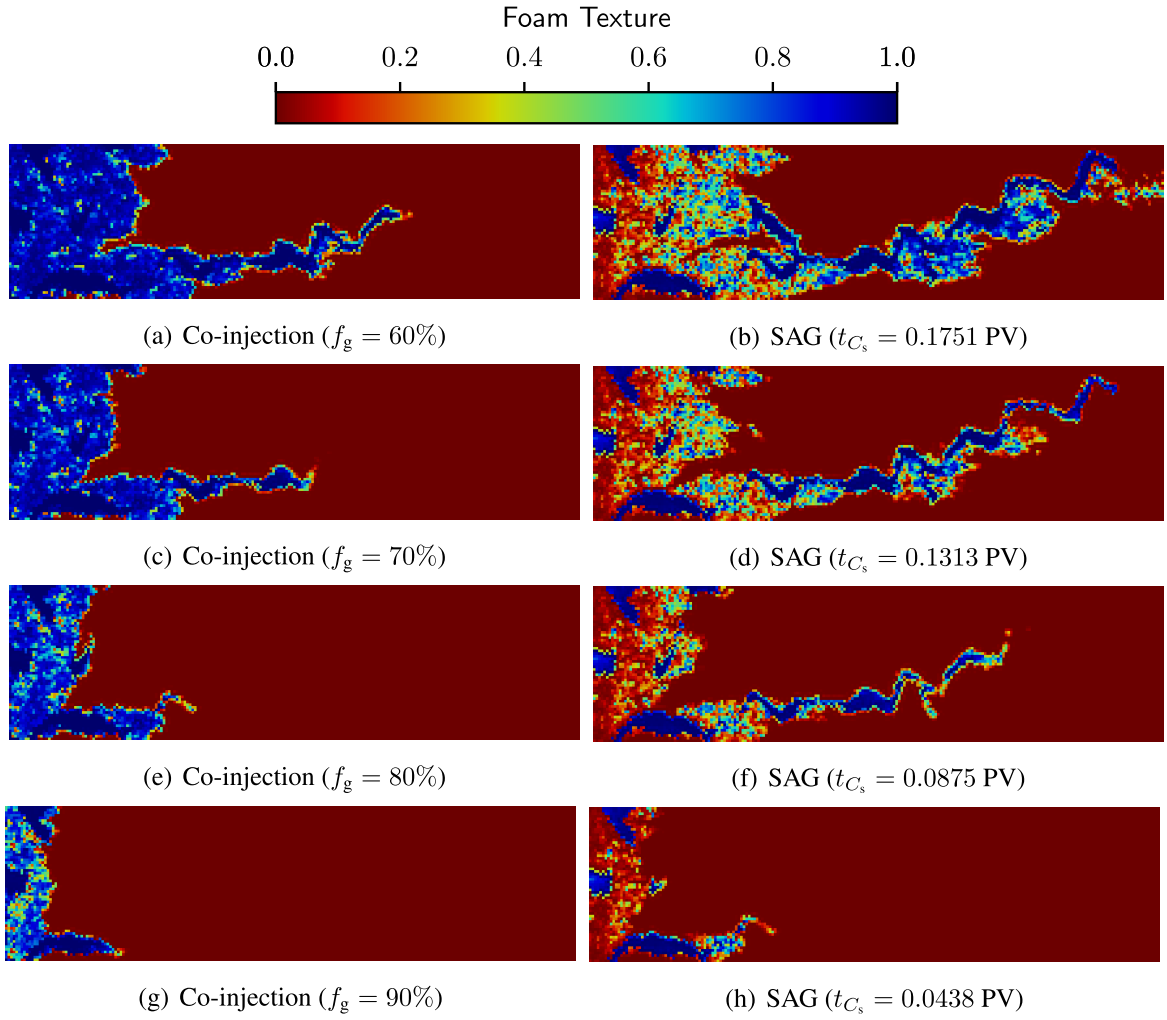

(a) Co-injection ($f_{\mathrm{g}} = 60\%$)

(b) SAG ($t_{C_{\mathrm{s}}} = 0.1751$ PV)

(c) Co-injection ($f_{\mathrm{g}} = 70\%$)

(d) SAG ($t_{C_{\mathrm{s}}} = 0.1313$ PV)

(e) Co-injection ($f_{\mathrm{g}} = 80\%$)

(f) SAG ($t_{C_{\mathrm{s}}} = 0.0875$ PV)

(g) Co-injection ($f_{\mathrm{g}} = 90\%$)

(h) SAG ($t_{C_{\mathrm{s}}} = 0.0438$ PV)

Source: Prepared by the author.

the total cumulative water production (defined as cumulative production at the simulation time 20 000 s) with the amount of surfactant injected into the medium (including the case with no foam). Applying the co-injection method, it is possible to observe the surfactant injection over 0.3 $\mathrm{wt.\%}$ does not significantly alter the cumulative water production, see Fig. 52(a). On the other hand, in Figure 52(b), the SAG injection achieved higher water production than the co-injection for all surfactant concentrations. This production increment is due to a greater amount of injected surfactant generating a greater concentration in the preferential channels inducing foam formation and reducing the gas mobility. Notice that the maximum value for SAG cumulative production does not present an expressive elevation when $C_{\mathrm{s}} \geq 1.0\,\mathrm{wt.\%}$. That behavior indicates that the surfactant concentration reaching the limit point corresponds to the maximum P_{c}^{*} defined in (2.55), and adding more surfactant will not improve foam mobility reduction. This behavior agrees with the literature describing when the surfactant concentration

Figure 49 – Apparent viscosity μ_g^f computed at $t = 20\,000$ s. Left: co-injection, varying the foam quality f_g. Right: SAG, varying slug sizes of surfactant solution t_{C_s}.

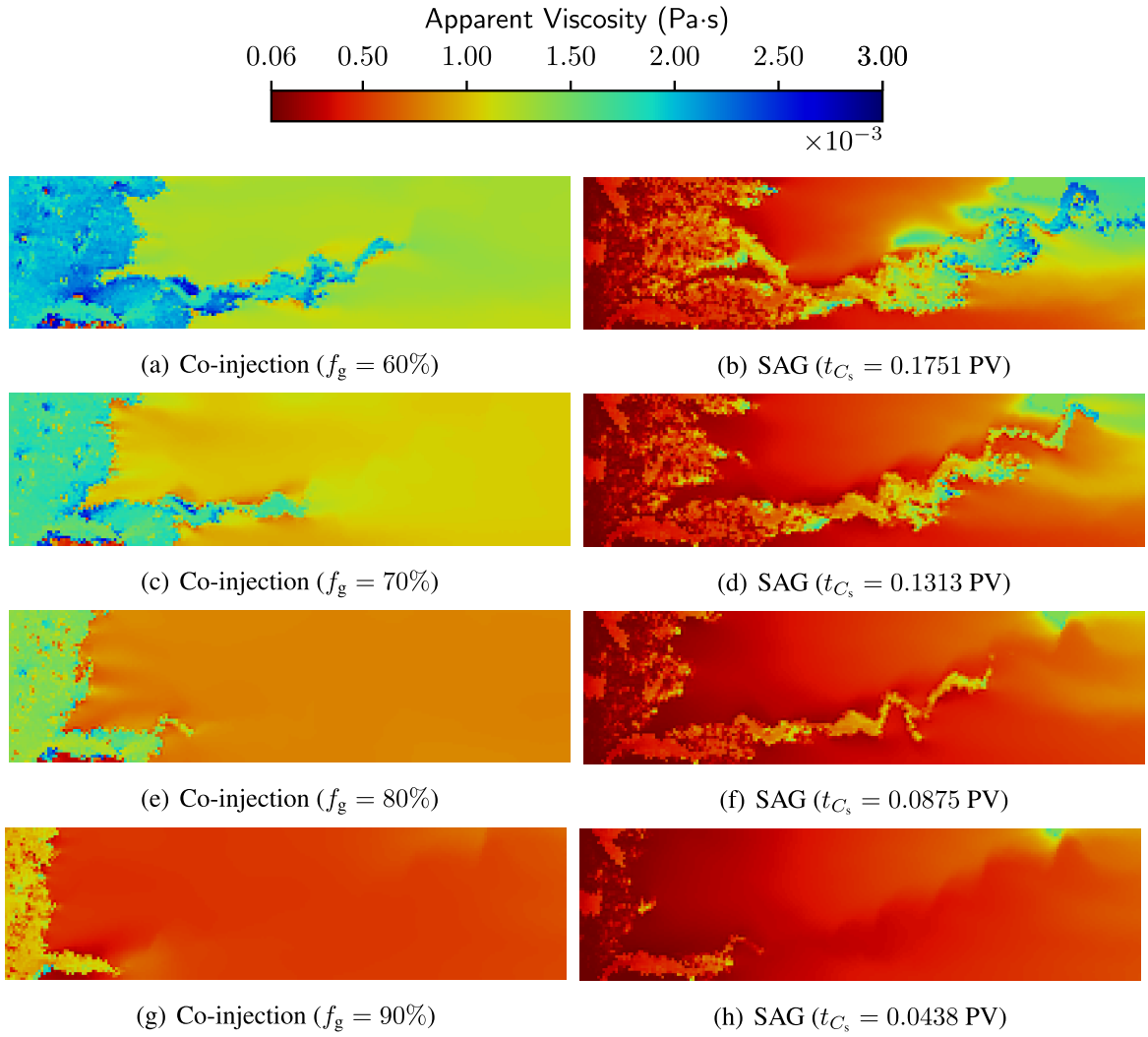

(a) Co-injection ($f_g = 60\%$)

(b) SAG ($t_{C_s} = 0.1751$ PV)

(c) Co-injection ($f_g = 70\%$)

(d) SAG ($t_{C_s} = 0.1313$ PV)

(e) Co-injection ($f_g = 80\%$)

(f) SAG ($t_{C_s} = 0.0875$ PV)

(g) Co-injection ($f_g = 90\%$)

(h) SAG ($t_{C_s} = 0.0438$ PV)

Source: Prepared by the author.

exceeds the critical micelle concentration (CMC).

Based on the results presented in Figure 52, the cumulative water production at $t = 20{,}000$ s as a function of the amount of injected surfactant for the co-injection and SAG techniques is presented in Figure 53. The curves in Figure 53 were obtained using the least square method with the logarithmic function applied to all points of the 0.1 wt.% surfactant concentration curve (green line in Figures 52(a) and 52(b)) and the maximum cumulative production values for each remaining surfactant concentration curves (diamond markers in Figures 52(a) and 52(b)). The least-square fit allows us to extrapolate the obtained simulation results for a higher amount of surfactant, showing a threshold for the production improvement by the surfactant concentration. Although in both cases, a plateau of maximum production was formed after a certain cumulative surfactant injection, the SAG injection resulted in a higher production when compared with the

Figure 50 – Water saturation S_{w} computed at $t = 20\,000$ s. Left: co-injection, varying the foam quality f_{g}. Right: SAG, varying slug sizes of surfactant solution $t_{C_{\mathrm{s}}}$.

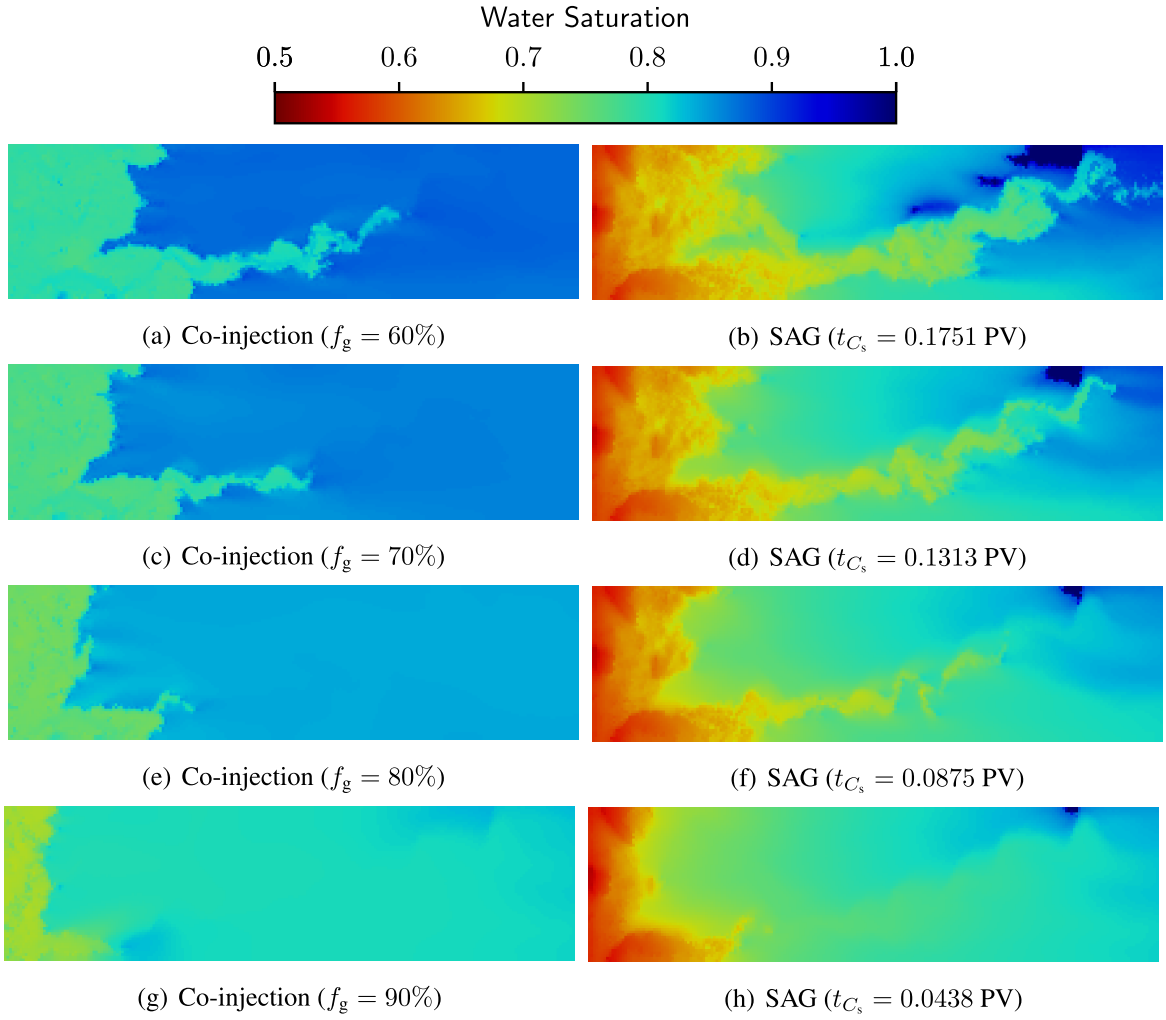

(a) Co-injection ($f_{\mathrm{g}} = 60\%$)

(b) SAG ($t_{C_{\mathrm{s}}} = 0.1751$ PV)

(c) Co-injection ($f_{\mathrm{g}} = 70\%$)

(d) SAG ($t_{C_{\mathrm{s}}} = 0.1313$ PV)

(e) Co-injection ($f_{\mathrm{g}} = 80\%$)

(f) SAG ($t_{C_{\mathrm{s}}} = 0.0875$ PV)

(g) Co-injection ($f_{\mathrm{g}} = 90\%$)

(h) SAG ($t_{C_{\mathrm{s}}} = 0.0438$ PV)

Source: Prepared by the author.

co-injection technique. Furthermore, regardless of the amount of surfactant injected, the total cumulative water production by co-injection is limited to around 0.32 PV, while SAG reaches approximately 0.40 PV.

For the SAG simulations in heterogeneous porous media, the surfactant concentration value where the mobility reduction reaches its maximum is somewhere around $C_{\mathrm{s}} \approx 1.0\,\mathrm{wt.\%}$ (as can be seen in Figure 52(b)). For the co-injection case, the limiting surfactant concentration is $0.3\,\mathrm{wt.\%}$, see Figure 52(a). In that way, it is possible to optimize the amount of surfactant injected, so the maximum production is reached with the lowest surfactant quantity possible, and the operation costs can be minimized and the profits maximized.

It is interesting to mention that, the heterogeneous porous media with a high permeability channel is mainly responsible for the differences in production curves in Figure 52. If the porous media is chosen to have a homogeneous permeability distribution, it turns out that, the

Figure 51 – Cumulative water production. Left: co-injection, with and without surfactant, varying the foam quality f_{g}. Right: SAG, varying slug sizes of surfactant solution $t_{C_{\mathrm{s}}}$ and WAG, varying the water slug size $t_{S_{\mathrm{w}}}$.

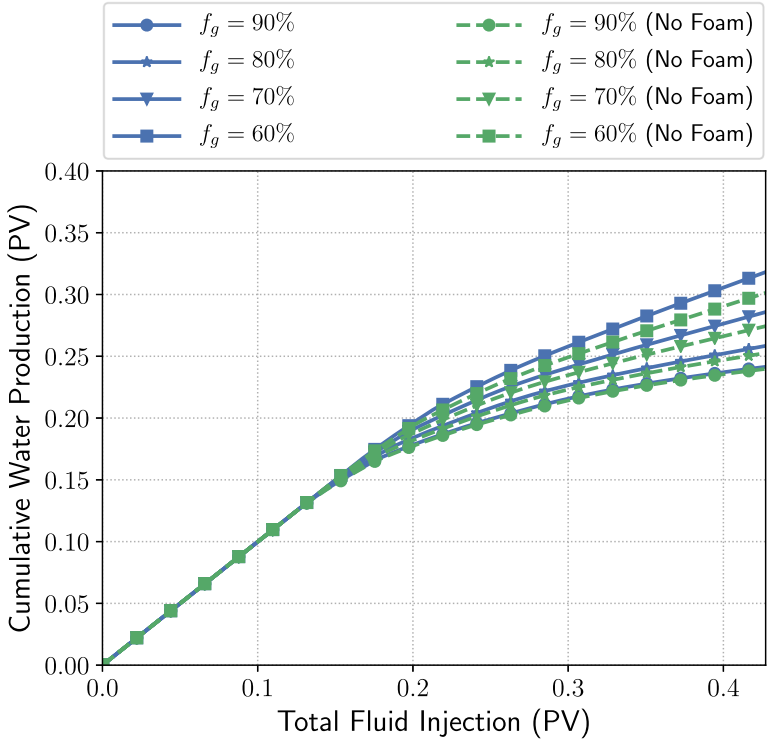

(a) Co-injection

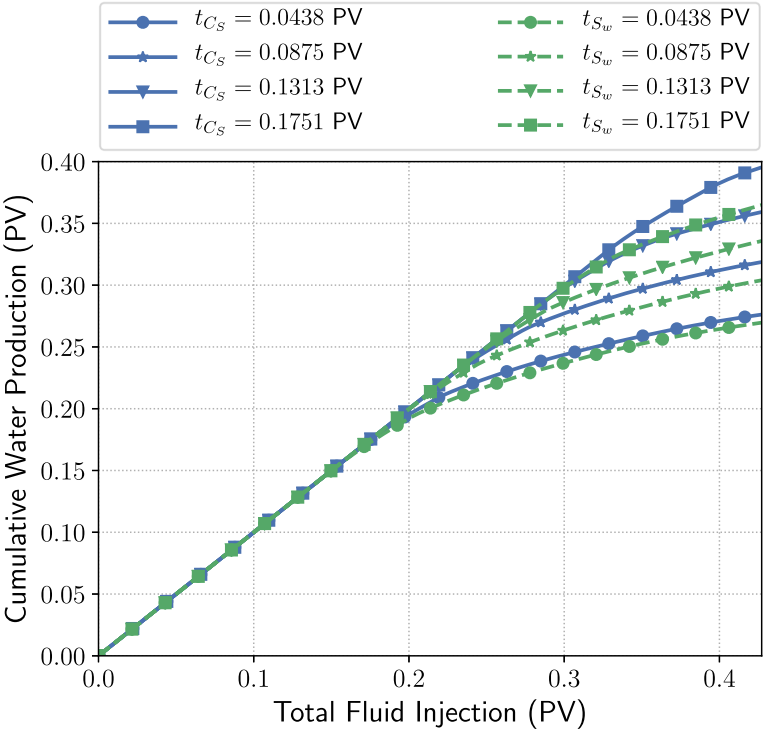

(b) SAG and WAG

Source: Prepared by the author.

Figure 52 – Maximum cumulative water production as a function of cumulative surfactant injection for different concentrations of surfactant in the injected aqueous solution, adopting co-injection (left) and SAG (right) at $t = 20{,}000\,\mathrm{s}$. The circle, star, triangle and diamond line markers refer to the injection condition with $f_g = 0.9,\ 0.8,\ 0.7$ and 0.6 for co-injection and $t_{C_s} = 0.0438,\ 0.0875,\ 0.1313$ and 0.1751 PV for SAG, respectively.

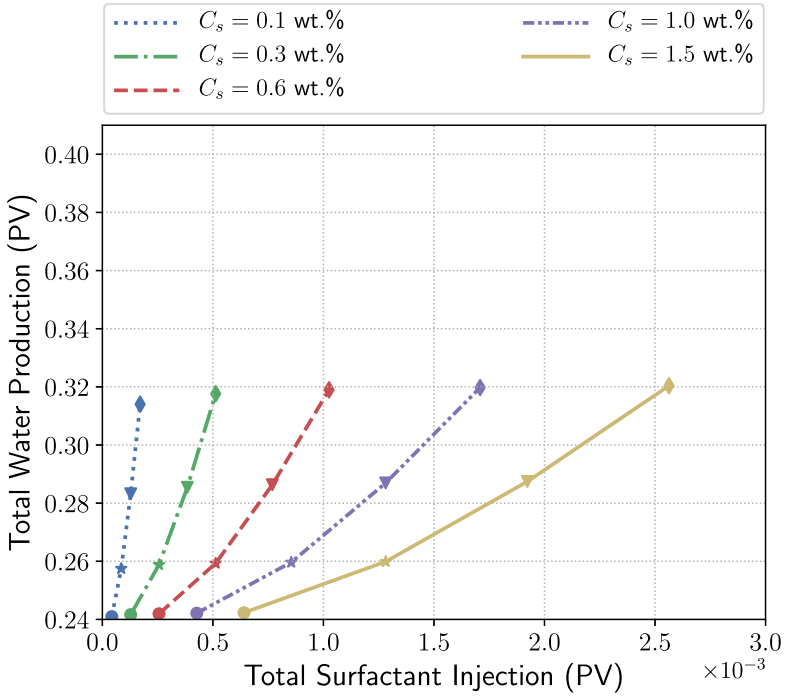

(a) Co-injection

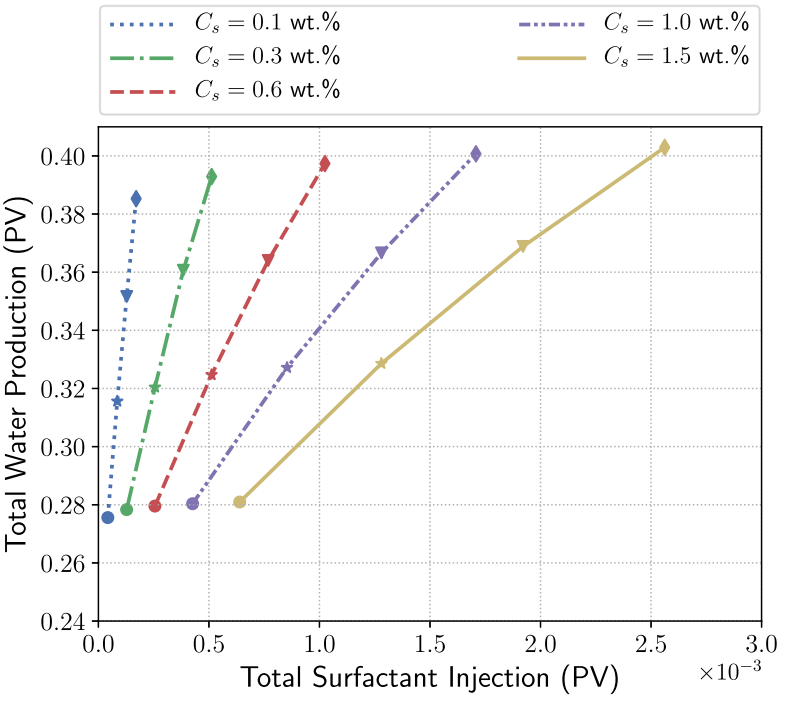

(b) SAG

Source: Prepared by the author.

Figure 53 – Relationship between maximum cumulative water production and amount of surfactant injected for co-injection and SAG.

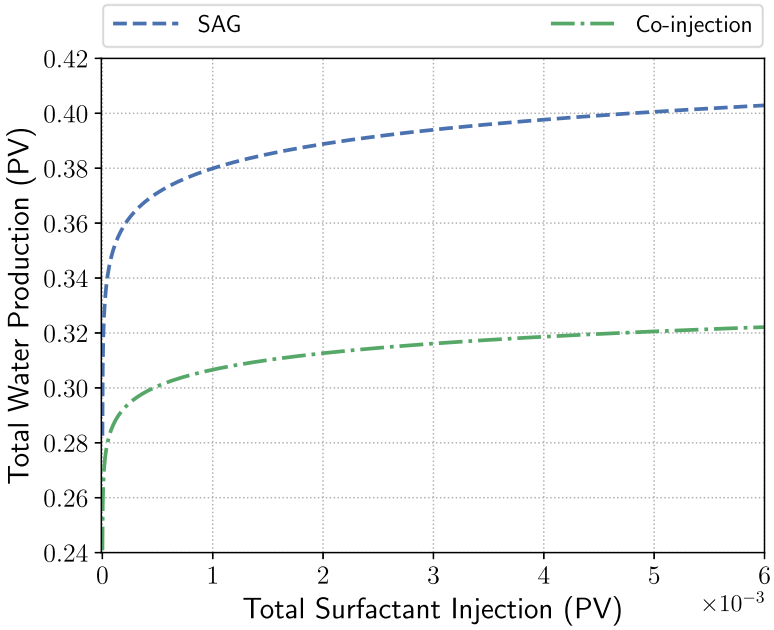

Source: Prepared by the author.

production curves for different surfactant concentration injections are virtually the same. That happens because there are no preferential paths or high permeability regions and the surfactant is evenly distributed throughout the flow wavefront. Hence, the behavior for the different surfactant concentration injections tends to be very close to each other, both in the co-injection and SAG strategies, although SAG still presents better results.

6.4 Influence of Surfactant Adsorption on Foam Displacement

In this section, although gravity is neglected and the flow is treated as incompressible, the adsorption phenomenon is taken into account, both equilibrium and kinetic. With that, we present the influence of the surfactant adsorption phenomenon on the foam-induced mobility reduction in heterogeneous porous media. The simulation parameter and domain configuration is the same of Section 6.3. The parameters related to the adsorption are given in Table 8.

Table 8 – Adsorption simulation parameters for the Kovscek's model adapted from.

Parameter	Value	Parameter	Value
K_1^{eq} [-]	0.1	K_1^{kin} [s^{-1}]	3.5×10^{-3}
K_2^{eq} [$\text{wt.}\%^{-1}$]	4.0	K_2^{kin} [$\text{wt.}\%^{-1}$]	100
K_{des} [s^{-1}]	2.0×10^{-4}	Non-dimensional density (ρ)	2.4

6.4.1 Influence of Adsorption Parameters

This section presents the influence of equilibrium adsorption and kinetic adsorption in the foam displacement in porous media. The general numerical experiment configuration follows the same methodology of Section 6.2: The simulations are run for a 0.6 m one-dimensional domain, for 1.0 PV, with an initial surfactant concentration of $1.0\,\mathrm{wt.\%}$. Other parameters can be found in Table 6 and 8.

The adsorption isotherms can be seen in Figure 54, which presents the influence of the surfactant concentration in the equilibrium model and the C_s and $C_\mathrm{s}^{\mathrm{kin},0}$ in the kinetic model. The Langmuir isotherm curves present a plateau, reaching a limit in the amount of adsorbed surfactant. Figures 55 and 56 show the results for the simulations for several injected porous volumes (PV) with $f_\mathrm{g} = 0.9$. Due to the adsorption phenomenon, the surfactant concentration in the aqueous phase presents a successive reduction (Fig. 55(c)). However, in the entry region, the surfactant concentration is kept relatively high due to the continuous injection of the solution. This behavior directly impacts the foam generation, as shown in Figure 55(b), reducing the foam texture in regions where the surfactant concentration is lowered by adsorption. As a result, the foamed gas mobility increases, and the adsorption affects water saturation solution profiles. The amount of adsorbed surfactant by kinetic and equilibrium mechanisms is compared in Figure 56.

6.4.2 Co-injection in a Heterogeneous Porous Medium Including Adsorption Effects

In order to investigate equilibrium and kinetic adsorption phenomena during foam flow in heterogeneous porous media using the co-injection strategy, simulations with the layer 36 of the 10$^{\mathrm{th}}$ SPE project [1] (see Fig. 11(b)) were used. The simulations were carried out for $50{,}000$ seconds in a two-dimensional domain measuring 3.67×1.0 m, with a mesh of 220×60 cells. The medium is pre-saturated with water ($S_\mathrm{w}^0 = 1.0$, $C_\mathrm{s}^0 = 0.0$ and $C_\mathrm{s}^{\mathrm{kin},0} = 0.0$), the effects of the trapped gas fraction are neglected ($X_\mathrm{t} = 0$), the co-injection condition is $f_\mathrm{g} = 0.6$, and the injected aqueous solution contains surfactant at $1.0\,\mathrm{wt.\%}$ concentration. The remaining parameters can be found in Table 6 and Table 8.

Figure 57 shows the results for surfactant concentration, comparing the cases where adsorption is neglected and when it is accounted for in the simulations. Although the same amount of surfactant is injected in both cases, it is observed a better propagation of the surfactant through the porous medium (mainly in the preferential channel) when adsorption is neglected. This no-adsorption case behavior induces a greater foam formation in the preferential channel, unlike when the surfactant is adsorbed on the medium. The adsorption reduces the foam formation throughout the domain, as shown in Figure 58.

The computed apparent viscosity of the foamed gas is shown in Figure 59. The apparent viscosity is dependent on the foam texture and gas velocity (see (2.50)), leading to higher values in the areas of higher gas mobility and foam formation, as it can be verified in Figures 58 and 59.

Figure 54 – Behavior of the equilibrium model in relation to surfactant concentration and of the kinetic model in relation to time for different surfactant concentrations C_s and initial adsorbed surfactant $C_s^{kin,0}$.

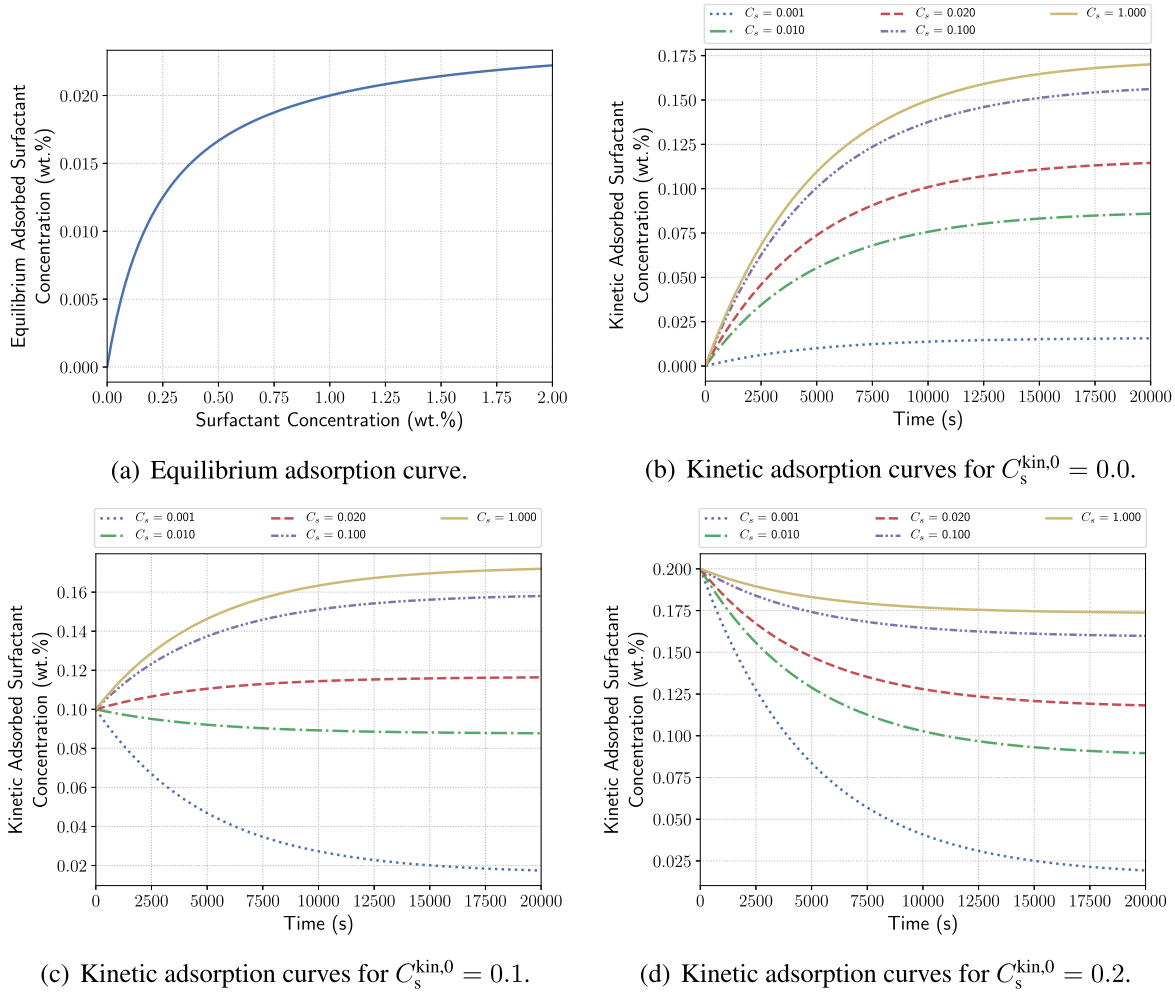

(a) Equilibrium adsorption curve.

(b) Kinetic adsorption curves for $C_s^{kin,0} = 0.0$.

(c) Kinetic adsorption curves for $C_s^{kin,0} = 0.1$.

(d) Kinetic adsorption curves for $C_s^{kin,0} = 0.2$.

Source: Prepared by the author.

This characteristic is advantageous to mitigate the channeling effect in porous media presenting high permeability regions, such as the one shown in Figure 11(b). In this scenario, the impact of apparent viscosity on the gas mobility reduction presents better sweep efficiency, reducing water saturation both at the entrance of the domain and in the preferential channel, as shown in Figure 60 for the no-adsorption simulation.

A comparison of the sweep efficiency between the no-adsorption and adsorption cases is shown in Figure 61, where the cumulative water production to each case is presented, in addition to the case without surfactant (no foam). The results confirm that the no-adsorption case presents higher production, as implied by the previous observation. On the other hand, when adsorption is taken into account, the production curve gets very close to the no-foam flow case, indicating that adsorption significantly affects sweep efficiency. In that way, by causing mass loss of surfactant and consequently reducing surfactant concentration, the adsorption phenomenon minimizes the

Figure 55 – Solution profiles when adsorption is taken into account, with $f_g = 0.9$.

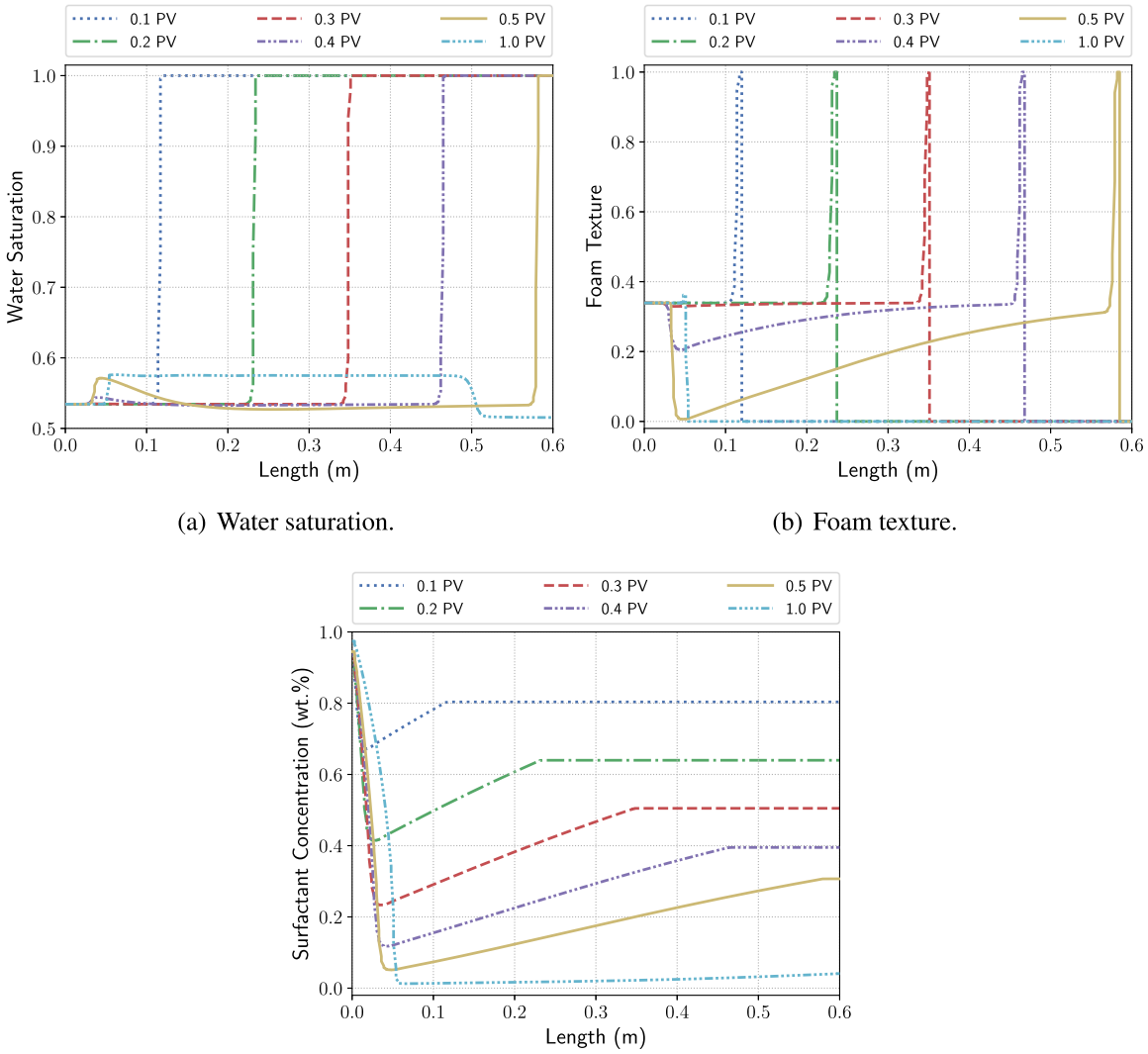

(a) Water saturation.

(b) Foam texture.

(c) Surfactant concentration in water.

Source: Prepared by the author.

strength and effectiveness of foam.

Figure 56 – Solution profiles for kinect- and equilibrium-adsorbed surfactant during injection, with $f_g = 0.9$.

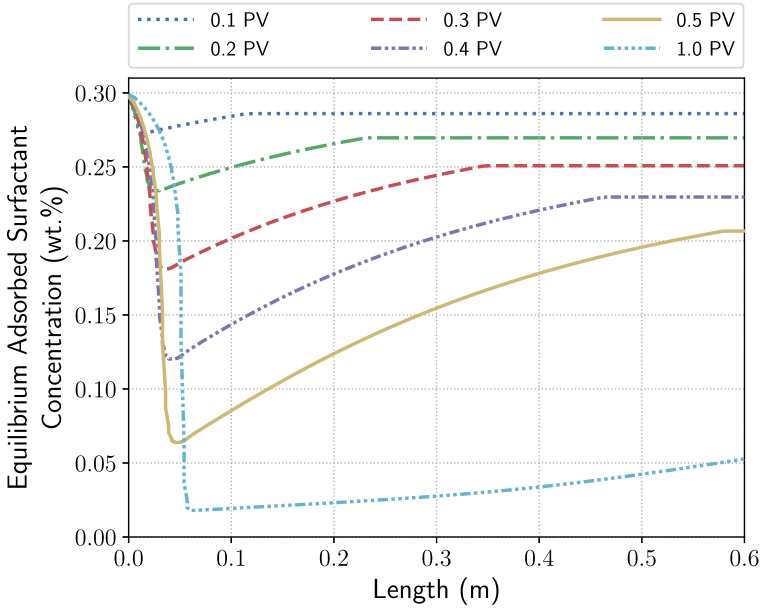

(a) Concentration of equilibrium-adsorbed surfactant (wt.%).

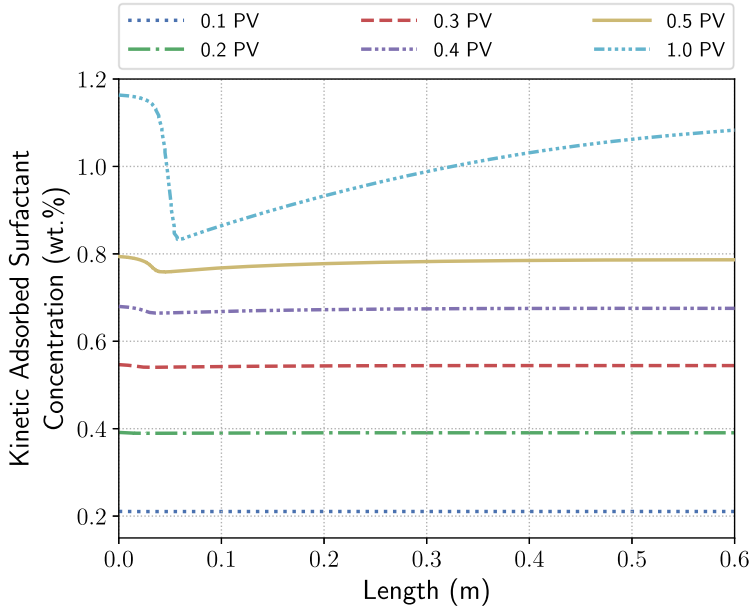

(b) Concentration of kinect-adsorbed surfactant (wt.%).

Source: Prepared by the author.

Figure 57 – Co-injection results for surfactant concentration in water (C_s).

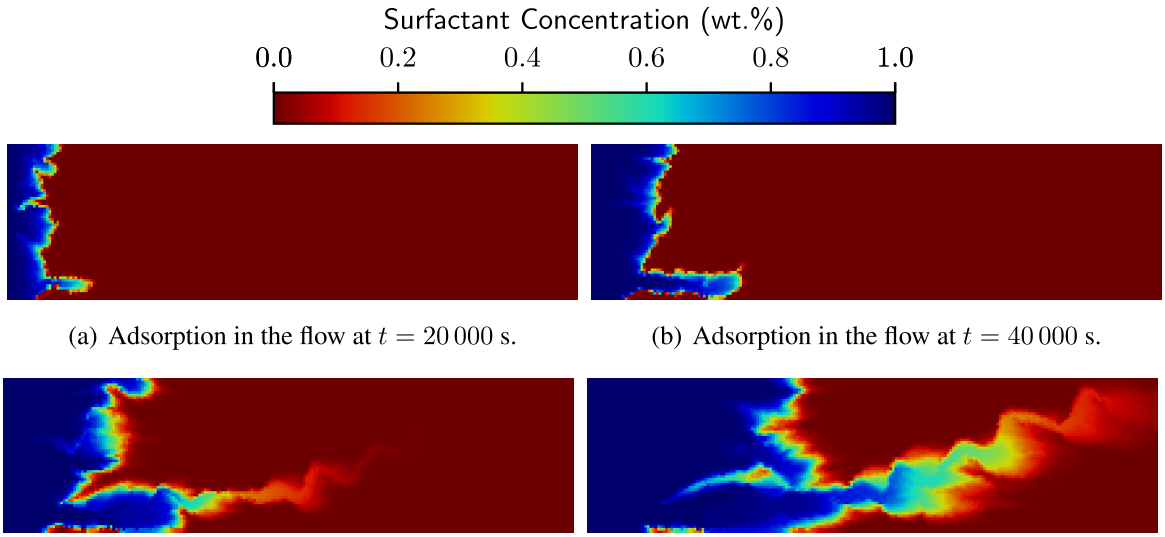

(a) Adsorption in the flow at $t = 20\,000$ s.

(b) Adsorption in the flow at $t = 40\,000$ s.

(c) No adsorption in the flow at $t = 20\,000$ s.

(d) No adsorption in the flow at $t = 40\,000$ s.

Source: Prepared by the author.

Figure 58 – Co-injection results for foam texture (n_D).

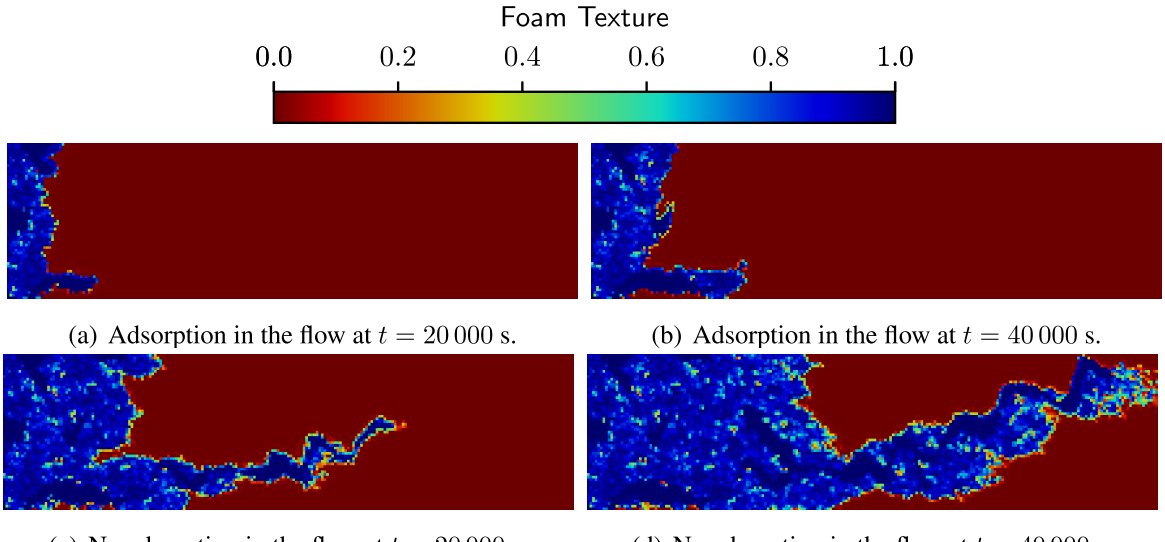

(a) Adsorption in the flow at $t = 20\,000$ s.

(b) Adsorption in the flow at $t = 40\,000$ s.

(c) No adsorption in the flow at $t = 20\,000$ s.

(d) No adsorption in the flow at $t = 40\,000$ s.

Source: Prepared by the author.

Figure 59 – Co-injection results for apparent viscosity $\left(\mu_{\mathrm{g}}^{\mathrm{f}}\right)$.

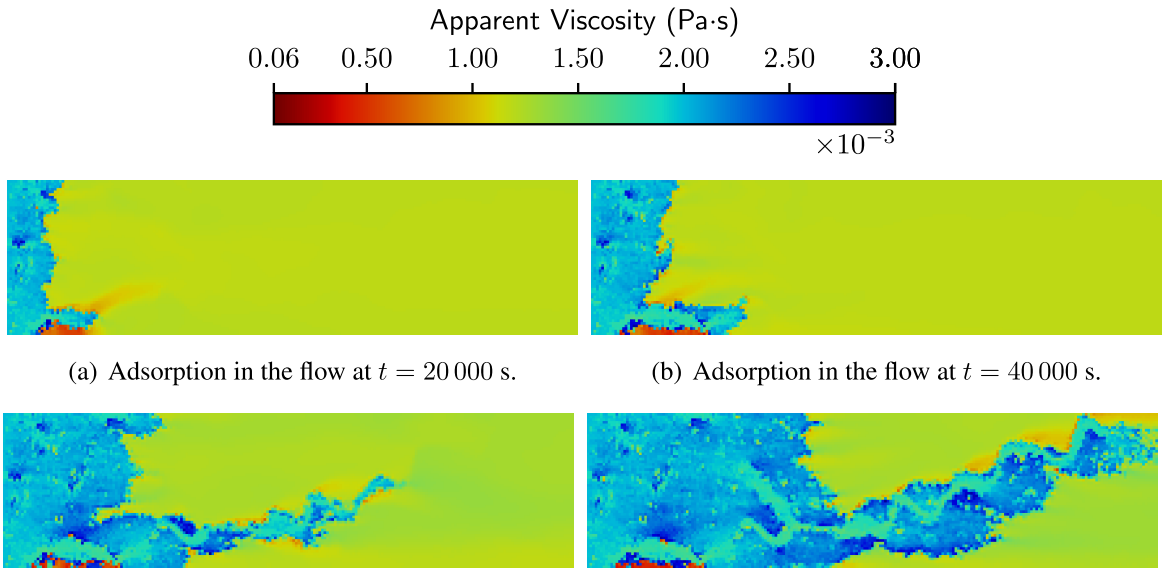

(a) Adsorption in the flow at $t = 20\,000$ s.

(b) Adsorption in the flow at $t = 40\,000$ s.

(c) No adsorption in the flow at $t = 20\,000$ s.

(d) No adsorption in the flow at $t = 40\,000$ s.

Source: Prepared by the author.

Figure 60 – Co-injection results for water saturation (S_{w}).

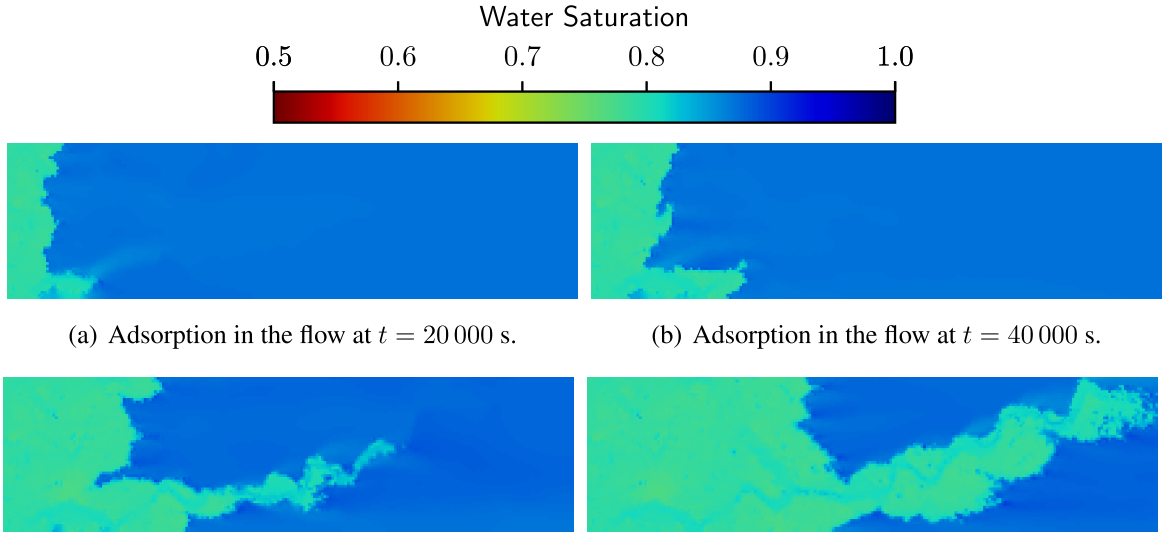

(a) Adsorption in the flow at $t = 20\,000$ s.

(b) Adsorption in the flow at $t = 40\,000$ s.

(c) No adsorption in the flow at $t = 20\,000$ s.

(d) No adsorption in the flow at $t = 40\,000$ s.

Source: Prepared by the author.

Figure 61 – Co-injection cumulative water production.

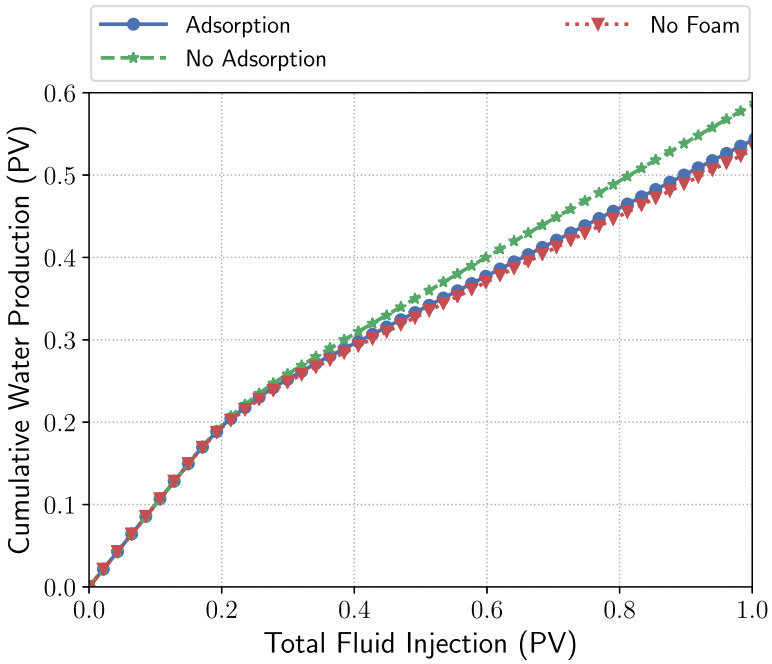

Source: Prepared by the author.

6.4.3 SAG Injection in a Heterogeneous Porous Medium Including Adsorption Effects

The next simulations adopt surfactant alternating gas injection. Using the same data from the co-injection presented in the previous section, the SAG technique starts the process by injecting an aqueous solution containing $1.0\,\mathrm{wt.\%}$ surfactant (with $f_g = 0.0$) for 20,000 s, then the medium is flooded with gas ($f_g = 1.0$) for 30,000 s.

The results for SAG injection strategy are shown in Figures 62–65. Similarly to the co-injection simulations, the surfactant penetration into the porous media, especially in the high permeability region, is higher in the case without adsorption, as can be seen in Figure 62. As observed before, the adsorption phenomenon reduces the surfactant concentration in the aqueous phase, which directly impacts the foam effectiveness, as modeled by Equations (2.58) and (2.55). That difference between adsorption and no-adsorption cases of surfactant availability to foam generation reflects in other flow results. More directly, foam texture is affected by surfactant concentration, as foam generation is more prominent in the no-adsorption numerical experiment (Fig. 63). Consequently, the apparent viscosity is higher in the no-adsorption simulation, especially in the high permeability channel, as can be seen in Figure 64. Ultimately, the previous foam flow characteristics result in a foamed gas mobility reduction, leading to a better aqueous phase displacement when adsorption is not accounted for, as shown in Figure 65.

In Figure 66, the cumulative water production for SAG (with and without adsorption) can be observed alongside the results for WAG (Water Alternating Gas) that does not include foam effects. The outcome is similar to the co-injection solutions: the no-adsorption simulation

Figure 62 – SAG results for surfactant concentration in water (C_s).

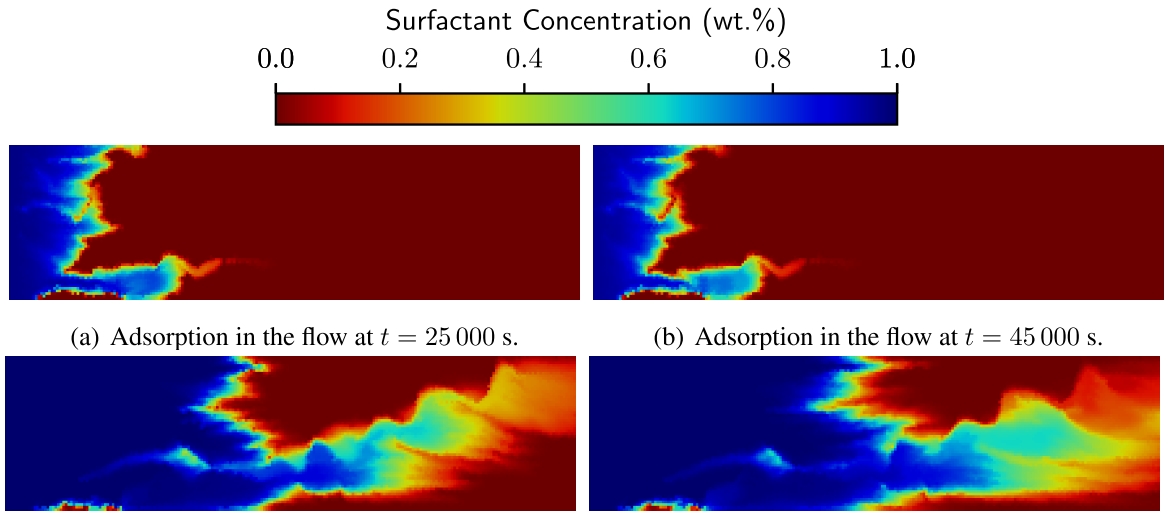

(a) Adsorption in the flow at $t = 25\,000$ s.

(b) Adsorption in the flow at $t = 45\,000$ s.

(c) No adsorption in the flow at $t = 20\,000$ s.

(d) No adsorption in the flow at $t = 40\,000$ s.

Source: Prepared by the author.

Figure 63 – SAG results for foam texture (n_D).

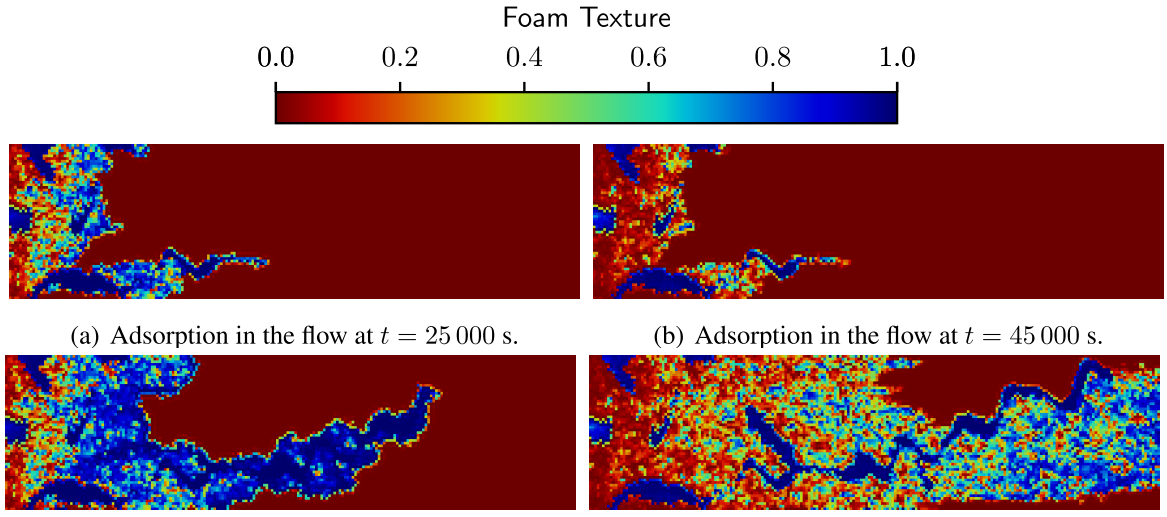

(a) Adsorption in the flow at $t = 25\,000$ s.

(b) Adsorption in the flow at $t = 45\,000$ s.

(c) No adsorption in the flow at $t = 25\,000$ s.

(d) No adsorption in the flow at $t = 45\,000$ s.

Source: Prepared by the author.

generates higher water production, while the production curve adopting adsorption gets very close to the WAG curve due to the loss of surfactant to the porous medium's solid matrix. As with co-injection, the SAG technique is also affected by the adsorption phenomena that negatively influence the foam flooding efficiency regarding water production. However, it is also worth noticing that the water production for SAG presents higher values than for co-injection, even though the same amount of gas and surfactant solution were injected in both cases.

Although the adsorption affects similarly both SAG and co-injection, the two strategies

Figure 64 – SAG results for apparent viscosity $\left(\mu_{\mathrm{g}}^{\mathrm{f}}\right)$.

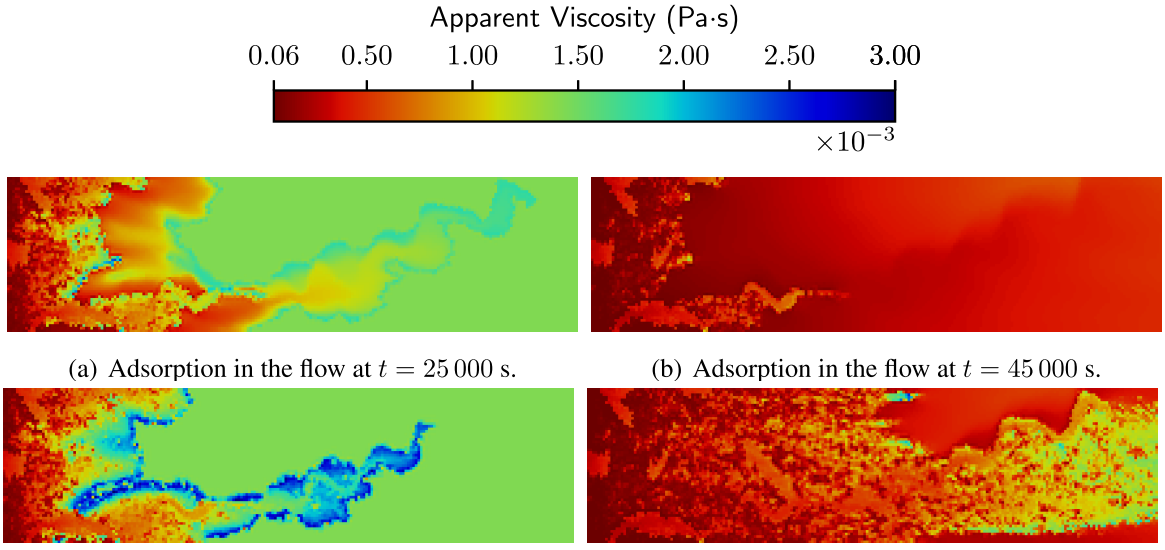

(a) Adsorption in the flow at $t = 25\,000$ s.

(b) Adsorption in the flow at $t = 45\,000$ s.

(c) No adsorption in the flow at $t = 25\,000$ s.

(d) No adsorption in the flow at $t = 45\,000$ s.

Source: Prepared by the author.

Figure 65 – SAG results for water saturation (S_{w}).

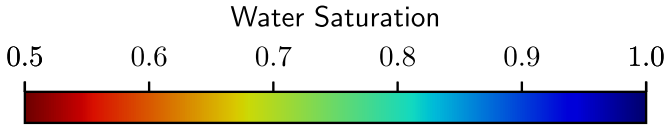

(a) Adsorption in the flow at $t = 25\,000$ s.

(b) Adsorption in the flow at $t = 45\,000$ s.

(c) No adsorption in the flow at $t = 25\,000$ s.

(d) No adsorption in the flow at $t = 45\,000$ s.

Source: Prepared by the author.

Figure 66 – SAG and WAG cumulative water production.

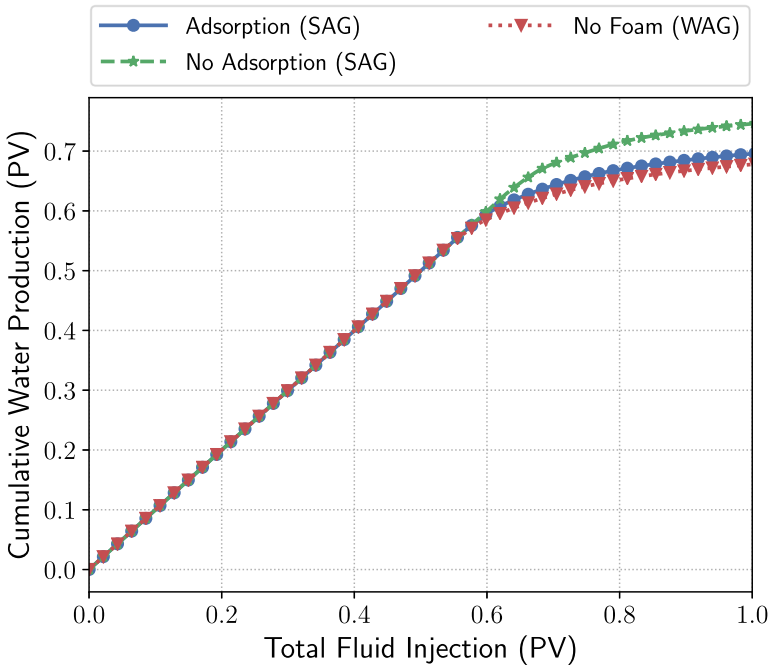

Source: Prepared by the author.

present different water production outcomes. Figure 66 shows the water cumulative production for SAG simulations, which presents a substantial improvement when compared to Figure 61. The main factors that contribute to the superiority of the SAG strategy are: (1) better surfactant percolation in the preferential channel, which leads to greater foam formation and consequently a greater reduction in gas mobility in the preferential paths; (2) The gas breakthrough is retarded in SAG injection compared to co-injection. The results are in concordance with the work of Blaker and collaborators [23], which states that in heterogeneous porous media, the SAG strategy can achieve better production results than the co-injection strategy.

It is clear from the previous results, that the adsorption phenomenon can play an important role in the foaming flood in porous media. More specifically, adsorption can be a negative factor regarding production improvement using foam, due to the reduction of foam effectiveness. In order to avoid the adsorption effect, the surfactant solution can be pre-flushed into the porous media, allowing the adsorption to take place only in the pre-flush stage [2, 3]. However, the surfactant is still lost to the solid matrix of the medium, still impacting operation costs. Another way to mitigate the effects of adsorption is to choose an appropriate type of surfactant, considering the rock surface chemistry and the surfactant structure, so that the physicochemical attraction leading to adsorption is reduced [46].

6.5 Partial Conclusions

The sequential algorithm proposed when used to solve two-phase flows including foam and surfactant effects proved to be robust, stable, accurate and with reduced numerical dissipation and computational cost. Numerical investigations, comparing the proposed numerical approach with classical techniques to stabilize the convective flow and integration in time are carried out. The comparison results showed that the KT method did not converge to the expected solution, showing spurious oscillations. However, the KNP method, due to its upwind nature, obtained the expected result with lower numerical dissipation than the classical upwind scheme. Moreover, the temporal integration BDF scheme presented a significant reduction in the computational cost in comparison with the Runge-Kutta method, usually adopted in this type of approach.

In the simulations comparing SAG and co-injection, the co-injection results indicated that the lower the foam quality, the higher the sweep efficiency, since the reduction of f_{g} in the injection, favors the inflow and propagation of more surfactant in the porous medium. It was also observed that by fixing the amount of surfactant injected, the results show that SAG injection has a better sweep efficiency, compared to co-injection, due to greater surfactant percolation in preferential channels. Additionally, at a certain point, it is not advantageous to increase the surfactant concentration for co-injection nor SAG strategies as there is no significant productivity improvement. That happens because surfactant achieves a critical concentration, and the limiting capillary pressure (2.55) reaches its maximum.

When the adsorption effects are incorporated into the model, the simulations showed that this phenomenon could significantly impact the sweep efficiency, as it reduces the amount of surfactant in the aqueous phase. The adsorption effect affects surfactant percolation significantly, leading to lower foam generation in the preferential channels compared to the non-adsorption case. In fact, this phenomenon is an important aspect of the economic viability of chemical flooding [121, 46]. The SAG and co-injection comparisons demonstrated that the negative impact of the adsorption on the sweep efficiency does not depend on the injection strategy since both co-injection and SAG injection strategies are affected similarly. Moreover, in the simulations with adsorption, SAG still presents better production results than co-injection.

7 ON THE INJECTIVITY ESTIMATION IN FOAM EOR

This chapter, as presented in [70], studies numerical treatments to circumvent the injectivity issues caused by the use of the Peaceman equation in the numerical simulation of chemically enhanced oil recovery (EOR) processes aimed at reducing fluid mobility, such as foam injection, on coarse grids.

The injection of foam in porous media has been identified as a promising enhanced oil recovery technique [122]. During foam injection, better conformation control is expected than when no-foamed gas (either in a single slug or in a WAG scheme) is injected, because foam is shown to increase apparent viscosity of the injected fluid, leading to reduced *gravity override* and *viscous fingering* [35, 37, 36]. However, when adopting the Peaceman well model [64] (the most used in commercial software, such as Stars [4]) in foam simulations, the well injectivity can be significantly underestimated when combined with a coarse grid [42, 62, 65, 66, 67, 68, 69].

The problem of injectivity loss in foam simulations occurs because the Peaceman equation assumes uniform water saturation near the well. That issue can be exacerbated in numerical simulations due to the reservoir spatial discretization, in which inevitably the dimensions of any grid block containing a well are much larger than the wellbore radius itself, and the wells are mathematically represented as sources (injection well) or sinks (production well) within the coarse grid block [64]. This well modeling approach is usually not adequate when dealing with viscous fluids, such as heavy oil [4], polymer solution [66], or foam [62, 68]. The reason is that it cannot adequately capture near-wellbore effects that can have a significant influence on overall reservoir simulation results [4].

Some techniques have been proposed in the literature to overcome the injectivity issues related to the foam EOR technique. [42] present a methodology based on the computation of the correct well injectivity from the analytical solution for the water saturation around the well region using a radial flow model. However, their solution is over-restricted by simplifying hypotheses, and the methodology lacks a procedure applicable in commercial simulators. On the other hand, [69] focused on developing a methodology that could be embedded into commercial simulators. They propose a modification to the well index that takes into account only the foam quality. Nonetheless, the well index alteration is oversimplified and cannot be used when only gas flows through the well (e.g., during a SAG process). To reduce the overestimation of using the Peaceman model in the SAG foam process, [67] proposed a negative constant for the skin factor based on a prediction obtained by a simplified radial flow model with fitted data from core flood experiments. [66] studied the difficulties in using the Peaceman model combined with an EOR by polymer flooding. In this case, since the Peaceman equation assumes an average velocity in the well block, the polymer apparent viscosity is incorrectly estimated, and so is the injectivity. The authors then propose a modification of the skin factor of the classical well model that can be readily input into Stars simulator.

In this context, this paper firstly investigates the issues encountered when the Peaceman model is used to compute the injectivity of foam using analytical solutions, as presented by [42]. This study demonstrates that the association between the assumptions of the Peaceman model with an excessively coarse well block generates wrong injectivity estimates when the foam is used to reduce the mobility of the gas phase. Our goal is to present a simple tool that engineers can immediately use to circumvent the injectivity estimate issue. That is why we focus on the implementation in Stars simulator. Thus, two types of grid partitioning are studied: Cartesian and hybrid. The Cartesian is characterized by increasing the number of Cartesian grid blocks around the wells (therefore, using smaller blocks). The hybrid grid method, readily available in Stars, is based on the definition of a cylindrical grid in the near-well region that can better capture the radial flow nature of the well injection/production flow. The hybrid grid technique depends on parameters associated with the number of grid partitions and the radius of the innermost cylinder. Notice that changing the grid partition using Peaceman model changes the physics of the model; it is not equivalent to grid refinement in the sense of standard Numerical Analysis. One of the goals of this work is to obtain the proper choice of these parameters generating better estimates for the bottom-hole pressure (BHP), and also controlling numerical instabilities.

Differently from several other methods proposed in the literature [42, 66, 67, 69], none of the well block partitioning approaches changes the input data or the commercial reservoir simulator injectivity model (including formulas or values for the well index or the skin factor, for instance). The results obtained with these strategies show a better estimation of the BHP (or equivalently, the well injectivity) as the number of well block partitions is increased, especially when the innermost block is closer to the wellbore. Moreover, the injectivity issues due to the use of the Peaceman equation are mitigated, and the deviations of the injectivity in real foam flooding applications from the simulations are greatly reduced. This leads to more reliable foam simulations that can be used to design field applications with more accuracy.

Local grid partitioning has been successfully applied to petroleum reservoir simulations for decades [123, 124, 125, 126]. This type of partitioning depends on several parameters, which are not directly determined. Up to our knowledge, a systematic parameter study is lacking in the context of the injectivity misestimation during the injection of high viscous fluids, such as foamed gas. We demonstrate the influence of the parameters (number of grid partitions and the radius of the innermost cylinder) of the hybrid grid technique in the estimation of BHP, emphasizing the values that present the best results and those resulting in numerical instabilities.

7.1 Radial Flow Model Including Foam Effects

We consider the problem of determining the pressure drop due to the injection of N_2 gas at a fixed volumetric rate Q through a well placed in the center of a reservoir block initially saturated with an aqueous solution of surfactant. For the matter of simplifying the presentation,

let us assume both the rock and fluids are incompressible, the flow is isothermal, the gravity effects can be neglected, and, in the neighborhood of the injection well the rock is homogeneous, the fluids are immiscible, and the oil phase is not present. Under these hypotheses, the flow is radial with the superficial velocity [91]

$$u(r) = \frac{Q}{2\pi r H}, \tag{7.1}$$

where r is the radius, and H is the block thickness. To formulate the problem, we need some standard fractional flow theory relations [91, 90], presented next. The superficial velocity of the water phase is defined by

$$\mathbf{u}_{\mathrm{w}} = u f_{\mathrm{w}}, \tag{7.2}$$

where f_{w} denotes the fractional flow of water (the ratio between the mobility of water phase, λ_{w}, and the total fluid mobility, $\lambda = \lambda_{\mathrm{w}} + \lambda_{\mathrm{g}}$): $f_{\mathrm{w}} = \lambda_{\mathrm{w}}/\lambda$. The mobility of water (λ_{w}) and gas (λ_{g}) phases are defined by $\lambda_{\mathrm{w}} = k_{\mathrm{rw}}/\mu_{\mathrm{w}}$, $\lambda_{\mathrm{g}} = k^{\mathrm{f}}_{\mathrm{rg}}/\mu_{\mathrm{g}}$, where μ_{w} and μ_{g} are the viscosities of water and gas and k_{rw} and $k^{\mathrm{f}}_{\mathrm{rg}}$ are the Corey-type relative permeabilities of water and (possibly foamed) gas phases given by

$$k_{\mathrm{rw}}(S_{\mathrm{w}}) = k^0_{\mathrm{rw}} \left(\frac{S_{\mathrm{w}} - S_{\mathrm{wc}}}{1 - S_{\mathrm{wc}} - S_{\mathrm{gr}}} \right)^{n_{\mathrm{w}}}, \tag{7.3}$$

$$k_{\mathrm{rg}}(S_{\mathrm{w}}) = k^0_{\mathrm{rg}} \left(\frac{1 - S_{\mathrm{w}} - S_{\mathrm{gr}}}{1 - S_{\mathrm{wc}} - S_{\mathrm{gr}}} \right)^{n_{\mathrm{g}}}, \tag{7.4}$$

$$k^{\mathrm{f}}_{\mathrm{rg}}(S_{\mathrm{w}}) = \frac{k_{\mathrm{rg}}}{\mathrm{MRF}}. \tag{7.5}$$

Notice that k^0_{rw} and k^0_{rg} represent the end-point relative permeabilities; S_{wc} and S_{gr} denote the connate water and residual gas saturations. The reduction of gas mobility due to foam injection [4],

$$\mathrm{MRF} = 1 + \mathrm{FMMOB} \times \mathrm{FDRY} \times \prod_{i=1}^{6} \mathrm{F}_i, \tag{7.6}$$

assumes local equilibrium between the dynamics of creating and coalescing bubbles and follows an implicit texture model that can incorporate the effects of surfactant in water (F_1), the presence of oil (F_2 and F_5), the balance between viscous forces and surface tension forces (i.e., capillary number) (F_3 and F_4), the salinity of the brine (F_6) and the dry-out effects (FDRY). FMMOB defines the maximum gas mobility reduction. This work is focused on the suitability of the Peaceman equation to compute injectivity during foam injection, and therefore we shall use a simplified foam model. Thus, we take $\mathrm{F}_i = 1, i = 1, \ldots, 6$. The only remaining function, FDRY, is represented by default in Stars [4] as

$$\mathrm{FDRY} = 0.5 + \frac{\arctan\left[\mathrm{SFBET} \times (S_{\mathrm{w}} - \mathrm{SFDRY})\right]}{\pi}, \tag{7.7}$$

where SFBET indicates the abruptness of the dry-out effect, and SFDRY is a critical water saturation (below which foam collapses). The parameter SFDRY is considered constant in agreement

Figure 67 – Gas, water, and foamed gas relative permeabilities.

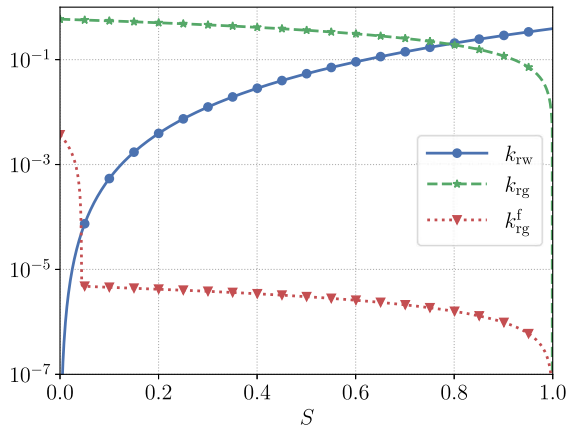

Source: Prepared by the author.

Figure 68 – Total fluid mobility with and without foam.

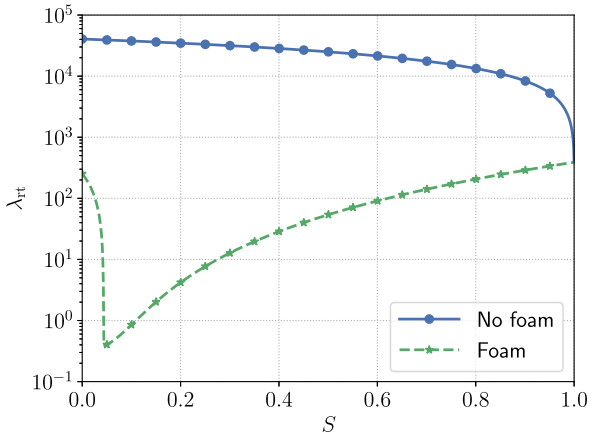

Source: Prepared by the author.

Table 9 – Parameter values for the foam flow in porous media based on data from [6] and [7] for Bentheimer sandstone.

Symbol	Value	Symbol	Value
S_{wc}	0.25 [-]	κ	1.9 darcy
S_{gr}	0.2 [-]	Q	2.5×10^{-4} m^3/s
k_{rw}^0	0.39 [-]	r_w	0.1 m
n_w	2.86 [-]	H	30 m
k_{rg}^0	0.59 [-]	h	36 m
n_g	0.70 [-]	FMMOB	120000 [-]
μ_w	10×10^{-3} Pa s	SFBET	10000 [-]
μ_g	$1.454{,}98 \times 10^{-5}$ Pa s	SFDRY	0.274 [-]
ϕ	0.24 [-]		

with the hypotheses of this work: the MRF does not depend on surfactant concentration, oil saturation, salinity, or flow rate. These expressions are functions of the water saturation S_w, which can be simplified by changing the variable to

$$S = \frac{S_w - S_{wc}}{1 - S_{wc} - S_{gr}}, \quad S \in [0, 1]. \tag{7.8}$$

The remaining parameters are listed in Table 9. The relative permeability and foam parameters were defined in [6] and [7] by adjusting the models to coreflood experiments on Bentheimer sandstone. A plot of the relative permeability curves (Eqs. (7.3) through (7.5)) is shown in Fig. 67. An illustration of the impact of foam on total mobility can be seen in Fig. 68.

The water saturation along the radius is the solution of the mass conservation equation

[91]

$$\phi \frac{\partial S_{\mathrm{w}}}{\partial t} + \frac{1}{r}\frac{\partial (r \mathbf{u}_{\mathrm{w}})}{\partial r} = 0, \tag{7.9}$$

where ϕ is the porosity of the grid block containing the injection well. We define dimensionless variables x_{D} and t_{D} to describe cylindrical flow with radial symmetry [42]:

$$x_{\mathrm{D}} = \frac{r^2 - r_{\mathrm{w}}^2}{r_{\mathrm{b}}^2 - r_{\mathrm{w}}^2}, \qquad t_{\mathrm{D}} = \frac{Qt\left(1 - S_{\mathrm{wc}} - S_{\mathrm{gr}}\right)^{-1}}{\pi H \phi \left(r_{\mathrm{b}}^2 - r_{\mathrm{w}}^2\right)}, \tag{7.10}$$

where r_{w} is the wellbore radius, and $r_{\mathrm{b}} = h/2$ is the block radius. Substituting Eqs. (7.1), (7.2), (7.8), and (7.10) into Eq. (7.9) yields

$$\frac{\partial S}{\partial t_{\mathrm{D}}} + \frac{\partial f_{\mathrm{w}}}{\partial x_{\mathrm{D}}} = 0. \tag{7.11}$$

To simulate the drainage of the well block we define the left (injection) state $J = S^- = 0$ and right (initial) state $I = S^+ = 1$.

7.2 Estimating Injectivity in a Grid Block

Let us describe how to estimate the injectivity, why the wrong injectivity estimates appear in simulations, and finally, how to circumvent this issue.

7.2.1 Peaceman Injectivity in a Grid Block

Following [64] and [127], the difference between the pressure in a well and in its block can be computed as

$$p_{\mathrm{w}} - P_{\mathrm{re}} = \frac{Q}{2\pi H \kappa \lambda} \ln \frac{r_{\mathrm{eq}}}{r_{\mathrm{w}}}, \tag{7.12}$$

where p_{w} is the well pressure, P_{re} is the pressure at the equivalent radius (which will also be the pressure in the well block, because the pressure is assumed piecewise constant), and r_{eq} is the equivalent radius, defined as

$$r_{\mathrm{eq}} = e^{-\pi/2} h. \tag{7.13}$$

The pressure drop estimate (Eq. (7.12)) is widely used in reservoir simulations. As it is based on the average saturation in the well block (and therefore, on a uniform λ), its application on coarse grids is limited to scenarios where the mobility of the fluid mixture does not change much near the well. Unfortunately, during foam injection, the total fluid mobility changes considerably (see Fig. 68), causing the pressure drop estimate given by Eq. (7.12) to be useless, as it often underestimates the injectivity of the well [42].

An alternative to the Peaceman model was presented by [42] providing a better injectivity estimate for the foam EOR processes. The idea is to drop the piecewise-constant hypothesis for

fluid phases' saturations (at least in the well block) and compute the pressure drop by integrating the ODE

$$\frac{\mathrm{d}P}{\mathrm{d}r} = \frac{-Q}{2\pi r H \kappa \lambda \left(S_{\mathrm{w}}(r)\right)}, \tag{7.14}$$

from r_{w} to r_{eq}. The water saturation profile is given by the solution of Eq. (7.11) using the Method of Characteristics as plotted in Fig. 69. The natural limitation of this approach is that it requires an analytical solution, which is not available for compressible foam flow in porous medium.

Figure 69 – Pressure drop in the injection well computed using Peaceman equation and Method of Characteristics (assuming incompressible phases), and Stars.

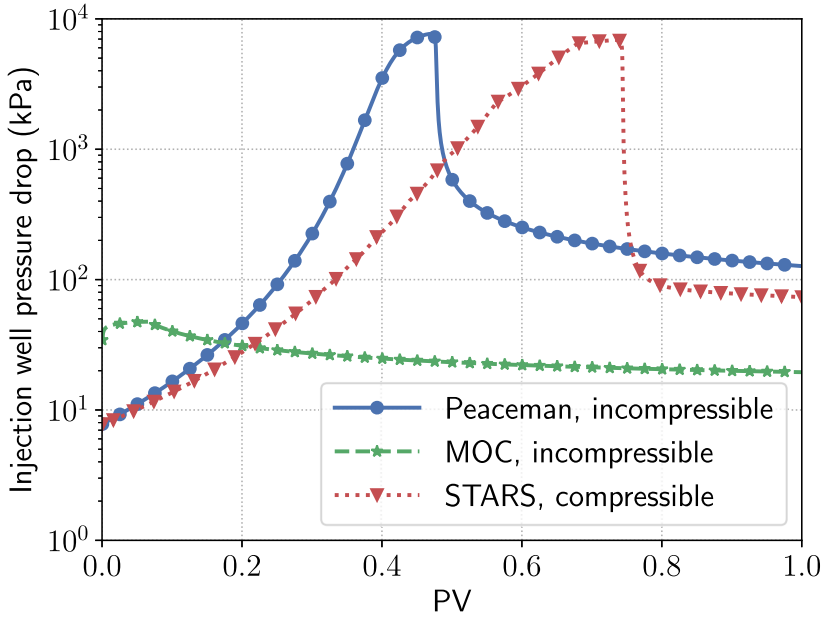

Source: Prepared by the author.

7.2.2 How Wrong Injectivity Estimates Appear in Numerical Simulators

Let us compare the pressure drop computed by using Eq. (7.14) with the one given by Eq. (7.12), where λ is dependent on the water saturation of a cylindrical well block, which is computed via the integration of the mass conservation equation

$$\frac{\mathrm{d}S_{\mathrm{w}}}{\mathrm{d}t} = -\frac{Q f_{\mathrm{w}}(S_{\mathrm{w}})}{H \pi r_{\mathrm{b}}^2 \phi}, \tag{7.15}$$

by a combination of an implicit Euler scheme and Newton's method. Fig. 69 shows these pressure drops and the one computed using Stars software for compressible fluids using parameter values listed in Table 9. As one can see, the large spatial variation in water saturation (therefore, in the total mobility) causes the hypothesis of piecewise constant mobility in the Peaceman model to be far from valid when foam alters the gas phase mobility.

The pressure drop computed assuming uniform mobility increases until the water saturation in the well block reaches the SFDRY value, at which point the maximum pressure drop is attained. As the gas injection continues, the pressure drop rapidly decays. Although the physics of this problem requires a higher pressure drop initially to maintain the flow rate (due to the mobility reduction caused by foam) and a subsequent decrease in the pressure drop (due to the destruction of the bubbles caused by the water saturation reaching the SFDRY value), the analytical solution developed using the Method of Characteristics indicates the Peaceman approach underestimates the injectivity most of the time, as can be seen in Fig. 69.

Notice that the simplifying hypothesis of incompressible phases (adopted to obtain the analytical solution) leads to a faster decrease in the water saturation of the well block, which in turn leads to an earlier increase in the pressure drop (after the injection of around 0.4 PV of gas) when compared to the pressure drop simulated in Stars (which reaches its maximum value after the injection of around 0.7 PV of gas). However, the pressure drop peak region and the overestimated behavior obtained by the Peaceman model in Stars remain.

In Fig. 70, we compare Peaceman and MOC-based approaches, varying the FMMOB and SFDRY parameters and fixing the other values of Table 9. In both cases, it is possible to observe that the Peaceman equation overestimates the pressure drop when compared to the MOC solution, even for the scenario with no foam (FMMOB $= 0$), a phenomenon also observed in other works, as commented by [42]. As shown in Fig. 70(a), the increase in the FMMOB parameter implies more significant differences between the pressure drops obtained using Peaceman and MOC, indicating that the error caused by the Peaceman equation is accentuated with the increase in the mobility reduction factor. On the other hand, the increase of SFDRY (presented in Fig. 70(b)) causes a reduction in the maximum pressure drop given by the Peaceman equation; this is due to the critical water saturation being reached earlier, causing the destruction of the bubbles and consequently an abrupt decrease in the pressure drop required to maintain the injection flow rate.

7.3 Circumventing Injectivity Issues in Stars Simulator

As observed previously, the use of the classical Peaceman well model [64] for reservoir simulation can lead to improper handling of the total mobility near the well and therefore resulting in an overestimation of the pressure drop (or equivalently the well BHP). This behavior is especially exacerbated when the well radius is much smaller than the well block itself, resulting in a poor estimate of the water saturation (and therefore, of the phase mobility) in the well block, a region that presents high saturation variation [42, 68]. For an injection well located within a coarse grid block, if the BHP is fixed, the injectivity is excessively low, and if the injection flow rate is imposed, the BHP can get extremely high [4]. Similarly, for producer wells the breakthrough time prediction cannot be adequately handled [4, 128, 129].

Figure 70 – Pressure drop in the injection well for various scenarios, obtained using the Peaceman equation and the MOC.

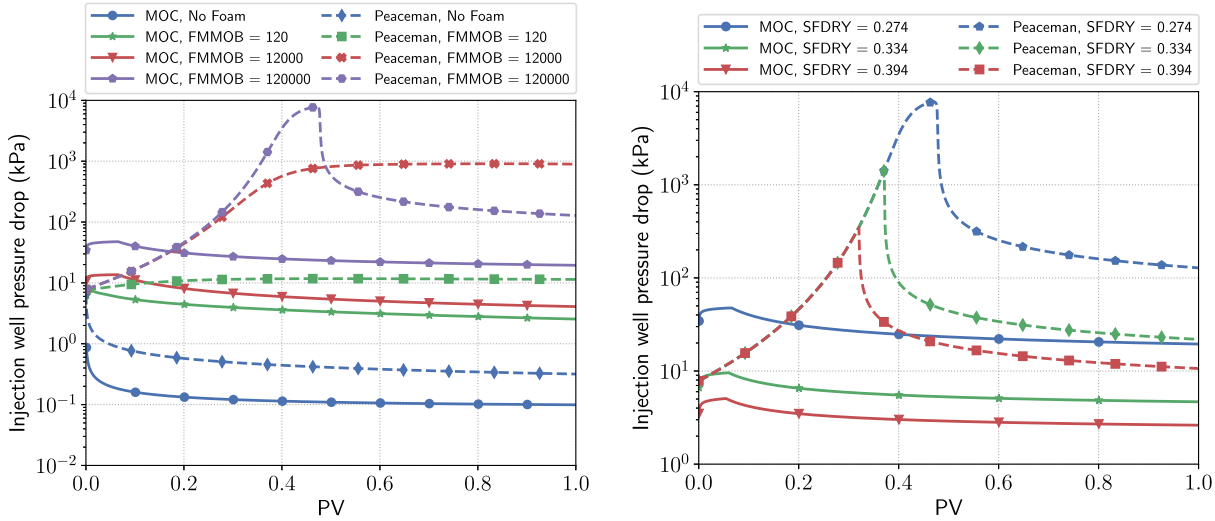

(a) Variation of the FMMOB parameter.

(b) Variation of the SFDRY parameter.

Source: Prepared by the author.

A local Cartesian well block grid partitioning technique was proposed in [123] and [124] improving well modeling for two-phase flow. This method defines a grid partitioning of the well region only, avoiding an excessive global grid refinement and reducing computational costs. A schematics of the local Cartesian grid partitioning can be seen in Fig. 71(a). The effect of the additional blocks on the computational costs, however, should not always be neglected. Also, a Cartesian grid partitioning does not match the radial geometry of the near-well flow [123].

Knowing that the accurate approximation of near-wellbore flow phenomena has a strong influence on the overall reservoir simulation, the hybrid grid concept was developed by [123] in order to match the need for an accurate and simple way to represent the two-phase flow in near-wellbore regions in reservoir simulators. In the hybrid grid approach, the entire reservoir is divided into well and reservoir regions, as shown in Fig. 71(b):

- *Well regions*. A cylindrical grid system is used in the region around the well within the Cartesian well block, allowing for a more rigorous treatment of the near-well radial flow effects and mitigating the overestimation problem in the Peaceman well model.
- *Reservoir region*. Far away from the wells, the flow geometry may be considered to be approximately linear. Therefore, a Cartesian grid is appropriate for this region.

We follow both Cartesian and hybrid methodologies to study how to circumvent the injectivity misestimate for the foam EOR.

Figure 71 – The two block grid treatment strategies studied in this work.

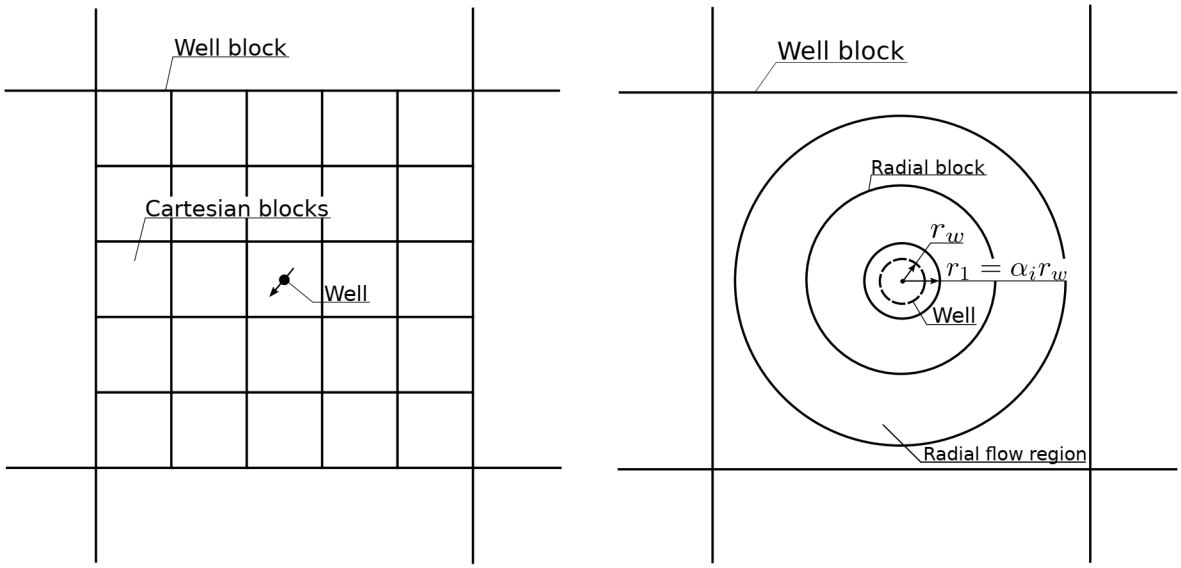

(a) Well block region with a Cartesian grid partitioning. (b) Well block region with a hybrid grid partitioning.

Source: Prepared by the author.

In Stars, the hybrid grid feature has several parameters; among them, we chose to analyze the following: the number of radial blocks, n_{rd}, the ratio between the first radial block radius (denoted as r_1) and the well radius [4],

$$r_1 = \alpha_{\mathrm{i}} r_{\mathrm{w}}, \tag{7.16}$$

as show in Fig. 71(b). In the next section, we show how to improve the well injectivity estimate by adjusting these parameters. Notice that changing the grid partitioning for the foam flow simulations changes the physics through Peaceman equation. That is why the effects of the grid refinement (see the next section) are not equivalent to the standard Numerical Analysis, where the physics is fixed.

7.3.1 Parameter Investigation Through Numerical Simulations

This section reports computational results based on a five-spot pattern obtained using the Stars simulator, version 2019.10. The production wells were located far enough apart, with a BHP of 1,000 kPa, so that no gas breakthrough would occur during the simulated period. The remaining parameters are the ones from Table 9. More details and the input file are in the supplementary material.

The Cartesian and hybrid strategies are used to produce two sequences of partitioned grids. The resulting injection well BHP for these grids is shown in Fig. 72. When a local (hybrid or Cartesian) grid partitioning strategy is applied, the average BHP required to maintain a fixed injection flow rate reduces significantly (Figs. 72(a) and 72(b)). Although even the most

Figure 72 – Evolution of the injection well BHP computed in Stars using several local grid partitions. The injected volume is measured with respect to the pore volume of the non-refined well block. (a) and (c): Hybrid grid partitioning; (b) and (d): Cartesian grid partitioning. Panels (c) and (d) are zoomed parts of the panels (a) and (b), respectively.

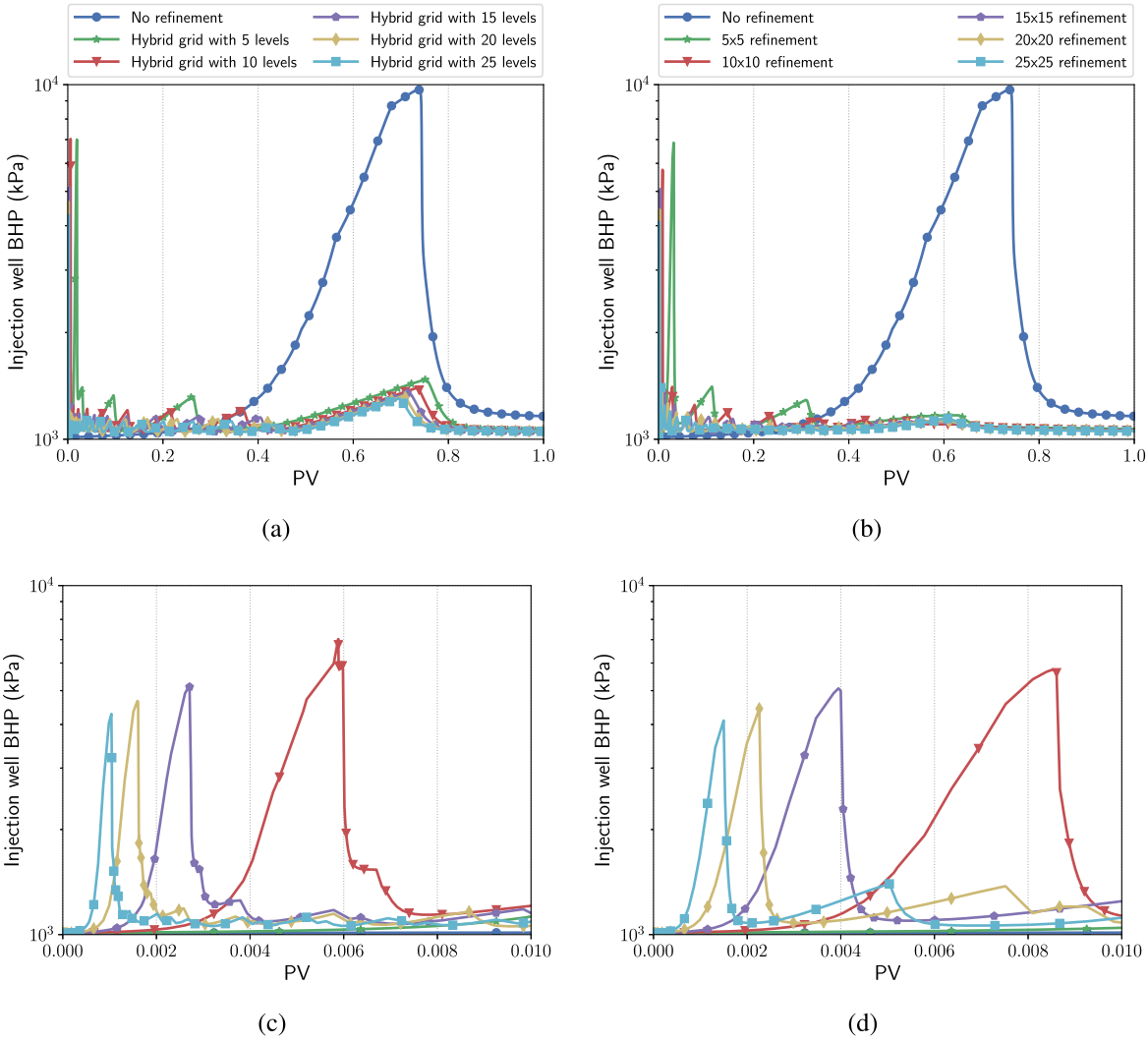

Source: Prepared by the author.

Figure 73 – The maximum injection well BHP is reduced with the well block grid partitioning.

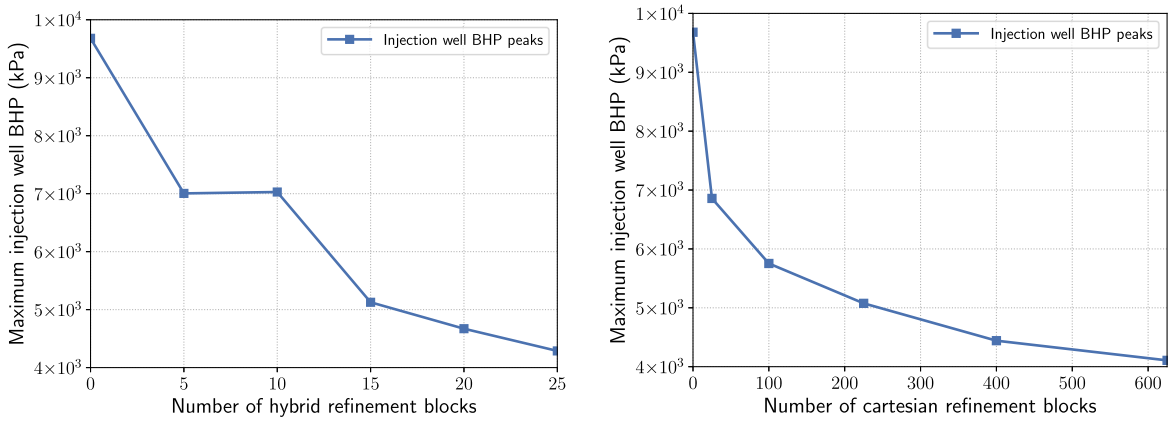

(a) Hybrid grid partitioning.

(b) Cartesian grid partitioning.

Source: Prepared by the author.

partitioned grids still present peaks in pressure (see the zoom in the peak regions in Figs. 72(c) and 72(d)), the maximum BHP clearly diminishes as the well block gets more partitioned, as shown in Fig. 73. Hence, it is expected that these peaks will vanish in an asymptotic successive grid partitioning.

In the hybrid grids, the radius of the first block is, by default, computed by Stars using relation [4]

$$r_1 = \frac{h}{(n_{\text{rd}} + 1)\sqrt{\pi}}. \tag{7.17}$$

In the most refined case ($n_{\text{rd}} = 25$), r_1 is approximately 0.781 m and, from Eq. (7.16), $\alpha_{\text{i}} \approx 7.81$.

We now show the results of a second study, in which we analyze the influence of α_{i} in the injectivity computation. In Fig. 74, the reference result ($\alpha_{\text{i}} \approx 7.81$) is compared with $\alpha_{\text{i}} = 2.0, 3.25, 4.5, 5.75, 7.0$, which generates the values $r_1 = 0.2\,\text{m}$, $0.325\,\text{m}$, $0.45\,\text{m}$, $0.575\,\text{m}$, $0.7\,\text{m}$ for the radius of the first block. The results show that the well BHP peaks get lower and narrower as α_{i} value reduces, i.e., as the grid partitioning becomes more concentrated near the well (see Fig. 75). The minimum value for the injection well BHP peak is $1{,}975\,\text{kPa}$, when $n_{\text{rd}} = 25$ and $\alpha_{\text{i}} = 2.0$.

7.4 Discussions

The approach studied in this work has advantages over the analytical methodology presented by [42]: (1) the analytical technique can compute only the well pressure drop, not being able to provide the well BHP (that is usually the desired quantity for well operation). Up to our knowledge, this limitation is due to the difficulties to obtain an analytical solution for the pressure equation; (2) Stars is based on a mathematical model that includes complex

Figure 74 – Evolution of the injection well BHP using several values of the parameter α_i. The injected volume is measured with respect to the pore volume of the non-refined well block. (a) Injection well BHP for several values of α_i; (b) Zoomed region of the injection well BHP for several values of α_i.

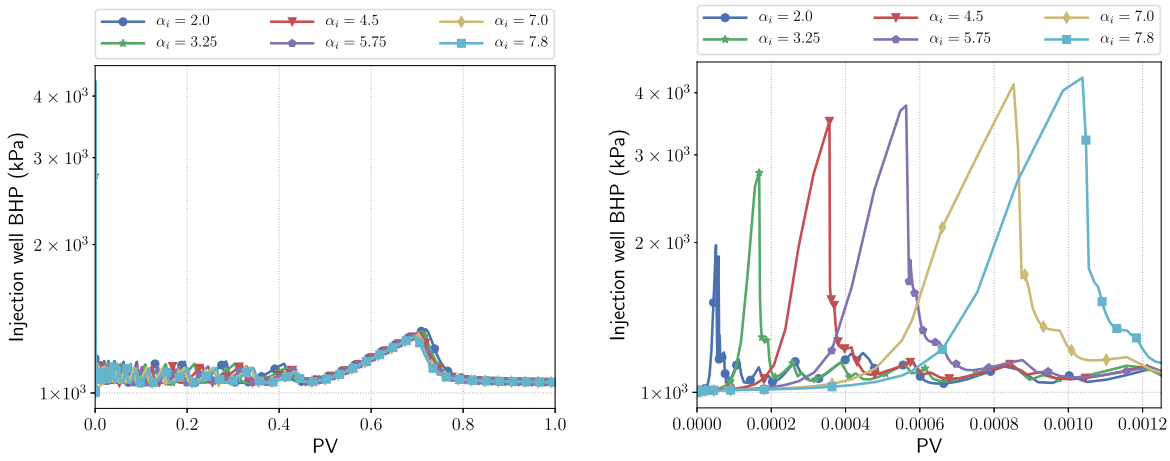

Source: Prepared by the author.

Figure 75 – Maximum injection well BHP for each α_i value.

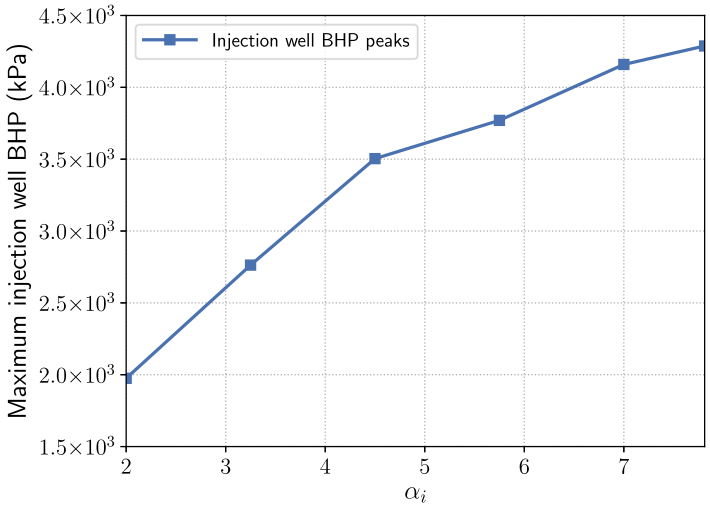

Source: Prepared by the author.

physical phenomena of multi-phase flow in porous media, such as compressibility, three-phase flow, and various EOR techniques; when the well block grid partitioning is applied in Stars, these phenomena are automatically taken into account. Analytical solutions are not available for these advanced model characteristics due to inherent difficulties that analytical methods, such as MOC, have when handling the equations.

On the other hand, the hybrid grid partitioning technique can have practical limitations:

- By manipulating the parameter α, that controls the ratio between the outer radius and the inner radius for the remaining annular blocks (*i.e.*, $\alpha = r_2/r_1 = r_3/r_2 = \dots$), it is possible to increase the number of block grid partitions beyond $n_{\text{rd}} = 25$. However, the number of grid partitions has a limit. It is not possible to indiscriminately partition because the computational cost increases, and numerical instabilities appear after a grid partitioning threshold.
- Although the maximum value of the BHP decreases as $r_1 \to r_{\text{w}}$, numerical instabilities arise in the interval $1 < \alpha_{\text{i}} < 2$. These instabilities increase the computational cost as Stars is forced to use smaller time steps in the simulation. The BHP peaks can also be affected by these instabilities, presenting higher values than when $\alpha_{\text{i}} \geq 2$, which is not consistent with our expectations.

In the results presented in this work, the parameter combination with the best output was $n_{\text{rd}} = 25$, $\alpha_{\text{i}} = 2.0$ and α computed by Stars using the relation [4]

$$\alpha = \left(\frac{h^2}{\pi r_1^2}\right)^{\frac{1}{2(n_{\text{rd}}-1)}}. \tag{7.18}$$

It is worth noticing that the outcome of using a specific parameter combination can strongly depend on the grid characteristics and the other simulation parameters. It can be inferred that the choice for moderate values of α_{i} and n_{rd}, combined with the default α calculation, leads to more promising results and reduced numerical instabilities.

Even though the numerical experiments using well block grid partitioning still present high BHP peaks, these peaks are expected to vanish in an asymptotic behavior. However, these high peaks can be used to estimate the deviations of the simulations results from the reality of field applications.

7.5 Preliminary Conclusions

The analysis by the Method of Characteristics shows the pressure drop computed using the Peaceman equation (implemented in STARS) can greatly misestimate the injectivity during foam injection. The leading causes of this issue are the simplifying Peaceman model assumptions, such as a uniform water saturation in the well block, associated with a coarse grid. In

order to circumvents this injectivity problem, well block grid treatment was adopted using the commercial software STARS, proving to be a viable and effective technique. Differently from other methodologies, the employed block well partitioning method (Cartesian or hybrid) does not change the input data nor the characteristics of the injectivity model of the STARS simulator. It applies a local grid partitioning only in the blocks that contain wells, without significant computational impact;

The results show that the well block grid partitioning, either Cartesian or hybrid, significantly improves the estimation of the injection well BHP needed to maintain a constant injection flow rate. The increase in well block grid partitioning, following both strategies, significantly reduces the BHP peaks. This reduction is especially accentuated with the hybrid grid associated with a thin first radial block. Moreover, The proper choice of parameters for the hybrid grid technique can improve the estimation of BHP. On the other hand, inadequate choices can increase computational costs and generate inaccurate estimates due to numerical instabilities.

8 CONCLUDING REMARKS

In this thesis, we presented a model for the foam flow in porous media. The complete model included physical phenomena such as capillary pressure, gas phase compressibility, gravity, foam transport, generation and coalescence, surfactant transport, and surfactant adsorption. Additionally, it was assumed that the porous medium is rigid and always fully saturated, the aqueous phase is incompressible, and the thermal effects are negligible. The resulting system of equations was rewritten based on the global pressure concept, leading to a fractional flow formulation. The main objective in using this approach was to weaken the coupling of the equations, especially the Darcy equation and transport equations. That modeling technique allowed us to rewrite the partial differential equations into conservation relations, which made it possible to split the mathematical problem into two subsystems of equations. Each sub-problem has specific mathematical properties and was approximated by suitable numerical methods.

Considering the mathematical nature of each sub-problem (hydrodynamics and transport), we approximated the Darcy problem employing a hybrid mixed finite element method and the transport equations using a high-order central-upwind finite volume method combined with the BDF method for time integration. From these choices, we proposed a sequential algorithm able to handle several complexities inherent to the mathematical model studied in this thesis, such as discontinuities, non-linearities, stiffness, and natural instabilities. This numerical method combination also preserves important properties, such as local mass conservation, shock capture, non-oscillatory solutions, and accurate approximations.

The sequential algorithm proposed proved to be robust, stable, and accurate. The central-upwind scheme (KNP) converged to the corrected solutions in all simulated problems, while the KT method failed to provide the expected solution, presenting spurious oscillations. It was also verified that the implicit time integration BDF scheme showed a significant reduction in computational cost compared to the Runge-Kutta method, usually adopted in the literature to advance in time hyperbolic equations.

Simulations using a two-dimensional, highly heterogeneous porous medium were conducted to investigate how foam can reduce viscous fingering and improve production. As viscous fingering can be potentialized in highly heterogeneous porous media, the results show an early gas breakthrough and poor sweep efficiency in the no-foam cases, especially due to the high gas mobility. On the other hand, when the foam is present in the flow, gas breakthrough can be significantly delayed. In this case, foam injection minimizes wavefront instabilities, reducing the fingering and maximizing the water displacement. In this context, the numerical results proved that the foam is an efficient EOR technique.

Numerical experiments using Newtonian and non-Newtonian models were performed in two-dimensional heterogeneous porous media to asses the foam influence in the gravitational flow. The results for the scenario without foam show an excessive gas gravitational segregation

in the higher parts of the reservoir, which can be potentialized in deep reservoirs. However, based on the models adopted, the results pointed out the remarkable foam's ability to reduce the gravitational effect and viscous fingering. Foam capability to actively mitigate gravity segregation is mainly due to gas mobility reduction. That way, foam usage can present several advantages in improving reservoir sweep efficiency, leading to higher production rates.

Comparisons between SAG and co-injection were conducted to investigate the injection strategy's influence on the foam flow. The numerical results, to a fixed amount of surfactant, demonstrated that the SAG technique presents higher water production when compared to the co-injection method. That behavior is mainly due to the greater surfactant penetration into preferential channels, which leads to higher foam generation and, consequently, higher gas mobility reduction. Moreover, it was observed that increasing surfactant concentration above a certain value in both SAG and co-injection is not advantageous. At a certain point, adding surfactant in the aqueous phase does not present a significant productivity improvement.

Numerical investigations developed considering surfactant adsorption show that this phenomenon can play an important role in foam injection in porous media. The adsorption effect is responsible for reducing the amount of surfactant in the aqueous phase, and consequently, foam generation is reduced, ultimately impacting production negatively. In fact, this phenomenon is an important aspect of the economic viability of foam flooding. From the parameters and model adopted, the production in the adsorption case is very similar to the no-foam case, showing that the adsorption directly affects the foaming capability to improve reservoir sweep efficiency. In addition, the SAG and co-injection comparisons demonstrated that the negative impact of the adsorption on water production does not depend on the injection strategy since both co-injection and SAG injection strategies are affected similarly. Moreover, in the simulations with adsorption, SAG presents better production results than co-injection.

The mathematical foam flow model adopted in this work contains six partial differential equations, one ordinary differential equation, and others constitutive relations. Over thirty parameters are needed to simulate the complete problem. As for now, to the best of the authors' knowledge, no published laboratory experiments or numerical simulations take into account the complete system described in Section 2.4. In that context, numerical experiments using the complete foam model are not presented, as no reported data can be used as parameters in the simulations.

Studies of the foam injectivity issues related to the Peaceman well model were conducted using the STARS simulator. The analysis by the Method of Characteristics shows the pressure drop computed using the Peaceman equation can greatly misestimate the injectivity during foam injection. The leading causes of this issue are the simplifying Peaceman model assumptions, such as a uniform water saturation in the well block, associated with a coarse grid. Aiming at mitigating this injectivity problem, well block grid treatments were adopted and investigated, using STARS. The results show that the well block grid partitioning, either Cartesian or hybrid,

significantly improves the estimation of the injection well BHP needed to maintain a constant injection flow rate. Also, as the well block grid partitioning increases, in the Cartesian or hybrid cases, the BHP peaks are significantly reduced. This reduction is especially pronounced when the hybrid grid is associated with a thin first radial block.

The results presented in this work demonstrate the efficiency of the mathematical and numerical models proposed to reproduce several scenarios of the two-phase flow in porous media, including foam displacement. FOSSIL was able to provide reliable and accurate solutions to all problems treated. Therefore, this thesis could better understand the foam flow in porous media and propose a more accurate and realistic simulation framework.

8.1 Academic Contributions

The main contributions of this thesis can be summarized in the following presentation and articles:

- "High order finite volume method to solve the two-phase flow with foam injection in porous media". 3rd br-Interpore Conference on Porous Media, Petrópolis, RJ, Aug 2019. Presented by F. F. DE PAULA.
- DE PAULA, F. F., QUINELATO, T., IGREJA, I., CHAPIRO, G., "A Numerical Algorithm to Solve the Two-Phase Flow in Porous Media Including Foam Displacement". In: *Lecture Notes in Computer Science*, v. 12143, pp. 18–31, 2020. https://doi.org/10.1007/978-3-030-50436-6_2
- QUINELATO, T. O., DE PAULA, F. F., IGREJA, I., LOZANO, L. F., CHAPIRO, G., "On the injectivity estimation in foam EOR", *Journal of Petroleum Exploration and Production Technology*, pp. 1–12, 2022. https://doi.org/10.1007/s13202-022-01474-5
- DE PAULA, F. F., IGREJA, I., QUINELATO, T., CHAPIRO, G., "A numerical investigation into the influence of the surfactant injection technique on the foam flow in heterogeneous porous media", *Advances in Water Resources*, pp. 104358, 2022. https://doi.org/10.1016/j.advwatres.2022.104358
- DE PAULA, F. F., IGREJA, I., QUINELATO, T., CHAPIRO, G., "Computational Simulation of foam displacement influenced by surfactant adsorption", *in preparation*, 2022.

8.2 Future Works

In order to extend the overall methodology proposed in this thesis, some future works can be pointed out:

- Numerical investigation of the three-phase (oil-gas-water) foam flow. The addition of the oil phase and its influence on the foam generation and coalescence mechanisms. Although the oil-foam interaction is not fully known, efforts can be made to include the oil phase in the foam flow simulation using existing studies.

- Injectivity estimation during foam EOR. The Peaceman equation, commonly applied to mathematical modeling of the injectivity in commercial simulators, can lead to errors of more than two orders of magnitude in the injection well pressure drop when the gas-water foam flow effects near the well are considered. Using the commercial software CMG-STARS, we circumvent this issue through numerical treatments focused on the grid of well blocks adopting local grid partitioning strategies improving the injection well bottom-hole pressure (BHP) estimation, as presented in Chapter 7 and published in [70]. In this sense, this approach can be extended to an oil-gas-water foam flow using FOSSIL and CMG-STARS.

- Higher-order approximations to solve the transport problem. By increasing the approximation order, the accuracy and precision of the solution are also increased. However, care must be taken with stability, which can be impaired when high-order approximations are adopted.

- Further studying and modeling the adsorption phenomenon can present a challenge in the foam flow simulation context, as studies that consider the effects of surfactant adsorption foam displacement are still scarce in the literature.

Bibliography

[1] "SPE Comparative Solution Project", `https://www.spe.org/web/csp/datasets/set02.htm`, Accessed: 2022-06-01.

[2] CHEN, Q., GERRITSEN, M., KOVSCEK, A. R., "Modeling foam displacement with the local-equilibrium approximation: theory and experimental verification", *SPE Journal*, v. 15, n. 01, pp. 171–183, 2010.

[3] SIMJOO, M., ZITHA, P. L. J., "Modeling of Foam Flow Using Stochastic Bubble Population Model and Experimental Validation", *Transport in Porous Media*, v. 107, n. 3, pp. 799–820, 2015.

[4] COMPUTER MODELING GROUP, *STARS user's guide, version 2019*, Calgary, Alberta, Canada, 2019.

[5] DING, L., GUERILLOT, D., "A Simplified Mechanistic Population Balance Model for Foam Enhanced Oil Recovery (EOR)". In: *ECMOR XVII*, v. 2020, pp. 1–19, 2020.

[6] KAPETAS, L., BONNIEU, S., FARAJZADEH, R., EFTEKHARI, A., SHAFIAN, S. M., BAHRIM, R. K., ROSSEN, W., "Effect of permeability on foam-model parameters: An integrated approach from core-flood experiments through to foam diversion calculations", *Colloids and Surfaces A: Physicochemical and Engineering Aspects*, v. 530, pp. 172–180, 2017.

[7] ROSSEN, W. R., BOEIJE, C. S., "Fitting Foam-Simulation-Model Parameters to Data: II. Surfactant-Alternating-Gas Foam Applications", *SPE Reservoir Evaluation & Engineering*, v. 18, n. 02, pp. 273–283, 2014.

[8] VALDEZ, A. R., ROCHA, B. M., DA FONSECA FAÇANHA, J. M., DE SOUZA, A. V. O., PÉREZ-GRAMATGES, A., CHAPIRO, G., DOS SANTOS, R. W., "Foam-Assisted Water–Gas Flow Parameters: From Core-Flood Experiment to Uncertainty Quantification and Sensitivity Analysis", *Transport in Porous Media*, pp. 1–21, 2021.

[9] JONES, S. A., GETROUW, N., VINCENT-BONNIEU, S., "Foam flow in a model porous medium: I. The effect of foam coarsening", *Soft Matter*, v. 14, pp. 3490–3496, 2018.

[10] STONE, H. L., "Vertical Conformance In An Alternating Water-Miscible Gas Flood". In: *SPE Annual Fall Technical Conference and Exhibition*, 1982.

[11] SHI, J., ROSSEN, W., "Improved surfactant-alternating-gas foam process to control gravity override". In: *SPE/DOE improved oil recovery symposium*, 1998.

[12] SHI, J. X., ROSSEN, W. R., "Simulation of gravity override in foam processes in porous media", *SPE Reservoir Evaluation & Engineering*, v. 1, n. 2, pp. 148–154, 1998.

[13] ROSSEN, W. R., SHEN, C., "Gravity segregation in gas-injection IOR". In: *EUROPEC/EAGE conference and exhibition*, 2007.

[14] SHOJAEI, M. J., KOFI, O.-B., PAUL, G., SHOKRI, N., "Foam Flow Investigation in 3D-Printed Porous Media: Fingering and Gravitational Effects", *Industrial & Engineering Chemistry Research*, v. 57, pp. 7275–7281, 2018.

[15] DE PAULA, F. F., QUINELATO, T., IGREJA, I., CHAPIRO, G., “A Numerical Algorithm to Solve the Two-Phase Flow in Porous Media Including Foam Displacement”. In: *Lecture Notes in Computer Science*, v. 12143, pp. 18–31, 2020.

[16] SKAUGE, A., SOLBAKKEN, J., ORMEHAUG, P. A., AARRA, M. G., “Foam generation, propagation and stability in porous medium”, *Transport in Porous Media*, v. 131, n. 1, pp. 5–21, 2020.

[17] HOMSY, G. M., “Viscous fingering in porous media”, *Annual review of fluid mechanics*, v. 19, n. 1, pp. 271–311, 1987.

[18] SINGH, B. K., AZAIEZ, J., “Numerical simulation of viscous fingering of shear-thinning fluids”, *The Canadian Journal of Chemical Engineering*, v. 79, n. 6, pp. 961–967, 2001.

[19] BOEIJE, C. S., ROSSEN, W. R., “Fitting foam-simulation-model parameters to data: I. coinjection of gas and liquid”, *SPE Reservoir Evaluation & Engineering*, v. 18, n. 02, pp. 264–272, 2015.

[20] FARAJZADEH, R., EFTEKHARI, A. A., HAJIBEYGI, H., KAHROBAEI, S., VAN DER MEER, J. M., VINCENT-BONNIEU, S., ROSSEN, W. R., “Simulation of instabilities and fingering in surfactant alternating gas (SAG) foam enhanced oil recovery”, *Journal of Natural Gas Science and Engineering*, v. 34, pp. 1191–1204, 2016.

[21] HEMATPUR, H., MAHMOOD, S. M., NASR, N. H., ELRAIES, K. A., “Foam flow in porous media: Concepts, models and challenges”, *Journal of Natural Gas Science and Engineering*, v. 53, pp. 163–180, 2018.

[22] LAKE, L., *Enhanced oil recovery*. Prentice Hall: New Jersey, 1989.

[23] BLAKER, T., CELIUS, H. K., LIE, T., MARTINSEN, H. A., RASMUSSEN, L., VASSENDEN, F., “Foam for gas mobility control in the Snorre field: the FAWAG project”. In: *SPE annual technical conference and exhibition*, 1999.

[24] SHAN, D., ROSSEN, W. R., “Optimal Injection Strategies for Foam IOR”, *SPE Journal*, v. 9, n. 2, pp. 132–150, 2004.

[25] KLOET, M., RENKEMA, W. J., ROSSEN, W. R., “Optimal design criteria for sag foam processes in heterogeneous reservoirs”. In: *EUROPEC/EAGE conference and exhibition*, 2009.

[26] SCHRAMM, L. L., *Foams: fundamentals and applications in the petroleum industry*. ACS Publications: Washington, 1994.

[27] HIRASAKI, G. J., MILLER, C. A., SZAFRANSKI, R., TANZIL, D., LAWSON, J. B., MEINARDUS, H., JIN, M., LONDERGAN, J. T., JACKSON, R. E., POPE, G. A., “Field demonstration of the surfactant/foam process for aquifer remediation”. In: *SPE Annual Technical Conference and Exhibition*, 1997.

[28] HIRASAKI, G. J., MILLER, C. A., SZAFRANSKI, R., LAWSON, J. B., AKIYA, N., “Surfactant/foam process for aquifer remediation”. In: *International symposium on oilfield chemistry*, 1997.

[29] PORTOIS, C., BOEIJE, C. S., BERTIN, H. J., ATTEIA, O., “Foam for environmental remediation: generation and blocking effect”, *Transport in Porous Media*, v. 124, n. 3, pp. 787–801, 2018.

[30] WANG, S., MULLIGAN, C. N., “An evaluation of surfactant foam technology in remediation of contaminated soil”, *Chemosphere*, v. 57, n. 9, pp. 1079–1089, 2004.

[31] SHOJAEI, M. J., OR, D., SHOKRI, N., “Localized Delivery of Liquid Fertilizer in Coarse-Textured Soils Using Foam as Carrier”, *Transport in Porous Media*, v. 143, n. 3, pp. 787–795, 2022.

[32] SÆLE, A., GRAUE, A., ALCORN, Z. P., “Unsteady-state CO_2 foam injection for increasing enhanced oil recovery and carbon storage potential”, *Advances in Geo-Energy Research*, v. 6, pp. 472–481, 2022.

[33] FARAJZADEH, R., ANDRIANOV, A., KRASTEV, R., HIRASAKI, G., ROSSEN, W. R., “Foam-oil interaction in porous media: Implications for foam assisted enhanced oil recovery”. In: *SPE EOR Conference at Oil and Gas West Asia*, 2012.

[34] KAM, S. I., “Improved mechanistic foam simulation with foam catastrophe theory”, *Colloids and Surfaces A: Physicochemical and Engineering Aspects*, v. 318, n. 1, pp. 62–77, 2008.

[35] SMITH, D. H., (ed), *Surfactant-Based Mobility Control*, n. 373, *ACS Symp. Ser.*, Washington, D.C., 1988, Am. Chem. Soc.

[36] HIRASAKI, G. J., “A Review of the Steam Foam Process Mechanisms”, 1989, Paper SPE 19518.

[37] HIRASAKI, G. J., “The Steam-Foam Process”, *Journal of Petroleum Technology*, v. 41, n. 5, pp. 449–456, 1989.

[38] MYERS, T. J., RADKE, C. J., “Transient Foam Displacement in the Presence of Residual Oil: Experiment and Simulation Using a Population-Balance Model”, *Industrial & Engineering Chemistry Research - IND ENG CHEM RES*, v. 39, pp. 2725–2741, 2000.

[39] MA, K., REN, G., MATEEN, K., MOREL, D., CORDELIER, P., “Modeling Techniques for Foam Flow in Porous Media”, *SPE Journal*, v. 20, n. 3, pp. 453–470, 2015.

[40] MA, K., MATEEN, K., REN, G., LUO, H., BOURDAROT, G., MOREL, D., “Mechanistic Modeling of Foam Flow Through Porous Media in the Presence of Oil: Review of Foam-Oil Interactions and an Improved Bubble Population-Balance Model”. In: *SPE Annual Technical Conference and Exhibition*, 2018.

[41] ASHOORI, E., MARCHESIN, D., ROSSEN, W. R., “Dynamic foam behavior in the entrance region of a porous medium”, *Colloids and Surfaces A: Physicochemical and Engineering Aspects*, v. 377, pp. 217–227, 2011.

[42] LEEFTINK, T. N., LATOOIJ, C. A., ROSSEN, W. R., “Injectivity errors in simulation of foam EOR”, *Journal of Petroleum Science and Engineering*, v. 126, pp. 26–34, 2015.

[43] ROSSEN, W. R., BOEIJE, C. S., “Fitting foam simulation model parameters for SAG foam applications”. In: *SPE Enhanced Oil Recovery Conference*, 2013.

[44] BEAR, J., *Modeling Phenomena of Flow and Transport in Porous Media. Theory and Applications of Transport in Porous Media*, Springer International Publishing, 2018.

[45] BEAR, J., CHENG, A. H.-D., *Modeling groundwater flow and contaminant transport*. v. 23. Springer, 2010.

[46] KALAM, S., ABU-KHAMSIN, S. A., KAMAL, M. S., PATIL, S., "A review on surfactant retention on rocks: mechanisms, measurements, and influencing factors", *Fuel*, v. 293, pp. 120459, 2021.

[47] FALLS, A. H., HIRASAKI, G. J., PATZEK, T. W., GAUGLITZ, D. A., MILLER, D. D., RATOULOWSKI, T., "Development of a Mechanistic Foam Simulator: The Population Balance and Generation by Snap-Off", *SPE Reservoir Engineering*, v. 3, pp. 884–892, 1988.

[48] KOVSCEK, A. R., RADKE, C. J., "Fundamentals of Foam Transport in Porous Media", chap. 3, pp. 115–163, *Advances in chemistry series*, American Chemical Society: Washington, DC, 1994.

[49] GAUGLITZ, P. A., FRIEDMANN, F., KAM, S. I., ROSSEN, W. R., "Foam generation in homogeneous porous media", *Chemical Engineering Science*, v. 57, n. 19, pp. 4037–4052, 2002.

[50] ASHOORI, E., MARCHESIN, D., ROSSEN, W. R., "Roles of transient and local equilibrium foam behavior in porous media: traveling wave." *Colloids and Surfaces A: Physicochemical and Engineering Aspects*, v. 377, pp. 228–242, 2011.

[51] KOVSCEK, A. R., PATZEK, T. W., RADKE, C. J., "Mechanistic prediction of foam displacement in multidimensions: A population balance approach". In: *SPE/DOE Improved Oil Recovery Symposium*, 1994.

[52] ZITHA, P. L. J., "A new stochastic bubble population model for foam in porous media". In: *SPE/DOE Symposium on Improved Oil Recovery*, 2006.

[53] HIRASAKI, G. J., LAWSON, J. B., "Mechanisms of foam flow in porous media: apparent viscosity in smooth capillaries", *SPE Journal*, v. 25, n. 02, pp. 176–190, 1985.

[54] PEREIRA, W. D. S., CHAPIRO, G., "Traveling wave solutions for non-Newtonian foam flow in porous media", *arXiv preprint arXiv:2209.15134*, 2022.

[55] KOVSCEK, A. R., PATZEK, T. W., RADKE, C. J., "A mechanistic population balance model for transient and steady-state foam flow in Boise sandstone", *Chemical Engineering Science*, v. 50, n. 23, pp. 3783–3799, 1995.

[56] ARONSON, A. S., BERGERON, V., FAGAN, M. E., RADKE, C. J., "The influence of disjoining pressure on foam stability and flow in porous media", *Colloids and Surfaces A: Physicochemical and Engineering Aspects*, v. 83, n. 2, pp. 109–120, 1994.

[57] FARAJZADEH, R., LOTFOLLAHI, M., EFTEKHARI, A., ROSSEN, W., HIRASAKI, G., "Effect of permeability on implicit-texture foam model parameters and the limiting capillary pressure", *Energy & fuels*, v. 29, n. 5, pp. 3011–3018, 2015.

[58] ROSSEN, W. R., VAN DUIJN, C. J., “Gravity segregation in steady-state horizontal flow in homogeneous reservoirs”, *Journal of Petroleum Science and Engineering*, v. 43, n. 1-2, pp. 99–111, 2004.

[59] KAM, S. I., NGUYEN, Q. P., LI, Q., ROSSEN, W. R., “Dynamic Simulations With an Improved Model for Foam Generation”, *SPE Journal*, v. 12, n. 1, pp. 35–48, 2007.

[60] ZITHA, P. L. J., DU, D. X., UIJTTENHOUT, M., NGUYEN, Q. P., “Numerical analysis of a new stochastic bubble population foam model”. In: *SPE/DOE Symposium on Improved oil recovery*, 2006.

[61] AFSHARPOOR, A., *Mechanistic foam modeling and simulations: gas injection during surfactant-alternating-gas processes using foam-catastrophe theory*, Ph.D. Thesis, Louisiana State University, 2009.

[62] ROSSEN, W. R., “Numerical Challenges in Foam Simulation: A Review”. In: *Proceedings - SPE Annual Technical Conference and Exhibition*, Society of Petroleum Engineers, 2013.

[63] MA, K., FARAJZADEH, R., LOPEZ-SALINAS, J. L., MILLER, C. A., BISWAL, S. L., HIRASAKI, G. J., “Non-uniqueness, Numerical Artifacts, and Parameter Sensitivity in Simulating Steady-State and Transient Foam Flow Through Porous Media”, *Transp. Porous Media*, v. 102, n. 3, pp. 325–348, 2014.

[64] PEACEMAN, D. W., “Interpretation of well-block pressures in numerical reservoir simulation (includes associated paper 6988)”, *Society of Petroleum Engineers Journal*, v. 18, n. 03, pp. 183–194, 1978.

[65] ROSSEN, W. R., “A critical review of Roof snap-off as a mechanism of steady-state foam generation in homogeneous porous media”, *Colloids and Surfaces A: Physicochemical and Engineering Aspects*, v. 225, n. 1, pp. 1–24, 2003.

[66] LI, Z., FORTENBERRY, R., LUO, H., DELSHAD, M., “An examination of the concept of apparent skin factor in modeling injectivity of non-Newtonian polymer solutions”, *Journal of Petroleum Science and Engineering*, v. 158, pp. 160–174, 2017.

[67] GONG, J., VINCENT-BONNIEU, S., KAMARUL BAHRIM, R. Z., CHE MAMAT, C. A., TEWARI, R. D., GROENENBOOM, J., FARAJZADEH, R., ROSSEN, W. R., “Modeling of Liquid Injectivity in Surfactant-Alternating-Gas Foam Enhanced Oil Recovery”, *SPE Journal*, v. 24, n. 03, pp. 1123–1138, 2019.

[68] GONG, J., FLORES MARTINEZ, W., VINCENT-BONNIEU, S., KAMARUL BAHRIM, R. Z., CHE MAMAT, C. A. N. B., TEWARI, R. D., MAHAMAD AMIR, M. I., FARAJZADEH, R., ROSSEN, W., “Effect of superficial velocity on liquid injectivity in SAG foam EOR. Part 2: Modelling”, *Fuel*, v. 279, pp. 118302, 2020.

[69] SOULAT, A., DOUARCHE, F., FLAURAUD, E., “A modified well index to account for shear-thinning behaviour in foam EOR simulation”, *Journal of Petroleum Science and Engineering*, v. 191, pp. 107146, 2020.

[70] QUINELATO, T. O., DE PAULA, F. F., IGREJA, I., LOZANO, L. F., CHAPIRO, G., “On the injectivity estimation in foam EOR”, *Journal of Petroleum Exploration and Production Technology*, pp. 1–12, 2022.

[71] DARIPA, P., DUTTA, S., “Modeling and simulation of surfactant–polymer flooding using a new hybrid method”, *Journal of Computational Physics*, v. 335, pp. 249–282, 2017.

[72] CHAVENT, G., JAFFRÉ, J., *Mathematical models and finite elements for reservoir simulation: single phase, multiphase and multicomponent flows through porous media*. v. 17. North-Holland: Amsterdam, 1986.

[73] CHEN, Z., EWING, R. E., “Fully discrete finite element analysis of multiphase flow in groundwater hydrology”, *SIAM J. Numer. Anal.*, v. 34, n. 6, pp. 2228–2253, 1997.

[74] BABUŠKA, I., “Error-bounds for finite element method”, *Numer. Math.*, v. 16, pp. 322–333, 1971.

[75] BREZZI, F., “On the existence, uniqueness and approximation of saddle-point problems arising from lagrangian multipliers”, *ESAIM: Math. Model. and Numer. Anal.*, v. 8, n. R2, pp. 129–151, 1974.

[76] RAVIART, P. A., THOMAS, J. M., “A mixed finite element method for 2-nd order elliptic problems”, v. 606, pp. 292–315, Springer, 1977.

[77] IGREJA, I. H. A., *Métodos de Elementos Finitos Híbridos Estabilizados para Escoamento de Stokes, Darcy e Darcy-Stokes Acoplados*, Ph.D. Thesis, LNCC, 2015.

[78] LEVEQUE, R. J., *Numerical Methods for Conservation Laws*. Birkhäuser Basel: Basel, 1990.

[79] LAX, P. D., “Weak solutions of nonlinear hyperbolic equations and their numerical computation”, *Communications on pure and applied mathematics*, v. 7, n. 1, pp. 159–193, 1954.

[80] NESSYAHU, H., TADMOR, E., “Non-oscillatory central differencing for hyperbolic conservation laws”, *Journal of Computational Physics*, v. 87, n. 2, pp. 408–463, 1990.

[81] KURGANOV, A., TADMOR, E., “New High-Resolution Central Schemes for Nonlinear Conservation Laws and Convection-Diffusion Equations”, *Journal of Computational Physics*, v. 160, n. 1, pp. 241–282, 2000.

[82] GODUNOV, S. K., “A difference method for numerical calculation of discontinuous solutions of the equations of hydrodynamics”, *Matematicheskii Sbornik*, v. 89, n. 3, pp. 271–306, 1959.

[83] KURGANOV, A., NOELLE, S., PETROVA, G., “Semidiscrete central-upwind schemes for hyperbolic conservation laws and Hamilton-Jacobi equations”, *SIAM Journal on Scientific Computing*, v. 23, n. 3, pp. 707–740, 2001.

[84] ARNOLD, D. N., BREZZI, F., “Mixed and nonconforming finite element methods: implementation, postprocessing and error estimates”, *ESAIM: Mathematical Modelling and Numerical Analysis-Modélisation Mathématique et Analyse Numérique*, v. 19, n. 1, pp. 7–32, 1985.

[85] HINDMARSH, A. C., BROWN, P. N., GRANT, K. E., LEE, S. L., SERBAN, R., SHUMAKER, D. E., WOODWARD, C. S., “SUNDIALS: Suite of nonlinear and differential/algebraic equation solvers”, *ACM Transactions on Mathematical Software (TOMS)*, v. 31, n. 3, pp. 363–396, 2005.

[86] ARNDT, D., BANGERTH, W., BLAIS, B., CLEVENGER, T. C., FEHLING, M., GRAYVER, A. V., HEISTER, T., HELTAI, L., KRONBICHLER, M., MAIER, M., MUNCH, P., PELTERET, J.-P., RASTAK, R., THOMAS, I., TURCKSIN, B., WANG, Z., WELLS, D., "The `deal.II` Library, Version 9.2", *Journal of Numerical Mathematics*, 2020, in press.

[87] DE PAULA, F. F., IGREJA, I., QUINELATO, T., CHAPIRO, G., "A numerical investigation into the influence of the surfactant injection technique on the foam flow in heterogeneous porous media", *Advances in Water Resources*, pp. 104358, 2022.

[88] CORREA, M. R., "A semi-discrete central scheme for incompressible multiphase flow in porous media in several space dimensions", *Mathematics and Computers in Simulation*, v. 140, pp. 24–52, 2017.

[89] CORREA, M. R., MURAD, M. A., "A new sequential method for three-phase immiscible flow in poroelastic media", *Journal of Computational Physics*, v. 373, pp. 493–532, 2018.

[90] BUCKLEY, S. E., LEVERETT, M. C., "Mechanism of Fluid Displacement in Sands", *Transactions of the AIME*, v. 146, 1942.

[91] CHEN, Z., HUAN, G., MA, Y., *Computational Methods for Multiphase Flows in Porous Media. Computational Science and Engineering*, Society for Industrial and Applied Mathematics, 2006.

[92] DARIPA, P., DUTTA, S., "On the convergence analysis of a hybrid numerical method for multicomponent transport in porous media", *Applied Numerical Mathematics*, v. 146, pp. 199–220, 2019.

[93] LANGMUIR, I., "Chemical Reactions at Low Pressures", *Journal of the American Chemical Society*, v. 37, n. 5, pp. 1139–1167, 1915.

[94] LANGMUIR, I., "The adsorption of gases on plane surfaces of glass, mica and platinum", *Journal of the American Chemical Society*, 1918.

[95] KAM, S. I., ROSSEN, W. R., "A model for foam generation in homogeneous media", *SPE Journal*, v. 8, n. 4, pp. 417–425, 2003.

[96] ZITHA, P. L. J., DU, D. X., "A New Stochastic Bubble Population Model for Foam Flow in Porous Media", *Transport in Porous Media*, v. 83, n. 3, pp. 603–621, 2010.

[97] KHATIB, Z. I., HIRASAKI, G. J., FALLS, A. H., "Effects of capillary pressure on coalescence and phase mobilities in foams flowing through porous media", *SPE Reservoir Engineering*, v. 3, n. 3, pp. 919–926, 1988.

[98] CURTISS, C. F., HIRSCHFELDER, J. O., "Integration of stiff equations", *Proceedings of the National Academy of Sciences of the United States of America*, v. 38, n. 3, pp. 235, 1952.

[99] BREZZI, F., DOUGLAS JR, J., MARINI, L. D., "Two families of mixed finite elements for second order elliptic problems", *Numerische Mathematik*, v. 47, n. 2, pp. 217–235, 1985.

[100] ARNOLD, D. N., "Mixed Finite Element Methods for Elliptic Problems", *Comput. Methods Appl. Mech. Eng.*, v. 82, n. 1–3, pp. 281–300, 1990.

[101] GUYAN, R. J., “Reduction of stiffness and mass matrices”, *AIAA journal*, v. 3, n. 2, pp. 380, 1965.

[102] BOFFI, D., BREZZI, F., FORTIN, M., *Mixed Finite Element Methods and Applications*. v. 44. *Springer Series in Computational Mathematics*, Springer: Berlin, Heidelberg, 2013.

[103] SAMII, A., MICHOSKI, C., DAWSON, C., “A parallel and adaptive hybridized discontinuous Galerkin method for anisotropic nonhomogeneous diffusion”, *Computer Methods in Applied Mechanics and Engineering*, v. 304, pp. 118–139, 2016.

[104] LEVEQUE, R. J., *Finite volume methods for hyperbolic problems*. Cambridge University Press, 2002.

[105] VAN LEER, B., “Towards the ultimate conservative difference scheme”, *Journal of Computational Physics*, v. 135, n. 2, pp. 229–248, 1997.

[106] AFSHARPOOR, A., LEE, G. S., KAM, S. I., “Mechanistic simulation of continuous gas injection period during surfactant-alternating-gas (SAG) processes using foam catastrophe theory”, *Chemical Engineering Science*, v. 65, n. 11, pp. 3615–3631, 2010.

[107] HINDMARSH, A. C., SERBAN, R., REYNOLDS, D. R., *CVODE user guide*, Tech. rep., Lawrence Livermore National Laboratory, 2019.

[108] DAVIS, T. A., “Algorithm 832: UMFPACK V4. 3—an unsymmetric-pattern multifrontal method”, *ACM Transactions on Mathematical Software (TOMS)*, v. 30, n. 2, pp. 196–199, 2004.

[109] DE CARVALHO TRISTÃO, D. S., *Esquemas centrais para leis de conservação em meios porosos*, Dissertação de mestrado, Programa de Pós-Graduação em Modelagem Computacional, Universidade Federal de Juiz de Fora, 2013.

[110] LOZANO, L. F., ZAVALA, R. Q., CHAPIRO, G., “Mathematical properties of the foam flow in porous media”, *Computational Geosciences*, v. 25, n. 1, pp. 515–527, 2021.

[111] SIMJOO, M., DONG, Y., ANDRIANOV, A., TALANANA, M., ZITHA, P. L. J., “Novel Insight into Foam Mobility Control”, *SPE Journal*, v. 18, n. 3, 2013.

[112] SIMJOO, M., ZITHA, P. L. J., “Modeling and Experimental Validation of Rheological Transition During Foam Flow in Porous Media”, *Transport in Porous Media*, v. 131, n. 1, pp. 315–332, 2020.

[113] AKIN, A., KOVSCEK, A. R., “Computed tomography in petroleum engineering research”, *Geological Society, London, Special Publications*, v. 215, n. 1, pp. 23–38, 2003.

[114] URUMOVIĆ, K., URUMOVIĆ SR., K., “The referential grain size and effective porosity in the Kozeny-Carman model”, *Hydrology and Earth System Sciences*, v. 20, n. 5, pp. 1669–1680, 2016.

[115] PEKSA, A. E., WOLF, K.-H. A. A., ZITHA, P. L. J., “Bentheimer sandstone revisited for experimental purposes”, *Marine and Petroleum Geology*, v. 67, pp. 701–719, 2015.

[116] SIMJOO, M., DONG, Y., ANDRIANOV, A., TALANANA, M., ZITHA, P. L. J., “CT Scan Study of Immiscible Foam Flow in Porous Media for Enhancing Oil Recovery”, *Industrial & Engineering Chemistry Research*, v. 52, n. 18, pp. 6221–6233, 2013.

[117] IZADI, M., KAM, S. I., “Investigating Supercritical CO2 Foam Propagation Distance: Conversion from Strong Foam to Weak Foam vs. Gravity Segregation”, *Transport in Porous Media*, v. 131, n. 1, pp. 223–250, 2020.

[118] DE PAULA, F. F., IGREJA, I., QUINELATO, T., CHAPIRO, G., “Computational Simulation of foam displacement influenced by surfactant adsorption”, *in preparation*, 2022.

[119] LOZANO, L. F., CEDRO, J. B., ZAVALA, R. Q., CHAPIRO, G., “How simplifying capillary effects can affect the traveling wave solution profiles of the foam flow in porous media”, *International Journal of Non-Linear Mechanics*, v. 139, pp. 103867, 2022.

[120] ZENG, Y., KAMARUL BAHRIM, R. Z., GROOT, J. A. W. M., VINCENT-BONNIEU, S., GROENENBOOM, J., MOHD SHAFIAN, S. R., ABDUL MANAP, A. A., TEWARI, R. D., MOHAMMADIAN, E., AZDARPOUR, A., HAMIDI, H., BISWAL, S. L., “Probing Methane Foam Transport in Heterogeneous Porous Media: An Experimental and Numerical Case Study of Permeability-Dependent Rheology and Fluid Diversion at Field Scale”, *SPE Journal*, v. 25, n. 04, pp. 1697–1710, 08 2020.

[121] TROGUS, F., SOPHANY, T., SCHECHTER, R., WADE, W., “Static and Dynamic Adsorption of Anionic and Nonionic Surfactants”, *Society of Petroleum Engineers Journal*, v. 17, n. 05, pp. 337–344, oct 1977.

[122] GASSARA, O., DOUARCHE, F., BRACONNIER, B., BOURBIAUX, B., “Equivalence between semi-empirical and population-balance foam models”, *Transport in Porous Media*, v. 120, n. 3, pp. 473–493, 2017.

[123] PEDROSA JR., O. A., AZIZ, K., “Use of a hybrid grid in reservoir simulation”, *SPE Reservoir Engineering*, v. 1, n. 06, pp. 611–621, 1986.

[124] VON ROSENBERG, D. U., “Local Mesh Refinement for Finite Difference Methods”. *SPE Annual Technical Conference and Exhibition*, 1982, SPE-10974-MS.

[125] AZIZ, K., “Reservoir Simulation Grids: Opportunities and Problems”, *Journal of Petroleum Technology*, v. 45, n. 07, pp. 658–663, 07 1993.

[126] DING, Y., RENARD, G., WEILL, L., “Representation of Wells in Numerical Reservoir Simulation”, *SPE Reservoir Evaluation & Engineering*, v. 1, n. 01, pp. 18–23, 02 1998.

[127] CHEN, Z., ZHANG, Y., “Well Flow Models for Various Numerical Methods”, *International Journal of Numerical Analysis and Modeling*, v. 6, n. 3, pp. 375–388, 2009.

[128] LETKEMAN, J. P., RIDINGS, R. L., “A numerical coning model”, *Society of Petroleum Engineers Journal*, v. 10, n. 04, pp. 418–424, 1970.

[129] MACDONALD, R. C., “Methods for numerical simulation of water and gas coning”, *Society of Petroleum Engineers Journal*, v. 10, n. 04, pp. 425–436, 1970.

[130] MOHAMED, I. M., NASR-EL-DIN, H. A., “Formation damage due to CO2 sequestration in deep saline carbonate aquifers”. In: *SPE International Symposium and Exhibition on Formation Damage Control*, 2012.

[131] PEACEMAN, D. W., “Interpretation of well-block pressures in numerical reservoir simulation with nonsquare grid blocks and anisotropic permeability”, *Society of Petroleum Engineers Journal*, v. 23, n. 03, pp. 531–543, 1983.

APPENDIX A – Core-Flood Experiments

A computational experiment was performed to assess the capability of the numerical simulator in reproducing experimental data such as pressure drop and accumulated water production. Two experiments were carried out in LASURF[1] and published in [8] for cores with different permeability: 2.7×10^{-13} m^2 for Core 1 and 1.57×10^{-13} m^2 for Core 2. The laboratory experiments were done under high-pressure (10 MPa) using nitrogen and low concentration of an alpha-olefin sulfonate surfactant in brine using Indiana limestone carbonate core (more details in [8]). Gas and surfactant solution were injected in several foam qualities (f_{g}) during a certain period of time, as show in Table 10.

An important data to fit the foam model parameters is the apparent viscosity (μ_{app}), that can be calculated using collected data from the experiment for each foam quality injection. The apparent viscosity can be computed using the following relation:

$$\mu_{\text{app}} = \frac{\kappa}{u}\frac{\Delta P_{\text{foam}}}{L}, \tag{A.1}$$

where ΔP_{foam} is the pressure drop, κ is the absolute permeability, u is the superficial injection velocity and L is core length. Table 11 show the calculated μ_{app}, using measured quantities, for each foam quality injection values.

For the numerical simulation, it was selected three foam flow models: the STARS model, the Linear Kinetic model and a more direct data driven model, called Simplified model, that uses the μ_{app} directly. Table 12 shows the parameters for the fitted STARS and Linear kinetic models by [8]. It is assumed that foam is in local equilibrium, the flow is incompressible, there is no gravity and adsorption. In order to write a mathematical formulation for the Simplified model, we start by rewriting the apparent viscosity in the following terms

$$\frac{1}{\mu_{app}} = \lambda = \lambda_{\text{w}} + \frac{\lambda_{\text{g}}}{MRF},$$

that can be manipulated to result in the following relation to gas mobility reduction:

$$MRF = \frac{\mu_g}{k_{rg}}\left(\frac{1}{\mu_{app}} - \frac{k_{rw}}{\mu_w}\right), \tag{A.2}$$

where MRF stand for mobility reduction factor, a function that alters the mobility of the gas phase in presence of foam. Equation (A.2) gives a constant fixed gas mobility reduction for each

[1] https://www.lasurf-rio.com

Table 10 – Foam quality injection times for Core 1 and Core 2.

	$f_{\text{g}} = 0.5$	$f_{\text{g}} = 0.6$	$f_{\text{g}} = 0.7$	$f_{\text{g}} = 0.75$	$f_{\text{g}} = 0.8$	$f_{\text{g}} = 0.9$
Core 1	10830 s	10521 s	7238 s	8019 s	10512 s	5095 s
Core 2	11004 s	12615 s	7192 s	–	7360 s	8912 s

Table 11 – Experimental data for core 1 and 2 of μ_{app}.

f_{g}	μ_{app} (Core 1)	μ_{app} (Core 2)
0.5	0.0604	0.0372
0.6	0.1065	0.0670
0.7	0.1153	0.0853
0.75	0.1190	–
0.8	0.1190	0.0750
0.9	0.0840	0.0481

Table 12 – Foam models parameters for the simulated core-flood experiments [8]

	STARS			Linear Kinetic		
	$fmmob$	$sfdry$	$sfbet$	C_{mrf}	S_{w}^{*}	A
Core 1	269.342055	0.43766393	787.457944	259.623772	0.43498737	228.363779
Core 2	214.745344	0.44684282	333.045338	197.011352	0.44313506	170.989138

Table 13 – Additional parameters for the simulated core-flood experiments.

Parameter	Value	Parameter	Value
Water Viscosity (μ_{w}) [Pa s]	5.0×10^{-4}	Core length [m]	0.15
Gas Viscosity $\left(\mu_{\text{g}}\right)$ [Pa s]	2.112×10^{-5}	Δt_{u} [s]	10.0
Initial water saturation (S_{w}^{0})	1.0	Number of cells	100
Initial foam texture (n_{D}^{0})	1.0	Minmod parameter (θ)	1.0
Max foam texture $(n_{\max})$ [m^{-3}]	8.0×10^{13}	Absolute tolerance	1.0×10^{-6}
Injection velocity $(\bar{u})$ [m s^{-1}]	1.45×10^{-5}	Relative tolerance	1.0×10^{-4}
Porosity (ϕ)	0.25	$\mathcal{RT}$ index (k)	0
Core diameter [m]	0.038,2		

foam quality injection time period. The permeability curves are of the form:

$$k_{\text{rw}} = k_{\text{rw}}^{0} \left(\frac{S_{\text{w}} - S_{\text{wc}}}{1 - S_{\text{wc}} - S_{\text{gr}}} \right)^{n_{\text{w}}},$$

$$k_{\text{rg}}^{0} = k_{\text{rg}}^{0} \left(\frac{1 - S_{\text{w}} - S_{\text{gr}}}{1 - S_{\text{wc}} - S_{\text{gr}}} \right)^{n_{\text{g}}},$$

where the values for $k_{\text{rw}}^{0} = 0.302, k_{\text{rg}}^{0} = 0.04, n_{\text{w}} = 2.98, n_{\text{g}} = 0.96, S_{\text{wc}} = 0.4$ and $S_{\text{gr}} = 0.293$ are taken after [130]. Other simulation parameters are listed in Table 13.

The numerical results for the STARS, Linear Kinetic and Simplified models plotted against the experimental data are show in Figures 76 and 77 for the Core 1 and Core 2, respec-

tively. Figure 76(c) shows an unusual drop in pressure drop experimental results due to a delay in replacing the gas cylinder. One can observe that the three adopted models' responses were very similar to each other for both core simulations. For the accumulated water, the results presented a good agreement with the experimental data (see Figures 76(a), 77(a), 76(b) and 77(b)), whereas for pressure drop some discrepancies with the numerical results for STARS and Linear Kinetic models at the low-quality regime ($f_{\mathrm{g}} = 0.5$ and $f_{\mathrm{g}} = 0.6$) are observed. The Simplified model was able to capture the pressure drop at low-quality foam regime much better than the other models due to the difficulty in fitting the model's parameters in that regime, what do not happens in the Simplified model, because it uses experimental data directly and do not need fitting.

Figure 76 – Experimental results plotted against simulated results for Core 1.

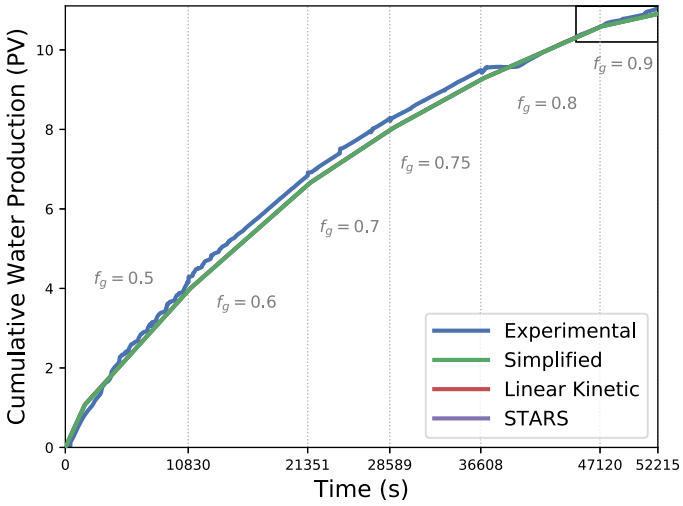

(a) Cumulative water production.

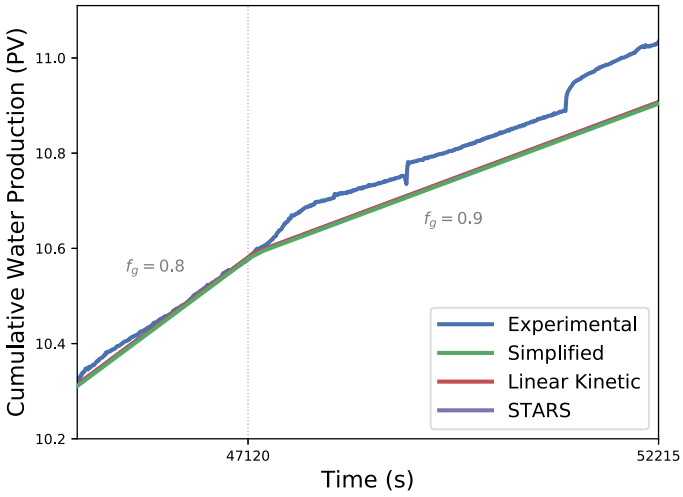

(b) Cumulative water production curve's zoom.

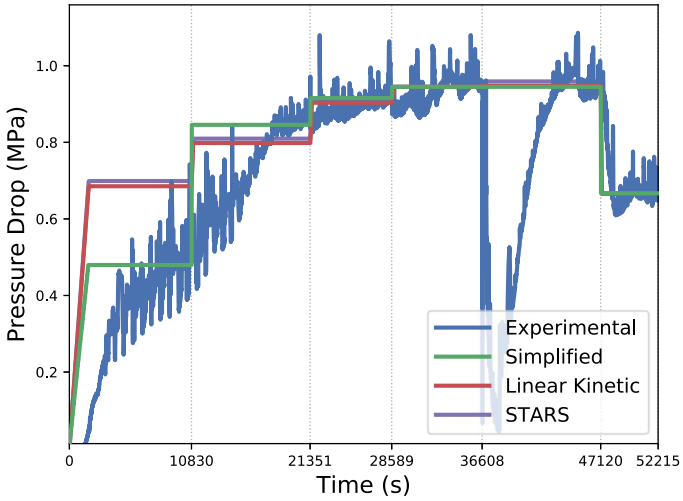

(c) Pressure drop throughout the core.

Source: Prepared by the author.

Figure 77 – Experimental results plotted against simulated results for Core 2.

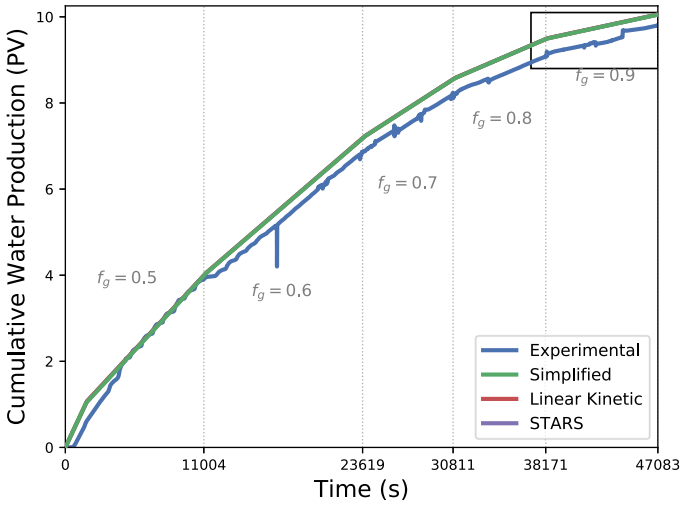

(a) Cumulative water production.

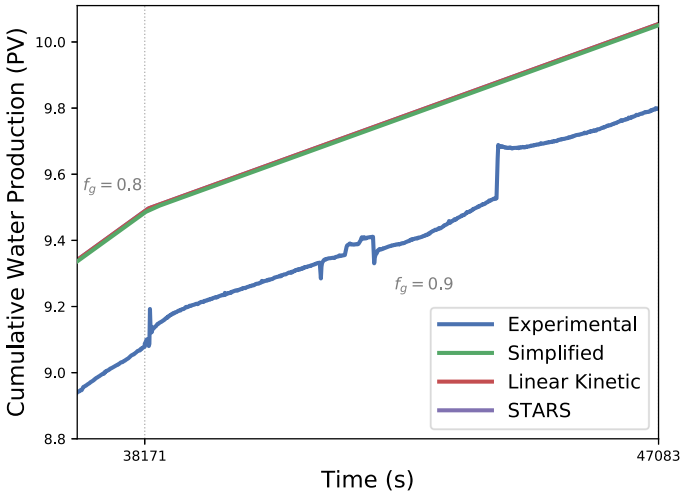

(b) Cumulative water production curve's zoom.

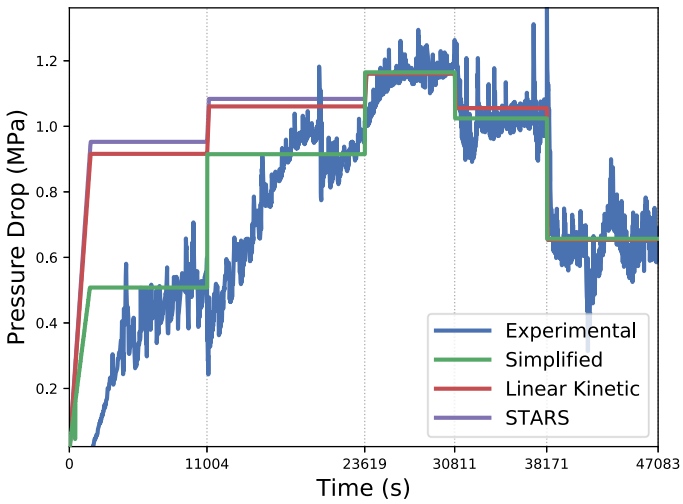

(c) Pressure drop throughout the core.

Source: Prepared by the author.

APPENDIX B – Well Modeling

The numerical implementation of injection and production wells is important for a more realistic characterization and simulation of fluid flow problems in reservoirs. In the numerical analysis, the reservoir must be spatially discretized, and inevitably the dimensions of any grid cell containing a well are much larger than the well bore radius of that well. The practical problem relate to that dimension discrepancy is that the region near the well, where pressure gradient is the largest, is much smaller than the cell size, leading to a non-negligible difference between the bottom hole pressure imposed in the well and the grid block pressure solution [64]. A local grid refinement around the well can mitigate the problem, but can elevate the computational simulation cost. In that context, it is necessary a correct modeling of fluid flow in the well bore.

In order to derive a vertical well flow equation, it is assumed that the flow is radial near the well [91]. Peaceman [64] presented the relation between well-block pressure and the flowing bottom hole pressure for a multi-phase flow as follow:

$$Q_\beta = \frac{2\pi h_z \rho_\beta \lambda_\beta W_{\text{frac}} \sqrt{\kappa_{xx}\kappa_{yy}}}{\ln\left(r_{eq}/r_w\right)} \left(p_{bh} - p\right), \quad \alpha = \{w,\ g\}, \tag{B.1}$$

where h_z is the reservoir thickness (or the height of the cell containing the well), κ_{xx}, κ_{yy} are the diagonal component of the permeability tensor $\mathbb{K}$, r_{eq} is the equivalent radius, r_w is the well radius, p_{bh} is the bottom hole pressure, Q_β is the well bore mass flow rate of fluid phase α and W_{frac} is the well fraction, that is related to the radial segment of the well in the grid block, for example $W_{\text{frac}} = 1$ for a well going approximately through the center of a grid block, 1/2 for a half well on a grid block boundary, and 1/4 for a quarter well at the corner of a grid block. [4]. Based on the methodology presented in [131, 4], the following relation gives the equivalent radius for a non-square grid and an anisotropic permeability tensor:

$$r_{eq} = \frac{CC}{\sqrt{W_{\text{frac}}\pi}} \frac{\left[\left(\kappa_{yy}/\kappa_{xx}\right)^{1/2} h_x^2 + \left(\kappa_{xx}/\kappa_{yy}\right)^{1/4} h_y^2\right]^{1/2}}{\left(\kappa_{yy}/\kappa_{xx}\right)^{1/4} + \left(\kappa_{xx}/\kappa_{yy}\right)^{1/4}}. \tag{B.2}$$

where CC is the geometric factor, that depends on the grid geometry of the well. Figure 78 shows several well geometric configurations and the respective CC and W_{frac} values.

Well constraints can be used to operate a well. There are two types of constraints: either the well bottom hole pressure p_{bh} is given, or a phase injection rate is fixed. In the former case, we have

$$p_{bh} = \bar{p}_{bh}, \tag{B.3}$$

where $\bar{p}_{bh}$ is a given bottom hole pressure at the well, and the phase mass flow rate is calculated using (B.1). In the case where the phase flow rate must be fixed, the Q_β value is given:

$$Q_\beta = \bar{Q}_\beta, \tag{B.4}$$

Figure 78 – Well fraction and geometrical factor for various common geometries.

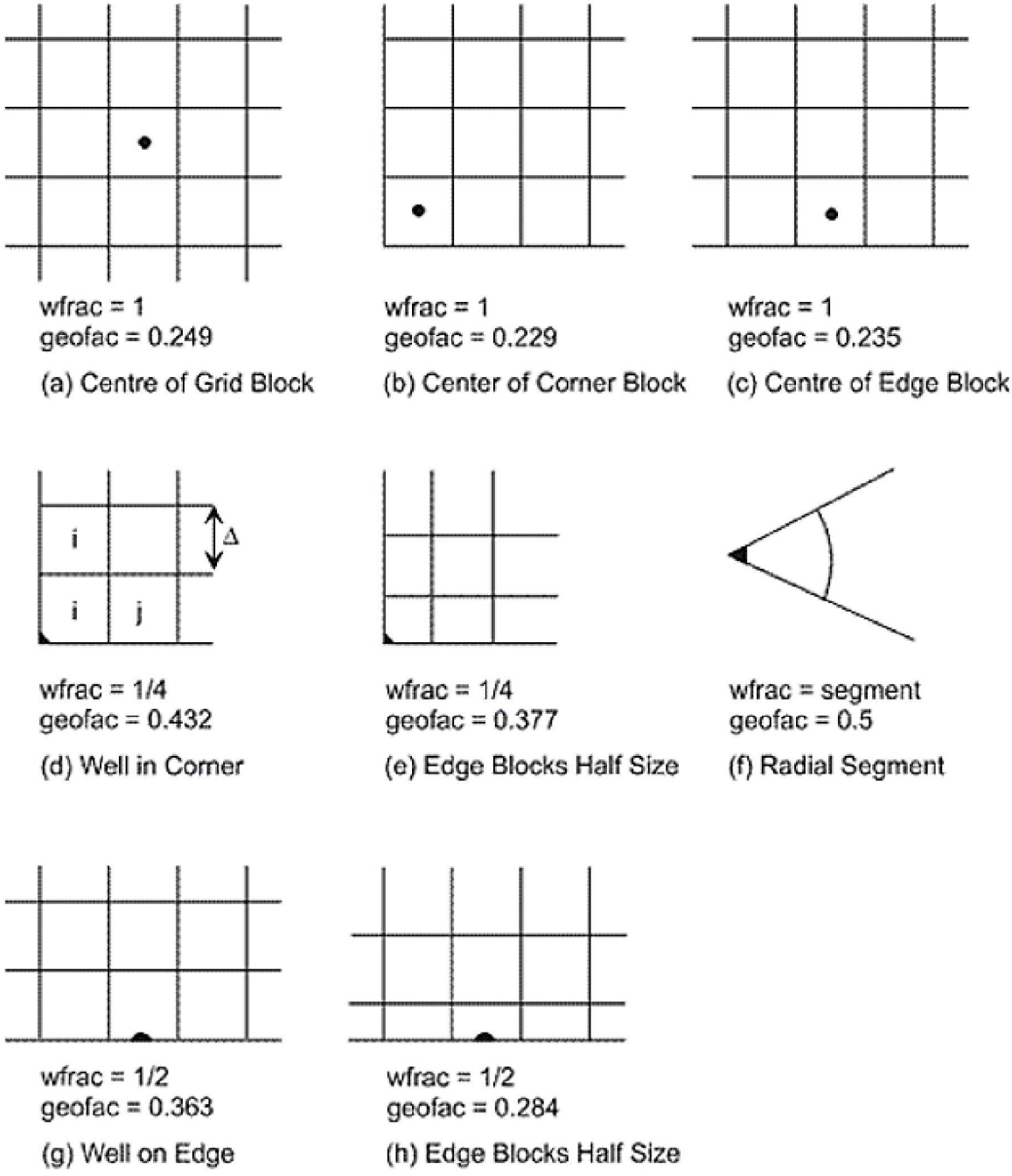

Source: [4].

where $\bar{Q}_\beta$ is a mass fixed flow rate for phase α. The bottom hole pressure is an unknown, that can be computed using relation (B.1).

There are two type of wells: injection and production wells. The injection type is used to flood the reservoir, and it is a source term in equation (2.32). The production wells extract the fluid from the porous medium, and it is a sink term in (2.32). Equation (B.1), can be used to

compute the values for the source/sink terms for relation (2.32) in the following way

$$q_\beta = \frac{Q_\beta}{\rho_\beta} \left(\prod_{i=x,y,z} 1/h_i \right). \tag{B.5}$$

APPENDIX C – Comparison Between FOSSIL and STARS Simulators

Simulation results obtained in FOSSIL and CMG-STARS are compared in this section. The objective is to compare the solutions in several scenarios, in order to assess FOSSIL's capability to reproduce the results of a commercial simulator, such as CMG-STARS [4]. The following test cases were selected:

1. Water injection in a water-saturated medium;
2. Gas injection in a gas-saturated medium;
3. Water injection in a gas-saturated medium;
4. Co-injection of water and gas at fixed BHP;
5. Foam injection at fixed BHP;
6. Co-injection of water and gas at constant flow rate;
7. Foam injection at constant flow rate.

Although some of these test cases represent simplified scenarios with little or no physical appeal, they are of utmost importance for the verification and validation of the simulators, for they would unveil the violation of basic physical requirements such as mass conservation, for instance.

Table 14 shows parameters that, unless otherwise indicated, are common in all simulations, for FOSSIL and CMG-STARS. The injection and production wells are located at the center of the first and last cells, respectively, as depicted in Figure 79.

Table 14 – Parameters used in the simulations.

Parameter	Value	Parameter	Value
Water viscosity [Pa s]	10×10^{-3}	Length [m]	0.3
Gas viscosity [Pa s]	1.455×10^{-5}	Height [m]	0.015
Water residual saturation	0.2	Block thickness [m]	1.0
Gas residual saturation	0.0	Final time [s]	1,140
Initial water saturation	1.0 or 0.2	Number of cells	20
Injection well BHP [kPa]	520	Well radius [m]	10×10^{-3}
Production well BHP [kPa]	500	Well fraction (wfrac)	1.0
Porosity	0.2	Well geometric factor (geofac)	0.229
Permeability [md]	100	Well skin factor (S)	0.0

Figure 79 – Injection and production wells in the simulation grid.

Source: Prepared by the author.

Figure 80 – Water production rate when water is injected in a water-saturated medium.

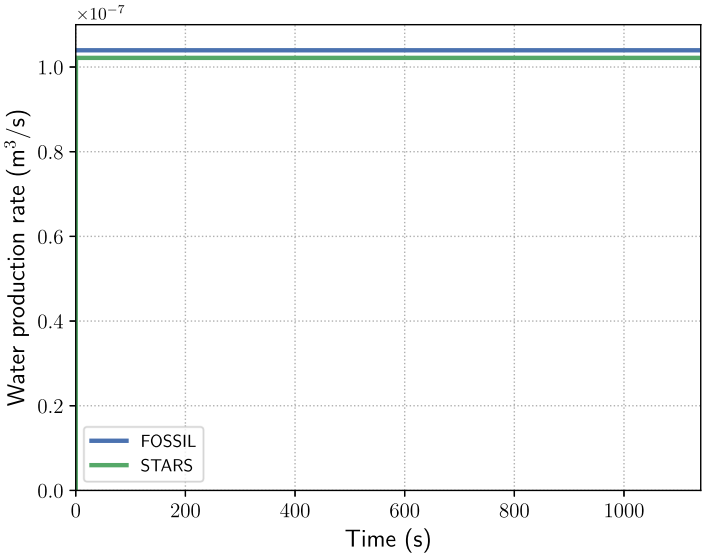

Source: Prepared by the author.

C.1 Water Injection in A Water-saturated Medium

In this experiment, water is injected in a water-saturated medium. Pressure and water production are the quantities that are compared using the in-house and commercial simulators.

The water production rate is shown in Figure 80. The pressure profile after 1,140 s is shown in Figure 81. We can see that the results computed by FOSSIL and STARS are very close, showing the FOSSIL's capability to reproduce the behavior of a commercial simulator in this simple case.

C.2 Gas Injection In A Gas-saturated Medium

In order to verify whether FOSSIL is able to handle gas flow, we simulate the injection of gas in a gas-saturated medium[1]. The gas phase is considered to be compressible, with

[1] Water saturation initial value is set at $S_{wc} = 0.2$, which in this case is equivalent to a gas-saturated medium, since the water is immobile.

Figure 81 – Pressure profile after 1,140 s of water injection in a water-saturated medium.

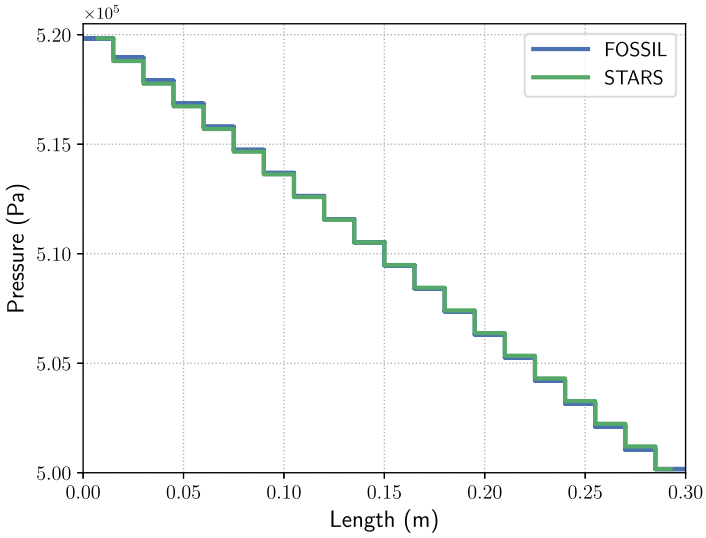

Source: Prepared by the author.

Figure 82 – Gas production rate when gas is injected in a gas-saturated porous medium.

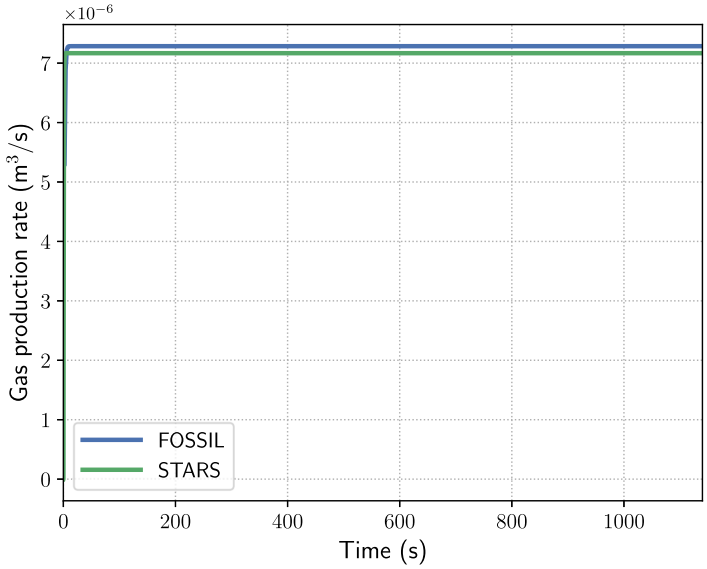

Source: Prepared by the author.

pressure-dependent mass density ρ_g given by:

$$\rho_g(p) = \rho_{ref}\frac{p}{p_{ref}}, \tag{C.1}$$

where $\rho_{ref} = 5.66$ kg/m^3 is a reference mass density, when $p = p_{ref}$ = 500 kPa.

In this simulation scenario, FOSSIL was able to reproduce the compressible behavior of the gas and match the results computed by STARS, as can be seen in Figure 82, which compares the gas production rates, and in Figure 83, which shows the pressure and gas density profiles after 1,140 s of gas injection.

Figure 83 – Profiles of pressure and gas density after 1,140 s of gas injection in a gas-saturated porous medium.

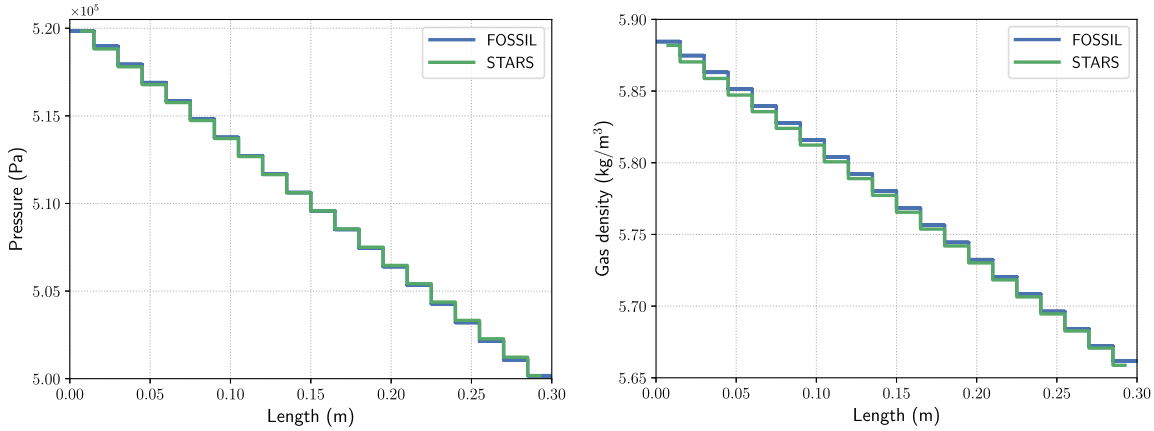

(a) Pressure. (b) Gas density.

Source: Prepared by the author.

Figure 84 – Profiles of water saturation and pressure after 1,140 s of water injection in a gas-saturated medium.

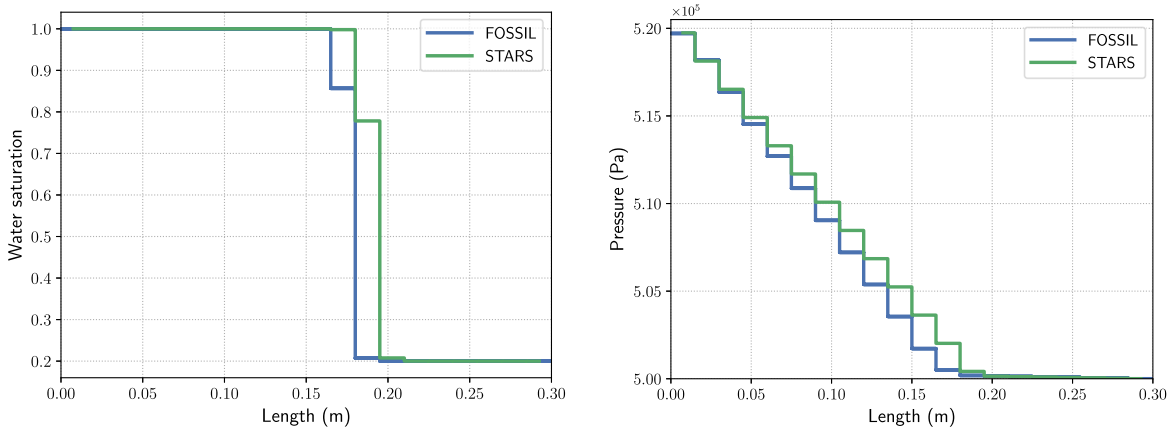

(a) Water saturation. (b) Pressure.

Source: Prepared by the author.

C.3 Water Injection In A Gas-saturated Medium

When water is injected in a gas-saturated medium, due to the viscosity difference it is to be expected the appearance of a shock wave front dividing the water-saturated zone from the gas-saturated zone. Indeed, this is the observed behavior after 1,140 s of water injection, both in FOSSIL and CMG-STARS, as shown in Figure 84(a). Two regions can be clearly seen in the pressure profile shown in Figure 84(b): a region with higher pressure drop (the water-saturated region, between the injection well and approximately 0.2 m), and a region with lower pressure drop (the gas-saturated region, from the shock front to the production well); the difference in

Figure 85 – Results of the simulation of water injection in a gas-saturated medium.

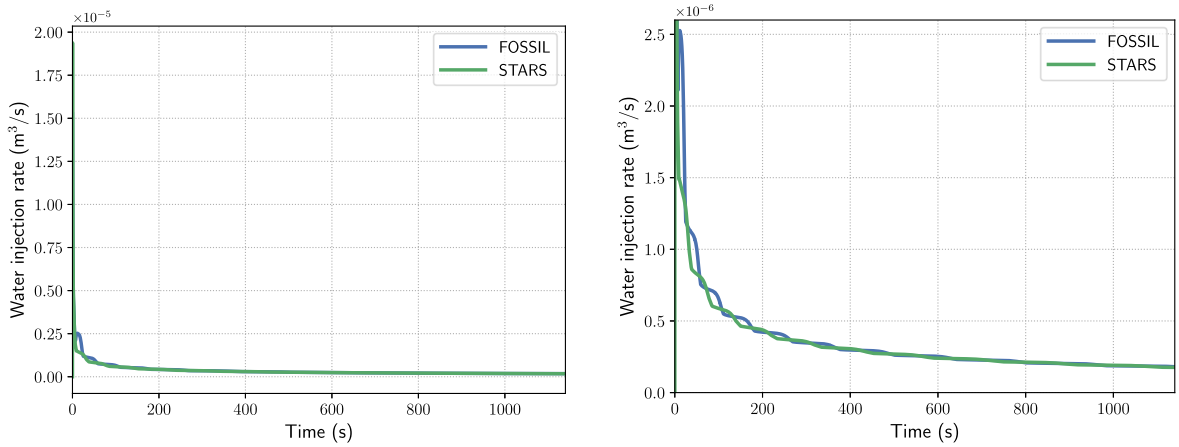

(a) Water injection rate.

(b) Zoom in the water injection rate.

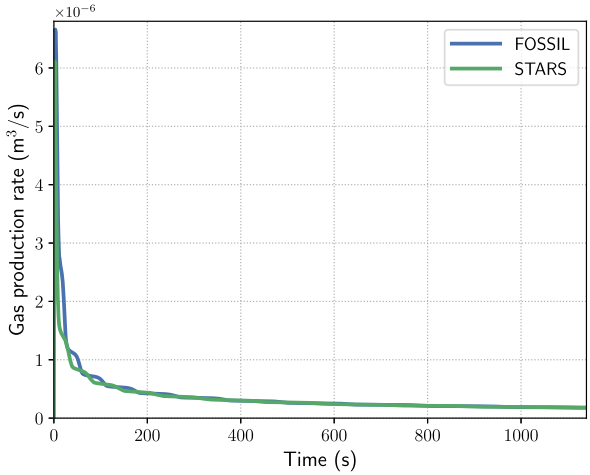

(c) Gas production rate.

Source: Prepared by the author.

pressure drop is explained by the total mobility of the fluid mixture in these regions: in the entrance region the total mobility coincides with the mobility of water phase, which is lower than the total mobility in the final region (which coincides with the mobility of the gas phase). Figure 85 shows a good agreement between the evolution of water and gas production rates computed with FOSSIL and STARS.

C.4 Co-injection of Water and Gas at Fixed BHP

When the co-injection technique is used, water and gas are injected simultaneously in the porous medium. In this scenario, a water-gas mixture with a volume fraction of 90% of gas and 10% of water is injected in a water-saturated medium.

The profiles of water saturation and pressure after 1,140 s of co-injection of water and gas

Figure 86 – Profiles of water saturation and pressure after 1,140 s of co-injection of water and gas at fixed BHP in a water-saturated medium.

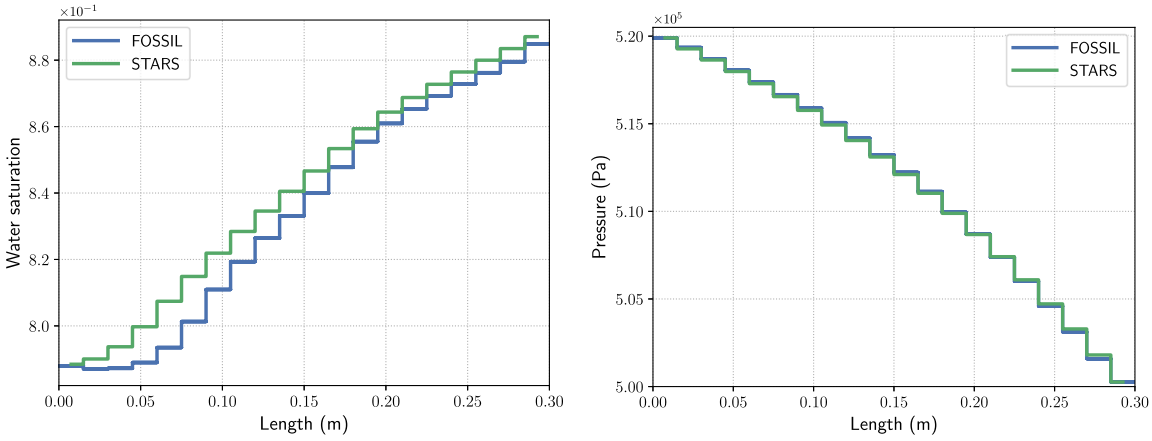

(a) Water saturation. (b) Pressure.

Source: Prepared by the author.

Figure 87 – Evolution of water and gas production rates during co-injection of water and gas at fixed BHP in a water-saturated medium.

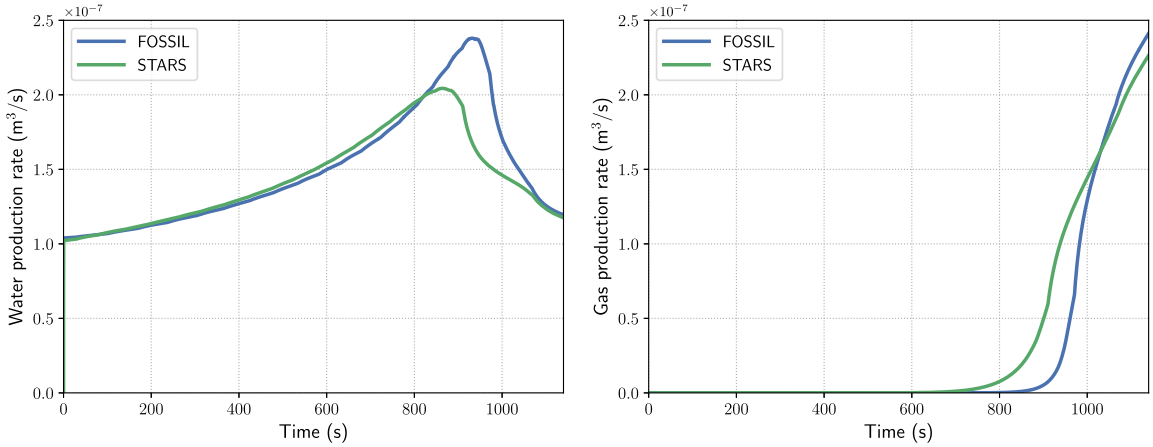

(a) Water production rate. (b) Gas production rate.

Source: Prepared by the author.

Table 15 – Parameters used in the grid refinement study.

Parameter	Value
Number of cells	100, 200, 300 and 500
Well radius [m]	0.0015
Well fraction (wfrac)	0.5
Well geometric factor (geofac)	0.175

Table 16 – Parameters of the foam model used in the simulations.

Parameter	Value
fmmob	500
sfbet	300
sfdry	0.3

are shown in Figure 86. Although the profiles of the pressure simulated by FOSSIL and STARS (Fig. 86(b)) show a very good match, this is not the case for the water saturation (Fig. 86(a)). Some discrepancy can also be observed between the water saturation profiles and the evolution of water and gas production rates (Fig. 87). A deeper investigation (described in the next section) was done to try to understand the difference in simulation results.

C.4.1 Grid Refinement Study

A possible explanation for the difference of the solutions in Figures 86(a), 87(a) and 87(b) is the difference in the numerical method used by each simulator. It is expected, however, that the solutions should converge to the each other if a mesh fine enough is used. Therefore, a grid refinement study was done to analyze the impact of using different numerical methods. The reference result, obtained in FOSSIL using a mesh with 100 cells, was compared with the simulation results computed by STARS for several grid sizes (shown in Table 15). The injection and production wells were moved to the center of the left and right boundaries, respectively, to maintain the compatibility between all problems. The modified parameters are also shown in Table 15. The well radii are a little bigger to account for the well fraction (wfrac = 0.5).

Figures 88 and 89 show the results of the co-injection problem described previously for several grid sizes. It is clear from the results that as the meshes in STARS get more refined, the solution tends to the FOSSIL reference solution. These results indicate that FOSSIL delivers more accurate solutions using fewer cells than STARS.

Figure 88 – Evolution of water and gas production rates during the co-injection of water and gas in a water-saturated porous medium using FOSSIL (100 cells) and STARS (100, 200, 300, and 500 cells).

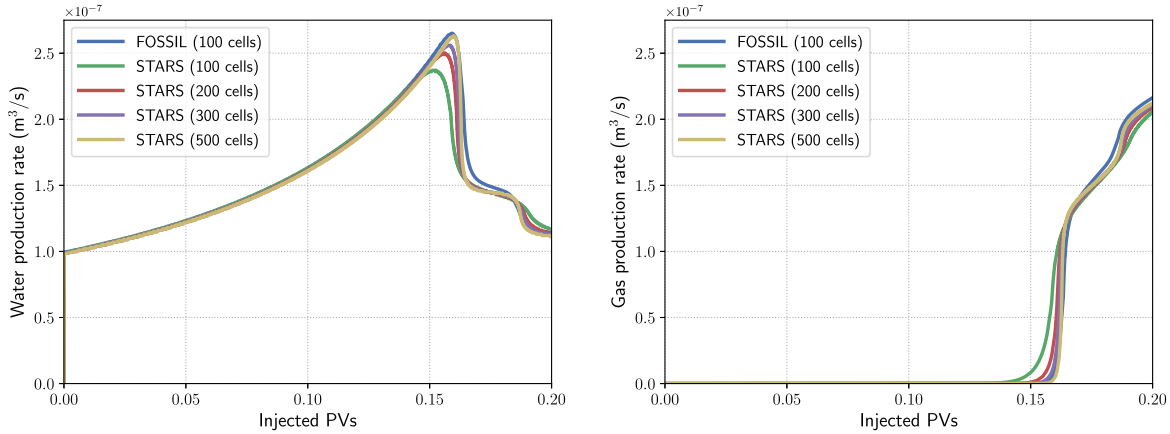

(a) Water production rate.

(b) Gas production rate.

Source: Prepared by the author.

Figure 89 – Profiles of water saturation and pressure after 1,140 s of co-injection of water and gas in a water-saturated porous medium using FOSSIL (100 cells) and STARS (several grid sizes).

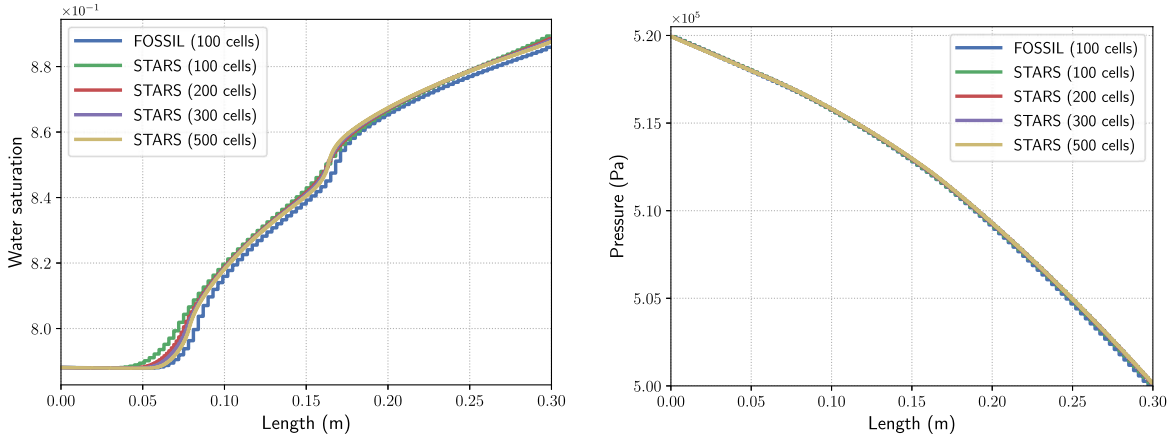

(a) Water saturation.

(b) Pressure.

Source: Prepared by the author.

Figure 90 – Evolution of injection and production rates when foam is injected at fixed BHP in a water-saturated porous medium.

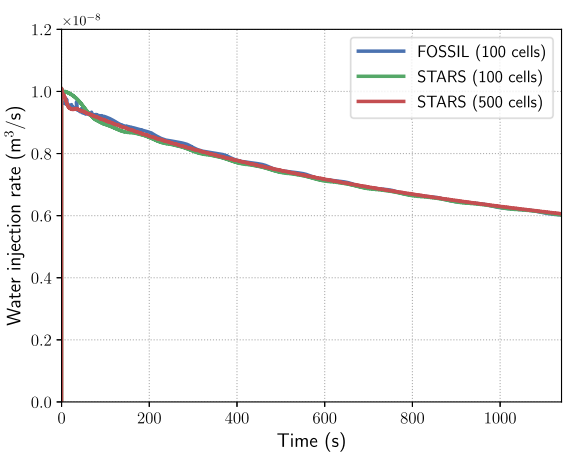

(a) Water injection rate.

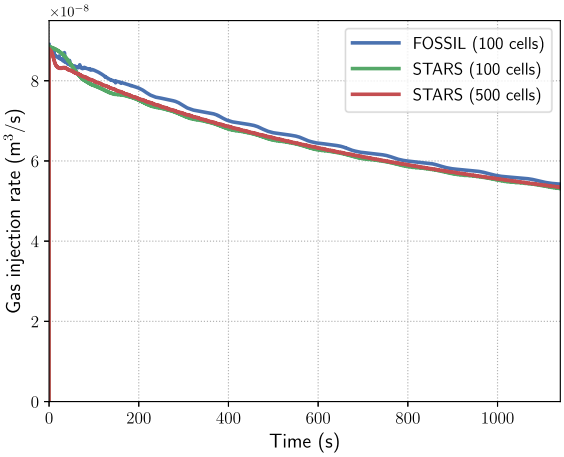

(b) Gas injection rate.

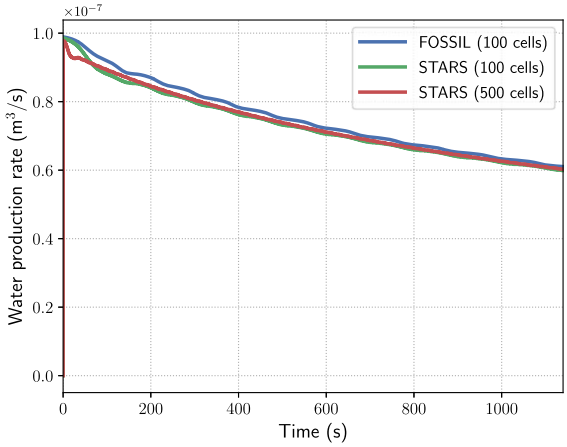

(c) Water production rate.

Source: Prepared by the author.

C.5 Foam Injection at Fixed BHP in a Water-saturated Medium

In order to reduce gas mobility, foam is used in the injection process. The parameters used in the simulations are shown in Table 14 and some modifications are in Table 15. The foam model adopted was the one from STARS simulator (2.42)–(2.44) that is an implicit (local equilibrium) model. Only the dry-out behavior was considered in the foam model. The foam model parameters are shown in Table 16.

The results of the simulations are shown in Figures 90 and 91. In this case, the results show that the discrepancy between the solutions computed using FOSSIL and STARS are not pronounced and, even for a grid of 100 cells, the results are quite similar. Another interesting conclusion is that gas and water rates (both production and injection) are reduced when foam is present (Figure 88(a)). This fact is mainly due to the reduction of gas mobility and since the

Figure 91 – Profiles of water saturation and pressure after 1,140 s of foam injection at fixed BHP in a water-saturated porous medium. Notice the good agreement between the solution computed using 100 cells in FOSSIL and the solutions computed by STARS using two different grid sizes (100 and 500 cells).

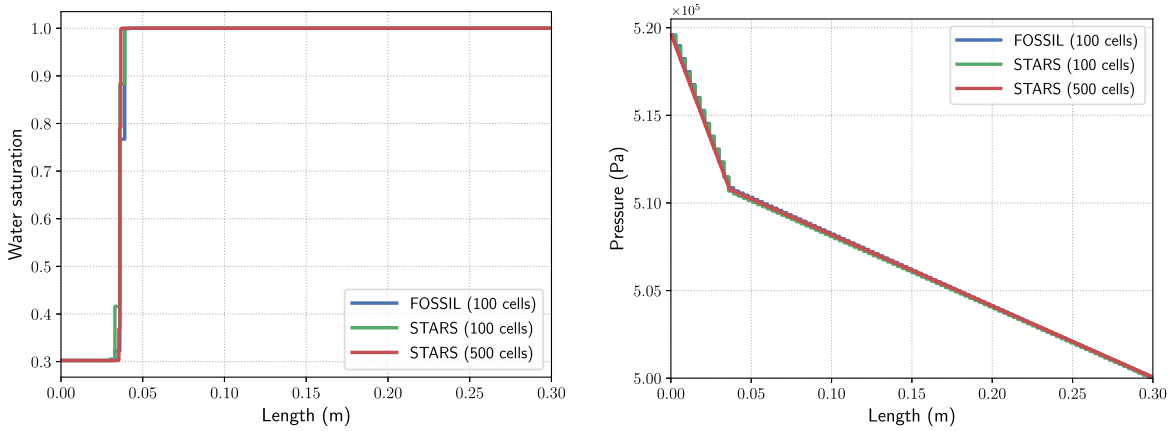

(a) Water saturation.

(b) Pressure.

Source: Prepared by the author.

bottom hole pressure of the injection well is fixed, the well injects less fluid in the medium, and therefore less water is recovered from it.

C.6 Co-injection of Water and Gas at Fixed Flow Rate

In this set of simulations, instead of fixing the bottom hole pressure in the injection well, the gas and water injection flow rates are fixed at 2.33×10^{-7}m^3/s and 5×10^{-8} m^3/s, respectively, resulting in $f_g = 0.82$.

Figure 92 shows the evolution in time of water and gas production rates, while Figure 93 shows the evolution of injection well BHP. Profiles of water saturation and pressure at t=1,140 s are shown in Figure 94.

C.7 Foam Injection at Fixed Flow Rate

In this scenario, foam is injected at a fixed flow rate of 2.83×10^{-7}m^3/s and quality $f_g = 0.82$. All other parameters remain the same as in the previous scenario (co-injection of water and gas at constant flow rate in a water-saturated medium).

The evolution of the BHP of the injector wells and of the water production rate are shown in Figures 95 and 96. The profiles of water saturation and pressure after 1,140 s of the injection of foam can be seen in Figure 97.

Figure 92 – Water and gas production rates as functions of time. Water and gas are co-injected at fixed flow rate.

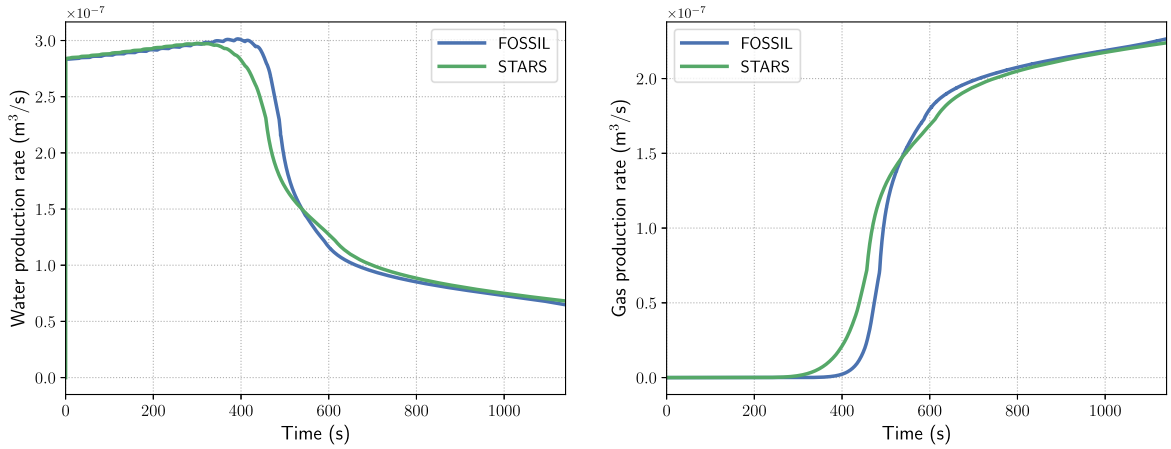

(a) Water production rate.

(b) Gas production rate.

Source: Prepared by the author.

Figure 93 – Evolution of the BHP of the injection well, where water and gas are co-injected at fixed flow rate.

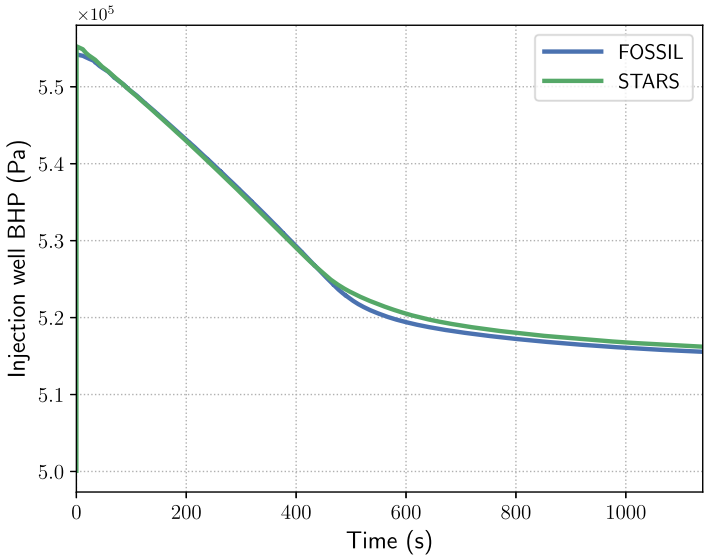

Source: Prepared by the author.

Figure 94 – Profiles of water saturation and pressure after 1,140 s of co-injection of water and gas at constant flow rate.

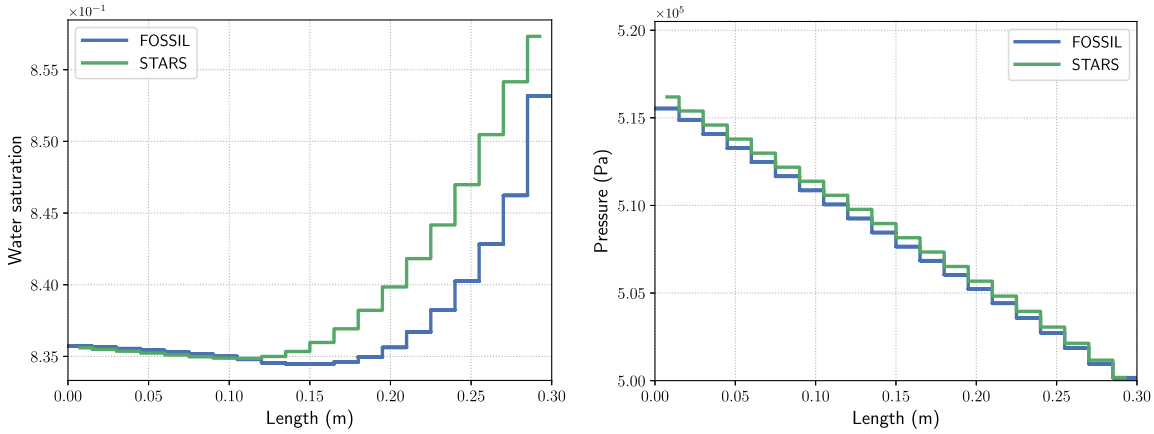

(a) Water saturation.

(b) Pressure.

Source: Prepared by the author.

Figure 95 – Evolution in time of BHP of injector wells during foam injection at fixed rate.

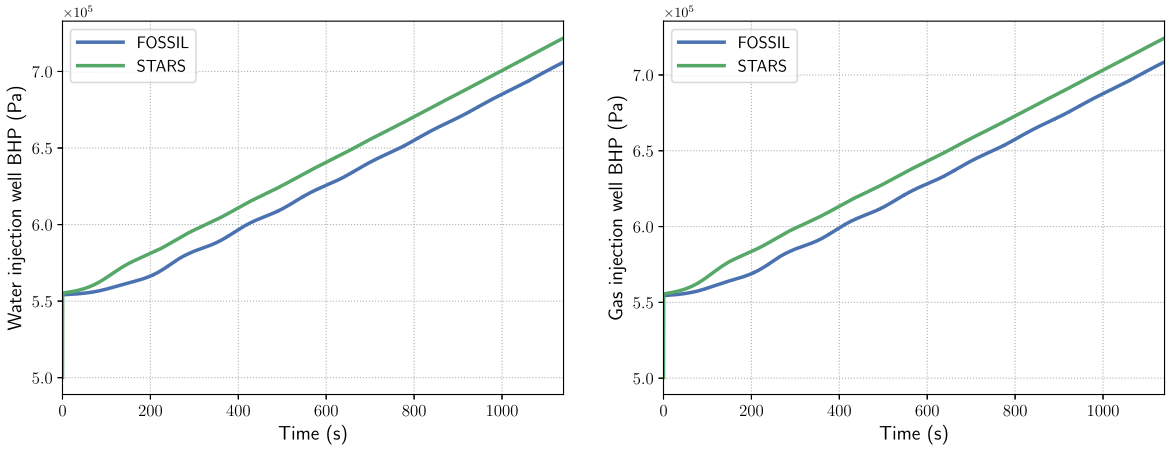

(a) BHP of water injector well.

(b) BHP of gas injector well.

Source: Prepared by the author.

Figure 96 – Water production rate as function of time during foam injection at fixed rate.

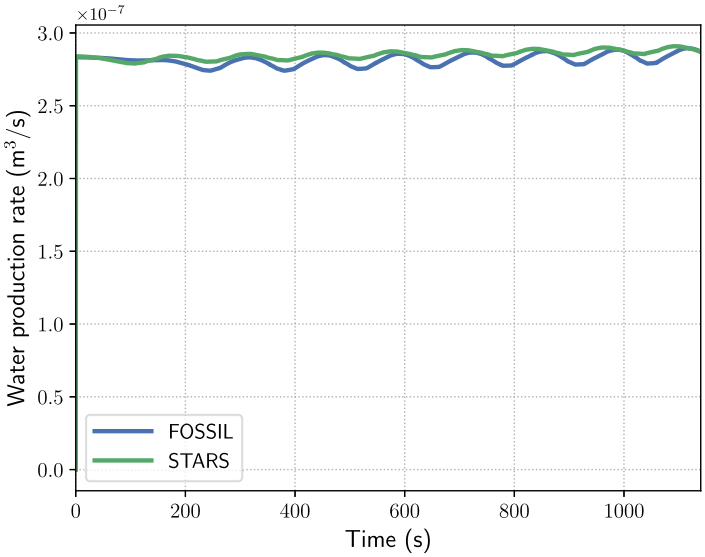

Source: Prepared by the author.

Figure 97 – Profiles of water saturation and pressure after 1,140 s of foam injection at fixed rate.

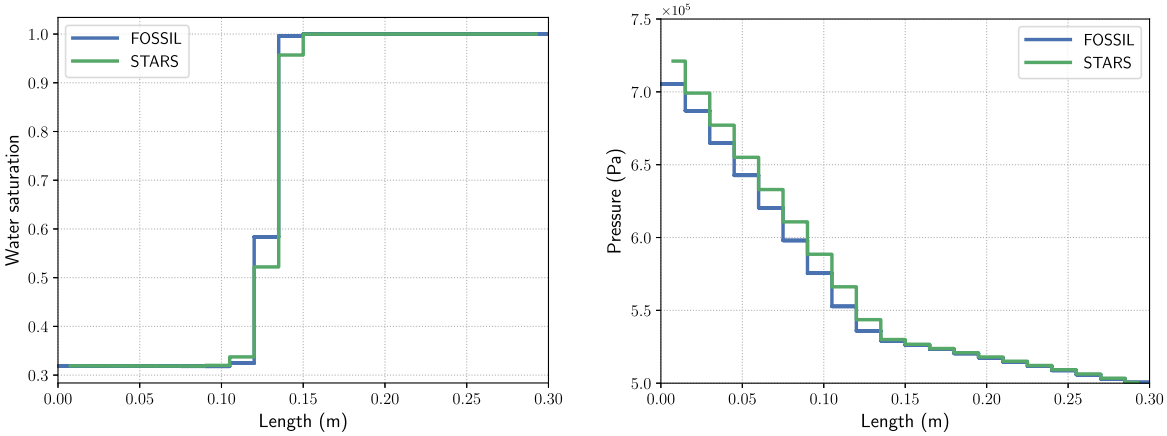

(a) Water saturation.

(b) Pressure.

Source: Prepared by the author.